Exploring kinetics and thermodynamics in fast-ion conductors and hydrogen-storage materials using *ab-initio* molecular dynamics

Brandon C. Wood

B.S., Physics
A.B., Slavic Languages and Literatures
Stanford University, 2001

Submitted to the Department of Materials Science and Engineering
in partial fulfillment of the requirements for the degree of

DOCTOR OF PHILOSOPHY IN MATERIALS SCIENCE AND ENGINEERING

at the

MASSACHUSETTS INSTITUTE OF TECHNOLOGY

September 2007

Author .....
Department of Materials Science and Engineering
July 27, 2007

Certified by .....
Nicola Marzari
Associate Professor of Materials Science and Engineering
Thesis Supervisor

Accepted by .....
Samuel M. Allen
POSCO Professor of Physical Metallurgy
Chair, Department Committee on Graduate Students

Exploring kinetics and thermodynamics in fast-ion conductors and hydrogen-storage materials using *ab-initio* molecular dynamics

Brandon C. Wood

Submitted to the Department of Materials Science and Engineering
on July 27, 2007, in partial fulfillment of the
requirements for the degree of
Doctor of Philosophy in Materials Science and Engineering

Abstract

We investigate the interplay between various kinetic processes and thermodynamic factors in three materials—silver iodide (AgI), cesium hydrogen sulfate ($CsHSO_4$), and sodium alanate ($NaAlH_4$)—using *ab-initio* molecular dynamics simulations.

The time-averaged and instantaneous silver substructure in the fast-ion conductor AgI is analyzed, resulting in a set of ordering rules that govern the distribution of the mobile silvers in the first coordination shell surrounding an iodine. We find evidence of an independent phase transition of the silver ions which drives the structural transformation to the high-mobility phase. A thermodynamic motivation for the existence of fast-ion conduction is suggested in terms of an entropic stabilization associated with the decrease in silver mobility upon melting. We also find a unique chemical signature for the fourth nearest-neighbor silver to an iodine. This fourth silver is weakly bound and relatively unconstrained, and we isolate it as the predominant agent in the diffusion process.

Next, a detailed statistical analysis is performed on simulations of the fuel-cell electrolyte $CsHSO_4$ to isolate the interplay between the dynamics of the O–H chemical bonds, the O$\cdots$H hydrogen bonds, and the SO_4 tetrahedra in promoting proton conduction. A high reversal rate limits the apparent success rate of the otherwise rapid chemical-bond dynamics, which are dominated by the Grotthuss mechanism of proton transfer. Rapid angular hops in concert with small reorientations of the SO_4 tetrahedra constitute a new dominant mechanism for hydrogen-bond network reorganization. The SO_4 dynamics are found to control the attempt rate of chemical-bond dynamical events and the success rate of hydrogen-bond dynamical events; this enables a novel interpretation of the diminished $CsHSO_4/CsDSO_4$ isotope effect. Two distinct timescales for SO_4 reorientation events are linked to different diffusion mechanisms along different crystal directions. Finally, a graph-theoretic analysis of the hydrogen-bond network topology demonstrates an increased likelihood for diffusion in connectivity configurations favoring linear network chains over closed rings.

We have discovered and characterized a new phase (γ) of the hydrogen-storage material $NaAlH_4$ that is energetically close to the known ground state. The manifestation of this phase is kinetically inhibited in the bulk but is favored in a (001) surface slab above 225 K. The transition involves first activating the surface AlH_4 rotational modes. This is followed by a lattice expansion perpendicular to the slab and a shear of successive lattice planes. A possible connection between γ-$NaAlH_4$ and the dehydrogenation product Na_3AlH_6 is suggested. We also show that hydrogen transport in $NaAlH_4$ can be treated independently from the observed phase transition, and that the presence of certain point defects can enable transport of hydro-

gen via a structural diffusion mechanism. A link between long-range hydrogen migration and the rotational mobility of AlH_x groups is demonstrated.

Thesis Supervisor: Nicola Marzari
Title: Associate Professor of Materials Science and Engineering

Acknowledgments

As a project of this magnitude rarely results from the effort of a single individual, I would like to acknowledge those who operated behind the scenes in helping this thesis to materialize. First and foremost, I am enormously grateful to my thesis advisor, Prof. Nicola Marzari, for his patience and tutelage throughout my years at MIT. He taught me not only how to approach scientific problems carefully and creatively but also how to effectively communicate results of my investigations to scientific and non-scientific audiences alike. Indeed, I owe much of what I have become as a scientist to his continual encouragement and enthusiasm.

I am also grateful to my thesis committee, Profs. Wuensch, Ceder, and Yip, for their helpful input in steering my research and helping me with the preparation of this document. Professor Wuensch has been particularly helpful in understanding and interpreting the results of my work on silver iodide. I would also like to thank Prof. Mei-Yin Chou of the Georgia Institute of Technology for our discussions on sodium alanate and for providing the vacancy formation energy calculations.

I would also like to thank the Krell Institute and U.S. Department of Energy Computational Science Graduate Fellowship, which has been a wonderfully enriching academic experience for me and has allowed me to explore research avenues that might otherwise have been closed to me.

I also wish to thank my research colleagues in the group for their invaluable assistance, especially Young-Su, who has been with me in the group since its beginning, answering my every question, whether scientific or logistical; Ismaila, who acted as my aesthetic consultant on my graphs and presentations; and Patrick, who helped me with much of my early molecular dynamics analysis. I'm also grateful for the friendship of Nick, Heather, Boris, and Mike Tambe, who collectively eased my long-time burden as the only American in the group. Thanks also to all of the other group members who have been a part of this journey over the years, including newcomers Nicolas, Elise, and Jivtesh, whose arrival marked a much-needed infusion of fresh ideas, perspectives, and enthusiasm.

Finally, I would like to thank my family and friends for their continual guidance and support during my time in Boston. I'm especially grateful to my sister Marissa and my brother Jason, who provided a wonderful support network for me when I moved to New England. I also want to acknowledge my parents, who taught me to always strive for what seemed outside my reach, and without whom I would undoubtedly not be where I am today. And last but not least, thanks to my wonderful wife Sarah, who has been my anchor these past few months as I have worked to write this thesis, offering me constant encouragement while keeping me nourished with midnight meals of pasta and sandwiches.

Contents

List of Figures

List of Tables

CHAPTER 1

Introduction

"The theory of our modern technic shows that nothing is as practical as theory."

— J. Robert Oppenheimer

1.1 The rise of computational science

FOR CENTURIES, society has dichotomized scientific research into rigid categories of theory and experiment. Scientists have been driven by the maxim that "theory guides, where experiment decides." But with the rise of computational science, we are faced with a novel research paradigm that is not so easily categorizable. Computer simulations draw from both communities by applying sets of rules solidly grounded in theory in order to perform virtual experiments. Such techniques have proven to be tremendously powerful predictive tools and have sped acceptance of computational science as a third pillar of scientific research that can stand on equal ground with its better-known predecessors. In this sense, the success of simulations has forced a basic reshaping of the guiding philosophy of scientific research [1,2].

The theory-experiment dichotomy underscores a still deeper divide in scientific thinking. Since the days of Newton, the physicist's quest has been to reduce the universe to an elegant set of governing equations. Historically, the chemist's approach has been more inductive, looking for commonalities in known reactions in order to extract sets of guidelines for future synthesis. Computer modeling requires faith in both the reductionist and empiricist approaches: empirical laws are extracted from virtual experiments by examining the common behavior of a set of complex interacting systems, each of which in turn evolves in strict accordance with the elegantly fundamental equations of physics. It is an ideal solution for those who embrace both the elegance of theory and the practicality of experiment, and for those who reject the reductionist-empiricist divide. In effect, computation is the sampler platter of

scientific research, representing the very best of seemingly opposite worlds, all rolled into a single package.

A computational "experiment" has the advantage of providing data that is too difficult, too laborious, too dangerous, or too expensive to obtain using traditional methods. The first of these conditions will prove the most relevant in the context of this thesis, since we will generally be exploring phenomena observable only at atomistic length- and timescales. We will also be using simulations to perform various *gedanken* experiments, which can probe the behavior of materials under experimentally unattainable conditions. These include investigating new crystal structures (Chapter 6) or supercooled phases (Chapter 4), as well as fixing specific degrees of freedom in the system (Chapters 4, 5, and 6).

Among the conceptually simplest yet most powerful computational techniques is molecular dynamics (MD), in which the motion of a set of particles is evolved according to Newtonian mechanics. Thermodynamic and kinetic information can then be extracted from the resulting trajectories. The inception of MD dates back to the dawn of the computer age and the early work of Alder and Wainwright [3, 4] on the mainframes at the University of California Radiation Laboratory (today the Lawrence Livermore National Laboratory). The primary focus of these early simulations was to understand the behavior of hard-sphere liquids. The earliest simulation of a realistic system using pair potentials was carried out by Rahman in 1964 on liquid argon [5], which he and Stillinger followed a decade later with the first dynamics simulation of liquid water [6].

More recently, MD has moved beyond the liquid state and is now seeing increasing application in materials science, thanks to recent advances in hardware technology and software algorithms. Much of this has been enabled by the adoption of advanced techniques such as *ab-initio* molecular dynamics (also known as first-principles molecular dynamics), which was popularized following the work of Car and Parrinello in the mid-1980s [7]. In this scheme, no experimental input is provided to the simulation, and the forces on the atoms are calculated using the quantum-mechanical techniques discussed in Chapters 2 and 3 of this thesis. It is worth emphasizing that *ab-initio* techniques are truly predictive and can therefore offer an unbiased description of atomistic behavior in a wide variety of chemical or physical environments. As will be shown repeatedly throughout this work, this allows one to gain insights into structure and dynamics that are inaccessible both to experiment and to simulations based on classical pair potentials. The underlying philosophy of this thesis is to use *ab-initio* molecular dynamics to explore the interplay between various complex dynamical processes, as well as between kinetics and thermodynamics, in select fast-ion conductors and hydrogen-storage materials.

1.2 Fast-ion conduction

Fast-ion conductors—sometimes referred to as *superionic conductors*—are solids that demonstrate liquid-like diffusive behavior for one or more ionic species. Such materials exhibit unusually high values of ionic conductivity, typically of the order 10^{-3} to 1.0 $\Omega^{-1}\cdot cm^{-1}$, but generally have electronic conductivities at least two orders of magnitude lower [8, 9]. Materials of this sort have been known about for centuries and studied in detail for decades. For instance, Faraday reported evidence of fast-ion conduction in the literature in the 1830s [10] while performing experiments on Ag_2S (which, incidentally, is a close relative of AgI, the focus of Chapter 4 of this thesis). He also recorded similar behavior in lead fluoride and mercury periodide [11]. In 1851, Hittorf [12] further investigated Ag_2S and Cu_2S, ultimately concluding that ionic diffusion had to play an important role in the conduction mechanism of these materials. The potential of these and similar materials as solid electrolytes in batteries and fuel cells was realized some time later in the pioneering work of Nernst [13], Haber [14], Katayama [15], and Schottky [16], who are widely credited with ushering in the field known today as *solid-state ionics* [17].

The changing nature of today's energy market has prompted the re-emergence of fast-ion conductors at the forefront of materials science, particularly for use as solid-state electrolytes in fuel cells and ion batteries. More generally, the phenomenon of fast-ion conduction is observable in wide variety of systems from planetary materials under extreme pressure conditions [18–20] to ion channels in biological membranes [21–24]. Fast-ion conductors are also featured ingredients in novel switching [25] and sensing [26, 27] devices and form the basis of certain modern processing techniques [28, 29]. Nevertheless, the detailed atomistic mechanisms involved in ion conduction through these materials remain ill understood, and it seems certain that existing technologies would derive great benefit from a qualitatively and quantitatively accurate description of the phenomenon.

Fast-ion conduction is particularly well suited to a computational investigation based on first principles, in part thanks to the high frequency of diffusion events observable within reasonable simulation timescales. However, to date, there have been very few *ab-initio* MD treatments of the phenomenon, and although some fast-ion conducting systems have been analyzed using classical molecular dynamics, these treatments suffer from the inability of classical potentials to accurately describe interactions in systems featuring a changing chemical environment. Indeed, as will be demonstrated throughout this thesis, accurate treatment of rapid bond breaking and forming is essential for obtaining a valid description of fast-ion conduction.

Chapters 4 and 5 apply *ab-initio* molecular dynamics results in order to characterize the structural, electronic, and thermodynamic properties of two fast-ion conducting systems, as well as to provide insight into the atomistic specifics of fast-ion conduction. Chapter 4 focuses primarily on understanding the thermodynamics of fast-ion conduction and how they relate

to the underlying dynamical structure. Chapter 5 showcases a detailed statistical approach for discovering the complex interplay between various atomistic processes involved in ion conduction and for obtaining information about the kinetics and timescales of each process.

1.3 Solid-state hydrogen storage

Reliable, lightweight onboard hydrogen storage has been identified as one of the key impediments to successful deployment of a vehicular hydrogen infrastructure [30]. Many of today's modern hydrogen fuel-cell designs have their roots in NASA's Apollo and Gemini programs, for which the technology was used to provide both electricity and drinking water [31–33]. Those designs had liquid hydrogen fuel stored onboard the spacecraft in expensive and heavy cryogenic tanks. However, pure hydrogen stored in gaseous or liquid form generally has too low volumetric density for practical use in hydrogen-powered vehicles. Instead, modern deployment of hydrogen-powered vehicles requires an efficient, lightweight storage solution that is also cost effective in order to compete with gasoline-based technologies. As such, research has focused on solid-state materials that have both high volumetric (volume percent) and high gravimetric (weight percent) hydrogen storage densities and also demonstrate quick and reversible hydrogen uptake and release [34].

A 2003 think-tank report on the hydrogen storage situation [35] prompted the U.S. Department of Energy to issue a "Grand Challenge" to the scientific and industrial community. The purpose of the challenge was to develop a reliable hydrogen-storage infrastructure for vehicular fuel cells. The preliminary report highlighted three of the most promising solid-state technologies for further research: metal hydrides, boron-based chemical solutions, and carbon-based materials [36,37]. The material explored in Chapter 6 of this thesis fits into the first of these categories. In particular, it represents a class of materials known as *complex light metal hydrides* [38–40]. These systems draw on the lightest elements in the periodic table to form crystals that can absorb and desorb hydrogen chemically to produce new structures with different stoichiometries [41].

Chapter 6 applies *ab-initio* molecular dynamics techniques to study a well-known but ill-understood complex metal hydride. The approach used in this chapter focuses on exploring the interplay between two component mechanisms necessary for the dehydrogenation process—namely, hydrogen migration and a structural phase transition. In doing so, we will offer an in-depth analysis of the relationship between kinetic and thermodynamic motivations for hydrogen release.

1.4 Thesis outline

The remainder of this thesis is outlined as follows:

- Chapter 2 reviews the basic theoretical framework behind *ab-initio* calculations in periodic solids, including the Born-Oppenheimer adiabatic approximation, density-functional theory and the Kohn-Sham representation, and the plane-wave pseudopotential method. The chapter concludes with a brief look at maximally localized Wannier functions and at a basic methodology for calculating vibrational dynamics from first-principles calculations.

- Chapter 3 extends this review by introducing the fundamentals of performing *ab-initio* molecular dynamics, both using the Born-Oppenheimer approach or the popular Car-Parrinello scheme. Application of extended-Lagrangian methods for simulating systems in other ensembles is also discussed. Finally, we define some of the useful statistical quantities that can be obtained from dynamics results; these will be referred to often in the subsequent chapters.

- Chapter 4 covers results on silver iodide, which represents a classic archetype of a fast-ion conductor. Following introductory comments on the motivation for the study of AgI and a discussion of the various relevant computational parameters, we proceed to characterize the basic structural and vibrational properties of the material. The time-averaged substructure of the silver ions is then discussed, followed by a look at certain rules and restrictions that govern the substructure in an instantaneous picture. Next, we use our results to speculate as to the nature of the transition to the fast-ion conducting phase and the underlying motivations for its existence. The chapter concludes with a discussion of the dynamics of the electronic structure of the system and how it relates to the observed ion conduction.

- In Chapter 5, a detailed statistical analysis is applied to dynamical simulations of $CsHSO_4$, a promising proton-conducting fuel-cell electrolyte candidate. Once the motivation for studying $CsHSO_4$ has been introduced and the simulation details have been discussed, we isolate the two primary microscopic phenomena responsible for proton conduction in the material and discuss the detailed atomistic mechanisms involved in each process. In doing so, we also extract information about the relevant timescales and kinetics from our dynamics results. Next, we gather statistics about the magnitude and timescale of the rotation dynamics of the SO_4 tetrahedral moieties and use this information to suggest two different dominant conduction mechanisms with different limiting factors for diffusion along the two nondegenerate crystallographic axes. We also apply a graph-theoretic analysis to the hydrogen-bond network to extract topologies that are most likely to induce microscopic transport phenomena. Finally, we apply the results of our timescale analysis to explain the lack of a prominent isotope effect in the $CsHSO_4/CsDSO_4$ system.

- Chapter 6 discusses the results of molecular dynamics simulations of sodium alanate, a

complex metal hydride that is being investigated for use as an onboard hydrogen storage material. In particular, we focus on understanding the motivations and mechanisms behind the tetrahydride-to-hexahydride ($NaAlH_4 \rightarrow Na_3AlH_6$) transition. Following an initial discussion of the background and motivation for studying $NaAlH_4$ (including its relationship to fast-ion conductors) and a characterization of the known reactant and product phases, we show that the two relevant ingredients in the phase transition—namely, the structural reorganization and the transport of hydrogen—can be treated independently. Focusing first on the structural transformation, we explore the observed differences between bulk and (001) surface slab simulations of $NaAlH_4$. Motivated by our (001) surface slab results, we report the discovery of a new phase of the tetrahydride that bears a structural resemblance to the hexahydride and offer a timescale analysis to isolate the various stages involved in the lattice reorganization. Next, we discuss how hydrogen mobility may be induced by the inclusion of various point defects and use these results to illuminate possible transport mechanisms for hydrogen and sodium relocation in the lattice. Finally, we integrate our results to speculate on an overall framework to describe dehydrogenation, concluding with a brief discussion on the possible role of transition-metal dopants in enhancing reaction kinetics.

- Chapter 7 begins by summarizing the key findings of each of the three previous chapters. These results are then synthesized into a discussion about the similarities and differences among each of the three materials. We will first describe the importance of the coupling between an electronic transition and one or more classical phonon processes in each material. We will then conclude by remarking on the various ways in which the interplay between ionic diffusion and phase transitions is manifest in our study.

CHAPTER 2

Fundamentals of electronic structure

2.1 The many-body problem

ANY DISCUSSION of modern electronic structure theory begins with an examination of the ground-state many-body Schrödinger equation, which we can write in the following schematic form:

$$\left\{\mathcal{H}_{\text{ion}} + \mathcal{H}_{\text{el}} + \mathcal{H}_{\text{ion-el}}\right\}\Psi_{\text{tot}} = E\Psi_{\text{tot}}. \tag{2.1}$$

Conventionally, the subscripts "el" and "ion" refer to the electrons and nuclei, respectively, although an alternative formulation will be introduced in Section 2.4. The first two terms contain contributions that are limited to just the nuclear system or just the electronic system, whereas the third term refers to all interactions involving both the electrons and the nuclei. However, the simple form of Equation 2.1 betrays the complexity of the underlying physics; directly obtaining the true solution for the total many-body wavefunction Ψ_{tot} is often impossible even for relatively small systems. In order to render a problem of any reasonable magnitude tractable, certain approximations and reformulations must be considered for the three terms in the left-hand side of the equation, each of which introduces a unique set of difficulties in the overall handling of the many-body problem. Much of the remainder of this chapter is devoted to an exploration of the following approaches toward the efficient and accurate handling of the three contributions to the Hamiltonian:

- the *Born-Oppenheimer adiabatic approximation* for isolating the nuclear degrees of freedom in $\mathcal{H}_{\text{ion}}$ (Section 2.2);
- *density-functional theory* for dealing with the ground-state electronic interactions in $\mathcal{H}_{\text{el}}$ (Section 2.3); and
- the *plane-wave pseudopotential framework* for more efficient calculation of interactions be-

tween electrons and ions in $\mathcal{H}_{\text{ion-el}}$ within a plane-wave basis set (Section 2.4).

We will conclude with a brief exploration of a pair of techniques grounded in electronic structure theory that are relevant to this work: the *Wannier function approach*, which introduces a powerful technique for the visualization of localized electronic orbitals in extended systems (Section 2.5); and *linear response theory*, which outlines a method for calculating the full phonon dispersion of a crystal within the harmonic approximation (Section 2.6).

2.2 The Born-Oppenheimer adiabatic approximation

The difference in the electronic and nuclear masses gives rise to electronic motion that is much faster than nuclear motion. In practice, this gives rise to a clear separation of the corresponding frequencies of interest, particularly for multi-electron atoms. This fact can be exploited, leading to a decoupling of the nuclear degrees of freedom from those of the electrons. The key to isolating the nuclear dynamics, thereby simplifying the $\mathcal{H}_{\text{ion}}$ term in Equation 2.1, resides in the application of two well-known approximations: the *adiabatic approximation* and the *Born-Oppenheimer approximation* [42, 43]. The two are often referred to collectively as the *Born-Oppenheimer adiabatic approximation*.

2.2.1 The adiabatic approximation

We begin by defining a basis of "electronic" eigenfunctions Ψ_i with corresponding eigenvalues $\mathcal{E}_i$, which themselves are solutions to the Hamiltonian obtained by letting the nuclear masses M_I go to infinity and solving the resulting problem in the potential field generated by the fixed nuclei:

$$\left\{\lim_{M_I\to\infty}\mathcal{H}\right\}\Psi_i(\vec{\mathbf{R}},\vec{\mathbf{r}}) = \left\{-\frac{\hbar^2}{2m_e}\sum_j\nabla_j^2 + V(\vec{\mathbf{R}},\vec{\mathbf{r}})\right\}\Psi_i(\vec{\mathbf{R}},\vec{\mathbf{r}}) = \mathcal{E}_i(\vec{\mathbf{R}}). \tag{2.2}$$

Here $\vec{\mathbf{R}}$ refers to the complete set of M nuclear coordinates $\{\mathbf{R}_1,\ldots,\mathbf{R}_M\}$; $\vec{\mathbf{r}}$ refers to the complete set of N electronic coordinates $\{\mathbf{r}_1,\ldots,\mathbf{r}_N\}$; and the index j runs over the electrons in the system. We can then expand the solution for the total wavefunction Ψ_{tot} in the basis of the electronic eigenfunctions Ψ_i:

$$\Psi_{\text{tot}}(\vec{\mathbf{R}},\vec{\mathbf{r}}) = \sum_i \Psi_i(\vec{\mathbf{R}},\vec{\mathbf{r}})\Phi_i(\vec{\mathbf{R}}). \tag{2.3}$$

Note that the coefficients Φ_i of the expansion must be functions of the nuclear positions to ensure completeness of the exact formulation for the solution to the full Hamiltonian.

Mathematically, the adiabatic approximation amounts to replacing the sum in Equation 2.3 by a single term, such that

$$\Psi_{\text{tot}}(\vec{\mathbf{R}},\vec{\mathbf{r}}) \approx \Psi_i(\vec{\mathbf{R}},\vec{\mathbf{r}})\Phi_i(\vec{\mathbf{R}}) \tag{2.4}$$

for the i^{th} excitation state. The physical result of this substitution is to neglect any coupling of the electronic eigenfunctions Ψ_i due to motion of the nuclei. The underlying rationale is that the motion of the nuclei is extremely slow compared to that of the electrons and therefore contributes negligibly to off-diagonal coupling terms in the representation of the total wavefunction Ψ_{tot}. The condition is usually applied to the electronic ground state, given that coupling between the ground- and first excited states is generally weakest. In this case, Equation 2.4 becomes

$$\Psi_{\text{tot}}(\vec{\mathbf{R}}, \vec{\mathbf{r}}) \approx \Psi_0(\vec{\mathbf{R}}, \vec{\mathbf{r}})\Phi_0(\vec{\mathbf{R}}). \tag{2.5}$$

When written in this way, we can interpret the adiabatic approximation by stating that from the point of view of the nuclei, the electrons can be assumed to always be in their ground state, which in turn is a function of the nuclear potential field.

The extent to which the ground-state adiabatic approximation is valid depends on how well the Ψ_0 obtained from the infinite-mass limit describes the true electronic ground state of the full Hamiltonian. As such, the accuracy of the method improves as the nuclear masses increase. Also, nonadiabatic coupling between the ground- and first excited states is minimized when the energetic difference between these eigenvalues can be assumed to be large when compared with the energetics of the nuclear motion, as is generally the case for semiconducting or insulating systems. For metals, where this difference is small, the adiabatic approximation can generally be justified as long as the plasma frequency is much larger than the energetics of the nuclear motion [44].

2.2.2 The Born-Oppenheimer approximation

The second step in separating the nuclear degrees of freedom from those of the electrons is contained within the Born-Oppenheimer approximation. We begin by rewriting the full Hamiltonian in the following form, substituting for the total wavefunction Ψ_{tot} within the ground-state adiabatic approximation:

$$\left\{-\frac{\hbar^2}{2}\sum_I \frac{1}{M_I}\nabla_I^2 + \mathcal{E}_i(\vec{\mathbf{R}})\right\}\Psi_0(\vec{\mathbf{R}}, \vec{\mathbf{r}})\Phi_0(\vec{\mathbf{R}}) \approx E\Psi_0(\vec{\mathbf{R}}, \vec{\mathbf{r}})\Phi_0(\vec{\mathbf{R}}), \tag{2.6}$$

with the index I running over all ions in the system. The underlying assumption in the Born-Oppenheimer approximation is that the electronic wavefunctions Ψ_i have only a weak dependence on the nuclear configuration, such that all derivatives of Ψ_i with respect to the nuclear coordinates can be safely ignored. This allows the nuclear kinetic energy operator in Equation 2.6 to act solely on the Φ_0 component of the ground-state adiabatic wavefunction. The end result is the formulation of a decoupled "nuclear" Schrödinger equation, in which ground-state ionic motion takes place on the potential energy surface defined by the electronic

eigenvalue $\mathcal{E}_0$:

$$\left\{-\frac{\hbar^2}{2}\sum_I \frac{1}{M_I}\nabla_I^2 + \mathcal{E}_0(\vec{\mathbf{R}})\right\}\Phi_0(\vec{\mathbf{R}}) \approx E\Phi_0(\vec{\mathbf{R}}). \tag{2.7}$$

For ease of computation, Equation 2.7 can usually be replaced by its classical analog, whose Hamiltonian can be written

$$\mathcal{H}_{\text{ion}} = \frac{1}{2}\sum_I M_I \dot{R}_I^2 + \mathcal{E}_0(\vec{\mathbf{R}}). \tag{2.8}$$

This is generally justifiable for atoms other than hydrogen, relying on the assumption that nuclear dynamics for such atoms are predominantly classical. Hydrogen dynamics may also be well approximated classically, but this must be substantiated on a case-by-case basis.

The potential energy surface $\mathcal{E}_0(\vec{\mathbf{R}})$ obtained by calculating the ground-state electronic energy as a function of the nuclear coordinates in the Born-Oppenheimer adiabatic limit is often referred to as the *Born-Oppenheimer surface*. It is worthwhile noting at this time that although we followed a wavefunction formulation in our derivation, the formalism applies equally well to the electronic-density formulation discussed in the following section.

2.3 Density-functional theory

In the mid-1960's, a milestone development in computational chemistry was achieved with the introduction of density-functional theory (DFT), which in the forty or so years since has become an established framework for dealing with the complex electronic interactions in the many-body Schrödinger equation. Moreover, the formulation of DFT is widely regarded as the key facilitator for mainstream adaptation of electronic-structure theory to real-world problems, prompting Walter Kohn's award of the 1998 Nobel Prize for chemistry [45].

Density-functional theory is more than simply a way of obtaining and expressing a solution to the ground-state electronic many-body Schrödinger equation; rather, it represents a complete reformulation of the equation itself. Its essence lies in restating the electronic problem using the electronic density scalar field $n_0(\mathbf{r})$ as the fundamental variable, which, neglecting any dependence on the nuclear configuration $\vec{\mathbf{R}}$, is connected to the many-body N-electron wavefunction $\Psi_0(\vec{\mathbf{r}})$ via the following relation:

$$n_0(\mathbf{r}) = N\int\cdots\int|\Psi_0(\mathbf{r}_1,\ldots,\mathbf{r}_N)|^2\,d\mathbf{r}_1\cdots d\mathbf{r}_N \tag{2.9}$$

In addition to the obvious conceptual benefit in formulating the many-body Schrödinger equation in terms of the experimentally measurable electronic density rather than the mathematical construct of the wavefunction, this has the notable effect of reducing the effective number of independent position variables in the electronic system from $3N$ to a much more manageable 3.

The basic framework that we use to solve the electronic problem via DFT can be laid out in two essential steps. In Section 2.3.1, we introduce the *Hohenberg-Kohn theorems*, which establish the ground-state electronic density as the new fundamental variable in the formulation of the quantum problem. Section 2.3.2 discusses the *Kohn-Sham representation*, which exploits the Hohenberg-Kohn theorems to map the interacting many-body problem to that of a system of noninteracting fictitious particles in an effective potential. In the process, we return the system to an orbital-dependent formulation but acquire a method for accurately approximating the unknown density functional. The ground-state properties of the original system can then be extracted from the fictitious system without loss of generality.

2.3.1 The Hohenberg-Kohn theorems

We start by expressing the Hamiltonian for the electronic states in the following form, having separated out the nuclear components under the Born-Oppenheimer approximation described in Section 2.2:

$$\mathcal{H}_e \equiv \mathcal{H}_{\text{el}} + \mathcal{H}_{\text{el-ion}} = -\frac{\hbar^2}{2m_e}\sum_j \nabla_j^2 + \sum_j V_{\text{ext}}(\mathbf{r}_j) + \frac{1}{2}\sum_{j\neq k}\frac{e^2}{|\mathbf{r}_j - \mathbf{r}_k|}, \tag{2.10}$$

where the summation index j runs over all N electrons in the system. The quantity V_{ext} is the "external" potential that arises from the action of the fixed nuclei on the electrons. Note that Equation 2.10 does not include the nuclear-nuclear interaction potential; this can easily be added in later. Treating the nuclear configuration only in terms of a fixed external potential now allows us to drop any explicit dependence of relevant quantities on the nuclear coordinates $\vec{\mathbf{R}} = \{\mathbf{R}_1, \ldots, \mathbf{R}_M\}$.

The first Hohenberg-Kohn theorem [46] establishes a unique one-to-one correspondence between the ground-state electronic density $n_0(\mathbf{r})$ and the external potential $V_{\text{ext}}(\mathbf{r})$ which gives rise to it. Thus, the external potential can be uniquely obtained from the ground-state electronic density to within an additive constant. This in turn means that in principle, the full electronic Hamiltonian—and consequently, all ground-state and excited-state system properties—can be generated by only a knowledge of $n_0(\mathbf{r})$, neglecting a shift in the energy.

Since the electronic Hamiltonian is uniquely determinable from the ground-state electronic density, we can write the expectation value of the Hamiltonian in Equation 2.10 using $n_0(\mathbf{r})$ as the fundamental variable:

$$\mathcal{V}_0 \equiv \langle \Psi_0[n_0] | \, \mathcal{H}_e \, | \Psi_0[n_0] \rangle = T_{\text{el}}[n_0] + E_{\text{el-el}}[n_0] + \int V_{\text{ext}}(\mathbf{r})\, n_0(\mathbf{r})\, \mathrm{d}\mathbf{r}, \tag{2.11}$$

where the terms containing n_0 in brackets now represent *functionals* of $n_0(\mathbf{r})$, or mappings of the Hilbert space of density functions onto a scalar field. Note that we have also expressed the electronic wavefunction Ψ_0 as a functional of $n_0(\mathbf{r})$. The first term on the right-hand side

represents the kinetic energy of the interacting electronic system. The second term contains all internal electron-electron interaction terms. The third term, which can now be expressed explicitly in terms of the electronic density, is the electronic interaction with the external potential.

The second Hohenberg-Kohn theorem proceeds by establishing a variational approach for the electronic energy functional in Equation 2.11 and defining a *universal functional* F_{HK} of the electronic density $n(\mathbf{r})$ as follows [46]:

$$F_{\mathrm{HK}}[n] \equiv T_{\mathrm{el}}[n] + E_{\mathrm{el-el}}[n]. \tag{2.12}$$

The functional $F_{\mathrm{HK}}[n]$ is universal in the sense that it contains no explicit dependence on the external potential $V_{\mathrm{ext}}(\mathbf{r})$ or, by extension, the nuclear configurations. The total-energy functional for the electronic system can then be written as

$$E_{\mathrm{HK}}[n] = F_{\mathrm{HK}}[n] + \int V_{\mathrm{ext}}(\mathbf{r})\, n(\mathbf{r})\, \mathrm{d}\mathbf{r}. \tag{2.13}$$

The variational character of $E_{\mathrm{HK}}[n]$ means the minimum, ground-state value $n_0(\mathbf{r})$ of the electronic density corresponds to the minimum, ground-state value of the electronic total-energy functional:

$$\mathcal{V}_0 = \min_n \left\{ E_{\mathrm{HK}}[n] \right\} = E_{\mathrm{HK}}[n_0]. \tag{2.14}$$

The above minimization, subject to the constraint that $\int n(\mathbf{r})\, \mathrm{d}\mathbf{r}$ recovers the total number of electrons N, yields the actual ground-state energy $\mathcal{V}_0$ of the electronic system within the Born-Oppenheimer adiabatic limit. The original proof required the minimization to take place over the subset of possible functions $n(\mathbf{r})$ that are *V-representable*, meaning they can be expressed as ground-state solutions to the electronic Hamiltonian in the presence of some well-defined external potential V_{ext}. However, subsequent reformulations of density-functional theory [47–49] have relaxed this restriction. It should also be noted that the functional $E_{\mathrm{HK}}[n]$ gives no explicit information about excited states.

2.3.2 The Kohn-Sham representation

Despite the elegant simplicity of the Hohenberg-Kohn theorems, their full potential was not realized until the development of the Kohn-Sham single-particle orbital representation. Recognizing the significance of the ground-state electronic density in determining much of the relevant physics of the full many-body problem, Kohn and Sham [50] derived a method for mapping the complex physical system of interacting electrons onto a much simpler fictitious system of *noninteracting* electrons that gives rise to the same ground-state electronic density $n_0(\mathbf{r})$ and therefore possesses the same ground-state physical properties.

The Kohn-Sham mapping imagines a set of N independent, noninteracting electrons that

give rise to N independent, single-particle Schrödinger equations, each acting in a local effective potential designated by v_{KS}. In this case, the equation for the j^{th} noninteracting particle ($j \in \{1, \ldots, N\}$) is given by:

$$\mathcal{H}^{\mathrm{KS}}\psi_j \equiv \left\{-\frac{\hbar^2}{2m_e}\nabla^2 + v_{\mathrm{KS}}\right\}\psi_j = \varepsilon_j\psi_j. \tag{2.15}$$

In order to ensure that the system of fictitious electrons reproduces the correct ground-state electronic density, we add an additional restriction on the eigenfunctions of Equation 2.15:

$$n_0(\mathbf{r}) = \sum_j^{\mathrm{occ}} f_j|\psi_j(\mathbf{r})|^2, \tag{2.16}$$

where the index j runs over all of the occupied orbitals, and f_j indicates the occupancy of the j^{th} Kohn-Sham state ($f_j = 2$ for a nonmagnetic, spin-independent calculation). The eigenfunctions ψ_j in Equations 2.15 and 2.16 are known as the *Kohn-Sham orbitals*, and the corresponding eigenvalues ε_j are known as the *Kohn-Sham energies*. In general, only the sum of the Kohn-Sham energies has any physical meaning; however, the magnitude of the Kohn-Sham energy for the highest occupied state has a special physical significance as the ionization energy.

It remains to find a form for the effective local potential v_{KS}, which contains the relevant physics of the Kohn-Sham representation. To do so, we first return to the universal functional F_{HK} from Equation 2.12, which Kohn and Sham proposed could be written in the following general form:

$$F_{\mathrm{HK}}[n] = T[n] + \frac{e^2}{2}\iint \frac{n(\mathbf{r})\,n(\mathbf{r}')}{|\mathbf{r}-\mathbf{r}'|}\,\mathrm{d}\mathbf{r}\,\mathrm{d}\mathbf{r}' + E_{\mathrm{xc}}[n]. \tag{2.17}$$

Here $T[n]$ is the kinetic energy term, and the electron-electron interaction has been split into a *Hartree* contribution representing the classical Coulomb interaction of the electron density $n(\mathbf{r})$ with itself, and an *exchange-correlation* contribution E_{xc} that contains all of the remaining quantum many-body interactions present in $E_{\mathrm{el-el}}[n]$.

The resulting expression for the electronic ground-state energy of the interacting system becomes

$$\mathcal{V}_0 = E_{\mathrm{HK}}[n_0] = T[n_0] + \int V_{\mathrm{ext}}(\mathbf{r})\,n_0(\mathbf{r})\,\mathrm{d}\mathbf{r} + \frac{e^2}{2}\iint \frac{n_0(\mathbf{r})\,n_0(\mathbf{r}')}{|\mathbf{r}-\mathbf{r}'|}\,\mathrm{d}\mathbf{r}\,\mathrm{d}\mathbf{r}' + E_{\mathrm{xc}}[n_0]. \tag{2.18}$$

The above equation is identical for the noninteracting system, with the kinetic energy now expressed in terms of the Kohn-Sham orbitals:

$$T_{\mathrm{KS}} = \sum_j^{\mathrm{occ}} -\frac{\hbar^2}{2m_e} f_j \langle\psi_j|\nabla^2|\psi_j\rangle \tag{2.19}$$

It is a straightforward exercise to extract from Equations 2.18 and 2.19 the external potential

$v_{\mathrm{KS}}(\mathbf{r})$ of the noninteracting system that gives rise to the proper ground-state electronic density $n_0(\mathbf{r})$:

$$v_{\mathrm{KS}}(\mathbf{r}) = V_{\mathrm{ext}}(\mathbf{r}) + e^2 \int \frac{n(\mathbf{r}')}{|\mathbf{r} - \mathbf{r}'|}\, \mathrm{d}\mathbf{r}' + \frac{\delta E_{\mathrm{xc}}[n]}{\delta n(\mathbf{r})}. \tag{2.20}$$

The potential $v_{\mathrm{KS}}(\mathbf{r})$ from Equation 2.20 can be supplied to Equation 2.15, which together with the constraint of Equation 2.16 forms a complete set of expressions describing the Kohn-Sham scheme. However, the potential depends on the electronic density according to Equation 2.20, but the electronic density also depends on the potential according to Equations 2.15 and 2.16. The solution is to solve the set of equations *self-consistently*. The conventional procedure for doing so is as follows:

1. An initial guess is made for the electronic density $n(\mathbf{r})$, say from a superposition of the atomic orbitals.
2. The potential $v_{\mathrm{KS}}(\mathbf{r})$ is calculated based on this density using Equation 2.20.
3. The result is inserted into Equation 2.15, and the Hamiltonian is diagonalized to obtain the Kohn-Sham orbitals $\psi_j(\mathbf{r})$.
4. A new guess for the electronic density is made from these eigenfunctions using Equation 2.16, and the process is repeated until a predefined convergence threshold is achieved.

Alternative methods for solving the self-consistent Kohn-Sham equations can be derived if one considers directly minimizing the electronic energy functional in Equation 2.18 with respect to the Kohn-Sham orbitals $\psi_j(\mathbf{r})$. In practice, this is often done in an iterative dynamics scheme by introducing a fictitious time variable, as is the case for the well-known *steepest descent* [51] and *conjugate gradient* [52] algorithms. This is also the basic principle underlying the Car-Parrinello method [7], which is discussed in detail in Section 3.3, as well as the closely related damped-dynamics approach [53]. In such cases, one must be careful to impose an appropriate orthonormality constraint on the Kohn-Sham orbitals, which can be done using the method of Lagrange multipliers.

2.3.3 Exchange-correlation functionals

It should be noted that the expression for the total energy as stated in Equation 2.18 is an *exact* representation for the actual ground-state electronic energy within the Born-Oppenheimer adiabatic approximation. However, up to this point we have avoided any discussion of how to obtain an explicit representation for the exchange-correlation functional $E_{\mathrm{xc}}[n]$.

The exchange-correlation functional is so named because it contains two primary quantum-mechanical contributions to the total electronic energy: the exchange and correlation energies. The *exchange energy* results from the Pauli exclusion principle and the antisymmetrization of the wavefunction, and amounts physically to a change in the quantum-mechanical energy due

to wavefunction overlap. The *correlation energy* is a quantum many-body effect describing how the probability of finding an electron at a particular position can depend on the positions of the other electrons in the system[†]. In particular, inclusion of correlation tends to decrease the likelihood of finding electrons at short distances from one another.

An exact formulation for the universal exchange-correlation functional $E_{\text{xc}}[n]$ remains elusive, and it is in this term that the exact nature of the density-functional approach breaks down. However, certain proposed approximations have proven extremely successful in accurately describing the physical properties of a wide variety of systems. The first of these was the *local density approximation* (LDA), proposed by Kohn and Sham in their original paper [50]. Within LDA, E_{xc} is calculated by integrating over all space the exchange-correlation energy density $e_{\text{xc}}^{\text{homo}}$ for a homogeneous electron gas, with the homogeneous electronic density replaced at each point by the actual electronic density $n_0(\mathbf{r})$ of the inhomogeneous system:

$$E_{\text{xc}}^{\text{LDA}} = \int e_{\text{xc}}^{\text{homo}}[n_0(\mathbf{r})]\, n_0(\mathbf{r})\, \mathrm{d}\mathbf{r}. \tag{2.21}$$

Initially, it was thought that LDA would apply only to systems featuring a slowly varying density. In practice, however, it has been shown to work well for a large number of systems of physical interest, including many with very inhomogeneous distributions (this is partly due to the satisfaction of sum rules, as pointed out in References [54] and [55]).

More recently, a number of modifications to the LDA approach have been widely adopted. Some of these introduce additional dependence on the gradient of the density $|\nabla n_0(\mathbf{r})|$ and as such fall under the umbrella of the *generalized gradient approximation* (GGA). Popular GGA formulations include that of Perdew and Wang (PW91) [56], and the Perdew, Burke, and Ernzerhof (PBE) formulation [57] that is used throughout this work. Gradient-corrected exchange-correlation functionals typically reduce the binding energy with respect to LDA [58,59], which often leads to better agreement with experiment.

2.4 The plane-wave pseudopotential framework

2.4.1 The plane-wave basis set

Up to this point, our discussion has treated the total electronic wavefunction $\Psi_0(\mathbf{r})$ and the Kohn-Sham orbitals $\psi_j(\mathbf{r})$ in abstract mathematical terms. In any practical implementation requiring wavefunction characterization, it is necessary to select a basis set in which to represent the problem. Isolated systems, such as atoms and molecules, tend to be well suited to descriptions based on Gaussian[‡] or atomic-orbital basis sets; as such, these are the most common

[†]The correlation energy can also be thought of as the error introduced in approximating the many-body wavefunction by a single Slater determinant, as is done in the Hartree-Fock approach.

[‡]Gaussians demonstrate improper exponential decay behavior, but they are nonetheless useful for Hartree-Fock based approaches.

approaches for quantum chemical calculations. On the other hand, for extended systems, it is often convenient to select a basis set consisting of mutually orthonormal plane waves. This section describes the procedure for doing so.

In principle, an infinite system requires full treatment of an infinite number of electrons. However, this difficulty can be circumvented by exploiting the natural periodicity of the lattice. The extended system is instead treated as an infinitely repeated array of *supercells*, each of which contains a sufficiently large sample of the ions in the system. At the supercell edges, we impose *periodic boundary conditions*, meaning opposite sides of a cell are assumed identical. This leads to a periodicity with the cell size for the nuclear potential, i.e., $V_{\text{ext}}(\mathbf{r}) = V_{\text{ext}}(\mathbf{r}+\mathbf{R}')$ for a real-space cell-cell separation given by the Bravais lattice vector $\mathbf{R}'$. The supercell method allows one to accurately treat an infinite extended system in a finitely representable manner without introducing surfaces or isolated samples. This approach also minimizes finite-size effects in simulations containing defects, since relevant physical quantities demonstrate rapid convergence with respect to supercell size in such instances. Accordingly, the method may also be applied to study surface slabs, point defects, or even isolated systems, provided the supercell size is chosen so as to remove any unphysical correlation effects between successive periodic images.

Within the periodic plane-wave scheme, we can make use of *Bloch's Theorem* [60] to write an electronic wavefunction in reciprocal space as a sum of plane waves over the reciprocal lattice vectors $\mathbf{G}$ of the extended system. Bloch noted [61] that the eigenfunction of a periodic system can be expressed as the product of two terms:

$$\psi_{j\mathbf{k}}(\mathbf{r}) = u_{j\mathbf{k}}(\mathbf{r})\, \mathrm{e}^{\mathrm{i}\mathbf{k}\cdot\mathbf{r}}. \tag{2.22}$$

The first term on the right-hand side is a function $u_{j\mathbf{k}}$ that carries the same periodicity as the nuclear potential; the second term represents the equation for a plane wave. Note that when written in this way, the wavefunction $\psi_{j\mathbf{k}}(\mathbf{r})$ acquires an additional index referring to the wavevector $\mathbf{k}$, which is stipulated to lie within the first Brillouin Zone (BZ). The periodic part $u_{j\mathbf{k}}$ can be further expanded in terms of the reciprocal lattice vectors $\mathbf{G}$ as follows:

$$u_{j\mathbf{k}}(\mathbf{r}) = \sum_{\mathbf{G}} C_{j\mathbf{k}}(\mathbf{G})\, \mathrm{e}^{\mathrm{i}\mathbf{k}\cdot\mathbf{r}}. \tag{2.23}$$

Equations 2.22 and 2.23 together identify $\psi_{j\mathbf{k}}$ as a *Bloch state*.

The overall electronic density $n(\mathbf{r})$ can then be calculated by summing the contribution from each of the occupied Bloch states at a given $\mathbf{k}$-point and integrating the result over all $\mathbf{k}$-points within the BZ:

$$n(\mathbf{r}) = \int_{\mathrm{BZ}} \sum_{j}^{\mathrm{occ}} f_j |\psi_{j\mathbf{k}}(\mathbf{r})|^2 \, \mathrm{d}\mathbf{k}. \tag{2.24}$$

As before, the sum runs over the occupied states, and f_j denotes the occupancy of the j^{th} state. Although the integral in Equation 2.24 in principle involves a continuous sum over every k-point in the system, it is sufficient to replace the integral with a sum over discrete k-points, usually a Monkhorst-Pack mesh [62–64] designed to take advantage of the symmetry of the system. In fact, for larger supercells consisting of multiple unit cells of a mostly periodic lattice, such as those common in finite-temperature dynamical simulations of crystalline systems or in point defect calculations, the integral is often sampled only at the BZ origin $\mathbf{k} = (0, 0, 0)$, also known as the Γ-*point*. This can be justified by considering that the supercell BZ of a perfect crystal contains folded contributions from each component unit cell, meaning the band structure at the Γ-point also features bands from each component unit cell. Single-**k** point sampling is also commonly employed in systems with very low symmetry, since in such instances the addition of extra k-points yields little new information. Note that the accuracy of the Γ-point sampling method generally improves as the size of the supercell increases, since reciprocal-lattice spacing is inversely proportional to real-lattice spacing.

It is straightforward to derive an expression for the kinetic energy of each plane wave:

$$T_{|\mathbf{k}+\mathbf{G}|} = \frac{\hbar^2 |\mathbf{k}+\mathbf{G}|^2}{2m}. \tag{2.25}$$

Equation 2.25 highlights one of the advantages of a plane-wave basis set. Since kinetic energy increases monotonically with $|\mathbf{k}+\mathbf{G}|$, convergence can be easily controlled by considering only those plane waves with a kinetic energy below a predefined cutoff E_{cut}. This corresponds to truncating the summation over **G**-vectors in Equation 2.23, resulting in a finite basis set that can be systematically improved given any atomic arrangement until a converged solution is obtained. This in turn helps to ensure that energies of successive timesteps in a dynamical simulation are computed with similar accuracy.

Plane-wave basis sets have additional advantages over competing alternatives [53]. Plane waves are delocalized and position independent, making them ideally suited for calculations in extended systems. This also means many quantities of relevant physical interest are particularly simple to calculate, including energies, forces, and stresses.

2.4.2 The pseudopotential approximation

Despite their usefulness, plane waves display certain disadvantages when applied to real systems. The most obvious is the unacceptably large number of plane waves that can be required to depict the electronic wavefunction in the vicinity of the nucleus. In this region, the wavefunctions of the valence electrons can have many nodes owing to the imposition of orthogonality constraints (this is particularly true for larger atoms, since nodality depends on the principal quantum number). In addition, the wavefunctions of the tightly bound core electrons are highly localized (see Figure 2-1). Both conditions necessitate inclusion of high-frequency

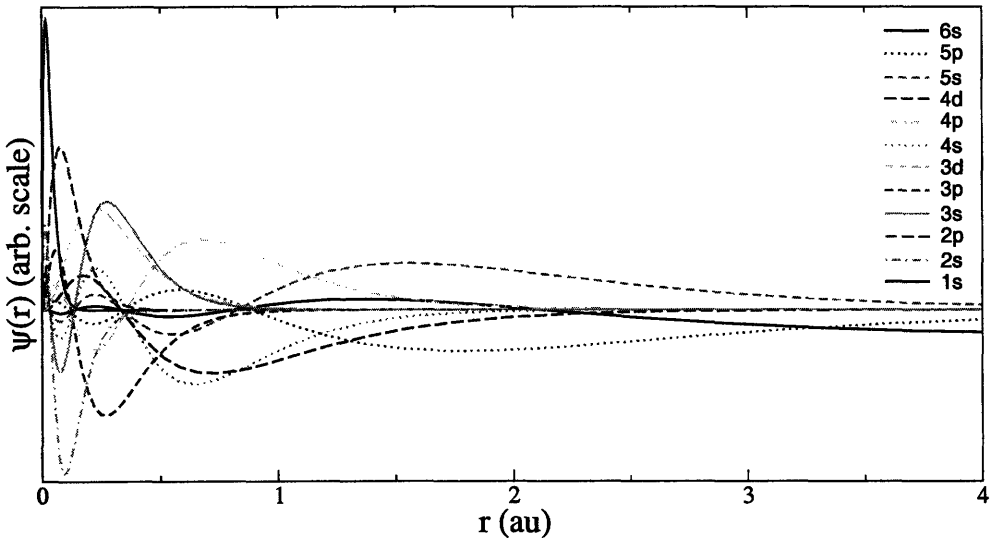

FIGURE 2-1: Radial electronic wavefunctions from an all-electron calculation of cesium ([Xe]$6s^1$).

plane waves for an accurate description, resulting in an unacceptably high value of E_{cut}. A solution to this problem can be found in the *pseudopotential approximation*, which replaces the actual nuclear potential in the electron-ion interaction terms with a much weaker counterpart engineered to retain the chemically relevant behavior of the full potential.

The basic method involves redefining the term "ion" in Equation 2.1 to include not only the atomic nuclei but also the core electrons. The rationale for doing so is that the core electrons are generally tightly bound to the nuclei and contribute little to chemical bonding, meaning they change negligibly in real systems with respect to the isolated atom case. The core electrons therefore act primarily to screen the nuclear potential. Accordingly, the "electrons" are redefined to refer only to the valence states, which in turn interact with the screened potential. For many elements, choosing which electronic states should be included in the core is a non-trivial exercise and must be decided on a case-by-case basis by combining physical intuition with reliable test calculations.

The net result of this reformulation is the replacement of the full nuclear potential with a much weaker *pseudopotential* V^{PS}. In this scheme, the valence electrons acquire a nodeless wavefunction in a potential that outside the core region replicates the effects of nuclear attraction, as well as Coulombic repulsion and orthogonality constraints with respect to the core electrons. The simplified problem is designed to maintain optimal *transferability*, meaning it will reproduce the behavior of the all-electron system in a variety of real chemical environments. In particular, good transferability requires that the pseudo-system properly replicate the chemical hardness (defined as the change in orbital eigenvalues with changes in orbital occupancies), the excitation energies, and the scattering properties of the all-electron system. In practice, it is generally sufficient to ensure transferability for a chemically relevant energy

range, usually within several electron volts of the electronic valence energy for the atomic configuration.

Norm-conserving pseudopotentials

In 1979, Hamann, Schlüter, and Chiang (HSC) [65] outlined a series of criteria for the generation of pseudopotentials that simplify the electronic wavefunction description in a plane-wave basis while ensuring accurate replication of the consequences of wavefunction orthogonality and maintaining good transferability. All modern *norm-conserving pseudopotentials* are rooted in the fulfillment of the HSC conditions, although specific recipes vary. The authors recognized that since scattering is an angular-dependent property, a transferable pseudopotential should be *nonlocal*, meaning it should act differently on each angular momentum channel. However, scattering phenomena are relevant only in the core region near the nucleus, so it is sufficient to create a *semilocal* pseudopotential consisting of a local component $V^{\mathrm{loc}}(r)$, which acts uniformly on all angular momentum channels, and a nonlocal component $V_\ell^{\mathrm{nloc}}(r)$, which acts differently on each angular momentum channel ℓ but is relevant only in the core region. The HSC method therefore defines a core cutoff radius R_c, which determines the extent of the nonlocal portion, resulting in a pseudopotential of the form

$$V^{\mathrm{PS}}(r) = \begin{cases} V^{\mathrm{loc}}(r) & \text{if } r \geq R_c \\ V^{\mathrm{loc}}(r) + \sum_{\ell,m} |Y_{\ell m}\rangle V_\ell^{\mathrm{nloc}}(r) \langle Y_{\ell m}| & \text{if } r < R_c \end{cases}, \tag{2.26}$$

where $Y_{\ell m}$ are the spherical harmonics. In the valence region ($r \geq R_c$), the fully local pseudopotential $V^{\mathrm{PS}}(r)$ is constructed to match the all-electron potential $V^{\mathrm{AE}}(r)$, and the radial pseudo-wavefunctions $\psi^{\mathrm{PS}}(r)$ match the radial all-electron wavefunctions $\psi^{\mathrm{AE}}(r)$ (here we have dropped the wavefunction indices j and k for simplicity of notation). At $r = R_c$, the radial pseudo-wavefunction is required to be continuous, as are its first and second derivatives. The HSC conditions also necessitate that the eigenvalues $\varepsilon_\ell^{\mathrm{PS}}$ of the pseudo-system faithfully reproduce the eigenvalues $\varepsilon_\ell^{\mathrm{AE}}$ of the all-electron system for each valence state. An additional stipulation is that pseudo-wavefunctions should be *norm conserving*, meaning $\langle \psi_{\ell m}^{\mathrm{PS}} | \psi_{\ell m}^{\mathrm{PS}} \rangle = 1$ for each angular momentum channel ℓ, m. This ensures that the pseudo-wavefunctions generate the proper total electronic density. Combining this with the restriction that $\psi^{\mathrm{PS}}(r) = \psi^{\mathrm{AE}}(r)$ for $r \geq R_c$ gives

$$\int_0^R |\psi^{\mathrm{PS}}(r)|^2 \, \mathrm{d}r = \int_0^R |\psi^{\mathrm{AE}}(r)|^2 \, \mathrm{d}r \tag{2.27}$$

for all $R \geq R_c$, which is the usual statement of norm conservation [58].

An identity introduced by Shaw and Harrison [66] relates Equation 2.27 to a condition on

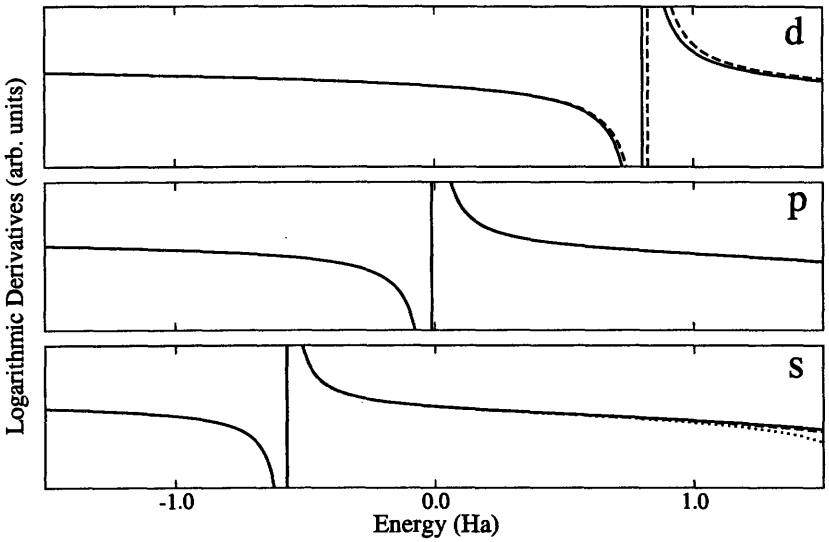

FIGURE 2-2: Wavefunction logarithmic derivatives for the *s*, *p*, and *d* angular momentum channels of chlorine, calculated at a radius of 2.52 au and a reference energy corresponding to the eigenenergy of the highest occupied orbital. Solid lines represent the results for the all-electron calculation, dashed lines are the results using a semilocal pseudopotential for the valence states, and dotted lines are the equivalent results using the Kleinman-Bylander separable form for the pseudopotential.

the logarithmic derivatives for $R \geq R_c$:

$$2\pi\Big((r\psi)^2 \frac{d}{d\varepsilon}\frac{d}{dr}\ln\psi\Big)\Big|_R = 4\pi\int_0^R \psi^2 r^2\,dr. \tag{2.28}$$

Equation 2.28 is relevant for faithful reproduction of the scattering properties, which require agreement of the logarithmic derivatives and their energy derivatives for the pseudo- and all-electron wavefunctions (this results from the fact that phase shifts in the Born approximation are related to logarithmic derivatives [67]). In the case of the energy derivative, agreement is explicitly forced at some reference energy ε_{ref}, leading to an additional pair of closely related equations that must hold for $R > R_c$:

$$\frac{d}{dr}\Big(\ln\psi^{\text{PS}}(r)\Big)\Big|_R = \frac{d}{dr}\Big(\ln\psi^{\text{AE}}(r)\Big)\Big|_R. \tag{2.29}$$

and

$$\frac{d}{dr}\frac{d}{d\varepsilon}\Big(\ln\psi^{\text{PS}}(r)\Big)\Big|_{R,\varepsilon_{\text{ref}}} = \frac{d}{dr}\frac{d}{d\varepsilon}\Big(\ln\psi^{\text{AE}}(r)\Big)\Big|_{R,\varepsilon_{\text{ref}}}. \tag{2.30}$$

The restrictions in Equations 2.29 and 2.30 represent probably the most significant contribution of the HSC scheme, since they offer an implicit guarantee of good transferability from the perspective of scattering. The general behavior of the logarithmic derivative in Equation 2.30 is depicted graphically in Figure 2-2.

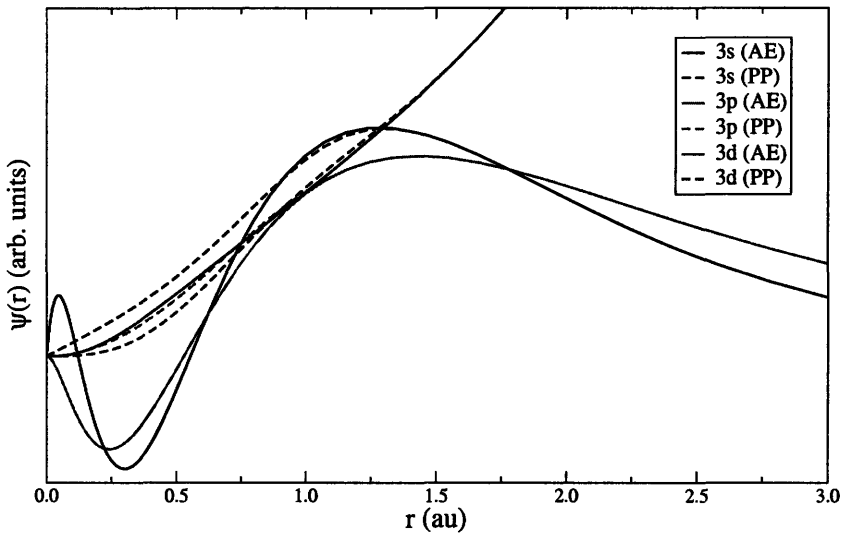

FIGURE 2-3: Comparison between pseudo- and all-electron radial wavefunctions for the 3*s*, 3*p*, and 3*d* (unoccupied) channels of chlorine. Solid lines represent the all-electron wavefunctions; dashed lines are the pseudo-wavefunctions.

The HSC pseudopotential criteria have the useful effect of removing all core-region nodes in the pseudo-wavefunctions $\psi_{\ell m}^{\mathrm{PS}}(r)$, thereby ensuring a low plane-wave cutoff E_{cut} for valence shells of larger atoms. As an example, Figure 2-3 illustrates the valence pseudo-wavefunctions with respect to their all-electron counterparts for the case of chlorine.

The electron-ion interaction potential for the periodic pseudosystem is calculated in reciprocal space as a sum of pseudopotential contributions from each of the reciprocal lattice points. For a local pseudopotential, the form of each contribution can be written as

$$V_{\mathrm{crys}}(\mathbf{G}) = \sum_{s} S_s(\mathbf{G}) V^{\mathrm{PS}}(\mathbf{G}), \tag{2.31}$$

where the index s runs over the ionic species in the system, and S_s represents the structure factor for species s, whose formula is given by

$$S_s(\mathbf{G}) = \sum_{i} \mathrm{e}^{\mathrm{i}\,\mathbf{G}\cdot\mathbf{R}_i}. \tag{2.32}$$

For the nonlocal part of the pseudopotential, the contribution to the total electron-ion interaction energy $E_{\mathrm{el-ion}}$ from angular momentum state ℓ, m is calculated in the following manner:

$$E_{\mathrm{el-ion};\,\ell m} = \sum_{\mathbf{G},\mathbf{G}'} \left\langle \psi^{\mathrm{PS}} \middle| Y_{\ell m} \right\rangle V_{\mathrm{crys}}(\mathbf{G}-\mathbf{G}') \left\langle Y_{\ell m} \middle| \psi^{\mathrm{PS}} \right\rangle. \tag{2.33}$$

However, the sum in Equation 2.33 presents a significant difficulty in terms of computation,

since as written it is not separable into independent sums over G and G′. This results in a computational cost that scales as the square of the number of plane waves in the finite basis set. A simple solution to this difficulty was suggested by Kleinman and Bylander [68]. They proposed replacing the nonlocal part $V_\ell^{\rm nloc}(r)$ of the pseudopotential in Equation 2.26 with a new operator of the form $E_{\ell m}^{\rm KB}|\xi_{\ell m}(r)\rangle\langle\xi_{\ell m}(r)|$ that acts on the wavefunction in much the same manner as $V_\ell^{\rm nloc}(r)$ (in particular, it is identical when applied to $|Y_{\ell m}\rangle$ but not when applied to a generic wavefunction). The expressions for the new quantities $E_{\ell m}^{\rm KB}$ and $\xi_{\ell m}(r)$ are defined as follows:

$$\xi_{\ell m}(r) \equiv \frac{V_\ell^{\rm nloc}(r)\psi_{\ell m}^{\rm PS}(r)}{\langle\psi_{\ell m}^{\rm PS}|(V_\ell^{\rm nloc})^2|\psi_{\ell m}^{\rm PS}\rangle^{1/2}} \tag{2.34}$$

and

$$E_{\ell m}^{\rm KB} \equiv \frac{\langle\psi_{\ell m}^{\rm PS}|(V_\ell^{\rm nloc})^2|\psi_{\ell m}^{\rm PS}\rangle}{\langle\psi_{\ell m}^{\rm PS}|V_\ell^{\rm nloc}|\psi_{\ell m}^{\rm PS}\rangle}. \tag{2.35}$$

For $r < R_c$, Equation 2.26 then becomes:

$$V^{\rm PS}(r) = V^{\rm loc}(r) + \sum_{\ell,m} \frac{|\psi_{\ell m}^{\rm PS}\, V_\ell^{\rm nloc}\rangle\langle V_\ell^{\rm nloc}\, \psi_{\ell m}^{\rm PS}|}{\langle\psi_{\ell m}^{\rm PS}|V_\ell^{\rm nloc}|\psi_{\ell m}^{\rm PS}\rangle} \tag{2.36}$$

It is a straightforward exercise to show that writing the pseudopotential using the Kleinman-Bylander representation allows separation of the sum in Equation 2.33 into the product of two sums. This allows the electron-ion interaction energy to be calculated with a computational cost that scales linearly with the size of the plane-wave basis set. However, Gonze et al. [69,70] showed that constructing separable Kleinman-Bylander pseudopotentials can in some cases lead to unphysical "ghost states" that are not represented in the set of all-electron eigenvalues. As such, proper care must be taken in the generation process, and pseudopotentials should be tested for proper transferability and for the absence of ghost states.

Since the work of Hamann, Schlüter, and Chiang, there have been a number of improvements to pseudopotential methodology. One is the inclusion of relativistic effects, enabling proper calculation of the spin-orbit coupling [71,72]. Another important modification, known as *nonlinear core correction*, compensates for false screening resulting from an overlap of core and valence states [73]. Nonlinear core correction enables good transferability for single-electron pseudopotentials in the case of alkali metals, for instance.

Ultrasoft pseudopotentials

An entirely new alternative to the norm-conserving pseudopotential was introduced by Vanderbilt in 1990 [74,75]. The motivation for doing so was that certain atoms, particularly those in the first rows of the periodic table, have highly localized charge densities in their valence shells as well as the core. This is particularly true for *2p*, *3d*, and *4f* elements, since these angular momentum channels contain no orthonormality repulsion from shells with lower princi-

pal quantum numbers. For such elements, implementing a norm-conserving pseudopotential scheme does little to reduce the total number of plane waves required by the problem. Recognizing that the primary limitation of the traditional method resides in the norm-conserving constraint of Equation 2.27, Vanderbilt proposed easing this restriction in the ℓ-dependent core channels, resulting in a formalism for the generation of smoother *ultrasoft pseudopotentials* that can substantially reduce the size of the plane-wave basis set in certain cases.

The ultrasoft method adopts a generalized eigenvalue formalism [76], whereby pseudo-wavefunctions are obtained by solving a generalized eigenvalue problem in the presence of the pseudopotential (the superscript "US" is used to distinguish from the norm-conserving case):

$$\left(\mathcal{H} - \varepsilon_j \mathcal{S}\right)\psi_j^{\mathrm{US}} = 0. \tag{2.37}$$

Here $\mathcal{S}$ is an overlap operator that can be expressed in terms of the augmentation charges Q_{jk}, which are related to the deviation of the pseudo-wavefunctions from the condition of norm conservation:

$$\mathcal{S} = \mathbb{I} + \sum_{j,k} Q_{jk} |\beta_j\rangle\langle\beta_k|. \tag{2.38}$$

The functions β_j are projector functions that depend on the ionic positions $\vec{\mathbf{R}}$. Mathematically, the Q_{jk} are defined as follows:

$$Q_{jk} = \int_0^{R_c} \left\{ \left[\psi_j^{\mathrm{AE}}(r)\right]^* \psi_k^{\mathrm{AE}}(r) - \left[\psi_j^{\mathrm{US}}(r)\right]^* \psi_k^{\mathrm{US}}(r) \right\} \mathrm{d}r. \tag{2.39}$$

Inclusion of these augmentation charges allow the system to recover the correct charge density. The introduction of the overlap operator $\mathcal{S}$ also requires a redefinition of the orthonormality condition on the ultrasoft wavefunction $\psi_j^{\mathrm{US}}(r)$:

$$\left\langle \psi_j^{\mathrm{US}} \middle| \mathcal{S} \middle| \psi_k^{\mathrm{US}} \right\rangle = \delta_{jk}. \tag{2.40}$$

In generating the ultrasoft pseudopotential, the generalized eigenvalues ε_j in Equation 2.37 can be matched to their corresponding all-electron values at as many energies j as required, enabling improved transferability.

2.5 The Wannier function approach

In characterizing interatomic bond interactions and valence charge distributions in periodic systems, it is often useful to examine the electronic wavefunctions in a localized basis set rather than an extended plane-wave basis. As such, Wannier proposed expressing the electronic wavefunction in a basis of atomic-like orthonormal orbitals w that span the same Hilbert space as the Bloch functions of Equation 2.22 but are localized in real space [77]. These *Wannier*

functions are generated from a Fourier transform of the Bloch states $\psi_{j\mathbf{k}}$:

$$w_{j\mathbf{R}'} = \frac{\Omega}{(2\pi)^3} \int_{\mathrm{BZ}} \psi_{j\mathbf{k}} e^{-\mathrm{i}\,\mathbf{k}\cdot\mathbf{R}'}\, \mathrm{d}\mathbf{k}, \tag{2.41}$$

where Ω refers the volume of the cell in real space. Note that the index $\mathbf{k}$ representing the wavevector in the Bloch state has been replaced by an index $\mathbf{R}'$ representing the real-space Bravais lattice vector in the Wannier function.

The general definition of the Wannier function as given in Equation 2.41 suffers from lack of uniqueness, however: multiplication of the Bloch function by any arbitrary phase factor will in general result in a different expression for $w_{j\mathbf{R}'}$, despite the fact that doing so leaves all physical observables unchanged. In addition, the Bloch states can be mixed together in any arbitrary fashion when generating the Wannier functions, leading to the more general formula

$$w_{j\mathbf{R}'} = \frac{\Omega}{(2\pi)^3} \int_{\mathrm{BZ}} \sum_{i}^{\mathrm{occ}} U_{ij} \psi_{i\mathbf{k}} e^{-\mathrm{i}\,\mathbf{k}\cdot\mathbf{R}'}\, \mathrm{d}\mathbf{k}. \tag{2.42}$$

Marzari and Vanderbilt [78] dealt with this indeterminacy by transforming the Bloch states into a representation designed to minimize the real-space spread η of the Wannier function, defined as

$$\eta = \sum_{j}^{\mathrm{occ}} \left\{ \langle w_{j\mathbf{0}} | r^2 | w_{j\mathbf{0}} \rangle - \langle w_{j\mathbf{0}} | \mathbf{r} | w_{j\mathbf{0}} \rangle^2 \right\}. \tag{2.43}$$

The Wannier functions that minimize this spread functional are referred to as *maximally localized Wannier functions* (MLWFs). As the name suggests, MLWFs give a highly localized description of the wavefunctions, making them particularly useful for analyzing and visualizing chemical bonding [79]. The centers of the MLWFs have an additional interesting property: for an insulating system, the net sum of their displacement vectors from the ion centers gives an expression corresponding to the total polarization of the cell [78].

2.6 Lattice dynamics from first principles

The various lattice-dynamical properties of a crystalline system—for example, phonon dispersions, infrared absorption, and Raman spectra—can be calculated from first principles using *linear-response theory*, which implements a first-order perturbative approach to ordinary density-functional theory [80, 81]. Although the details of the method are beyond the scope of this introduction, we will briefly outline the basic framework used for extracting the interatomic force constants and the full phonon dispersion from linear response.

Before proceeding, it should be emphasized this formulation assumes the Born-Oppenheimer adiabatic approximation, with the nuclei treated as classical particles (see Section 2.2). Within the context of linear-response theory, this translates to the statement that lattice-dyna-

mical properties are entirely determined by the nuclear dynamics on the Born-Oppenheimer surface, which is obtained as the solution to the electronic system for a configuration of fixed ions and as such is a function of the ion positions alone.

All of the basic physics of linear-response theory is contained in the various derivatives of the total energy E, calculated within the Born-Oppenheimer adiabatic approximation. We begin by introducing a set of perturbative displacements from equilibrium for the ions in the system as $\vec{\mathbf{u}} = \{u^{\alpha}_{I\tau}\}$, where I and τ represent the ion and supercell indices, respectively, and α represents the Cartesian direction of the displacement. The total energy can then be expanded as follows:

$$E(\vec{\mathbf{u}}) = E^{(0)} + \frac{1}{2}\sum_{I,\tau}\sum_{J,\tau'}\sum_{\alpha,\alpha'}\left(\frac{\partial^2 E}{\partial R^{\alpha}_{I\tau}\partial R^{\alpha'}_{J\tau'}}\right)u^{\alpha}_{I\tau}u^{\alpha'}_{J\tau'} + \ldots, \tag{2.44}$$

where $E^{(0)}$ represents the total energy of the equilibrium configuration. Note that we have neglected the first-order term in the expansion, since it contains the forces on the ions, which are zero at equilibrium:

$$\sum_{I,\tau}\sum_{\alpha}\frac{\partial E}{\partial R^{\alpha}_{I\tau}}u^{\alpha}_{I\tau} = -\sum_{I,\tau}\sum_{\alpha}F^{\alpha}_{I\tau}u^{\alpha}_{I\tau} = 0. \tag{2.45}$$

The second derivatives of the energy surface determine the interatomic force constants $C^{\alpha\alpha'}_{I\tau,J\tau'}$, which collectively describe the force response of ion I in supercell τ along Cartesian direction α to a displacement $u^{\alpha'}_{J\tau'}$ of ion J in supercell τ' along Cartesian direction α':

$$C^{\alpha\alpha'}_{I\tau,J\tau'} \equiv \frac{\partial^2 E}{\partial R^{\alpha}_{I\tau}\partial R^{\alpha'}_{J\tau'}}. \tag{2.46}$$

We now apply the *harmonic approximation* [82], in which the displacements $\vec{\mathbf{u}}$ from equilibrium are sufficiently small, allowing us to neglect all terms higher than second order in Equation 2.44. In this limit, the forces on the ions are linear with the displacements, and vibrational modes ω can be approximated by harmonic oscillations. Introducing the frequency response and scaling by the nuclear masses allows us to write

$$-\omega^2 M_I\, u^{\alpha}_{I\tau} = -\sum_{J,\tau'}\sum_{\alpha'}C^{\alpha\alpha'}_{I\tau,J\tau'}\, u^{\alpha}_{I\tau}. \tag{2.47}$$

Equation 2.47 can be reformulated as a secular equation involving a matrix whose eigenvalues produce the various vibrational modes ω_i of the system:

$$\det\left|\frac{1}{\sqrt{M_I M_J}}C^{\alpha\alpha'}_{I\tau,J\tau'} - \omega^2\mathbb{I}\right| = 0. \tag{2.48}$$

The periodicity of the system invites application of Bloch's Theorem [60], permitting decoupling of the crystal vibrational frequencies ω for each wavevector $\mathbf{k}$. Equation 2.48 is

thereby transformed into reciprocal space and becomes

$$\det \left| \frac{1}{\sqrt{M_I M_J}} \tilde{C}_{IJ}^{\alpha\alpha'}(\mathbf{k}) - \omega^2(\mathbf{k})\mathbb{I} \right| = 0. \tag{2.49}$$

Here $\tilde{C}_{IJ}^{\alpha\alpha'}(\mathbf{k})$ denotes the Fourier transform of the interatomic force constant matrix $C_{I\tau,J\tau'}^{\alpha\alpha'}$ and has the form

$$\tilde{C}_{IJ}^{\alpha\alpha'}(\mathbf{k}) = \frac{1}{N_c} \sum_{\tau,\tau'} C_{I\tau,J\tau'}^{\alpha\alpha'} e^{-i\mathbf{k}\cdot(\mathbf{R}_\tau - \mathbf{R}_{\tau'})}, \tag{2.50}$$

where N_c represents the number of periodic supercells in the crystal. The first term in Equation 2.49 is often expressed instead as the *dynamical matrix* $D_{IJ}^{\alpha\alpha'}(\mathbf{k})$:

$$D_{IJ}^{\alpha\alpha'}(\mathbf{k}) \equiv \frac{1}{\sqrt{M_I M_J}} \tilde{C}_{IJ}^{\alpha\alpha'}(\mathbf{k}), \tag{2.51}$$

The full phonon dispersion $\omega(\mathbf{k})$ is derived from the collective spectrum of square-rooted eigenvalues of the dynamical matrix at each wavevector $\mathbf{k}$. Given the interatomic force constants, the eigenvalue spectrum can be obtained by solving Equation 2.48.

In principle, the force constants can be calculated manually by displacing each ion within the linear regime and calculating the energy and the corresponding Hellman-Feynman force. However, this approach is limited to eigenvalue calculations $\omega(\mathbf{k})$ at $\mathbf{k}$-vectors that are compatible with the lattice periodicity. Although theoretically speaking, one can combat this difficulty by increasing the supercell size, doing so rapidly adds to the computational expense, and an infinite cell size would be required for a complete sampling of reciprocal space. A perturbative approach on the density functional is far more flexible and powerful, allowing one to sample eigenvalues at any arbitrary $\mathbf{k}$-vector. The detailed methodology for calculating the energy derivative in Equation 2.46 within density-functional perturbation theory can be found in References [81] and [80].

CHAPTER 3

First-principles molecular dynamics

3.1 Introduction

MOLECULAR DYNAMICS (MD) provides a simple yet powerful technique for sampling local configurational space given a set of initial ionic coordinates $\vec{\mathbf{R}} = \{\mathbf{R}_1, \ldots, \mathbf{R}_M\}$. It is ideally suited to problems for which static total-energy calculations are insufficient, such as probing reaction kinetics or visualizing the specific pathways and mechanisms involved in transport phenomena. It can also be used to explore free energy surfaces at finite temperatures. Moreover, a variety of useful thermodynamic properties can generally be obtained from MD simulation results by time averaging appropriate statistical quantities (see Section 3.5).

The basic methodology of classical molecular dynamics is grounded in Newtonian mechanics and has changed little since its original formulation in the late 1950s [4]. Essentially, it involves the deterministic propagation of particle trajectories in response to the instantaneous forces acting on them. These forces are calculated by differentiating the total energy $E(\vec{\mathbf{R}})$, such that the Newtonian equation of motion for particle $I \in \{1, \ldots, M\}$ can be written as

$$M_I \ddot{\mathbf{R}}_I = -\frac{\partial E(\vec{\mathbf{R}})}{\partial \mathbf{R}_I} = \mathbf{F}_I. \tag{3.1}$$

Equation 3.1 is then discretized and integrated numerically in time to obtain the trajectories.

One of the most popular discretization schemes is the Verlet algorithm [83]. The algorithm is particularly useful because it is both time reversible and symplectic (i.e., conserves volume in phase space) [84], meaning it accumulates minimal additional error as a dynamics simulation progresses. In practice, this allows for good long-term energy conservation, facilitating lengthy, well-behaved simulations. It is also extremely fast and memory efficient [85] but nonetheless retains reasonably good accuracy, with numerical integration errors of the order $\mathcal{O}\{(\Delta t)^4\}$. Initial ionic positions are specified along with initial velocities, from which ionic

positions at the previous timestep are linearly extrapolated backwards in time. The algorithm then predicts subsequent configurations as follows:

$$\mathbf{R}_I(t+\Delta t) = 2\mathbf{R}_I(t) + \mathbf{R}_I(t-\Delta t) + \frac{(\Delta t)^2}{M_I}\mathbf{F}_I(t). \tag{3.2}$$

An alternative but mathematically equivalent formulation known as the *velocity Verlet algorithm* [86, 87] is sometimes used instead. In this formulation, the ionic velocities are used directly in conjunction with the forces to compute the trajectories, and the velocities and positions are propagated independently:

$$\mathbf{R}_I(t+\Delta t) = \mathbf{R}_I(t) + \Delta t\,\dot{\mathbf{R}}_I(t) + \frac{(\Delta t)^2}{2M_I}\mathbf{F}_I(t) \tag{3.3}$$

$$\dot{\mathbf{R}}_I(t+\Delta t) = \dot{\mathbf{R}}_I(t) + \frac{\Delta t}{2M_I}\Big[\mathbf{F}_I(t+\Delta t) + \mathbf{F}_I(t)\Big]. \tag{3.4}$$

Regardless of the specific integration algorithm used, the timestep increment for the discretization must be sufficiently small to ensure that the calculated instantaneous force on each ion is a good approximation to the real force over the course of the timestep Δt.

3.2 Born-Oppenheimer molecular dynamics

Nearly all implementations of molecular dynamics based upon first principles are straightforwardly adapted from classical MD using Equation 3.1. This relies on the assumption that the ions can be safely approximated as classical point particles, which is justified for most systems (although for certain systems, such as those containing hydrogen, this claim must be substantiated on a case-by-case basis). We further assume we are operating under the Born-Oppenheimer adiabatic approximation (see Section 2.2), such that the nuclear and electronic degrees of freedom are separable and the electrons follow the motion of the nuclei in their instantaneous ground state. We can then calculate the forces on the ions using the *Hellman-Feynman theorem*, which states that

$$\mathbf{F}_I = -\frac{\partial E}{\partial \mathbf{R}_I} = -\left\langle \Psi_0 \middle| \frac{\partial \mathcal{H}_e}{\partial \mathbf{R}_I} \middle| \Psi_0 \right\rangle - \frac{\partial E_{\text{ion-ion}}}{\partial \mathbf{R}_I}. \tag{3.5}$$

Here Ψ_0 is the ground-state electronic wavefunction and $\mathcal{H}_e$ is the electronic Hamiltonian, defined within the Born-Oppenheimer adiabatic approximation according to Equation 2.10. The term $E_{\text{ion-ion}}$ refers to the classical Coulombic repulsive energy between the ions. If we assume that the external potential V_{ext} is local, the first term on the right-hand side of Equation 3.5 can also be formulated in terms of the electronic density $n(\mathbf{r})$ as follows:

$$-\left\langle \Psi_0 \middle| \frac{\partial \mathcal{H}_e}{\partial \mathbf{R}_I} \middle| \Psi_0 \right\rangle = -\int \frac{\partial V_{\text{ext}}(\mathbf{r})}{\partial \mathbf{R}_I}\, n(\mathbf{r})\, \mathrm{d}\mathbf{r}. \tag{3.6}$$

When $n(\mathbf{r})$ is calculated within the single-particle Kohn-Sham representation (Section 2.3), Equations 3.1, 3.5, and 3.6 generate a complete recipe for *Born-Oppenheimer molecular dynamics*. In this scheme, a fully self-consistent minimization is performed at each timestep to yield the proper electronic density, which is used to obtain the electronic energy of the current configuration. The Hellman-Feynman forces are calculated, and the Verlet algorithm (Equation 3.2) or some other approach is employed at each timestep to generate the nuclear trajectories from the forces. The energy of the new configuration is then calculated, and the process is repeated.

3.3 Car-Parrinello molecular dynamics

Although Born-Oppenheimer molecular dynamics is conceptually simple and relatively easy to implement, it requires a complete, self-consistent solution of the Kohn-Sham equations for every timestep. For systems of appreciable size, this calculation can become very computationally expensive, limiting the overall effectiveness of the method as a practical tool. A solution was devised in 1985 with the development of *Car-Parrinello molecular dynamics* [7,75], which outlines a scheme to *simultaneously* propagate the ions and find the electronic ground state, thereby dramatically reducing calculation time.

Recognizing that in the Kohn-Sham representation the total energy E in Equation 3.5 depends on the set of single-particle orbitals $\{\psi_j\}$ as well as the ionic positions $\vec{\mathbf{R}}$, Car and Parrinello proposed treating the Kohn-Sham electronic wavefunctions themselves as independent classical dynamical variables. The total energy can then be recast as a functional $E^{\mathrm{CP}}[\vec{\mathbf{R}}, \{\psi_j\}]$ describing the potential energy surface parameterized by the "configurations" of $\vec{\mathbf{R}}$ and $\{\psi_j\}$. It should be noted that this new functional E^{CP} contains the classical ion-ion repulsive energy, plus contributions from each of the terms in Equation 2.18: the Kohn-Sham kinetic energy, the interaction energy with the external potential, the Hartree energy, and the exchange-correlation energy. The total energy is recovered upon minimization with respect to $\{\psi_j\}$. The fictitious "coordinates" of each ψ_j are taken to be the coefficients of the respective plane-wave expansion, and a corresponding fictitious mass and classical kinetic energy are introduced. In principle, the entire system can then be relaxed in a dynamical scheme until the new energy functional is minimized, at which point the coordinates of the virtual electronic particles are extracted as the plane-wave coefficients of the actual ground-state Kohn-Sham system.

The classical Lagrangian of the Car-Parrinello system is given by:

$$\mathcal{L}^{\mathrm{CP}} = \frac{1}{2}\sum_j \mu \langle \dot{\psi}_j | \dot{\psi}_j \rangle + \frac{1}{2}\sum_I M_I \dot{\mathbf{R}}_I^2 - E^{\mathrm{CP}}[\vec{\mathbf{R}}, \{\psi_j\}] + \sum_{jk} \Lambda_{jk}\Big\{\langle \psi_j | \psi_k \rangle - \delta_{jk}\Big\}, \qquad (3.7)$$

where μ is the fictitious generalized mass corresponding to the electronic wavefunctions ψ_j. The first term on the right-hand side of the equation represents the classical kinetic energy of the fictitious electronic dynamics, and the final term is introduced as an orthonormality

constraint on the wavefunctions. The constraint is imposed using the method of Lagrange multipliers, which enter into the Lagrangian as Λ_{jk}. It should be noted that Equation 3.7 defines one instance of an *extended-Lagrangian formalism* [88], which will be discussed in more detail in Section 3.4.

The corresponding Euler-Lagrange equations of motion for the ions and the fictitious electrons are given by:

$$\mu\ddot{\psi}_j = -\frac{\delta E^{\mathrm{CP}}}{\delta \psi_j^*} + \sum_k \Lambda_{jk}\psi_k, \tag{3.8}$$

$$M_I\ddot{\mathbf{R}}_I = -\frac{\partial E^{\mathrm{CP}}}{\partial \mathbf{R}_I}. \tag{3.9}$$

The functional derivative $-\frac{\delta E^{\mathrm{CP}}}{\delta \psi_j^*}$ in Equation 3.8 can also be expressed in terms of the Kohn-Sham Hamiltonian as $-\mathcal{H}^{\mathrm{KS}}\psi_j$, with $\mathcal{H}^{\mathrm{KS}}$ defined according to Equations 2.15 and 2.20.

In principle, integration of Equation 3.9 results in ion dynamics which match those of the physical system only when the energy functional $E^{\mathrm{CP}}[\vec{\mathbf{R}}, \{\psi_j\}]$ attains its minimum value with respect to the fictitious electronic degrees of freedom $\{\psi_j\}$. However, if μ is chosen to be sufficiently small, the dynamics of the fictitious electrons will be very fast, and coupling to the dynamics of the ions will in practice be extremely weak as long as the system is an insulator. This means that any kinetic energy transfer between the electronic and ionic systems will be minimized, and the system will remain close to the Born-Oppenheimer surface. In this limit, the Car-Parrinello approach reliably approximates the actual dynamics of the system [89].

The Car-Parrinello equations of motion can be discretized in time using an appropriate integration algorithm. Using the Verlet algorithm, the discrete form for the ions follows Equation 3.2, whereas the solution to the electronic problem becomes [58,90]:

$$\psi_j(\mathbf{r}, t+\Delta t) = 2\psi_j(\mathbf{r}, t) - \psi_j(\mathbf{r}, t-\Delta t) - \frac{(\Delta t)^2}{\mu}\left\{\mathcal{H}^{\mathrm{KS}}\psi_j(\mathbf{r}, t) - \sum_k \Lambda_{jk}\psi_k(\mathbf{r}, t)\right\}. \tag{3.10}$$

It is worthwhile discussing in greater depth what motivates a proper choice for the fictitious mass μ. In effect, μ determines the tolerance with which the system adheres to the Born-Oppenheimer surface; smaller values therefore yield higher accuracy results. However, μ also limits the integration timestep in Equation 3.10 if we are to ensure that the fictitious electronic "forces" integrate correctly. This limitation is particularly significant considering changes in μ are reflected in the *square* of Δt, given that the coefficient $(\Delta t)^2/\mu$ of the force term ultimately determines the extent of the propagation in time. Although there is no firm law governing a proper choice, μ should be chosen such that the timestep can be maximized under the constraint that the system remains close to the Born-Oppenheimer surface throughout the entirety of the simulation time. A convenient estimate can be obtained by comparing the kinetic energy of the fictitious electronic system (which scales with μ) to that of the ions; generally, the electronic value should be no more than 10% of the ionic one, with the electrons

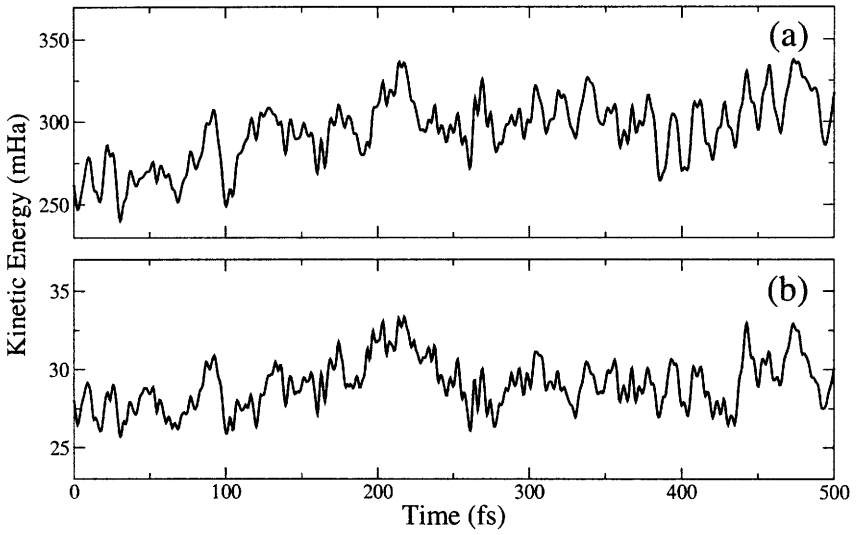

FIGURE 3-1: Evolution of the (a) ionic and (b) fictitious electronic kinetic energies for a simulation of $CsHSO_4$ at 550 K, sampled over a period of 0.5 ps ($\mu = 700$ au, $\Delta t = 7$ au). The scale of the bottom graph is set to 1/10 that of the top graph in order to evidence the electrons' adiabatic following of the ion dynamics.

following the same qualitative trend as the ions throughout the simulation (Figure 3-1). This usually mandates relatively short timesteps when compared with Born-Oppenheimer molecular dynamics, but this is more than compensated by the computational savings.

A nonobvious benefit of the Car-Parrinello method is that it allows for the definition of a *constant of motion* E^{cons}, which should be conserved in any properly configured simulation. This quantity can therefore be monitored to ensure numerical stability in the integration, making it a useful measure for fine tuning simulation parameters such as the integration timestep Δt. This constant of motion can be extracted from the Car-Parrinello extended Lagrangian (Equation 3.7) and takes the form:

$$E^{\text{cons}} = \frac{1}{2}\sum_j \mu \langle \dot{\psi}_j | \dot{\psi}_j \rangle + \frac{1}{2}\sum_I M_I \dot{\mathbf{R}}_I^2 + E^{\text{CP}}[\vec{\mathbf{R}}, \{\psi_j\}]. \tag{3.11}$$

For a properly chosen value of Δt, E^{cons} should display negligible drift as the simulation progresses, and any fluctuations should be tiny on the energetic scale of the fluctuations in E^{CP} (see Figure 3-2).

3.4 Simulations within other ensembles

Up to this point, our discussion has presupposed that the system is in the microcanonical *NVE* ensemble, such that the total energy of the system is conserved at each timestep. In practice, it

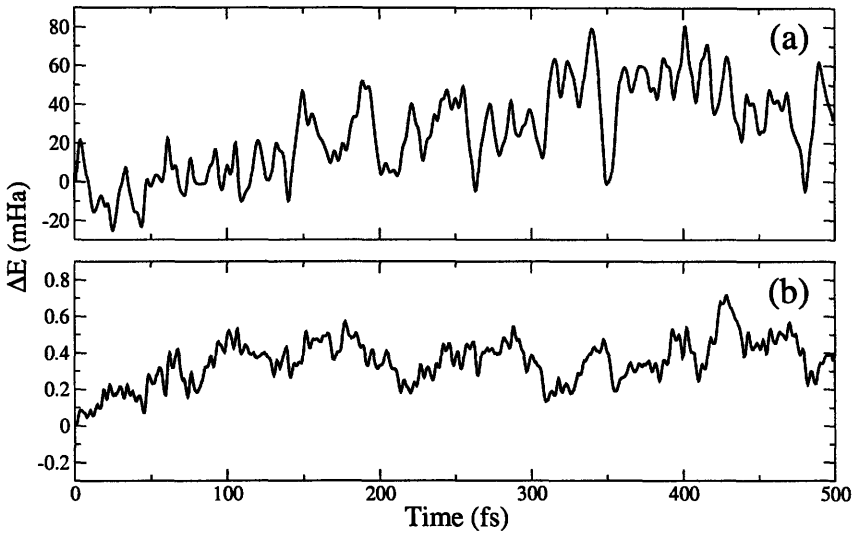

FIGURE 3-2: Comparison of the magnitude of the fluctuations in (a) the total internal energy of the system and (b) the Car-Parrinello constant of motion. The reference energy is taken to the be the corresponding value at the start of the represented simulation period, and the scale of the bottom graph is 1/100 that of the top graph. Data represents 0.5 ps of a simulation of $CsHSO_4$ at 550 K.

is often more convenient to perform MD simulations in other ensembles. For instance, fixed-temperature simulations are useful for examining phases that manifest themselves only at finite temperatures, or for exploring thermally activated events such as those common in transport phenomena. Similarly, fixed-pressure simulations allow for the investigation of structural phase transformations that are incompatible with the constraints of a fixed-volume supercell.

Many algorithms exist for extending MD simulations to other ensembles [85,91]. However, the extended-Lagrangian formalism used by the Car-Parrinello approach offers a particularly convenient way of doing this by addition of generalized coordinates involving temperature or pressure [87,88]. These can then be treated as fictional dynamical variables in much the same way as the virtual electronic wavefunctions in Equation 3.7. In this section, we will explore two extended-Lagrangian methods in greater detail: the *Nosé-Hoover thermostat* for isothermal simulations and the *Parrinello-Rahman method* for isobaric simulations. Other notable extensions exist, however. One more recent example is the *electric enthalpy method* [92,93], which uses an extended Lagrangian based on the pairing between polarization and displacement to simulate the application of an external electric field.

3.4.1 The Nosé-Hoover thermostat

The extended-Lagrangian method for finite-temperature simulation in the canonical *NVT* ensemble is attributed to Nosé and Hoover [94–98]. Nosé proposed coupling the system to a thermostat using a generalized coordinate s and a corresponding generalized mass Q. The

variable s acts to regulate the temperature by rescaling the velocities of the ions in a deterministic manner. Addition of a Nosé-Hoover thermostat to the ionic components of Equation 3.7 results in the following modified Car-Parrinello Lagrangian:

$$\mathcal{L}_{\mathrm{NH}}^{\mathrm{CP}} = \frac{1}{2}\sum_j \mu \langle \dot{\psi}_j | \dot{\psi}_j \rangle + \frac{1}{2}\sum_I M_I s^2 \dot{\mathbf{R}}_I^2 - E^{\mathrm{CP}}[\vec{\mathbf{R}}, \{\psi_j\}] + \sum_{jk} \Lambda_{jk}\Big\{\langle \psi_j | \psi_k \rangle - \delta_{jk}\Big\} + \frac{1}{2}Q\dot{s}^2 - gk_BT\ln s, \quad (3.12)$$

where g represents the degrees of freedom in the thermostated system (conventionally, $g = 3M + 1$, where M is the number of ions) and T indicates the target temperature. Note that in addition to modifying the ionic kinetic energy, a classical kinetic energy term corresponding to the thermostat system has been added. The final term in Equation 3.12 represents a constraint on the thermostat coordinate s designed to guarantee *canonicity*; that is, to ensure that physical fluctuations in the energy and temperature are preserved and distributed properly. This in turn generates correct values for quantities related to the natural energetic fluctuations, such as the heat capacity [85]. The corresponding constant of motion is given by:

$$E^{\mathrm{cons}} = \frac{1}{2}\sum_j \mu \langle \dot{\psi}_j | \dot{\psi}_j \rangle + \frac{1}{2}\sum_I M_I s^2 \dot{\mathbf{R}}_I^2 + E^{\mathrm{CP}}[\vec{\mathbf{R}}, \{\psi_j\}] + \frac{1}{2}Q\dot{s}^2 + gk_BT\ln s. \quad (3.13)$$

For certain materials, particularly those featuring a small electronic bandgap, it may become necessary to add a thermostat to the fictitious electronic system as well [99]. Doing so can effectively prevent minor energy transfer between the "hot" ionic system and the "cool" electronic system, thereby ensuring adiabaticity during the course of a very long simulation. An electronic thermostat is implemented in much the same way as the ionic one, except that the fictitious thermostat coordinate acts to instead rescale the virtual velocities $\dot{\psi}_j$ of the Kohn-Sham orbitals.

There may also be instances in which the Nosé-Hoover thermostat does not efficiently explore phase space and can become caught in the excitation of one or a very few of the vibrational modes. A solution to this problem was proposed by Martyna *et al.* in the form of *Nosé-Hoover chains* [100]. In this scheme, the initial thermostat is coupled to a second thermostat, which in turn can be coupled to a third thermostat, and so forth. The entire chain can be shown to generate a proper canonical distribution.

As with the Car-Parrinello fictitious mass μ, it may not be immediately clear what motivates a proper choice of the thermostat mass Q. In principle, any value of Q will ensure canonicity. However, by generating the equation of motion for the fictitious coordinate s from the Lagrangian (Equation 3.12), one can show that to first order, heat flow in the Nosé-Hoover scheme approximates a periodic oscillation of s, whose angular frequency ω is governed by

the choice of Q [87]:

$$\omega \approx \left(\frac{2gk_BT}{Q}\right)^{1/2}. \tag{3.14}$$

In order to ensure maximally efficient kinetic energy transfer to the ionic system, the mass Q should be chosen such that ω matches the typical optical frequency of the material. If Q is chosen to be too large, it will take a long time to generate a canonical distribution. Moreover, there will be an increased likelihood of incurring numerical errors in the integration of the equation of motion because of the large mass difference between the system and the thermostat, which could lead to energetic drift over time. On the other hand, if Q is chosen to be too small, the thermostat will be too aggressive, leading to dampening of desirable, realistic thermal fluctuations. In this case, unphysical high-frequency oscillations may also become manifest.

3.4.2 The Parrinello-Rahman method

Andersen was the first to suggest simulating an isobaric ensemble by treating the volume as a dynamical variable within an extended-Lagrangian scheme [88]. Parrinello and Rahman subsequently expanded this idea to include the supercell lattice vectors themselves as dynamical variables [101, 102]. Their method offers a simple yet powerful method for performing simulations at constant pressure in which the cell shape should be allowed to vary, such as those involving structural phase transitions.

The Parrinello-Rahman method begins by introducing a coordinate system based on the generalized supercell vectors, whose Cartesian coordinates can be expressed as column vectors in a *cell matrix*, denoted by $\vec{\mathbf{h}}$. The relationship between the coordinates of an ion in the original frame ($\mathbf{R}_I$) and in the new frame ($\mathbf{S}_I$) can then be expressed as $\mathbf{R}_I = \vec{\mathbf{h}}\,\mathbf{S}_I$. The method treats this matrix $\vec{\mathbf{h}}$ as the dynamical variable in the extended Lagrangian. When implemented within the Car-Parrinello scheme, the Lagrangian of Equation 3.7 is modified as follows:

$$\mathcal{L}_{\mathrm{PR}}^{\mathrm{CP}} = \frac{1}{2}\sum_j \mu \langle \dot{\psi}_j | \dot{\psi}_j \rangle + \frac{1}{2}\sum_I M_I \dot{\mathbf{S}}_I^{\mathrm{T}} \vec{\mathbf{h}}^{\mathrm{T}} \vec{\mathbf{h}} \dot{\mathbf{S}}_I - E^{\mathrm{CP}}[\vec{\mathbf{R}}, \{\psi_j\}] + \sum_{jk} \Lambda_{jk} \Big\{ \langle \psi_j | \psi_k \rangle - \delta_{jk} \Big\} + \frac{1}{2} W \mathrm{Tr}\,(\dot{\vec{\mathbf{h}}}^{\mathrm{T}} \dot{\vec{\mathbf{h}}}) - P\Omega. \tag{3.15}$$

Here P denotes the target pressure and Ω the instantaneous volume of the cell, which can be calculated as $\Omega = \det \vec{\mathbf{h}}$. In addition, the ionic coordinates in the kinetic energy term have been recast in terms of the instantaneous form of the cell matrix $\vec{\mathbf{h}}$. The parameter W represents the fictitious mass corresponding to the variable-cell coordinates, which should be chosen so as to optimize kinetic energy transfer between the cell and the ionic system. A common choice for W is the on the order of the total mass of the ions in the cell, although particular simulation circumstances may call for "stiffening" the cell by increasing W or "loosening" it by decreasing

W. Equation 3.15 has an analogous constant of motion, which takes the following form:

$$E^{\text{cons}} = \frac{1}{2}\sum_j \mu \langle \dot{\psi}_j | \dot{\psi}_j \rangle + \frac{1}{2}\sum_I M_I \dot{\mathbf{S}}_I^{\mathrm{T}} \vec{\mathbf{h}}^{\mathrm{T}} \vec{\mathbf{h}} \dot{\mathbf{S}}_I + E^{\text{CP}}[\vec{\mathbf{R}}, \{\psi_j\}] + \frac{1}{2} W \mathrm{Tr}\left(\dot{\vec{\mathbf{h}}}^{\mathrm{T}} \dot{\vec{\mathbf{h}}}\right) + P\Omega. \quad (3.16)$$

The Parrinello-Rahman method can easily be combined with a Nosé-Hoover thermostat to simulate within the isothermal-isobaric ensemble. Moreover, it is possible to couple the cell parameters to their own Nosé-Hoover thermostat. This can be useful for exploring the space of configurations more efficiently, or when attempting to overcome energy barriers to structural transformations.

3.5 Extracting useful quantities from simulations

3.5.1 Practical considerations

Molecular dynamics represents an especially useful technique for directly analyzing reaction kinetics, mechanisms, and pathways. However, it can also be an extremely powerful tool for extracting various statistical quantities, such as finite-temperature structural parameters, transport coefficients, and thermodynamic averages. Since practical constraints prevent the direct evaluation of statistical-mechanical Boltzmann integrals, extraction of observable quantities based upon statistical averages must instead rely on the principle of *ergodicity*. In an ergodic system, ensemble averages are replaced by time averages. Most well-behaved systems in equilibrium will obey ergodicity, but in principle, the ensemble and time averages are congruous only in the limit of infinite simulation time. However, in practice, it is sufficient to sample for a finite time as long as the quantities of interest can be shown to converge to within a desired accuracy.

In guaranteeing ergodicity, it is important to ensure that time averages take place across configurations that are representative of the probability distribution of the corresponding ensemble average. This assumption is usually safe except at initial timesteps, for which the system may not yet have reached equilibrium. As such, it is common practice to divide a molecular dynamics simulation into an *equilibration regime* and a *production regime*. All relevant statistical averages are taken only over the production timesteps, since these states are representative of the equilibrium system for a given set of input parameters and ensemble constraints. It should be noted that although equilibration data is generally ignored when extracting statistically averaged quantities, it can nonetheless prove useful for examining the detailed process by which a system evolves toward equilibrium.

Throughout this document, we will use angle brackets to denote an ensemble average, which is assumed to be calculated as a time average, in keeping with the assumption of ergodicity. There follows a brief discussion of how to obtain some of the most commonly used structural and dynamical quantities from an analysis of simulation data for structural and

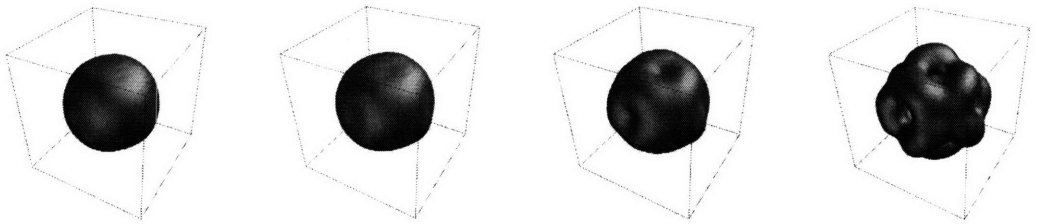

(a) (b) (c) (d)

FIGURE 3-3: Occupation density isosurfaces for the first four nearest-neighbor silvers to an iodine (in order from (a) to (d)), calculated using Equation 3.17. Data is from a simulation of α-AgI at 750 K.

dynamical properties.

3.5.2 Calculation of common quantities

Occupation density

Ion trajectories can be traced with respect to a fixed reference frame (such as a crystalline lattice) and averaged to calculate an *occupation density* $f(\mathbf{r})$, whose isosurface can be plotted to obtain a visual representation of most frequented pathways (Figure 3-3). In order to get smooth results from limited statistics, it is useful to introduce a Gaussian spread in the positions before averaging. The resulting formula for the surface representing occupancy probability is:

$$f(\mathbf{r}) = \left\langle \sum_{I}^{N_s} \tilde{f}(\mathbf{r}, \mathbf{R}_I) \right\rangle, \tag{3.17}$$

where $\tilde{f}$ represents a weighting function, which for the case of Gaussians is expressed by the general formula

$$\tilde{f}(\mathbf{r}, \mathbf{R}_I) \equiv \frac{1}{(\sigma\sqrt{2\pi})^3} \exp\left\{ -\frac{|\mathbf{r} - \mathbf{R}_I|^2}{2\sigma^2} \right\}. \tag{3.18}$$

Here N_s represents the total number of atoms included in the average, which is usually the number of atoms of a particular species in the supercell. The parameter σ, which controls the width of each Gaussian, can be tuned independently for each application. Note that the periodic boundary conditions must be explicitly accounted for if a Gaussian spreads beyond the supercell boundary.

Radial distribution function

The *radial distribution function* (RDF) $g(r)$, sometimes known as the *pair correlation function*, is a useful parameter for characterizing the structure of a solid or a liquid. It gives the probability of finding an ion pair separated by a distance r, normalized with respect to the corresponding probability in a random distribution of the same overall density (Figure 3-4). Mathematically, we can write $g(r)$ for any pair of ionic species (s, s') as follows [85, 103]:

$$g_{s\,s'}(r) = \frac{\Omega}{N_s N_{s'}} \left\langle \sum_{I}^{N_s} \sum_{J \neq I}^{N_{s'}} \delta(r - R_{IJ}) \right\rangle, \tag{3.19}$$

where $R_{IJ} \equiv |\mathbf{R}_I - \mathbf{R}_J|$ represents the interionic separation, Ω denotes the volume of the supercell, and N_s and $N_{s'}$ are the number of ions of the two respective atomic species representing the pair of interest.

In practice, the spatial grid is discretized, and the delta function is replaced by a function that is nonzero for some small range of separations $\left[r - \frac{\Delta r}{2}, r + \frac{\Delta r}{2}\right]$ and is normalized across the discretization region Δr. Equation 3.19 can then be written:

$$g_{s\,s'}(r; \Delta r) = \frac{\Omega}{N_s N_{s'}\, \Omega_{\text{shell}}} \left\langle \sum_{I}^{N_s} \sum_{J \neq I}^{N_{s'}} \tilde{\delta}(r - R_{IJ}\,; \Delta r) \right\rangle, \tag{3.20}$$

where Ω_{shell} is the volume of a shell of radius r and thickness Δr:

$$\Omega_{\text{shell}} \equiv \frac{4\pi}{3} \left[\left(r + \tfrac{\Delta r}{2}\right)^3 - \left(r - \tfrac{\Delta r}{2}\right)^3 \right]. \tag{3.21}$$

The modified delta function $\tilde{\delta}(z; \Delta z)$ is defined as:

$$\tilde{\delta}(z; \Delta z) \equiv \begin{cases} 1 & \text{if } \frac{\Delta z}{2} < z \leq \frac{\Delta z}{2} \\ 0 & \text{otherwise} \end{cases}. \tag{3.22}$$

In the classical limit, a perfectly ordered lattice at zero temperature has a radial distribution curve that is a periodic series of delta functions. In practice, finite temperatures spread the delta functions of a solid lattice. For a liquid with perfectly random disorder, $g(r)$ has a constant value of 1 beyond a short-ranged exclusion region (e.g., for r less than the rigid-sphere radius).

Coordination number

The *coordination number* $n(r)$ is another useful structural quantity, giving a measure of the average number of ions within a cutoff distance r of another ion (Figure 3-4). It can be easily calculated from an integral of the radial distribution function (Equation 3.20). The expression

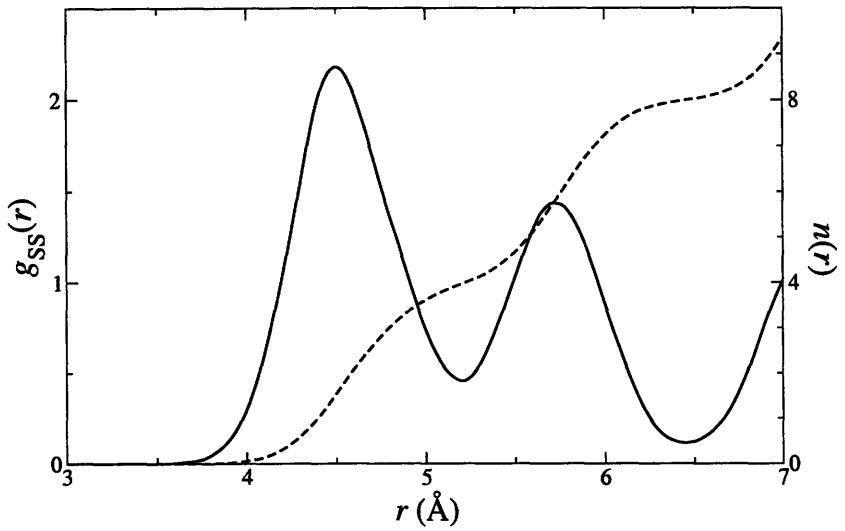

FIGURE 3-4: Sulfur-sulfur radial distribution function $g_{SS}(r)$ in $CsHSO_4$ at 550 K, calculated using Equation 3.20 (solid line, left axis). Also plotted is the corresponding coordination number $n_{SS}(r)$, calculated using Equation 3.23 (dashed line, right axis). The first and second coordination shells, each of which contain four atoms, are clearly visible in the plateau behavior of $n_{SS}(r)$.

for the coordination number for ions of species s' surrounding an ion of species s is given by:

$$n_{s\,s'}(r) = \frac{N_{s'}}{\Omega} \int_0^r 4\pi r'^2 g_{s\,s'}(r')\,\mathrm{d}r'. \tag{3.23}$$

Mean-square displacement

The *mean-square displacement* (MSD) gives a quantifiable measure of the net motion of an ionic species with time by examining the average distance traveled by an ion within a time t in the simulation. The MSD must be calculated with respect to some reference configuration. One possibility is to use the conventional set of ionic positions at the start of the simulation. In this case, the MSD is written as [85]:

$$\mathrm{MSD}(t) = \frac{1}{N_s} \sum_{I}^{N_s} \left|\mathbf{R}_I(t) - \mathbf{R}_I(0)\right|^2. \tag{3.24}$$

Depending on the nature of the simulation, it may be preferable to sample the MSD with respect to a different reference configuration or an entire set of reference configurations. For instance, simulations which detail a progression toward a final equilibrium state might be better sampled with respect to the last available timestep t_f, which is assumed to be fully

equilibrated:

$$\mathrm{MSD}(t) = \frac{1}{N_s}\sum_{I}^{N_s}\left|\mathbf{R}_I(t_f) - \mathbf{R}_I(t_f - t)\right|^2. \tag{3.25}$$

For steady-state dynamical processes such as self-diffusion, it is convenient to modify our definition for the MSD at time t in terms of an ergodic average over all time intervals of length t in the simulation. Doing so can substantially improve the statistical precision of the MSD, since the number of sampling intervals for the averaging is effectively increased (see Figure 3-5). However, this introduces a subtle complication, since the number of such ranges that are available depends inversely on t, meaning values of the MSD at short times are implicitly more precise than at long times. This must be accounted for in the calculation of any additional quantities based on the MSD (such as the diffusion coefficient), since statistical errors cannot be expected to remain constant throughout the calculation. An approach which is suitably cautious for most systems is to calculate the time-averaged MSD only for data points up to $t = t_f/2$, in which case Equation 3.24 becomes:

$$\left\langle \mathrm{MSD}(t) \right\rangle = \frac{2}{N_s t_f}\sum_{t_0=0}^{t_f/2}\sum_{I}^{N_s}\left|\mathbf{R}_I(t_0 + t) - \mathbf{R}_I(t_0)\right|^2. \tag{3.26}$$

For a solid, we typically observe a flat MSD curve following an initial increase in the ballistic thermalization region, with a plateau value corresponding to the square of the RMS amplitude of vibration. In contrast, the MSD for a liquid typically increases linearly beyond the thermalization regime, signifying net diffusion.

Velocity autocorrelation function

The *velocity autocorrelation function* (VAF) is one of a broader set of autocorrelation functions which correlate a particular quantity (in this case, velocity) for a particular ionic species at some reference time with the equivalent quantity at a time t later into the simulation (Figure 3-6). The VAF is a tremendously useful quantity in analyzing dynamical processes. For instance, the VAF decay time can be extracted to obtain a reasonable estimate of the typical correlation time for configurations. This method provides an appropriate choice for the sampling interval in applications requiring discrete sampling of "independent" configurations, such as often becomes necessary for error estimation. A Fourier transform of the VAF also offers a simple way to calculate the vibrational density of states.

As with the MSD, the choice of the reference configuration is not unique. If taken with respect to the starting configuration of the simulation, the basic formula for the VAF looks like [85]

$$\mathrm{VAF}(t) = \frac{1}{N_s}\sum_{I}^{N_s}\left[\dot{\mathbf{R}}_I(t)\cdot\dot{\mathbf{R}}_I(0)\right]. \tag{3.27}$$

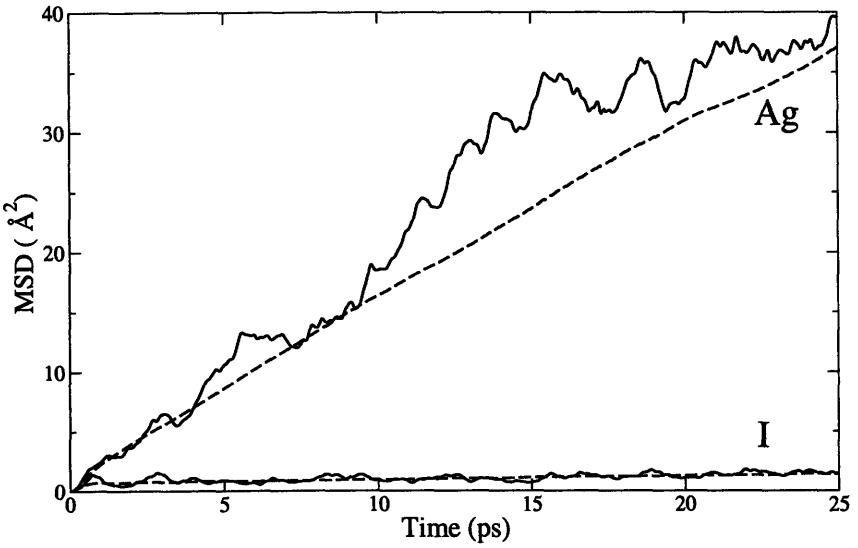

FIGURE 3-5: Comparison of the mean-square displacements calculated using Equation 3.24 (solid line) to those calculated using Equation 3.26 (dashed line). Results are for the silver and iodine ionic species of α-AgI at 500 K.

For a system in steady-state equilibrium, it is advisable to average Equation 3.27 over all intervals of length t in order to improve statistical sampling. However, as was the case for the MSD, doing so can create nonuniform precision in the VAF as a function of time, since values at short times are more precise than at long times. Again, a generally safe solution is to calculate the VAF for times up to $t = t_f/2$, which gives the following usual expression for the time-averaged equilibrium VAF:

$$\langle \mathrm{VAF}(t) \rangle = \frac{2}{N_s t_f} \sum_{t_0=0}^{t_f/2} \sum_{I}^{N_s} \left[\dot{\mathbf{R}}_I(t_0 + t) \cdot \dot{\mathbf{R}}_I(t_0) \right]. \tag{3.28}$$

Transport coefficients

Various transport coefficients, such as the viscosity, the thermal conductivity, and the self-diffusion coefficient, can also be calculated from the production regime of a steady-state equilibrium simulation using the *Green-Kubo relations*, which connect these properties to the integral of their appropriate autocorrelation function [104]. The self-diffusion coefficient D is a particularly important quantity for the purposes of this work. Its corresponding Green-Kubo relation involves the velocity autocorrelation function and can be written (in three dimensions) as [85]:

$$D = \frac{1}{3} \lim_{t \to \infty} \int_0^t \langle \mathrm{VAF}(t') \rangle \, \mathrm{d}t'. \tag{3.29}$$

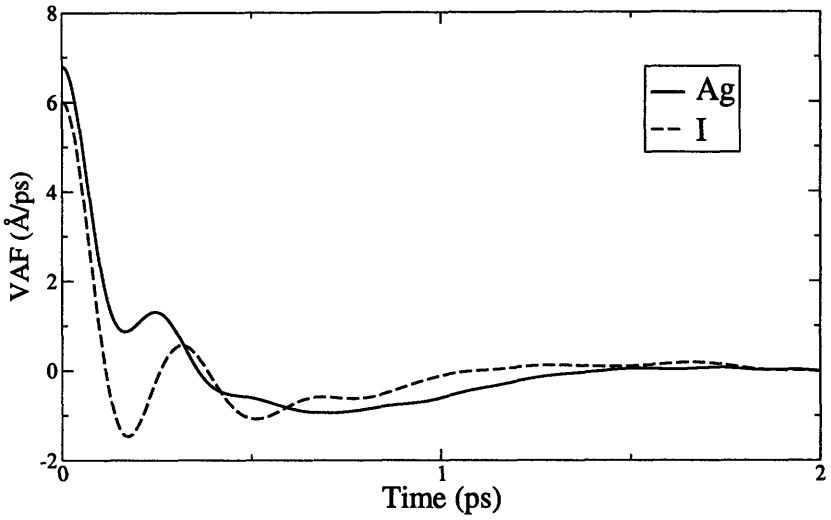

FIGURE 3-6: Velocity autocorrelation functions for the silver and iodine ions in α-AgI at 500 K.

Alternatively, the three-dimensional self-diffusion coefficient can be calculated from the long-time slope of the mean-square displacement using the *Einstein relation*:

$$D = \lim_{t\to\infty} \frac{1}{6t} \langle \mathrm{MSD}(t) \rangle. \tag{3.30}$$

Mathematically, Equations 3.29 and 3.30 are equivalent and interchangeable in the limit of infinite simulation time. Both assume isotropic, three-dimensional diffusion, although individual components of an anisotropic diffusion tensor may be extracted by projecting the MSD or the VAF onto the appropriate principal axis (in which case the conventional self-diffusion coefficient is just the one third of the trace of the diffusion tensor). However, in practice, it may be preferable to use one method or the other due to issues with convergence or error. For instance, systems with relatively short correlation times will exhibit more rapid convergence of D when calculated using the VAF, but integration errors using this method may become an issue, and extremely fine VAF sampling is required to capture the full phenomenology in the integration. The MSD method converges more slowly but is generally more robust with respect to coarse sampling or to errors accrued at long times. A detailed discussion of the delicate issue of error estimation in the calculation of the self-diffusion coefficient is provided in Appendix C.

Thermodynamic quantities from fluctuations

It is worthwhile mentioning that a number of potentially interesting thermodynamic coefficients can be obtained by examining the root-mean-square fluctuations of averaged quantities, sampled within the appropriate ensemble. These include (but are not limited to) the

isothermal compressibility, the thermal expansion coefficient, and the specific heat capacity. For instance, the expression for the constant-volume specific heat capacity C_V can be derived from the fluctuations of the total energy (or equivalently, the enthalpy) in the canonical (NVT) ensemble as follows:

$$C_V = \frac{1}{k_B T^2} \sigma_E^2, \tag{3.31}$$

where σ_E^2 is the variance of the energy in the canonical ensemble, defined as:

$$\sigma_E^2 \equiv \langle E^2 \rangle - \langle E \rangle^2 = \frac{1}{t_f} \sum_{t'=0}^{t_f} \Big[E(t') - \langle E \rangle \Big]^2. \tag{3.32}$$

Equation 3.31 is detailed because of its specific relevance to this work, but the remaining quantities listed above are calculated in an analogous fashion. The reader is encouraged to consult Reference [85] for a more complete discussion of the methodology behind the calculation of thermodynamic coefficients from ensemble fluctuations, as well as for detailed derivations of additional such expressions.

CHAPTER 4

α-AgI: An archetype of fast-ion conduction

4.1 Background and motivation

THE FAST-ION CONDUCTING properties of of silver iodide (AgI) have been widely studied for decades, having been mentioned in the work of Tubandt and Lorenz [105] as early as 1914. Even today, it exhibits one of the highest ionic conductivities among the known solid-state ion conductors and such remains of great interest to the materials community. In fact, AgI and its related silver halides and sulfides have garnered a great deal of attention over the past several years for their potential as practical components in a variety of devices from batteries to switches and sensors [25,29,106,107].

In addition to its technological importance, however, AgI has long been the focus of an intensive research effort towards understanding the mysteries of fast-ion conduction in more general terms. Its seeming simplicity masks an underlying complexity that makes it a perfect embodiment of the enigmatic dual nature of fast-ion conductors. Its basic structural and conductive properties are well established experimentally [108–112], including the high-symmetry body-centered cubic (bcc) crystal structure of its fast-conducting α phase. It is also a known archetype for the class of fast-ion conductors known as *Type I*, in which conductivity results intrinsically from the multiple lattice occupancy sites that are made available to the diffusive species (in this case, the silver cations). However, despite their usefulness in characterizing the conductive properties of AgI, the various detailed investigations over the past several decades have made limited headway in terms of understanding the peculiar thermodynamic, chemical, and structural motivations for the existence of a fast-ion conducting phase, or in gaining a fundamental understanding of the atomistic mechanisms involved in cation transport at the microscale. Finding an answer to these basic questions has formed the focus of a wealth of theoretical studies, including several originating from the atomistic modeling

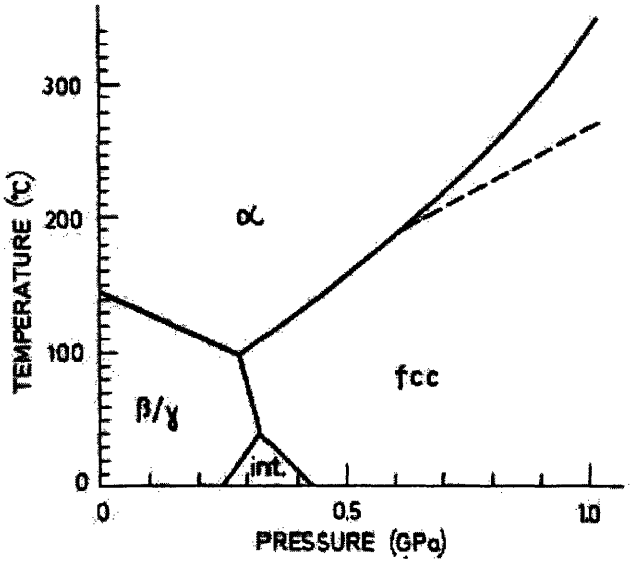

FIGURE 4-1: Phase diagram of AgI. At standard pressure, the phase transition to the fast-ion conducting α phase occurs at $T_c = 420$ K. Taken from Reference [113].

community, yet to date, many details have remained elusive.

The phase diagram of AgI is depicted in Figure 4-1. It is well established that at standard pressure, the material exhibits a transition from its low-temperature β phase (often mixed with a zinc-blende γ phase) to its fast-ion conducting α phase at $T_c = 420$ K. Above this temperature, the conductivity of the silver ions displays a sudden increase by about three orders of magnitude to 1.31 $(\Omega \cdot \text{cm})^{-1}$ [111] and is accompanied by a well-defined structural transformation from a hexagonal wurtzite crystal structure to a body-centered cubic structure [108, 109, 113, 114]. However, experimental data suggests that this structure is predominantly maintained by the iodine anions, whereas the location of the silver cations is much less distinct. Rather, the silvers reside in the unusually high number of otherwise unoccupied interstitial sites (12*d* tetrahedral, 6*b* octahedral, and 24*h* trigonal) made available by the bcc lattice symmetry. In particular, diffraction and scattering experiments suggest that in practice, the tetrahedral sites are occupied nearly 70% of the time, whereas the octahedral sites have the lowest statistical occupancy [110, 115]. The commonly held view in the literature is that low-energy pathways between these many possible lattice sites facilitate fast cation transport, most likely between neighboring tetrahedral sites via intermediate trigonal sites. The structure of α-AgI is depicted schematically in Figure 4-2.

Previous molecular dynamics studies have made use of classical pair potentials to successfully reproduce various experimental characteristics of the α and β phases, including their basic diffusive properties [116–123]. Most of these employed some version of the well-tested potentials developed by Vashishta, Rahman, and Parrinello [116, 117], which was originally

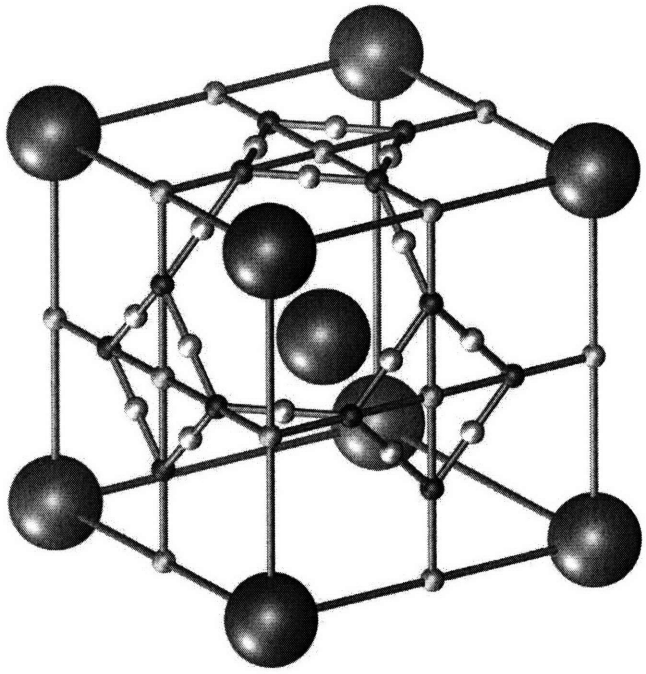

FIGURE 4-2: Schematic illustration of the conventional unit cell of α-AgI (space group *Im3m*). The locations of the iodine atoms are shown in blue. The remaining spheres designate a subset of the possible tetrahedral (red), octahedral (yellow), and trigonal (white) interstitial sites available for silver occupancy.

designed to adequately describe both the $\alpha \rightarrow \beta$ transition and the high-pressure phases of AgI. An excellent summary of these investigations can be found in the review articles of References [9] and [8]. However, these methods cannot offer the same level of accuracy or depth of insight afforded by first-principles calculations. For instance, they are inherently unable to describe the electronic structure in a nonuniform chemical environment. There is reason to expect that this might be a particularly important consideration in fast-ion conductors, since local electronic and structural environments can exhibit rapid and dramatic changes; as will become evident later in the chapter, this point is indeed relevant for obtaining an accurate description of AgI. Classical methods are also inadequate for capturing the full phenomenology of the melting transition, since the potentials were optimized for lower-temperature interatomic interactions in the solid state. In these regards, dynamical simulations based on first principles provide unique and unbiased predictive power. Fortunately, owing to the extraordinarily high ionic conductivity displayed by the material, timescales of diffusive events in α-AgI are now readily accessible to Car-Parrinello molecular dynamics using reasonable computational facilities, making such a study feasible for the first time.

4.2 Computational parameters

In studying AgI, we used an ultrasoft pseudopotential for silver that had been generated previously using a $4d^{10}5s^1$ valence configuration (i.e., with the semicore d states in the valence shell). This pseudopotential was obtained from the Quantum-ESPRESSO website [124], and transferability tests had already been performed. As there was no suitable iodine pseudopotential available, we generated a new scalar-relativistic norm-conserving pseudopotential with a $5s^25p^5$ valence configuration using Martin Fuchs' pseudopotential generation package fhi98pp [125]. The software implements the Troullier-Martins procedure [126] and performs certain internal transferability tests, such as checking for spurious ghost states in the Kleinman-Bylander representation (see Section 2.4 for details). A complete listing of the input parameters for our iodine pseudopotential, as well as the results of all of the additional transferability tests that were performed, is provided in Appendix A. As with all of the pseudopotentials used for this thesis work, the gradient-corrected Perdew-Burke-Ernzerhof (PBE) recipe was used for calculating the exchange and correlation contributions to the total energy. Suitable energetic cutoffs for the electronic wavefunctions (22 Ry) and the charge density (176 Ry) were selected using a force-convergence method, in which cutoffs were systematically increased until convergence of the magnitude of the atomic forces was observed to within a threshold of ~ 0.05 eV/Å.

Dynamics simulations were performed within the plane-wave pseudopotential framework using the Car-Parrinello technique. The canonical *NVT* ensemble was used to simulate at a range of temperatures from 200 K to 1225 K, and the ion temperature was maintained by the application of a Nosé-Hoover thermostat. A second, weaker thermostat was attached to the electrons to ensure adiabaticity over the long simulation runs, each of which lasted 50 ps following 5 ps of equilibration time. Unless otherwise indicated, all simulations were carried out in a 54-atom supercell (sampled only at the Γ-point in reciprocal space), excepting the Wannier function calculations (Section 4.7), which were performed in a 32-atom cell. The choice of the lattice parameter ($a_0 = 5.174$ Å), which remained fixed for all temperatures, will be discussed further in the next section. The fictitious Car-Parrinello mass was chosen to be $\mu = 700$ au, with $\Delta t = 20$ au (≈ 0.5 fs) for $T \leq 950$ K, 15 au for 1100 K, and 10 au for 1225 K.[†] Justification for our chosen integration timestep and fictitious mass is offered in Figure 4-3, which shows the stabilities and relative magnitudes of the kinetic energies of the ionic and the fictitious electronic systems for a simulation at 200 K, and in Figure 4-4, which shows the stability and conservation of the *NVT* Car-Parrinello constant of motion (Equation 3.13) for the same simulation. For each temperature, the constant of motion fluctuated by no more than $\pm 1.5\%$ of the magnitude of the fluctuations in the total internal energy.

[†]The decrease in timestep for higher temperatures owes to the increased ionic velocities at those temperatures, which necessitate a finer Verlet integration step.

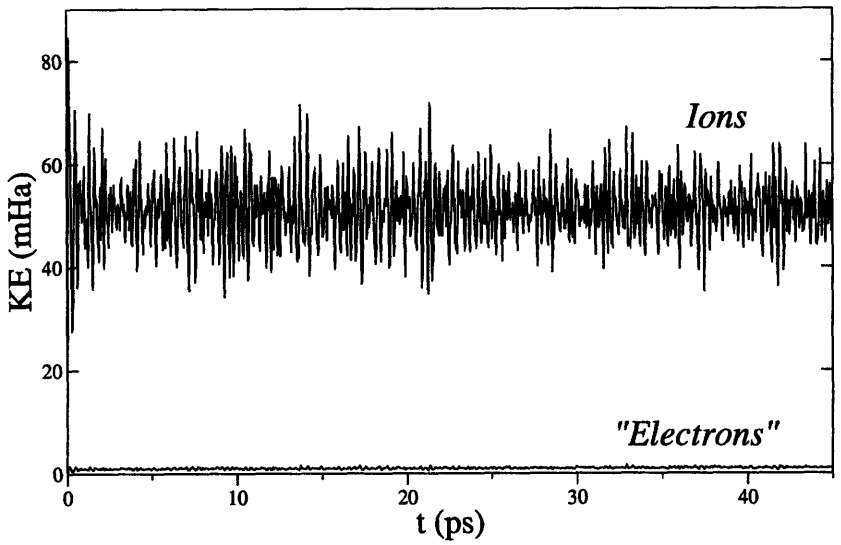

FIGURE 4-3: Evolution of the kinetic energies of the ionic and fictitious electronic systems for a simulation of α-AgI at 200 K.

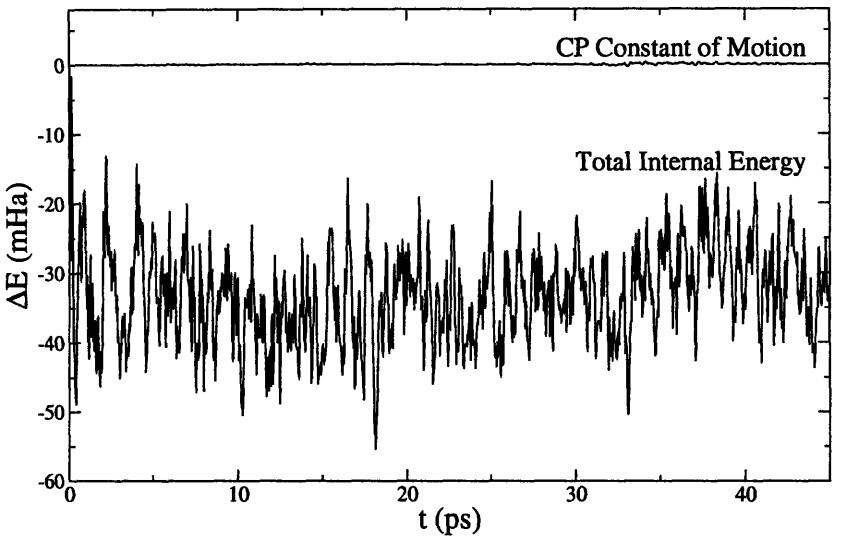

FIGURE 4-4: Evolution of the total internal energy and the Car-Parrinello constant of motion for a simulation of α-AgI at 200 K. The zero reference energy represents the value of the respective quantity at the initial simulation timestep.

4.3 Material characterization and finite-size effects

4.3.1 Structural characterization

To estimate the equilibrium lattice parameter a_0, we fit results from a series of self-consistent energy calculations at different values of a_0 to a second-order Birch-Murnaghan equation of state [127]. These calculations were done on cubic unit cells using a four-atom basis and an evenly spaced $8 \times 8 \times 8$ grid of k-points, and the silver atoms were forced to occupy preselected tetrahedral sites. Reasonable agreement with experiment was obtained using this method (see Table 4.1), but since the silver atoms are in practice highly mobile and expected to fill multiple sites, it was desirable to get an idea of how much this value might be expected to change with different instantaneous configurations of the silver substructure. To do so, we isolated four additional configurations from independent snapshots of a molecular dynamics simulation of 54 atoms, doing a full relaxation of the electronic degrees of freedom for each configuration. We then performed a series of Γ-point-sampled self-consistent energy calculations for different volumes by isotropically expanding or contracting the cell relative to its original size. The results of these calculations are presented in Figure 4-5. It is immediately evident from the figure that although the energy minima differ among configurations, there is little appreciable change in the lattice parameter as the silver positions are changed. This suggests that the lattice structural properties are primarily determined by the iodine ions (albeit compensated by the silver ions), which remain essentially fixed through each of the four configurations.

However, Figure 4-5 also demonstrates that in addition to containing inherent disorder, AgI is a relatively soft material, a fact which has long been documented in the literature [113, 128, 129]. This makes it difficult to determine the lattice parameter to high accuracy, for instance using constant-pressure molecular dynamics techniques. As a result, once approximate quantitative agreement between theory and experiment had been proven to our satisfaction (bearing in mind that gradient-corrected exchange-correlation functionals are expected to slightly overestimate lattice parameters), it was decided that all subsequent dynamics simulations would use the experimental value of a_0 at the melting point, as determined from Reference [110]. Since thermal expansion was also neglected (this was necessary for the specific-heat capacity analysis of Section 4.6), we ran a series of test simulations in which we systematically increased the volume of the supercell by up to 8%. This cell expansion was seen to have no appreciable effect on the diffusive properties, so we remained satisfied with our choice for a_0. It should be noted, however, that allowing for expansion did effect a slight increase in the observed melting temperature.

4.3.2 Vibrational and dielectric properties

Using linear-response theory [80], we have calculated the full phonon dispersion $\omega(\mathbf{q})$ of α-AgI. The results are displayed in Figure 4-6(a). For purposes of computational savings, the

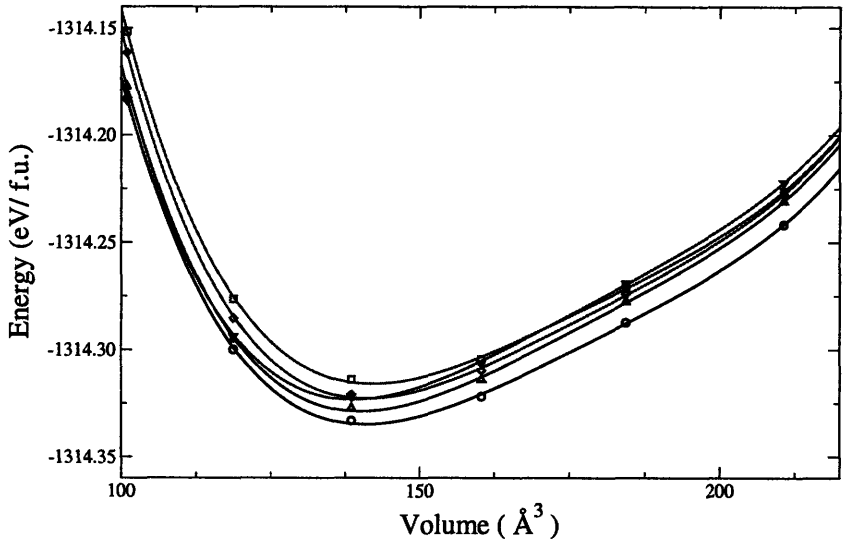

FIGURE 4-5: Energy as a function of volume for five different initial configurations of the silver substructure in α-AgI. Each data point represents the energy obtained by isotropically changing the cell volume following an initial full ionic relaxation of the starting configuration. The black curve is the configuration in which all silver ions occupy the tetrahedral interstitial sites (used to obtain the structural data in Table 4.1); remaining curves are calculated starting from independent timesteps of a 54-atom dynamics simulation at 500 K. Energies are given in units of eV per AgI formula unit.

calculation was performed on the two-atom bcc primitive cell, necessitating placement of all silver ions in the same tetrahedral interstitial site. The smaller cell size also required finer sampling in reciprocal space, so the number of grid points was expanded to form a 12×12×12 k-point mesh. The Acoustic Sum Rule [130,131], which states that the dynamical charges in the cell should sum to zero, was also imposed. Our calculations show excellent agreement with available experimental results from IR and neutron scattering studies. It should be mentioned that the slight discontinuity in the dispersion relation of the high-frequency optical modes at Γ may indicate a directional dependence of the phonon modes, probably arising from the broken symmetry introduced by our choice to preferentially occupy only a single tetrahedral site.

An important feature emerging from Figure 4-6(a) is the softening of the phonon mode at $\mathbf{q} = (\frac{2}{3}\frac{2}{3}\frac{2}{3})$. An examination of the associated eigenvectors reveals the physical interpretation of the soft mode: essentially, it translates to every third {111} plane remaining fixed, while the two central planes compress with respect to one another along the ⟨111⟩ direction. This low-energy transformation, indicated schematically in Figure 4-6(b), is sometimes referred to as the *ω-phonon* and is known to be a key enabler of martensitic phase transitions in certain bcc materials [133,134]. Its existence is also relevant to our discussion of finite-size effects, as will become clear. A second interesting feature of the α-AgI phonon dispersion is the unusually high frequency of the highest acoustic mode, which appears to mix with the optical modes at q-points away from Γ.

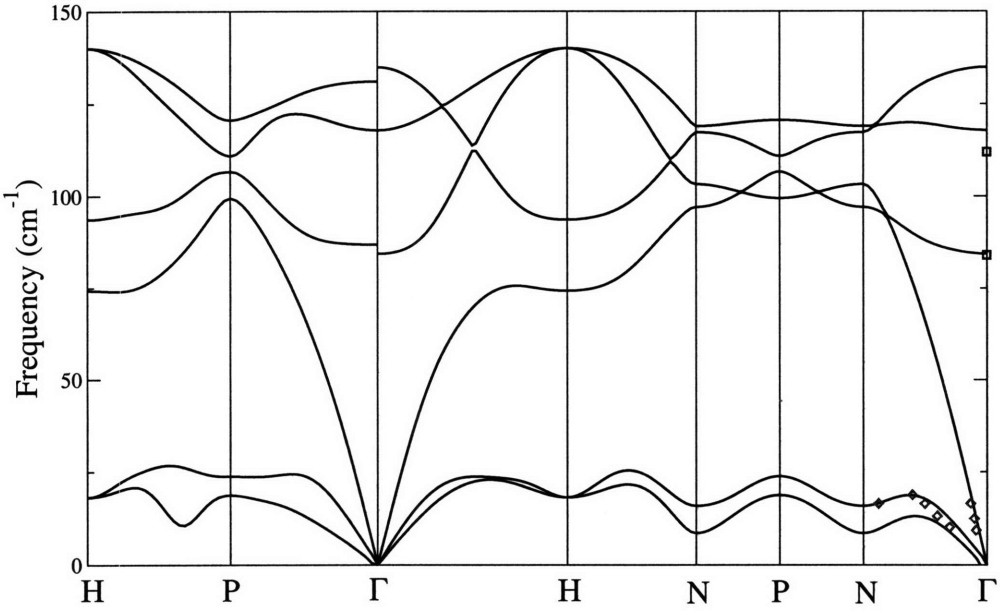

(a)

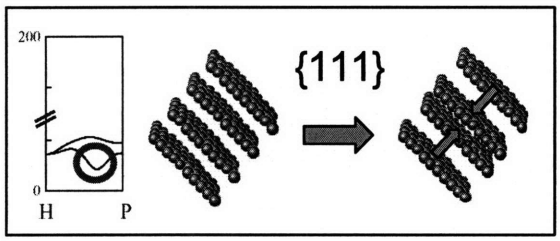

(b)

FIGURE 4-6: (a) Calculated zero-temperature phonon dispersion $\omega(\mathbf{q})$ along the high-symmetry directions of the first Brillouin zone in α-AgI. Results from neutron scattering (red squares) and infrared absorption (blue diamonds) are also indicated [132]. Calculations were performed on the 2-atom primitive cell with a $12 \times 12 \times 12$ k-point mesh and the with the silver ion occupying the tetrahedral interstitial site. (b) Schematic illustration of the softening of the $\mathbf{q} = \left(\frac{2}{3}\frac{2}{3}\frac{2}{3}\right)$ phonon mode. This low-energy transformation occurs when every third $\{111\}$ atomic plane remains fixed while the remaining planes contract with respect to one another. The contraction is along the $\langle 111 \rangle$ direction, taken in the figure to be perpendicular to the planes shown.

TABLE 4.1: Calculated lattice parameter, Born effective charges, and dielectric constant for α-AgI. Lattice parameter calculations were performed using a 4-atom basis set and an evenly spaced $8 \times 8 \times 8$ mesh of k-points. LR denotes the calculation of the Born effective charges for the 2-atom bcc primitive cell using linear response theory, whereas EE denotes the use of the electric-enthalpy method. For the 2- and 4-atom cells, the silver ions occupy only the tetrahedral interstitial sites. The effective charges obtained from the electric-enthalpy calculation represent averages over several independent atomic configurations from a molecular dynamics simulation of a 32-atom supercell. Experimental values are taken from References [110,135,136].

Description	*This work*	*Experiment*	*% Deviation*
Bulk Lattice parameter (Å)	5.186	5.069	+2.3
Dielectric constant ε_∞	5.88	4.80	+22.5
Born effective charges Z^* (LR)	$\pm$1.27	$\pm$1.26	+0.8
Born effective charges Z^* (EE)	$\pm$1.22	$\pm$1.26	-3.2

Linear-response theory also permitted ready calculation of the dielectric constant in the high-frequency limit ε_∞, and of the Born dynamical effective charges Z^*. Results of these calculations are summarized and compared with available experimental data in Table 4.1. As is typical of density-functional calculations, the dielectric response is overestimated, but agreement of the effective charges is extremely good. Nevertheless, calculating the effective charges in this manner is ill advised, since it is based on small perturbations of the perfect crystal and presumes tetrahedral interstitial occupancy for the silver substructure, meaning it is better suited to a description of the zero-temperature limit. To get a better measure of the dynamical effective charges at finite temperature, we have instead employed the electric-enthalpy method (Section 3.4) to measure the force response of the silver substructure to an applied homogeneous electric field in the linear regime. This calculation was repeated for several independent configurations taken from a molecular dynamics simulation of a 32-atom supercell at 500 K. The results were then averaged to obtain final values for Z^*, which are listed alongside their linear-response equivalents in Table 4.1. We note that in a pure ionic-bonding description of AgI, one should expect the Born effective charges for the ionic species to be $\pm$1. However, the numbers are appreciably far from unity, suggesting the presence of some covalent character in the interatomic bonding. This point will be addressed in detail in Section 4.7.

4.3.3 Finite-size effects

In order to ensure that conclusions drawn from the molecular dynamics simulation data are reliable and appropriate, it is desirable to analyze the possible unphysical effects that can arise when sampling a finite system. This is particular important for first-principles simulations, since the accrued computational expense severely restricts system sizes relative to classical simulations. One such complication is the possible presence of unphysical correlations between nearby images resulting from the application of periodic boundary conditions (Section 2.4). These can occur if the correlation lengths are on the order of the supercell lattice

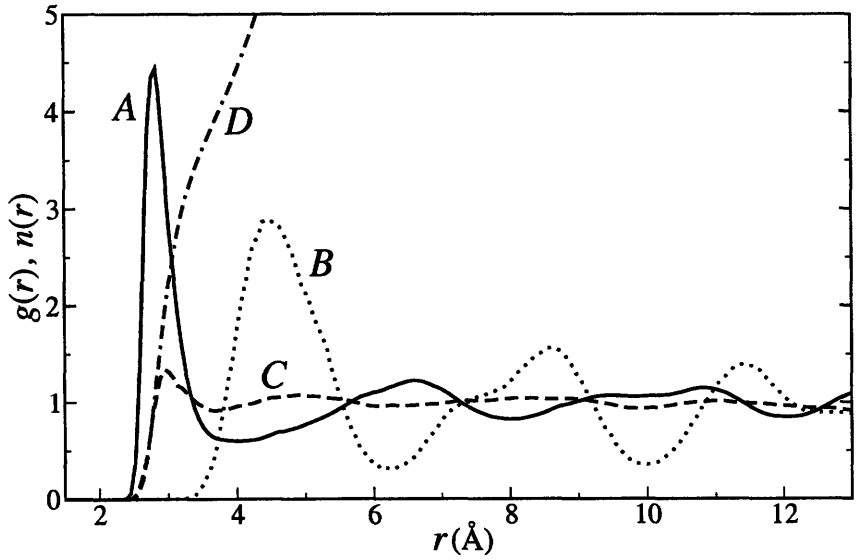

FIGURE 4-7: Radial pair distribution functions for (*A*) Ag–I, (*B*) I–I, and (*C*) Ag–Ag. Curve (*D*) is the integrated $n(r)$ curve, indicating an approximate silver coordination of four in the first shell surrounding an iodine. Data is from a simulation at 750 K.

spacing. One approach for quantifying the correlation length involves examining the pair correlation function $g(r)$ for the diffusive species, calculated according to Equation 3.20. The silver-silver pair correlation function $g_{\mathrm{Ag-Ag}}(r)$, obtained from a 54-atom dynamics simulation at 750 K, is plotted as curve (*C*) in Figure 4-7. The effective independence of silver atoms separated by more than $\approx$ 4.5 Å is immediately evident from the rapid convergence of the curve to unity. Note that this value is much smaller than the repeat-cell distance of $\approx$ 12.6 Å, suggesting finite-size correlation effects can be safely neglected at this temperature.

The relevance of the ω-phonon mode appearing at $\mathbf{q} = \left(\frac{2}{3}\frac{2}{3}\frac{2}{3}\right)$ (Figure 4-6(b)) has already been mentioned. Returning to this point, it should be noted that in a dynamics simulation, in order to properly observe this vibrational mode—which manifests itself as a compression of middle {111} planes with respect to every third stationary plane—our simulation supercell must contain at least three independent successive {111} planes. This fact can be easily confirmed by investigating the presence of the anomalous mode in different-sized supercells of α-AgI. Accordingly, for a 32-atom supercell, which contains only two unique {111} planes due to symmetry restrictions, we detect no evidence of the $\mathbf{q} = \left(\frac{2}{3}\frac{2}{3}\frac{2}{3}\right)$ vibrational mode. However, upon increasing the cell size to include 54 atoms, this mode features prominently in the simulation, with the vibration occurring uniformly along one of the ⟨111⟩ directions. The selection of this direction of vibration can be influenced by a proper choice of the initial silver ion configuration.

The presence or absence of the ω-phonon mode as a function of system size is one example of an entire class of finite-size effects, in which long-wavelength phonon modes are frozen out

by symmetry restrictions in the finite cell. These can often act to retard structural phase transitions or even inhibit them altogether. With specific relevance to our work on AgI, the transition to the hexagonal wurtzite β phase has been prevented via a combination of fixed-volume and finite-size effects. As such, it should be remembered that all simulations performed below the $\beta \rightarrow \alpha$ transition temperature temperature of $T_c = 420$ K were actually on the supercooled α phase rather than the β phase. This fact is crucial to understanding the motivations behind the conclusions presented in Section 4.6. Similarly, finite-size effects are also responsible for artificially elevating the melting temperature in our simulations.

4.4 Time-averaged dynamical structure

4.4.1 Silver ion site occupancy

Using our occupation-density method described in Section 3.5, in which ion trajectories are traced via a superimposition of Gaussian spreads, we have investigated the most frequently traveled pathways for the silver ions in the course of the simulations. In this way, we were able to determine preferred lattice positions and transition pathways for the mobile silver ions with respect to the stationary iodine ions. In the limit of infinite simulation time, resulting occupancy distributions should follow the observed macroscopic symmetry of the cubic crystal lattice. However, as our simulations record a statistically small number of diffusion events, we have taken steps to increase the size of our statistical sample by taking explicit advantage of the translational symmetry of the iodine substructure. The original data set was superimposed with images of the same set, translated by integral multiples of the conventional cell lattice parameter a_0 in each of the three crystallographic directions. Since the width of the 54-atom supercell is three times that of the conventional unit cell, taking advantage of translational symmetry means we are able to boost our sample size by a factor of $3^3 = 27$ without redundancy (assuming uncorrelated statistics). Figure 4-8 shows the resulting isosurface for the silver ion occupation density (Equation 3.17) in the conventional cubic unit cell surrounding an iodine. Slices along the {100}, {110}, and {111} families of planes are plotted in Figure 4-9. It is evident from Figure 4-9 that the regions of highest density lie near the 12*d* tetrahedral sites, with some density smeared toward the 6*b* octahedral sites (we will revisit this smearing in Section 4.7). The octahedral sites themselves, however, exhibit low statistical occupancy. In addition, Figure 4-8 confirms that the preferred diffusion pathway is via the trigonal sites. We note that our profile is in extremely good agreement with the experimental profile found in Reference [110].

An examination of the pair correlation functions (Figure 4-7) offers additional evidence for the preferred location of the silver ions. Integrating $g_{\mathrm{Ag-I}}(r)$ over the first peak and using Equation 3.23 reveals that on average, each iodine has four nearest neighbors in the first coordination shell. This is consistent with geometric expectations for occupancy of the tetrahedral

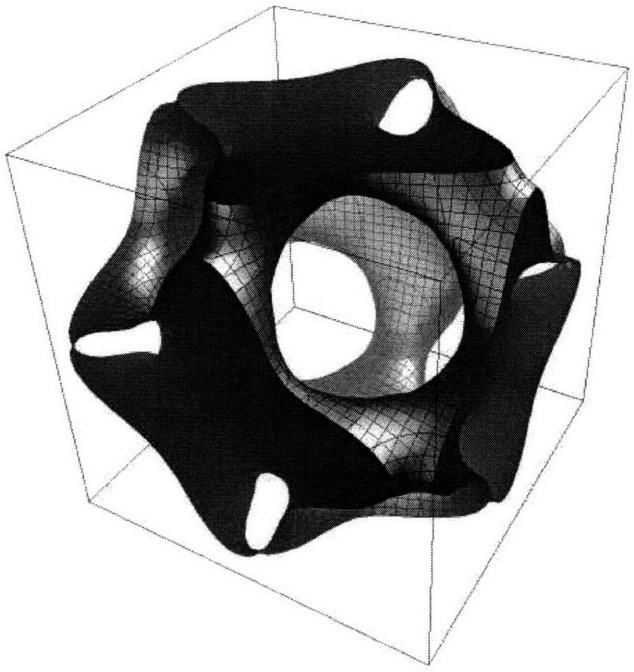

FIGURE 4-8: The isosurface of silver trajectories at 750 K in the conventional cubic unit cell surrounding an iodine. The eight nearest-neighbor iodines surrounding the iodine at the center are located at the vertices of the cube.

interstitial sites. In addition, $g_{\mathrm{Ag-I}}(r)$ indicates that the highest-probability distance for silvers surrounding an iodine is at $R_{\mathrm{Ag-I}} = 2.8$ Å, which corresponds to the distance from an iodine lattice site to its nearest tetrahedral interstitial site.

By defining a threshold radius for an interstitial site, it is possible to track overall occupancy of the tetrahedral sites as a function of temperature. Defining this radius to be one-third of the distance between nearest-neighbor tetrahedral interstitial sites, the average fraction of silver ions occupying tetrahedral sites varies from 62–75% over the experimental range of stability of the α phase (420–828 K [113]), with higher temperatures favoring lower tetrahedral site occupancy. These values generally agree with the estimated 70% occupancy found in the experimental literature [110,115]; however, it should be acknowledged that our results depend on the somewhat arbitrary choice of threshold radius.

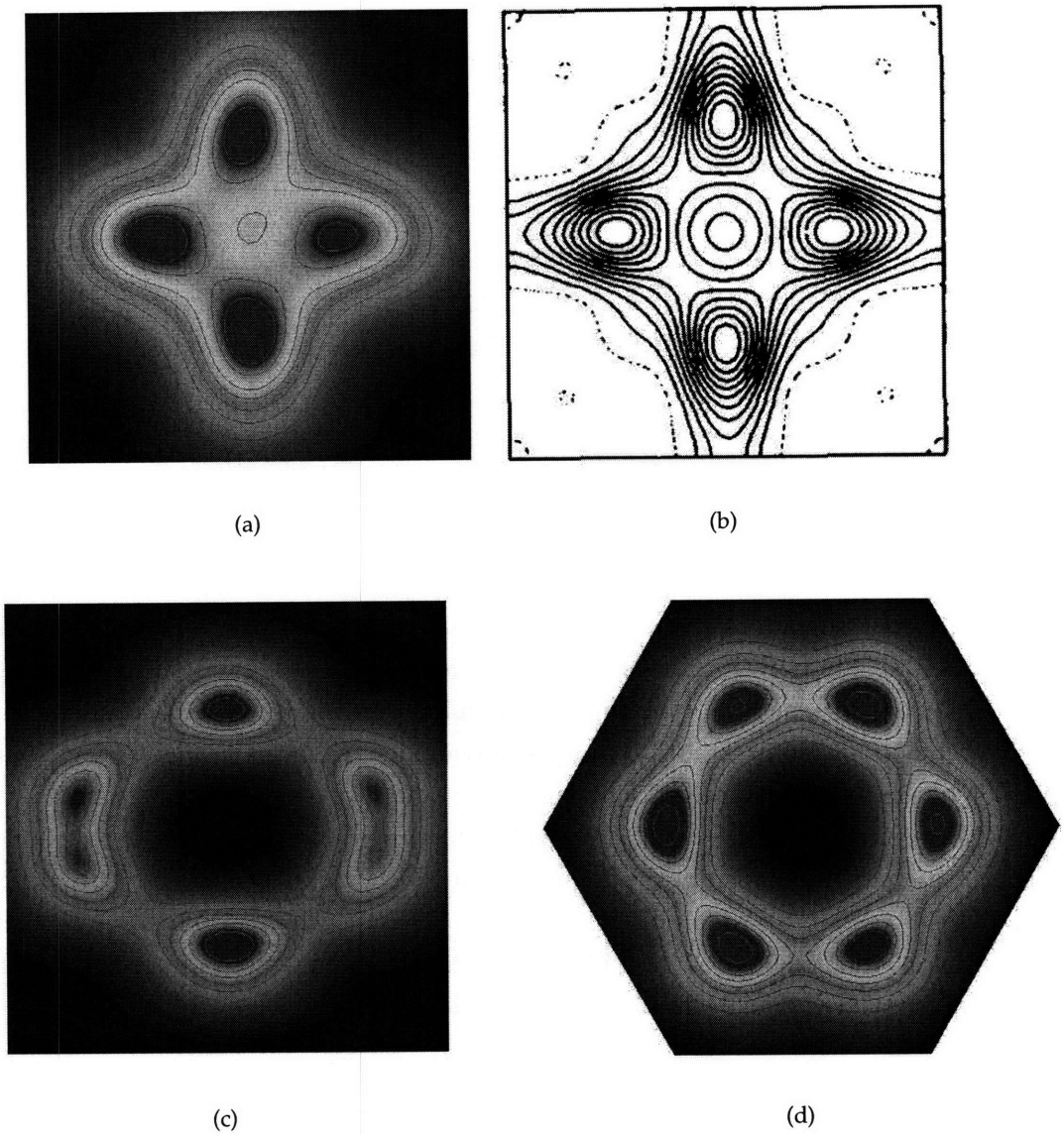

FIGURE 4-9: Occupation density of silver ions in the (a) (100), (c) (110), and (d) (111) planes of α-AgI at 750 K. Areas of high occupancy are shown in red and correspond to the tetrahedral interstitial sites; areas of low occupancy appear in blue. Panel (b) shows the experimental density in the (100) plane at 433 K, taken from References [110, 137].

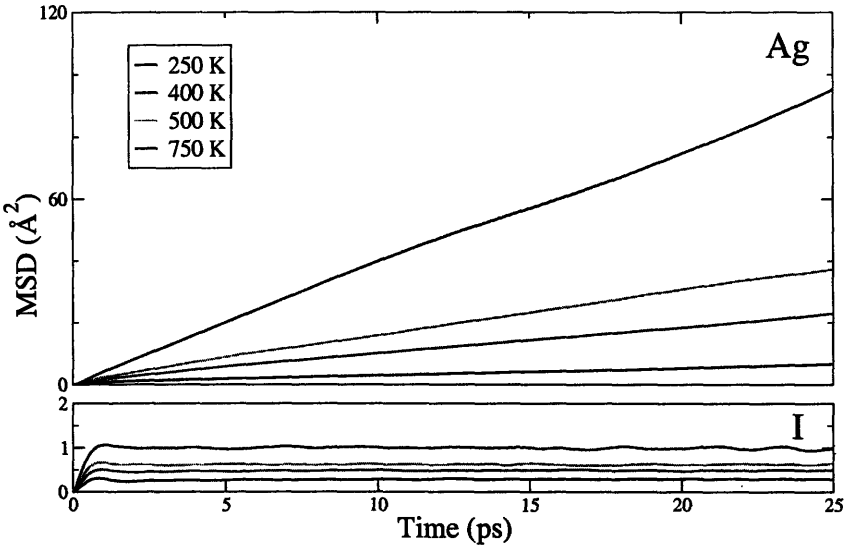

FIGURE 4-10: Mean-squared displacement of the silver and iodine ions in 54-atom simulations of α-AgI at 250 K, 400 K, 500 K, and 750 K. The linear increase in the silver mean-squared displacement indicates liquid-like diffusive behavior.

4.4.2 Demonstration of fast-ion transport

Superionic behavior can be confirmed by independently analyzing the mean-square displacements (MSDs) of the silver and iodine ions. We have plotted the MSDs calculated using Equation 3.26 for a small subset of the sampled temperatures in Figure 4-10. The liquid-like diffusive behavior of the silver ions is immediately evident from the positive linear slope of the MSD, whereas the plateau behavior of the MSD for the iodine ions designates that the material nonetheless remains a solid at all sampled temperatures. Notably, silver conduction continues even at temperatures far below $T_c = 420$ K; this behavior is facilitated by the suppression of the $\alpha \rightarrow \beta$ phase transition due to volume- and finite-cell constraints (see Section 4.3.3). Nevertheless, in Section 4.6.1 we will demonstrate a fundamental difference between silver diffusive character in the low- and high-temperature regimes.

4.5 Instantaneous dynamical structure

One of the most powerful and unique aspects of molecular dynamics is its ability to provide a time-resolved picture of the dynamical structure of a material. Such information is typically inaccessible to most experimental observations, which tend to reproduce time-averaged properties. For AgI, the ionic trajectories allow for definition of a set of ordering rules which govern the instantaneous distribution of the silvers around an iodine. We begin by returning to the pair correlation functions (Figure 4-7) for additional insight into the preferred organization of the silver ions. The silver-silver function $g_{\mathrm{Ag-Ag}}(r)$ illustrates a zero probability of finding

silver ions closer together than $R_{Ag-Ag} = 2.4$ Å. Notably, this precludes simultaneous occupation of nearest-neighbor tetrahedral interstitial sites (likely due to the electrostatic penalty that would be incurred). In addition, we have already mentioned that integrating over the first peak of the silver-iodine function $g_{Ag-I}(r)$ gives a coordination number of four; this is also observed in most of the instantaneous snapshots.

However, a time-resolved analysis also suggests a more detailed decomposition of the first peak of $g_{Ag-I}(r)$. In doing so, we find that most commonly, three of the four nearest-neighbor silver ions simultaneously occupy a shell corresponding to the tetrahedral site distance[‡]. The fourth silver is seen to transition regularly between this shell and its counterpart for a neighboring iodine such that when averaged in time, it fills an unstable transition zone between the two, defined by $3.0 \lesssim R_{Ag-I} \lesssim 4.2$ Å. This phenomenon can be seen in greater detail in Figure 4-11, which tracks the time evolution of the distance from one of the iodines to its closest silver in a simulation. The rate of transition between these two shells is seen to be temperature dependent. Interestingly, these transitions disappear rapidly for $T < T_c$, which gives an early clue that certain properties of the transition to the fast-ion conducting phase are preserved in spite of the inhibition of the structural transition. This will be discussed further in Section 4.6. The fourth silver also possesses an angular distribution that is quite distinct from its three inner counterparts, as indicated in Figure 4-12. The Ag–I–Ag angles for the closest three silvers reveal preferences at 65° and 105°, and higher angles are uncommon. However, the distribution of the new Ag–I–Ag angles introduced by the inclusion of the fourth nearest-neighbor silver is comparatively diffuse and indicates a significant probability for larger-valued angles. This suggests that whereas the closest three silvers remain clustered and correlated in their positions, the fourth silver is relatively unconstrained in its angular configuration. Moreover, it is affected only marginally by the orientations of the remaining three. We find that it is the transitions of this unconstrained fourth silver between first coordination shells of neighboring iodine ions that represent the primary factor behind silver diffusion—an observation that would escape experimental investigations. The unique properties of this diffusive fourth silver will be revisited in Section 4.7. It should be noted that for both the inner and outer silvers in the first shell, there is a zero probability of finding Ag–I–Ag angles measuring less than about 30°; this is consistent with a picture in which nearest-neighbor tetrahedral interstitial sites are prevented from being occupied simultaneously.

Given the above analysis, we now proceed to define of a set of ordering rules for the instantaneous distribution of silver ions in the first shell surrounding an iodine:

1. Four silver ions populate the first shell.

2. No two silver ions occupy neighboring tetrahedral sites.

[‡]The actual number can be obtained by integrating $g_{Ag-I}(r)$ over the appropriate range, as identified in Figure 4-11 and related plots. Calculated in this way, the average tetrahedral occupancy varies from 2.7 to 3.0, with lower temperatures favoring higher values

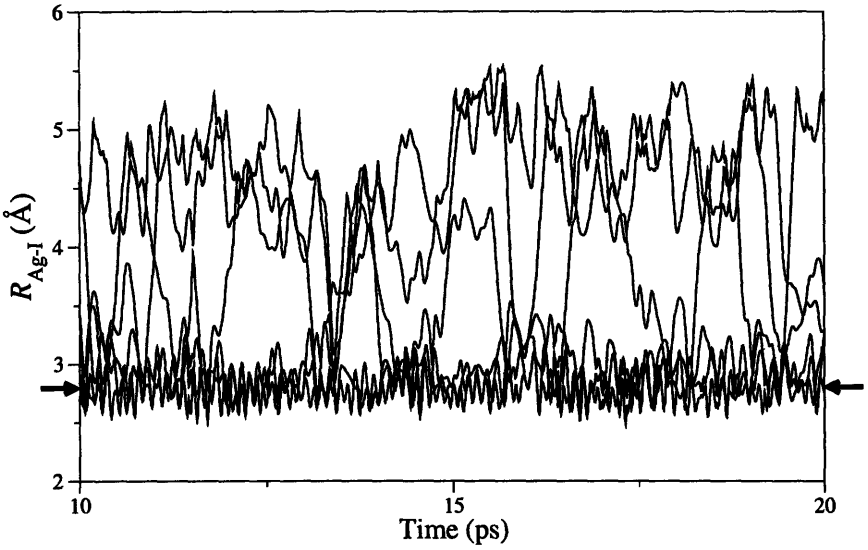

FIGURE 4-11: Distance from one of the iodine atoms to its six nearest silver neighbors, tracked over 10 ps of simulation time. The arrows indicate the distance to the tetrahedral interstitial site in the ideal crystal. Mobile silvers occupy the "transition zone", defined by $3.0 \lesssim R_{Ag-I} \lesssim 4.2$ Å, as they travel rapidly between high-occupancy sites. Data is from a 54-atom simulation of α-AgI at 500 K.

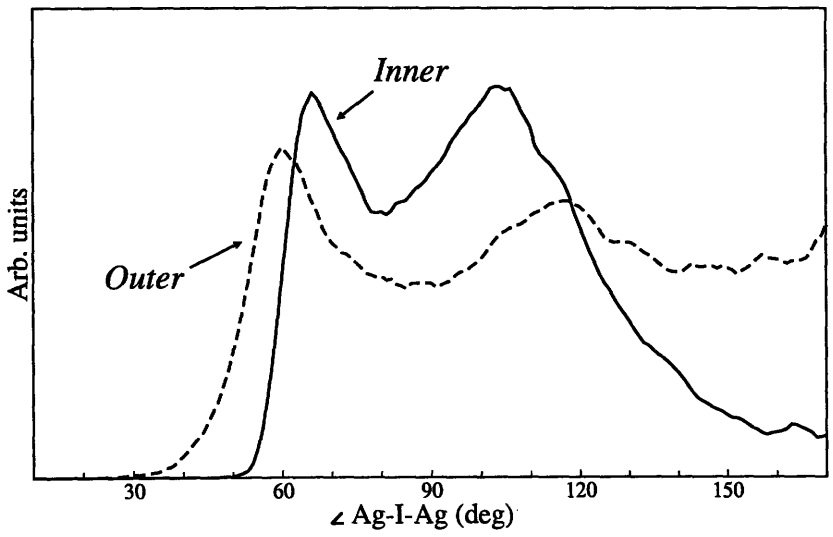

FIGURE 4-12: Distribution of ∠Ag–I–Ag angles for the four silvers in the first coordination shell surrounding an iodine. The solid line indicates the $\angle Ag^{(i)}$–I–$Ag^{(i)}$ distribution and the dashed line indicates the $\angle Ag^{(i)}$–I–$Ag^{(o)}$ distribution, where $Ag^{(i)}$ represents one of the three innermost silvers in the first shell and $Ag^{(o)}$ is the fourth (outermost) silver in that same shell. The most pronounced difference between the two distributions is manifest at angles greater than 120°. Data is from a 54-atom simulation of α-AgI at 750 K.

3. On average, three silver ions surround an iodine at a radius of $R_{Ag-I} = 2.8$ Å, corresponding to the distance to the tetrahedral interstitial sites.

4. The fourth silver transitions between that shell and a second shell at $R_{Ag-I} \gtrsim 4.2$ Å, associated with a neighboring iodine; the transition rate between the two is temperature dependent and disappears below T_c.

5. The angular positions of the three inner silvers are correlated, whereas the fourth (outer) silver remains relatively unconstrained.

4.6 Nature of the transition to the fast-ion conducting phase

Silver iodide offers an excellent case study for understanding the underlying nature of and motivation for the transition to the high-mobility phase in Type-I fast-ion conductors. In Section 4.5, we presented preliminary evidence that at least one element of the fast-ion transition of the silvers is preserved in the observed disappearance of the transitions between shells of the fourth-nearest neighbor silver below the experimental T_c. This is in spite of the inhibition of the experimentally known structural transformation of the iodine substructure to the low-temperature hexagonal wurtzite β phase. Upon further investigation, we find additional evidence of a phase transition of the silver ions near the experimental T_c that is independent of the conformation and dynamics of the iodine ions and signals the transition into the fast-ion conducting α phase. In this section, we substantiate our claims and discuss their implications in terms of understanding the fundamental nature of the fast-ion conducting α phase of AgI from three perspectives: first, as an independently driven phase transition of the cations; second, as an example of a special type of order-disorder transition; and third, as an entropically stabilized phase that sits midway between a solid and a liquid.

4.6.1 An independent phase transition of the silver ions

Evidence from dynamics

As has been mentioned, we find evidence of a phase transition of the silver ions near T_c that does not depend on either the structure or the dynamics of the iodines. This transition in turn signals the structural transformation of the iodines into the fast-ion conducting α phase. The independent transition can be seen in the dynamical behavior by examining the silver self-diffusion coefficient D_{Ag} as a function of temperature. This quantity was calculated from the slope of the mean-square displacements using the Einstein relation (Equation 3.30) and is plotted as curve (*A*) in Figure 4-13. Error bars at each temperature were calculated using the method described in Appendix C. The slope of the Arrhenius plot of D_{Ag} shows a characteristic discontinuity near the experimental T_c. The sharp decrease exhibited in the silver ion

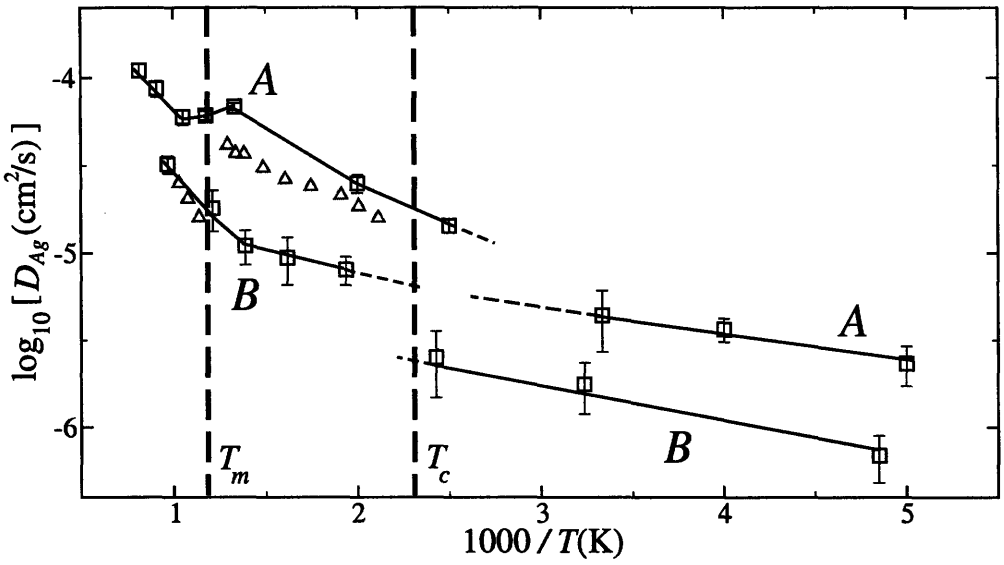

FIGURE 4-13: Arrhenius plot of D_{Ag} for the fully mobile system (*A*) and with the iodine substructure fixed (*B*), as obtained from the MSD. Red triangles indicate available experimental data, taken from References [112, 138]. Experimental values for T_c and T_m at 1 atm are also indicated. The discontinuity in both curves near T_c indicates a phase transition of the silvers.

diffusion behavior upon cooling below T_c remains even though cubic boundary conditions forbid the iodine structural transition to the hexagonal wurtzite β phase.

We have also included in Figure 4-13 the result for an additional set of simulations we performed with a fixed bcc iodine substructure (curve (*B*)). The motivation for these simulations was to determine what effect, if any, the iodine dynamics might have on the diffusion of the silver ions through the lattice. Immobilizing the iodine substructure does lead to an overall decrease in D_{Ag}, suggesting local lattice fluctuations beneficial for silver mobility are frozen out; significantly, the system retains its fast-ion conducting behavior. In fact, the discontinuity in the slope of the Arrhenius plot is actually enhanced for the fixed-iodine case, although the transition temperature T_c shifts slightly towards higher temperatures. This provides a secondary, stronger indicator of the independence of the silver transition from the dynamics of the iodines.

We also note that agreement between our calculations and available experimental results for the silver self-diffusion coefficient [112, 138] is quite reasonable for temperatures within the stability range of the fast-ion conducting α phase (420–828 K). In particular, we obtain very good results for the energetic barrier ΔE_a associated with self-diffusion of the silver ions, which can be approximated from the slope of Figure 4-13 if one assumes a standard Arrhenius form for the expression of the self-diffusion coefficient:

$$D_{\mathrm{Ag}} = D_0 e^{-\frac{\Delta E_a}{k_B T}}. \tag{4.1}$$

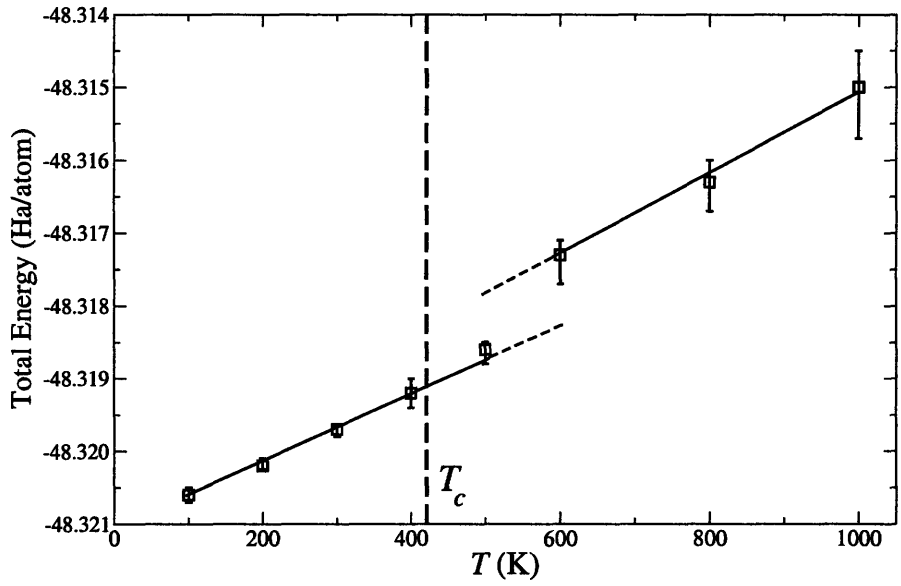

FIGURE 4-14: Total internal energy of AgI as a function of temperature for the fixed-iodine simulations. The experimental T_c is indicated. The discontinuity just beyond 500 K indicates a phase transition of the silvers.

Using Equation 4.1 gives a value for ΔE_a of 0.116 $\pm$ 0.019 eV, compared with the experimental value of 0.095 eV [111, 112]. It is worthwhile noting that the primary effect of fixing the iodine substructure (curve (*B*) of Figure 4-13) is manifest in the exponential prefactor term; the corresponding effect on the energetic barrier is minor.

Evidence from thermodynamics

The described phase transition should also be manifest in the behavior of the total internal energy of the system as a function of temperature. This quantity is depicted in Figure 4-14 for the simulations in which the iodine substructure remained fixed. A characteristic discontinuity corresponding to the latent heat of transition into the fast-ion conducting phase is immediately visible. For the fully mobile simulation, the observed latent heat (not shown) is within the error bounds of the simulation data and therefore remains inconclusive as evidence of the transition to fast-ion conduction. However, it will be demonstrated that the independent silver transition can instead be observed by tracking the evolution of other thermodynamic quantities, such as the specific heat capacity. To do so, we will define a new method for resolving the specific heat capacity into respective contributions from the silvers and iodines.

Although it is generally impossible to separate the total internal energy of the system into respective contributions from each ionic species, we can get a quantitative picture of the energetic fluctuations associated with the silvers or iodines by instead integrating the forces on the ions, which are trivially lattice resolved. Doing so gives the following expression for the

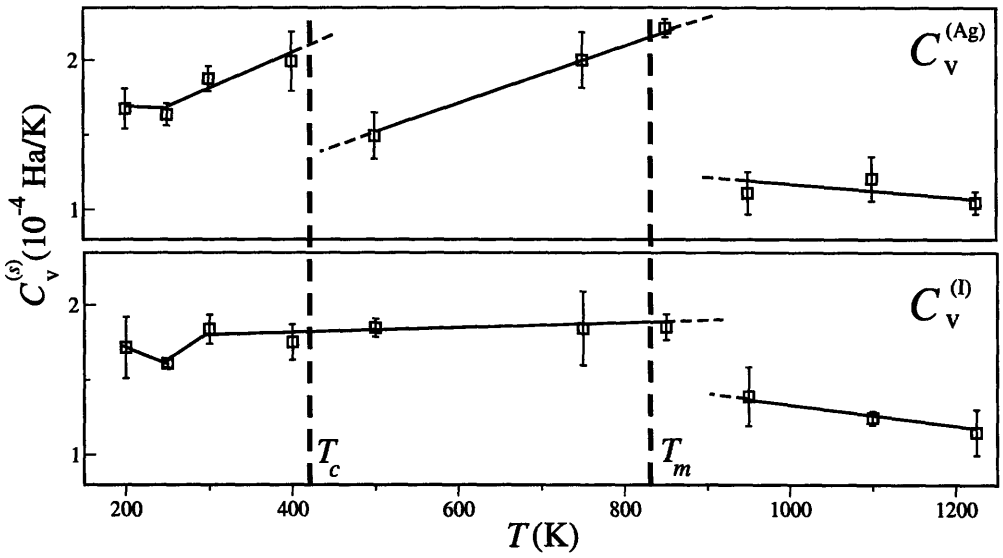

FIGURE 4-15: Specific heat capacities (see text) for the silvers (top) and for the iodines (bottom), with the experimental T_c and T_m indicated. Solid lines are intended as a guide for the eye. The dropoffs indicate the presence of a phase transition for that particular ionic species.

evolution of the species-resolved energy, which we denote as $U^{(s)}(t)$ for species s:

$$U^{(s)}(t) - U^{(s)}(0) = \sum_{J=1}^{N_s} \int_{t'=0}^{t} \mathbf{F}_J(t') \cdot \dot{\mathbf{R}}_J(t')\, \mathrm{d}t', \tag{4.2}$$

where $t' = 0$ represents some equilibrated reference configuration and the index I runs over all N_s ions of the given species. Since in the canonical NVT ensemble, fluctuations in the total energy are related to the specific heat capacity C_V according to Equation 3.31, we can derive a heat capacity-like quantity which we denote $C_V^{(s)}$ that is resolved for species s using the fluctuations in the evolution of the species-resolved energies, as derived independently from the ionic forces according to Equation 4.2. The numerical robustness of this new method was verified by ensuring that the evolution of the total internal energy (which is tracked independently by the code as a function of time) could be recovered to within numerical error by summing species-resolved energetic contributions from both the silvers and the iodines. Plots of $C_V^{(\mathrm{Ag})}$ and $C_V^{(\mathrm{I})}$ are shown in Figure 4-15. In the silver-resolved $C_V^{(\mathrm{Ag})}$ curve, we observe clear dropoffs at 400 K and 850 K, corresponding to the critical temperature T_c and the melting temperature T_m, respectively. Examination of the iodine-resolved $C_V^{(\mathrm{I})}$ curve, however, reveals no detectable dropoff near T_c, although the corresponding behavior at T_m is clearly visible. As was the case for the analysis of Figure 4-13, we can thus link the transition to fast-ion conduction to the silvers only.

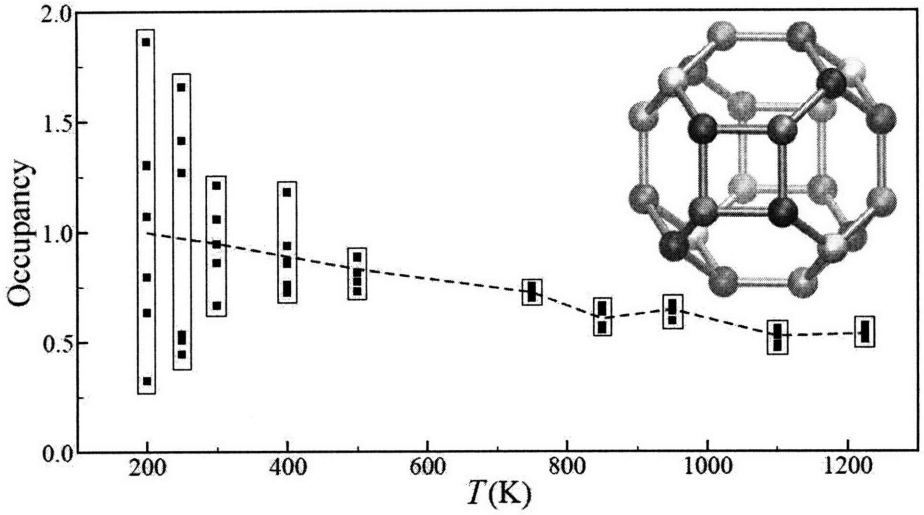

FIGURE 4-16: Average silver occupancies of the six inequivalent tetrahedral bcc interstitial sublattices of Reference [142], normalized against the case for which all ions occupy random tetrahedral sites. The inset shows the network of tetrahedral sites surrounding a single iodine, and the dashed line indicates the overall fraction of silver ions occupying tetrahedral sites. In the inset, spheres of a given color represent tetrahedral sites that are equivalent by symmetry. A separation into high- and low-occupancy tetrahedral sites can be seen for temperatures below 500 K.

4.6.2 An order-disorder transition

We note here that an order-disorder transition of the silver ions at T_c has been reported previously in the literature [139–141]. Symmetry arguments allow the 24 bcc tetrahedral interstitial sites surrounding each iodine to be organized into six inequivalent sublattices [142]. The occupancies of these sublattices can be tracked independently and act as a signal of the transition, as is evident from Figure 4-16. Our results confirm an ordering tendency for the silvers below T_c, characterized by a splitting into higher- and lower-occupancy sublattices. The independent ordering tendency of the silver sublattice upon cooling is observable despite the inhibition of the $\alpha \rightarrow \beta$ transition, in agreement with Reference [139]. The cited references show some disagreement as to the exact structure and occupancy of the low-temperature ordered phases, however. A comparison of our data with References [139–141] to determine which ordered phase is manifest would necessitate more extensive statistical sampling for the *ab-initio* simulation, particularly given the low temperatures in question. Nevertheless, it remains an interesting interpretation of the transition to the fast-ion conducting phase as an order-disorder transition.

4.6.3 An entropically stabilized phase between a solid and a liquid

Figure 4-13 has an additional curious feature that was neglected in our previous discussion—namely, the unusual decrease of the silver ion diffusion coefficient upon melting at about

850 K. This tendency is also visible (and is even more dramatic) in the the experimental data shown in the figure, but it is not captured by classical potentials. The thermodynamic implication offers valuable insight into understanding the stability of the fast-ion conducting phase. We have discussed the liquid-like behavior of the silver ions in the lattice and demonstrated the effective independence of the diffusive properties of the silver cations from both the structure and the dynamics of the iodine substructure. These observations prompt a fundamental conceptual question: if the silver ions' diffusive behavior is nearly independent of the iodine substructure, why does the system not prefer to be in its liquid state above the fast-ion transition, rather than maintaining crystallinity? The answer can be found in the decreased mobility of the silver ions upon melting, which signals a likely decrease in the corresponding silver entropic contribution. Conversely, upon cooling below T_m, the immediate entropic gain achieved in the enhanced mobility of the silver ions effectively stabilizes the phase at intermediate temperatures. In other words, one can suppose that the iodines crystallize into the fast-ion conducting phase below T_m to increase the entropy of the silvers. Accordingly, the fast-ion conducting phase acts as an intermediate between a pure solid and a pure liquid, with a high-entropy liquid species flowing through a low-energy solid matrix. An entropically driven picture of the stabilization of the α phase is also consistent with experimental results [143], which determine the entropy difference between fast-ion conducting and liquid phases to be unusually small.

4.7 Dynamical electronic structure

4.7.1 A unique chemical signature

In characterizing the dynamics of interatomic bonding and the valence charge distributions for a first-principles simulation, it is often useful to examine the electronic wavefunctions in a representation of maximally localized Wannier functions (MLWFs), as described in Section 2.5. We have made use of the Wannier function method to characterize the bonding between ions of each species by calculating the maximally localized orbitals for a large number of independent dynamics timesteps taken from a 32-atom simulation at 500 K and averaging the results. Typical maximally localized orbitals for silver and iodine within AgI are depicted in Figure 4-17. In a general sense, the valence electron distributions surrounding both atoms show a predictably ionic character. For iodine, the full ionic valence shell manifests itself as four hybridized sp^3-like orbitals tetrahedrally oriented about each iodine atom center; for silver, the orbitals are d-like and tend to be centered on the atoms themselves.

Figure 4-18 shows a histogram of the average radial spreads of the MLWFs over the course of the 500 K simulation. These spreads provide a measure of the extent of delocalization for the MLWFs. For comparison, we have also included the spread results for the MLWFs associated with a lattice of singly ionized iodines (I^-) in a diffuse jellium of positive charge spread evenly

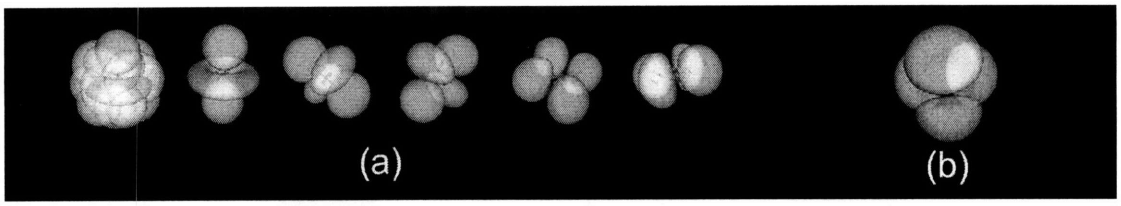

FIGURE 4-17: Isosurfaces of maximally localized Wannier-function representations of the electronic orbitals for (a) silver and (b) iodine in a 32-atom simulation of α-AgI at 500 K. For the case of silver, the individual orbitals are also shown separately for clarity.

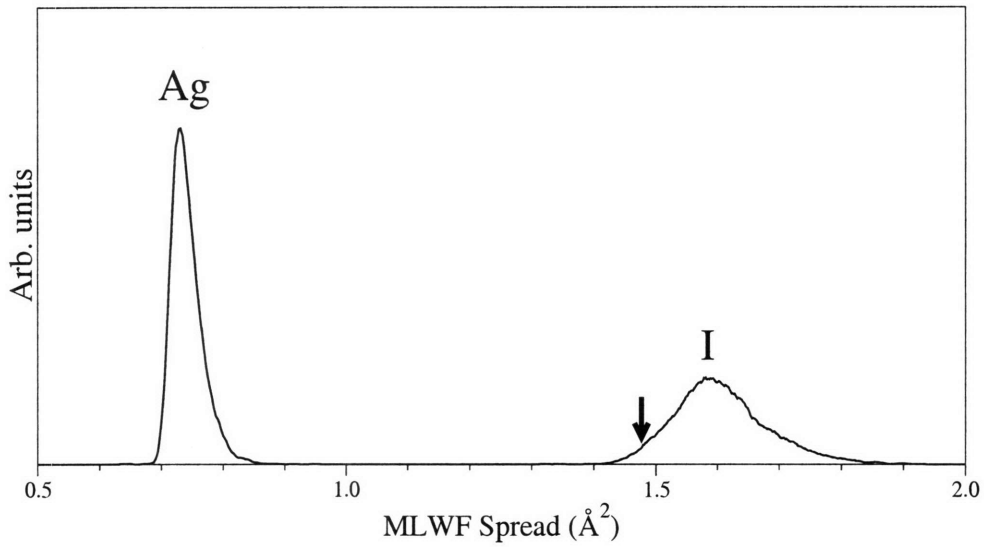

FIGURE 4-18: Histogram of the spreads of the maximally localized Wannier functions of silver and iodine in α-AgI, averaged over 50 ps of a 32-atom simulation at 500 K. The arrow indicates the average Wannier function spread of a bcc lattice of singly charged I^- ions in a diffuse jellium of positive charge. The asymmetry in the distribution of the silver spreads points to a possible non-Coulombic interaction.

throughout the lattice. The distributions of the spreads of the Wannier functions do not exhibit the symmetric Gaussian character expected for a purely ionic solid. Rather, the distributions for both the silvers and the iodines demonstrate an asymmetric skew towards higher values of the spread, pointing to the existence of possible stronger, partial covalent interactions between the two ionic species. The argument for partial covalency in the silver-iodine interactions is strengthened by the results of our calculations of the dynamical effective charges (Table 4.1), which demonstrate significant deviations from integral values.

Recognizing that this possibility warrants further investigation, we plotted the time-averaged distribution of the Wannier function centers (WFCs) with respect to the location of their parent ion. Expectedly, the silver orbitals are centered on their ion centers, whereas the iodine orbitals are located some distance away from their ion centers, consistent with picture shown in Figure 4-17. However, when we plot the distribution of the locations of the iodine WFCs

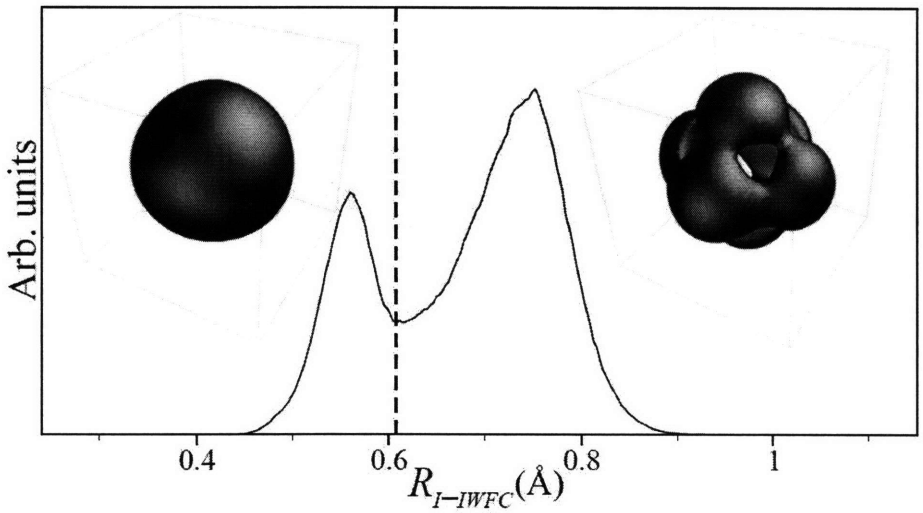

FIGURE 4-19: Histogram of distances between iodine WFCs and iodine nuclei. The insets are contours of the iodine WFC distribution about their nuclei for WFCs on either side of the broken line. The random spatial distribution short-distance WFCs points to predominantly Coulombic interactions, whereas the structured distribution of the long-distance WFCs indicates partial covalent interactions.

(Figure 4-19), the result reveals the significant finding of an unexpected bimodal separation. In particular, the WFCs can be partitioned into short-distance, highly localized WFCs and longer-distance, partially delocalized WFCs. Note that for a material featuring only a single homogeneous chemical environment, one would expect the WFCs to be normally distributed.

Further isolating Wannier functions associated with each of the two peaks and plotting the time- and statistical-averaged contours for the WFCs around the iodines yields the isosurfaces shown in the insets of Figure 4-19. The long-distance Wannier centers (LWFCs) tend to align along the cubic axes toward the octahedral interstitial sites. Their orientations relate to the observed smearing of the silver occupancy from the electrostatically preferred tetrahedral sites towards the octahedral face centers, suggesting that these orbitals correspond to highly directional chemical interactions between silvers and iodines. In other words, LWFCs indicate some covalent-like character in the Ag–I bond. On the other hand, short-distance iodine Wannier centers (SWFCs) exhibit a random angular distribution, as should be expected for a strictly Coulombic picture. Comparing the peak areas in Figure 4-19 reveals that of the four WFCs surrounding an iodine, 30% on average can be classified as SWFCs. Not coincidentally, this figure agrees with the likelihood for a first-shell silver to be found in the mobile transition zone (Section 4.5). It also correlates well with the experimental and theoretical likelihood of a silver to be located outside the tetrahedral interstitial site (see Section 4.4.1). The significance of this correlation will be explored in the next section.

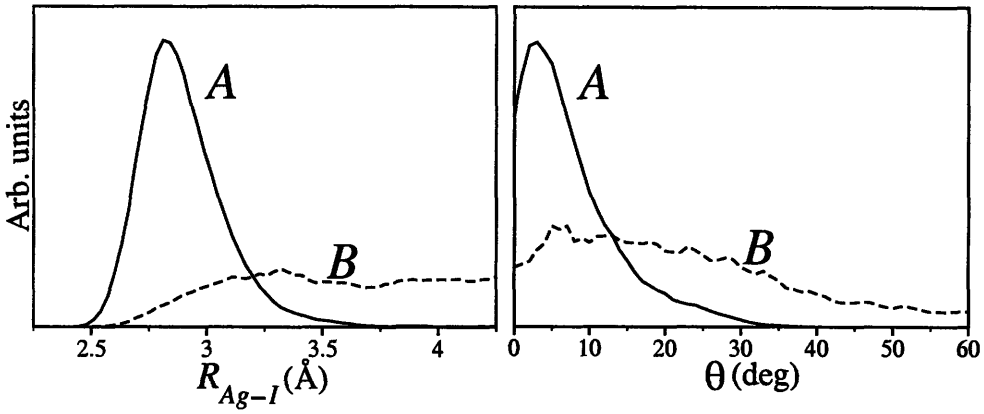

FIGURE 4-20: Histograms of interionic bond distances and bond angles for the silvers closest to iodine WFCs, resolved into (*A*) long-distance and (*B*) short-distance Wannier functions (see text). The bond angle θ is defined as the angle between $\mathbf{R}_{\mathrm{Ag-I}}$ and $\mathbf{R}_{\mathrm{IWFC-I}}$. The long-distance WFCs demonstrate clear thresholds for both the bond distance and bond angle, whereas the short-distance WFCs do not.

4.7.2 Chemical picture of the conduction mechanism

A detailed picture of the correlation between delocalization extent of the iodine MLWFs and the positions of nearby silver atoms is offered in Figure 4-20. There is clear evidence of a chemical interaction between LWFCs and silver atoms within a threshold radius of $R_{\mathrm{Ag-I}} \lesssim 3.25$ Å and a solid bond angle of $|\theta| \lesssim 15°$, indicating that bonding with LWFCs is indeed highly directional. Figure 4-20 reveals no corresponding directionality for bonding with SWFCs, indicating these interactions can be attributed to weaker electrostatics. Moreover, examination of the radial distribution for first-shell silvers closest to SWFCs (not shown) places them within the defined transition zone. We therefore conclude that silvers contributing to D_{Ag} are those which are not bound to LWFCs, meaning they are minimally constrained both radially and angularly. Most commonly, the outermost of the four first-shell silvers fills these criteria, as a lack of stronger directional interactions with LWFCs also increases the average Ag–I bond distance. This comparatively unconstrained, mobile fourth silver fleetingly occupies the transition zone until it is captured by a neighboring iodine, leading to net diffusion. At higher temperatures, thermal disordering breaks a greater number of bonds between silvers and LWFCs, promoting more nearby silvers on average into the transition zone. As such, the overall fraction of occupied tetrahedral sites decreases and diffusion is further enhanced.

The proposed chemically driven capture mechanism that leads to silver ion transport is illustrated schematically in Figure 4-21. If a silver occupying the transition zone comes within the predefined threshold distance and solid bond angle, it can be captured via its interaction with the iodine orbital. This leads simultaneously to a SWFC → LWFC chemical transition of the orbital and a corresponding rapid decrease in the Ag–I bond distance.* This decrease in

*This chemically driven transition the silvers in the neighborhood of the octahedrally oriented LWFCs also conveniently explains the observed anharmonicity in the Ag–I bond as reported in Reference [110].

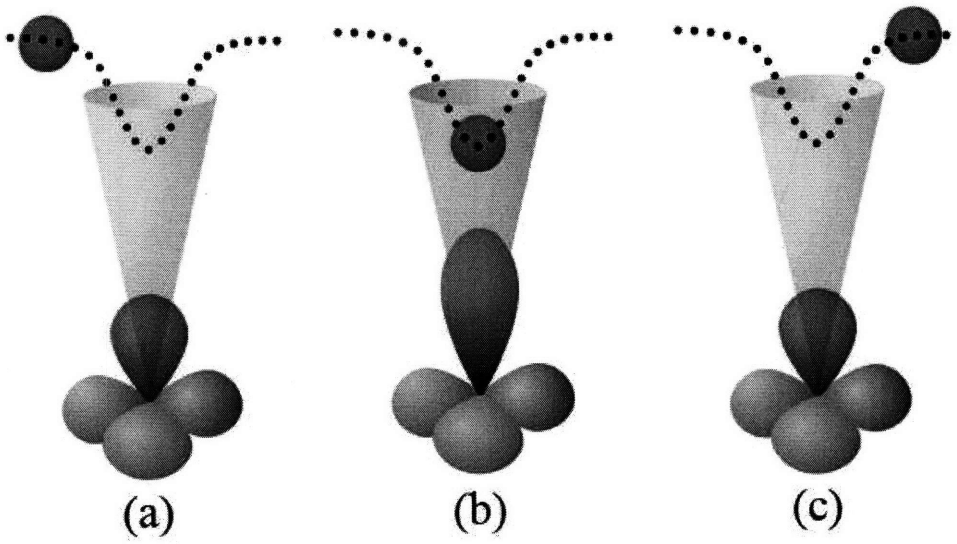

FIGURE 4-21: Schematic illustration of the chemically driven capture-and-release mechanism for a silver ion in the neighborhood of an iodine orbital: (a) initially, the mobile silver ion lies outside the capture zone, and the nearest iodine orbital exhibits SWFC character; (b) once the silver ion crosses the threshold it can be captured by the iodine orbital, leading to a decrease in the Ag–I bond distance and a SWFC → LWFC chemical transition of the iodine orbital; (c) the captured silver ion is eventually released by the iodine, and the SWFC is recovered.

the bond distance is also manifest in the silver ion velocities (not shown), which demonstrate elevated magnitudes in the capture region. Following capture of the silver, the host iodine may release one of its four nearest-neighbor silvers to recover the observed approximate three-to-one ratio of LWFCs to SWFCs, and the process repeats. The motivation for maintaining this ratio likely owes to a combination of thermodynamic and steric factors, the latter referring to the geometric incompatibility between the sixfold symmetry of the LWFC distribution (right inset, Figure 4-19) and the desire for fourfold symmetry in the distribution of the silvers in the first coordination shell, as motivated by electrostatics.

4.8 Summary and conclusions

In conclusion, we have shown that the transition to the fast-ion conducting α phase of AgI is signaled by an independent phase transition of the silver ions alone, characterized by a disordering of the silvers and a sharp increase in their diffusivity. Upon melting, D_{Ag} decreases, pointing to an unusual entropic contribution to the stabilization of the fast-ion conducting phase. We have also identified diffusion pathways for mobile silver ions above T_c, and a time-resolved analysis of ion trajectories has allowed us to define a set of ordering rules that govern the instantaneous distribution of silvers in the first shell surrounding an iodine. Finally, we have found that of the four first-shell silvers, the closest three are strongly correlated and re-

stricted in their angular distribution, and that they are involved in anisotropic, directional bonding to an iodine. The fourth silver is bound only weakly and is relatively unconstrained, and we have isolated it as the dominant contributor to diffusion. We have also proposed a chemically driven capture-and-release mechanism for this fourth silver and present it as the likely motivation for its observed high mobility.

The key findings of this work have been published in Reference [144].

CHAPTER 5

$CsHSO_4$: The kinetics of fast-ion conduction

5.1 Background and motivation

THE RECENT PUSH to realize the hydrogen economy [145] has seen scientists and engineers engaged in an active collaboration to develop environmentally sound technologies for stationary power generation as well as onboard vehicular energy conversion and storage. However, despite extensive efforts originating from the materials community, several key technological hurdles to the widespread adoption of fuel-cell technology remain. One of these challenges is the discovery and optimization of inexpensive, efficient proton-conducting electrolyte materials (a second challenge relates to hydrogen storage technologies and will be discussed in the next chapter). Electrolytes represent a crucial component of a standard fuel cell (Figure 5-1) and should generally be electronic insulators which are permeable to ions but not to neutral species. However, most devices available today use polymer electrolyte membranes (PEMs), which generally require hydration to enable proton conduction and are therefore subject to leakage and containment issues. Electrolytes based on PEMs also suffer from an elevated risk of degradation by attacks from free radicals and of cross contamination. More significantly, the presence of liquid water limits the range of PEM operating temperatures to below 100°C, making them difficult to implement for onboard operation in fuel-cell powered vehicles without the addition of expensive and heavy cooling equipment. In the quest for electrolyte materials tuned to operate at the mid-range temperatures optimal for onboard vehicular applications (100–350°C), a great deal of recent research effort has focused on anhydrous solid-state materials [146, 147]. These do not typically suffer from the same drawbacks as do PEMs and therefore offer greater flexibility in terms of mechanical and thermodynamic constraints.

The fast-ion conducting properties of $CsHSO_4$ were first investigated in detail by Baranov

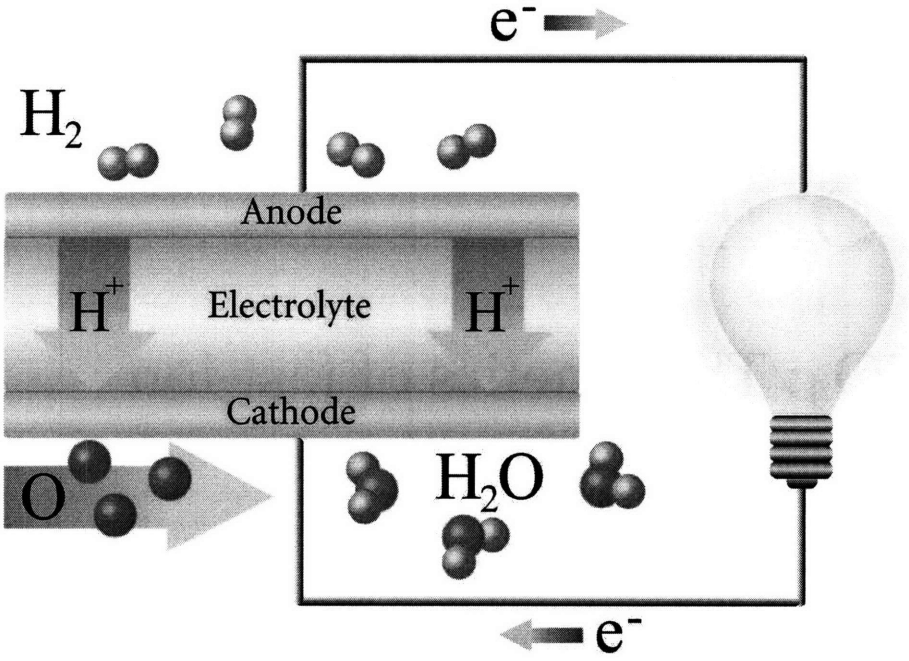

FIGURE 5-1: Schematic diagram of the operation of an ordinary hydrogen fuel cell. Hydrogen is stripped of its electron at the cathode, and the remaining proton diffuses through the ion-conducting electrolyte. Unable to penetrate the insulating electrolyte layer, the electron instead travels through an external circuit, carrying an electrical load in the process. Oxygen is reduced by the electron at the anode, and the protons and oxygen anions recombine to form water as the only byproduct.

et al. in the early 1980s [148]. Even then, its potential as a solid-state electrolyte material was recognizable; however, it was abandoned as a practical solution early on because of its solubility in water. Nearly twenty years later, Haile *et al.* revisited the issue and showed that under certain conditions, stable fuel-cell operation using a $CsHSO_4$ was indeed possible [149]. Subsequent research efforts [150] have focused on further fine-tuning of $CsHSO_4$ and its derivatives from the same family of solid acids, and these are now regarded as some of the more promising candidates for intermediate-temperature solid-state electrolytes. They are also inexpensive and relatively easy to produce [146, 151], making them further attractive from an economic point of view.

$CsHSO_4$ was the first known crystalline material to exhibit both hydrogen bonding and superprotonic behavior and has among the higher ionic conductivities of the known solid-acid materials ($> 10^{-2}$ $(\Omega\cdot\text{cm})^{-1}$ at target operating temperatures). Its phase diagram, depicted in Figure 5-2, is richly complex. The room-temperature phase at ambient pressure is monoclinic (space group $P2_1/c$ and features a static, well-defined network of hydrogen bonds linking SO_4 tetrahedra along the c-axis of the crystal. The high-temperature superprotonic phase—usually designated Phase I—possesses a body-centered tetragonal structure (space group $I4_1/amd$) and is stable above 414K [148]. The structural transition to this phase is accompanied by an

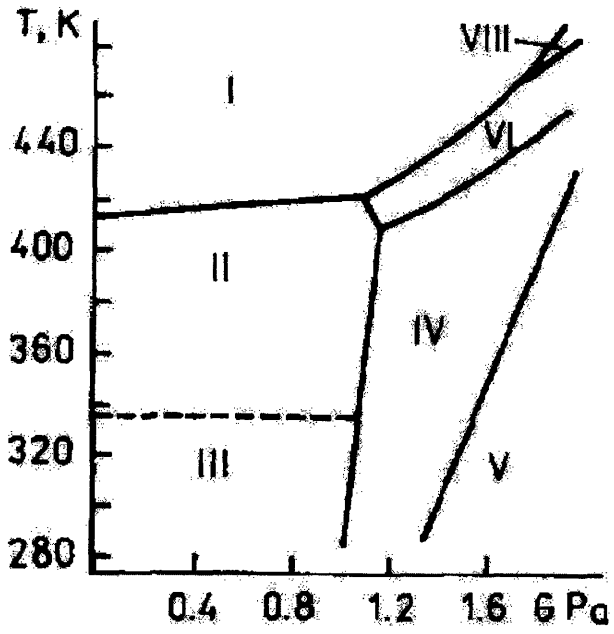

FIGURE 5-2: Phase diagram of $CsHSO_4$. At ambient pressure, the transition to the superprotonic Phase I occurs at $T_c = 414$K. Taken from References [152,153].

increase in the conductivity of more than three orders of magnitude. Its structure is depicted in Figure 5-3 and consists of a lattice of SO_4 tetrahedra, each bonded to a hydrogen via an O–H chemical bond. Each chemically bonded hydrogen also forms an O$\cdots$H hydrogen bond with an oxygen of a neighboring SO_4 tetrahedron. It is known that the resulting hydrogen-bond network becomes dynamic above the transition temperature and can visit a number of distinct topologies, owing to four possible oxygen binding sites for each SO_4 node in the network. However, there exists no theoretical consensus as to the specific atomistic mechanisms involved in proton transport within $CsHSO_4$ and related solid acids, nor have there been any atomistic studies of proton kinetics grounded in first principles. Resolving these shortcomings represents the primary aim of the present study.

The reigning view in the literature [154–158] is that long-range proton transport in superprotonic $CsHSO_4$ occurs as the net result of two distinct mechanisms: first, the reorientation of the hydrogen-bond network by rapid, nearly free rotations of the sulfate tetrahedra; and second, the hopping of the proton between oxygens of neighboring tetrahedra across the O–H$\cdots$O complex when a favorable local network arrangement is encountered. The second step has generally been considered rate limiting and is thought to occur at frequencies of the order 10^{-9} s^{-1}, whereas the first is expected to happen more frequently by at least two orders of magnitude [159, 160]. This two-step process is often referred to collectively as the *Grotthuss mechanism* [161–163] and is closely related to the similar mechanism in water. Since the hopping events are discrete and therefore readily countable, $CsHSO_4$ presents itself as a rele-

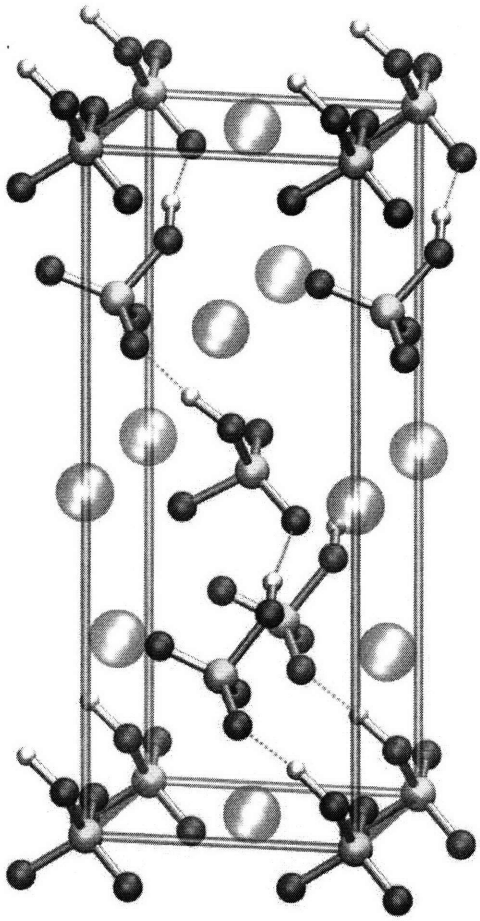

FIGURE 5-3: Structure of the conventional unit cell of Phase-I $CsHSO_4$. Hydrogen atoms are shown in white, oxygen in red, sulfur in yellow, and cesium in blue. Hydrogen bonds are denoted by broken green lines.

vant and interesting test case for examining transport dynamics and kinetics in network solids from a statistical standpoint. This chapter thereby exploits an approach which is quite different from the analytical methodology we employed in Chapter 4 and yet is equally powerful in terms of gaining deep insight into the atomistics of the material. As should become clear by the end of this chapter, our statistical analysis reveals an actual picture of conduction in $CsHSO_4$ that is substantially more complex than is commonly portrayed and features a subtle interplay between the dynamics of the O–H chemical bonds, the O$\cdots$H hydrogen bonds, and the SO_4 tetrahedra in promoting proton diffusion.

Previous molecular dynamics studies [123,164,165] of $CsHSO_4$ based on fitted interatomic potentials have aided in highlighting the basic phenomenology of proton transport and of the transition to the fast-ion conducting phase. However, such investigations are unable to describe the full complexity of hydrogen bonding and electronic interactions. This is particularly

true in a dynamic environment that features rapid bond breaking and forming, since such sudden and extreme changes in the chemical environment are extremely difficult to capture using classical potentials. Ke and Tanaka [166,167] were the first to incorporate first-principles methodologies, but their analysis was grounded in static rather than dynamics calculations. The present study differs in that it aims to elucidate the detailed atomistic pathways and mechanisms involved in hydrogen diffusion in fast-ion conducting $CsHSO_4$ using *ab-initio* molecular dynamics.

5.2 Computational parameters

Ultrasoft pseudopotentials for hydrogen, oxygen, and sulfur using the gradient-corrected Perdew-Burke-Ernzerhof (PBE) exchange-correlation functional were obtained from the Quantum-ESPRESSO website [124]. For cesium, we generated a PBE norm-conserving scalar-relativistic pseudopotential with a $6s^{0.5}5d^{0.05}6p^{0.05}$ valence configuration using Paolo Giannozzi's Atom code [168]. In generating the pseudopotential, the Troullier-Martins formalism [126] was used, and nonlinear core corrections (Section 2.4) were adopted to partially account for the overlap of the core and valence electrons. To prevent the appearance of ghost states, it was also necessary to make the s orbital the local channel in the Kleinman-Bylander formalism. The full input parameters, along with results of transferability tests, are listed in Appendix A. Energy cutoffs of 25 Ry for the electronic wavefunctions and 150 Ry for the charge density were chosen based on the results of a force-convergence calculation on the primitive cell of $CsHSO_4$, in which atomic forces were converged with respect to cutoffs to within a threshold of ~ 0.05 eV/Å.

Molecular dynamics simulations of Phase-I $CsHSO_4$ were performed using the Car-Parrinello technique [7] in the canonical NVT ensemble at temperatures of 550, 620, and 750 K. Ionic temperatures were maintained by means of Nosé-Hoover chains [94,95,97,100]. In each case, a second, weaker thermostat was added to the electronic system [99] to ensure adiabaticity over the course of the lengthy simulations. Since the conductivity is significantly lower in $CsHSO_4$ than in α-AgI, we chose to simulate the system at elevated temperatures to sample a maximal number of diffusive events. Structural constraints imposed by the finite supercell volume and periodic boundary conditions had the computational advantage of elevating the melting point of the material beyond its experimental value of 550 K, permitting sampling of a superheated Phase I. Each simulation covered 25 ps of thermalized dynamics following 5 ps of equilibration. This length of time proved sufficient for sampling several hundred to a thousand jump events, making statistical inferences possible. In each case, our supercell was comprised of 112 atoms (sixteen complete $CsHSO_4$ formula units), and periodic boundary conditions were imposed. The fictitious Car-Parrinello mass was chosen to be $\mu = 700$ au with $\Delta t = 7.5$ au, which allowed for conservation of the Car-Parrinello constant of motion while guaranteeing that the

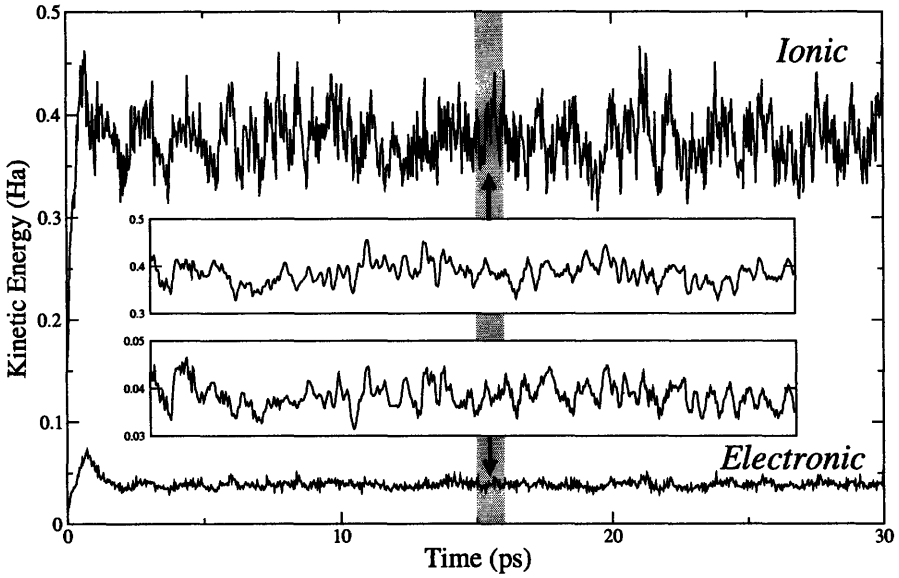

FIGURE 5-4: Evolution of the kinetic energy of the ionic and fictitious electronic systems in the 750 K simulation. The insets expand the gray region to illustrate the adherence of the Car-Parrinello electronic system to the adiabatic surface.

contribution of the electronic system to the total kinetic energy remained suitably small (see Figures 5-4 and 5-5). The lattice parameters for the simulations were chosen based on the experimental values [169] just above the fast-ion transition temperature at ambient pressure (a = 5.732 Å; $c/a = 2.48$).

5.3 Structure and finite-size effects

As a further verification of the suitability of our pseudopotentials, we proceeded to calculate the lattice parameters for $CsHSO_4$. Full ionic relaxations were performed in fixed-volume unit cells in which the a and c lattice parameters were varied, and results for a given c/a ratio were fit to a second-order Birch-Murnaghan equation of state [127]. Each calculation was performed using the 14-atom body-centered tetragonal primitive cell and a 2×2×2 mesh of **k**-points. The two hydrogens were placed in the ordered lattice positions shown in Figure 5-3. The results of the lattice parameter calculation for the superprotonic Phase I are plotted Figure 5-6 and summarized in Table 5.1. Also included in the table are the results of bond length calculations for certain relevant interatomic bonds in the $CsHSO_4$ crystal. In all cases, our results show very good agreement with experiment.

In Section 4.3.3, we used the pair correlation function for the diffusive species as a way to measure finite-size correlation effects. However, because $CsHSO_4$ is a network solid and features a mechanism involving discrete, rapid hopping of protons between neighboring SO_4 tetrahedra that occupy well-defined crystallographic sites, the hydrogen substructure can be

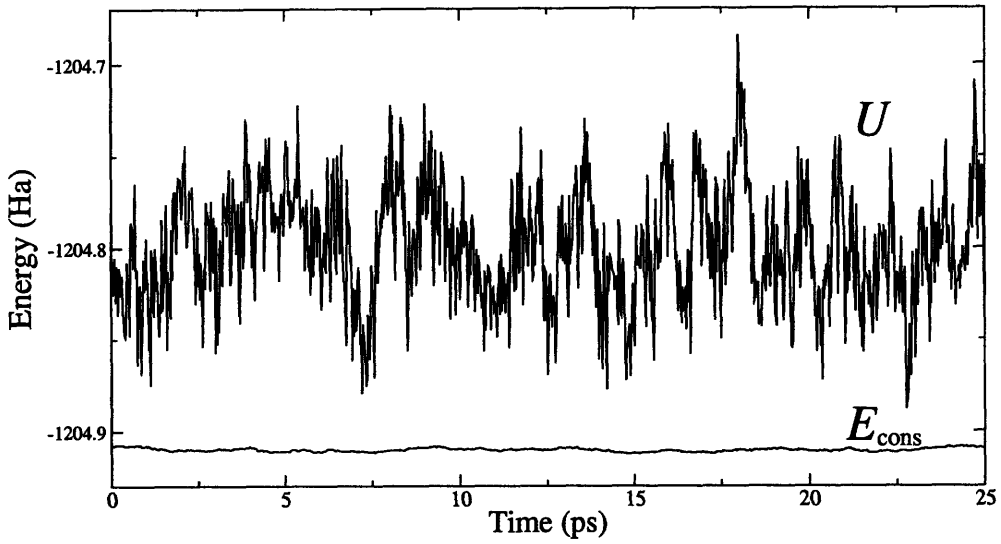

FIGURE 5-5: Evolution of the total internal energy U and the Car-Parrinello constant of motion E_{cons} in a 750 K simulation of $CsHSO_4$, following 5 ps of initial equilibration.

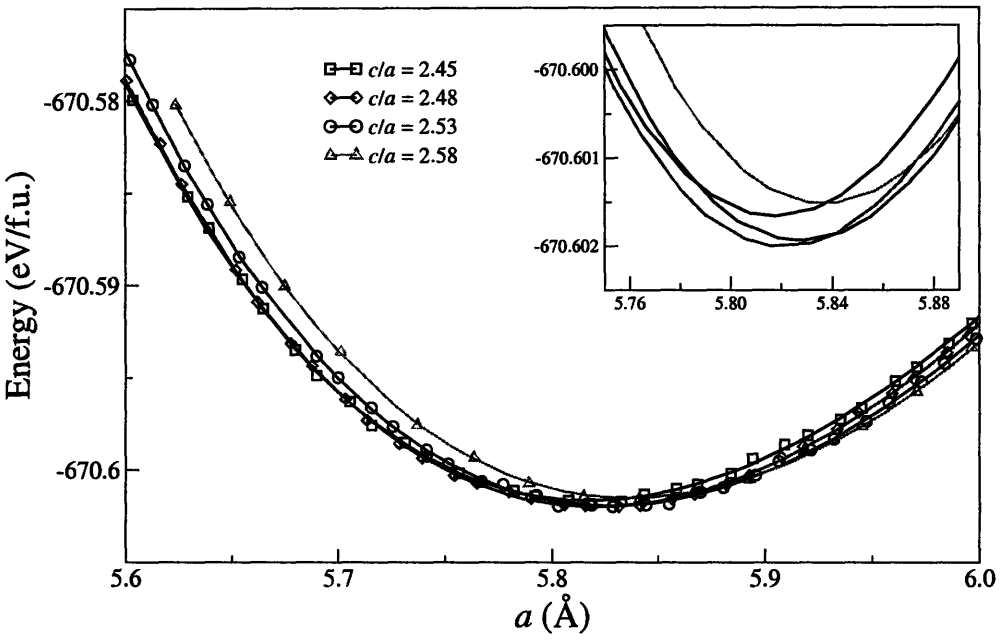

FIGURE 5-6: Equation-of-state calculations for various values of the c/a ratio in Phase-I $CsHSO_4$. Calculations were performed on the 14-atom primitive cell using a 2×2×2 mesh of **k**-points and an electronic wavefunction cutoff energy of 40 Ry.

TABLE 5.1: Calculation of the a and c lattice parameters, as well as various key bond lengths, for the fast-ion conducting Phase I of $CsHSO_4$. Calculations were performed on the 14-atom primitive cell using an evenly spaced 2×2×2 mesh of k-points and an electronic wavefunction cutoff energy of 40 Ry. Experimental values are from References [154,155,170].

Description	*This work*	*Experiment*	*% Deviation*
a (Å)	5.821	5.732	+1.6
c/a	2.48	2.48	0.0
d(H–O) (Å)	1.02	1.01	+1.0
d(H–O···H) (Å)	2.55	2.55	0.0
d(S–O) (Å)	1.50	1.51	-0.7

loosely tied to a lattice model and may therefore exhibit long-range order, even in the absence of any specific correlation between dynamical jump events for nearby hydrogens. As such, the mobile species in $CsHSO_4$ should not be expected to exhibit the true liquid-like behavior characterized by rapid convergence of the pair correlation function to unity. This retention of solid-like order in the hydrogen substructure of $CsHSO_4$ can be seen in Figure 5-7(a). Since the pair correlation function alone is an inadequate indicator of whether our supercell is sufficiently large to reliably discount the existence of finite-size effects, we also chose to examine the distance-dependent correlation of the directions of the velocities of the hydrogen atoms according to:

$$g_v(r) = \frac{2}{N_{\mathrm{H}}(N_{\mathrm{H}}-1)} \sum_{I=1}^{N_{\mathrm{H}}} \sum_{J>I}^{N_{\mathrm{H}}} \left\{ \frac{\langle \dot{\mathbf{R}}_I \cdot \dot{\mathbf{R}}_J \rangle}{|\dot{\mathbf{R}}_I||\dot{\mathbf{R}}_J|} \times \delta(r - R_{IJ}) \right\}, \tag{5.1}$$

where $R_{IJ} \equiv |\mathbf{R}_I - \mathbf{R}_J|$ represents the interatomic separation and N_{H} is the number of hydrogens in the supercell. The results of this calculation for the hydrogen atoms in $CsHSO_4$ are shown in Figure 5-7(b). For a solid substructure with minimal dynamical correlation, the quantity in Equation 5.1 would be expected to decay rapidly to the correlation-free value of $g_v = 0$. However, we still observe some degree of correlation even at the full cell-cell separation distance. Although the effect appears to be quite minor beyond the first nearest neighbor, it is possible that long-range correlations between periodic images may somewhat affect our diffusive statistics. We will return to this point in Section 5.7.

5.4 Proton dynamics

In presenting the results of our simulations, we have divided the dynamics into categories of chemical-bond dynamics and hydrogen-bond dynamics. We include in our definition of chemical-bond dynamics any breaking or forming of O–H chemical bonds by Grotthuss-type hopping of a proton between oxygens of neighboring tetrahedra. Any change in the hydrogen-bond network structure resulting from breaking or forming O···H hydrogen bonds that does not also involve breaking or forming O–H chemical bonds is considered in the category of

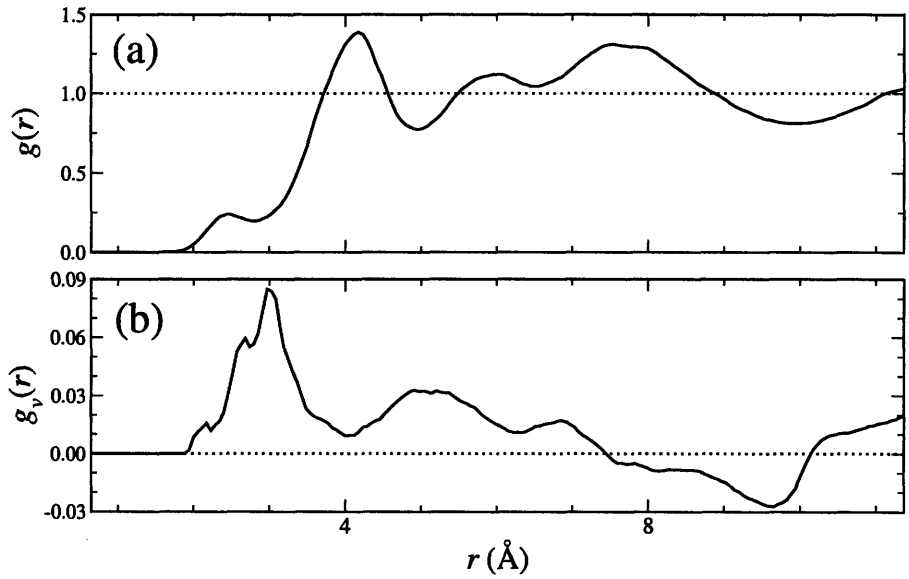

FIGURE 5-7: (a) The hydrogen-hydrogen pair correlation function $g(r)$ and (b) the corresponding velocity pair correlation function $g_v(r)$ (Equation 5.1) for Phase I of $CsHSO_4$ at 620 K. In each graph, the dotted line indicates the uncorrelated liquid-like limit. The lack of convergence of both quantities over the cell-cell separation distance indicates the presence of some long-range order.

hydrogen-bond dynamics. For additional clarity, Figure 5-8 offers schematic representations of sample jump events from both categories of dynamics.

5.4.1 Chemical-bond dynamics

An O–H chemical bond was defined by considering interactions with oxygens within a cutoff distance of $R_{OH} < 1.15$ Å, which represents the initial separation between the first and second coordination peaks of the calculated oxygen-hydrogen radial pair distribution function (RDF), displayed in Figure 5-9. Classification as chemical or hydrogen bond proved more difficult for O–H pairs separated by an intermediate distance $1.15 \leq R_{OH} < 1.35$ Å due to an inherent difficulty in resolving the overlap in the first two RDF peaks in that range. The ambiguity is also noticeable upon examination of the coordination number $n(r)$, which is nearly flat in this region. For such O–H pairs, we instead employed a history-dependent definition, basing the bond category on the last visited unambiguous bonding regime. Under this definition, an existent O–H chemical bond was considered broken only when $R_{OH} \geq 1.35$ Å; analogously, an existent O$\cdots$H hydrogen bond was considered broken only when $R_{OH} < 1.15$ Å.

Within the Grotthuss mechanism, local proton transfer via a series of correlated jumps prompts changes in the chemical-bond structure. Such jumps are first nucleated by the formation of a metastable H_2SO_4 defect, which subsequently propagates along the network backbone, acting as a successive proton donor for neighboring tetrahedra at each stage. The indi-

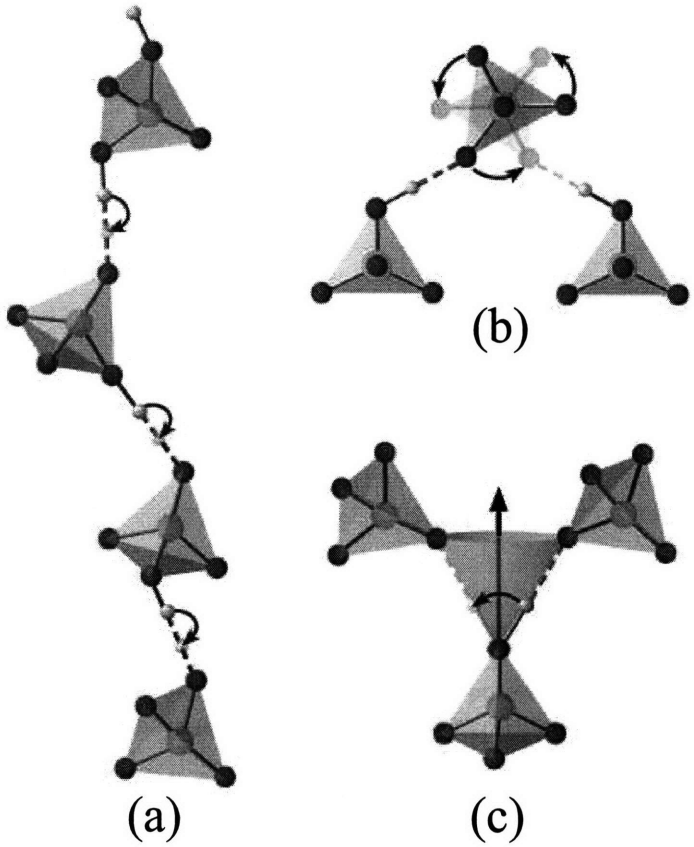

FIGURE 5-8: Schematic depiction of (a) a sequence of chemical-bond jumps nucleated by the formation of an H_2SO_4 defect in the uppermost tetrahedron; (b) a hydrogen-bond network change induced by rotation of a host SO_4 tetrahedron; and (c) a hydrogen-bond network change resulting from a direct hydrogen-bond hop with little or no rotation of the host SO_4 tetrahedron. The color scheme follows that of Figure 5-3, with final configurations in jumping events shown as semi-transparent.

vidual jumps are themselves short hops across a double-well potential barrier, where the two stable minima represent the O$\cdots$H and O–H distances and are separated by about 0.5 Å. A single Grotthuss hop therefore has the effect of swapping a chemical and a hydrogen bond, an action that is repeated as the proton transfer propagates across the hydrogen-bond network chain. This model of local proton transfer in superprotonic $CsHSO_4$, represented schematically in Figure 5-8(a), is easily observable in our simulations. Indeed, just over half (51%) of the chemical-bond jumps that we register at 620 K occur as a direct result of H_2SO_4 defect formation by the donation of a second proton from a neighboring tetrahedron, in accordance with the Grotthuss model (see Figure 5-10). The remaining jumps are nucleated as a result of random local fluctuations in the bond structure. It is reasonable to assume that this fraction of Grotthuss-type hops would increase even further in the presence of an excess proton.

It is likely that for such a cooperative diffusion mechanism, the effect of breaking or form-

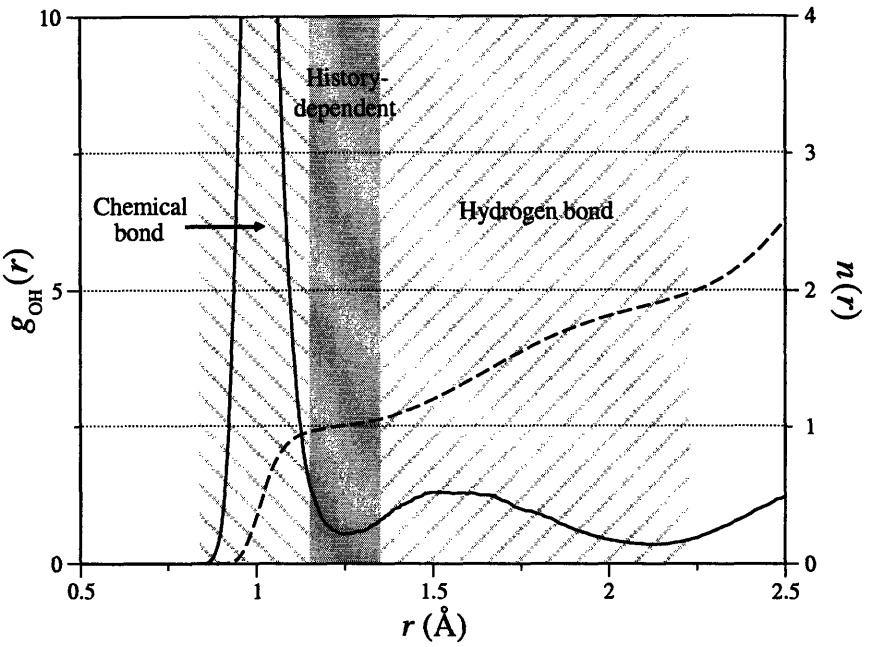

FIGURE 5-9: The oxygen-hydrogen radial pair distribution function $g_{OH}(r)$ (solid line, left axis) and the coordination number $n(r)$ (dashed line, right axis), calculated from a simulation at 620 K. Regions classified as chemical and hydrogen bonds are delineated, as well as the intermediate region for which the history-dependent definition was employed.

ing an O–H chemical bond should have a range that reaches at least to the nearest-neighbor SO_4 node in the hydrogen-bond network; that is, that all eight oxygens in the source and destination tetrahedra should "feel" the effect of the change in the chemical bond structure. Figure 5-11, which shows a charge-density difference plot for a single Grotthuss-type jump in a fixed lattice of $CsHSO_4$ in which only one proton is allowed to move, provides some indication that this is indeed the case. Upon formation of a new O–H chemical bond, the proton pulls charge from the remaining S–O bonds, weakening any O–H bond that may already exist on a different oxygen node on the same SO_4 tetrahedron, thereby decreasing the jump barrier for that second proton. Moreover, at the saddle point of the transition (Figure 5-11(b)), the oxygens on the receiving SO_4 tetrahedron already demonstrate a measurable redistribution of charge, suggesting that changes are felt continuously throughout the entire evolution of the H···O–H complex rather than simply upon O–H chemical bond breakage or formation. This indicates that any change in the local electronic structure—whether manifest in the hydrogen bonds or the chemical bonds—is likely to effect some appreciable long-range electronic consequences.

It is a straightforward process to track bond formation and annihilation, and we can define

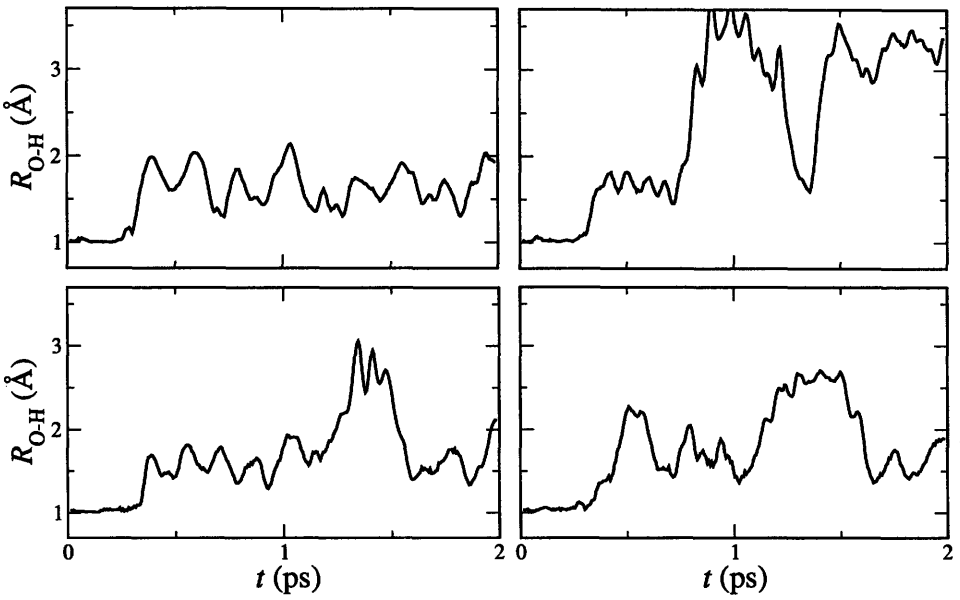

FIGURE 5-10: Distances between four diffusive hydrogen atoms and the oxygens to which they were originally bonded, tracked over the first two picoseconds of equilibrated simulation time at 620 K. Large increases in this distance correspond to proton hops between oxygens connected to different sulfate tetrahedra. The increases of the O–H distances for all four protons around 0.3–0.4 ps evidence a Grotthuss-type correlated jump event in which these protons are collectively involved.

a time autocorrelation function for bond existence as

$$C_e(t) = \frac{1}{N}\sum_{i=1}^{N}\langle \alpha(0) \times \alpha(t)\rangle, \tag{5.2}$$

where $\alpha(t)$ is defined to be 1 if a particular type of bond exists between a given hydrogen-oxygen pair at time t, and 0 otherwise (throughout the text, we will use angle brackets to denote averages in the time domain). Here the summation index i is assumed to run over all of the oxygen-hydrogen bonds in the system. Using Equation 5.2, we can obtain a detailed picture of the timescales of the chemical- and hydrogen-bond dynamics. The hydrogen-bond and chemical-bond existence autocorrelation functions are displayed in Figure 5-12.

Beyond about 20 fs, we observe a slow exponential decay in the chemical-bond existence autocorrelation $C_e(t)$, with characteristic exponential decay times in the 11–15 ps range. These values are recorded in Table 5.2, along with the observed average prevalence of chemical-bond jump events at each temperature and the fraction of such jumps that subsequently reverse themselves. As a reminder, we define a chemical-bond jump as a complete exchange of a chemical and a hydrogen bond across an O–H$\cdots$O complex, in accordance with the original definition proposed by Grotthuss. The surprising commonality of chemical-bond jump events

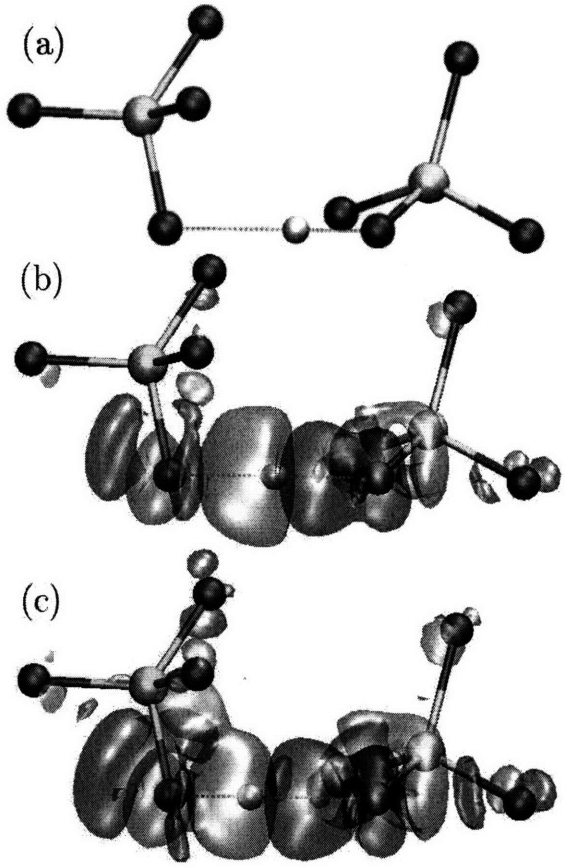

FIGURE 5-11: Isosurface (95%) of charge density difference showing regions of charge redistribution associated with a single proton hop across the O–H$\cdots$O double-well potential. Propagation originates with (a) the proton chemically bonded to the right-hand tetrahedron and proceeds (b) through the transition state to (c) a configuration with the proton chemically bonded to the left-hand tetrahedron. Regions of positive change are depicted in orange and negative change in blue.

is reconcilable with the slow decay rate only when one considers the extremely high rate of jump reversal, which averages around 85% and features no significant variability with temperature. The combination of frequent jumping and a high, temperature-independent reversal rate is suggestive of a potential energy surface featuring an especially shallow activation barrier and bears a marked resemblance to similar findings in simulations of proton transport in water [171,172]. The existence of such a low barrier can be further substantiated by the lack of a distinct separation between the first two peaks in the oxygen-hydrogen radial pair distribution function (Figure 5-9), indicating a surprisingly high probability for the proton to occupy the transition state.

At very short times (<10 fs), we observe a fast fall-off before transitioning to the slower decay regime. In this region, we are below the timescale of any jump reversal subsequent to chemical-bond breaking and forming, resulting in a much more rapid decay. The absence of any noticeable high-frequency periodicity in Figure 5-12 indicates that jump reversal car-

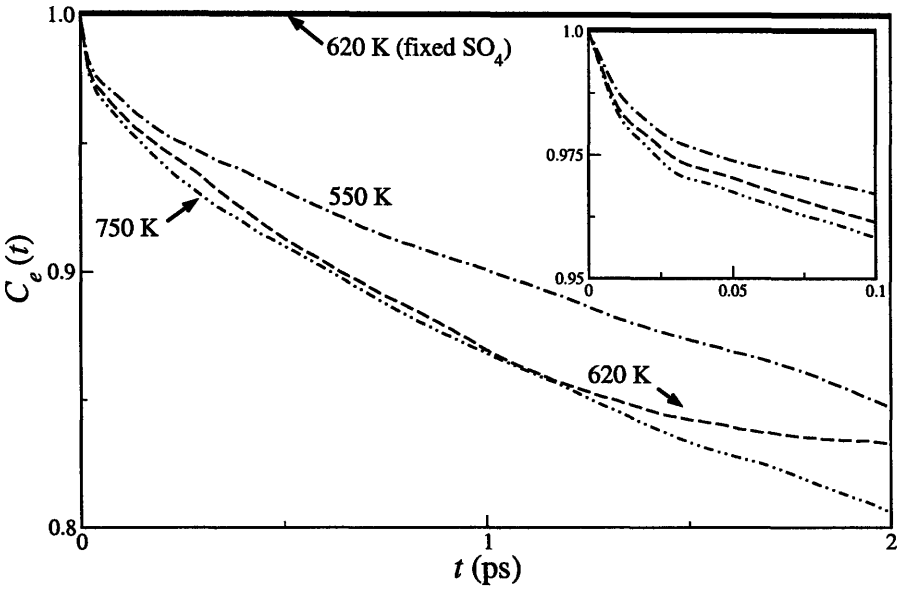

FIGURE 5-12: Autocorrelation functions for existence of chemical bonds after a time t for simulations at 550 K, 620 K, and 750 K, as well as at 620 K with fixed sulfate tetrahedra. The inset expands the region for small times. For the fixed-sulfate simulation, no chemical-bond breaking is observed.

TABLE 5.2: Various quantities derived from a statistical analysis of the chemical-bond dynamics at 550 K, 620 K, and 750 K. Featured columns indicate (1) the characteristic decay time τ in an exponential fit $Ae^{-(t/\tau)}$ of the long-time data in Figure 5-12; (2) the average overall frequency ν_c of chemical-bond jump events per ion, calculated by directly tallying the number of such events that are observed per unit time; and (3) the fraction of these events that subsequently reverse themselves.

Temp. (K)	τ (ps)	ν_c (THz)	% *rev.*
550	15.2	0.58	83
620	12.5	0.80	85
750	11.2	0.94	85

ries no preferred timescale. Rather, it is likely that the reversal probability is a consequence of stabilization or destabilization of the local potential energy surface from SO_4 tetrahedral reorientations.

As an indicator of the potential effect of the motion of the SO_4 tetrahedra on the chemical- and hydrogen-bond dynamics, we have also chosen to run a second simulation at 620 K in which all ions except for the hydrogens were immobilized (denoted "fixed-SO_4" in Figures 5-12 and 5-13). The initial configuration was chosen from a well-equilibrated timestep of the fully mobile simulation. Interestingly, all chemical-bond dynamics ceased in this simulation. This fact is particularly notable in light of previous investigations [156,164,165] which postulated that the most important factor in inducing chemical-bond jumping is a reduction in the O–O distance across the O–H$\cdots$O complex due to SO_4 reorientation. However, in our fixed-SO_4 simulation, not a single chemical-bond jump event was registered, despite the continuous

presence of O–O distances as short as 2.30 Å across O–H$\cdots$O complexes. Notably, this value is approximately 0.15 Å shorter than the average O–O distance across O–H$\cdots$O complexes of hydrogens actively involved in chemical-bond jumps in the fully mobile simulation. Moreover, in our fully mobile simulations, we find only a negligible 0.01 Å difference between the average O–O distances across O–H$\cdots$O complexes of hydrogens involved in chemical-bond jumping events and ordinary hydrogens not involved in jump events of any sort. We therefore conclude that the primary contribution of the SO_4 tetrahedra to chemical-bond jumping must result from their vibrational or rotational dynamics rather than simply their instantaneous orientation. Also, despite the low apparent barrier for Grotthuss-style chemical-bond hopping, dynamic degrees of freedom connected solely to the hydrogens are nevertheless insufficient to permit chemical-bond breaking or forming, detailing the necessary role of the oxygen modes in that process. This observation underscores the difficulty of extracting from the simulation a reliable estimate for the effective barrier of a single Grotthuss jump: any barrier calculation would have to guarantee inclusion of all relevant degrees of freedom, yet the complex interplay between the various resulting dynamical processes generally prevents straightforward decoupling of such an isolated event.

The fact that we were unable to observe any chemical-bond jumps in our fixed-SO_4 simulation also provides insight into the relationship between proton mobility and the transition to the fast-ion conducting phase. Our results clearly indicate that SO_4 dynamics are necessary in inducing proton transport. On the other hand, a classical molecular dynamics study of $CsHSO_4$ [123] found that the transition to the fast-ion conducting phase, as detected in the disordering of SO_4 orientations, could be reproduced even in a rigid-body simulation in which proton dynamics were explicitly inhibited. Together with our results, these findings imply that proton mobility is a direct result of the structural phase transition and the accompanying orientational disorder of the SO_4 tetrahedra rather than the other way around. Note that this contrasts with what we found in our study of AgI in Chapter 4.

Our results also reveal that the general chemical-bond jump frequency is relatively high; moreover, it is of the same order as the hydrogen-bond dynamics (compare Tables 5.2 and 5.3). This contrasts with the view of chemical-bond jumping as substantially rate limiting and differing in timescale from the hydrogen-bond dynamics by two or more orders of magnitude. We instead find that the limiting factor in the *effective* rate of chemical-bond jumps is the extraordinarily high rate of jump reversal, which we suggest is linked to the dynamics of the SO_4 tetrahedra. Yet even when jump reversals are considered, our effective chemical-bond dynamics are significantly faster than the proposed nanosecond scale. However, our results are consistent with a recent set of NMR experiments [173] on Phase-I $CsHSO_4$, which point to much faster chemical-bond dynamics than have hitherto been supposed (on sub-picosecond scales), causing the authors to contend that the atomistic mechanism for Grotthuss-type chemical bond jumping across the O–H$\cdots$O complex is not rate limiting.

It should be noted that in our analysis of jump reversals, we have considered only *sin-*

gle jumps that are subsequently reversed. In so doing, we have neglected the reversal of collective sequences of jump events. Such higher-order jump sequences are especially difficult to properly consider given the inherent time- and lengthscale limitations imposed by the first-principles methodology. It is expected that accounting for the potential reversal of such longer sequences would limit the number of counted "successful" jumps (those contributing to macroscopic proton diffusion). The magnitude of any such limitation is difficult to predict, however.

5.4.2 Hydrogen-bond dynamics

For the purposes of this work, we have defined a hydrogen bond in terms of the oxygen-hydrogen distance alone, with the additional restriction that hydrogen bonding cannot involve oxygens attached to the same host sulfate tetrahedron as the hydrogen. Under this definition, the usual practice of restricting ∠O–H···O had no appreciable effect on the counted hydrogen bonds and was omitted for sake of simplicity. A hydrogen-bond maximum cutoff distance of $R_{OH} < 2.23$ Å was chosen based on the distance for which the coordination number $n(r) = 2$, indicating the tail end of the second coordination peak (associated with H···O) in the calculated oxygen-hydrogen RDF (Figure 5-9). The minimum cutoff of $R_{OH} \geq 1.35$ Å was chosen based on the clear point of separation for the second RDF peak and the end of the plateau region in the coordination number. As for the chemical bonds, we implement the aforementioned history-dependent definition for categorizing bonds in the intermediate range of $1.15 \leq R_{OH} < 1.35$ Å.

Figure 5-13 shows the bond-existence autocorrelation function $C_e(t)$ for the hydrogen bonds in simulations at 550 K, 620 K, 750 K, and for the "fixed-SO_4" simulation at 620 K in which all ions except the hydrogens are immobilized, calculated using Equation 5.2. At longer times, we observe an exponential decay of the hydrogen bonds for the fully mobile simulations that far outpaces that of the chemical bonds (compare Figure 5-12). The graph also reveals that at short times (<50 fs; see figure inset), the hydrogen bond network in the fixed-SO_4 simulation remains very dynamic, approximately following the equivalent curve for the fully mobile system. However, $C_e(t)$ soon begins to oscillate around a fixed running average, indicating repeated visitation of a few alternating configurations. Interestingly, the overall frequency of hydrogen-bond breaking is actually greater for the fixed-SO_4 simulation than for the fully mobile simulation.

Table 5.3 contains these hydrogen-bond breaking frequencies, as well as likelihoods for reversal of hydrogen-bond network reorganization events. In addition to providing overall values, we have divided the hydrogen-bond dynamics into two categories based on the location of the newly formed hydrogen bond with respect to its predecessor. Our first category consists of hydrogen bonds transferred between oxygens of the same destination SO_4 tetrahedron; the second contains hydrogen bonds transferred between oxygens of neighboring SO_4

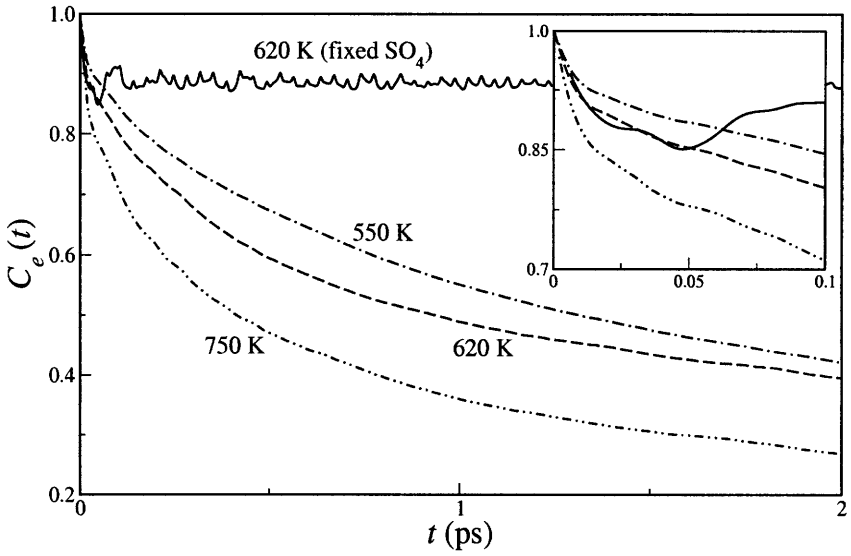

FIGURE 5-13: Autocorrelation functions for existence of hydrogen bonds after a time t for simulations at 550 K, 620 K, and 750 K, as well as at 620 K with fixed sulfate tetrahedra. The inset expands the region for small times. At 620 K, the curve for the fixed-sulfate simulation follows that for the fully mobile simulation for about 50 fs before the two diverge.

TABLE 5.3: Various quantities derived from a statistical analysis of the hydrogen-bond dynamics at 550 K, 620 K, 750 K, and for the fixed-SO_4 simulation at 620 K (designated f-SO_4). The data is separated into statistics for hydrogen-bond exchanges between oxygens of the same SO_4 tetrahedron, those of different SO_4 tetrahedra, and overall totals for either type of exchange. Featured columns include (1) the fraction of total hydrogen-bond exchanges representing a particular class of exchange; (2) the average overall frequency ν_h of hydrogen-bond jump events per ion, calculated by directly tallying the number of such events that are observed per unit time; and (3) the fraction of these events that subsequently reverse themselves.

	Same SO_4			*Different SO_4*			*Overall*	
Temp. (K)	*% tot.*	ν_h	*% rev.*	*% tot.*	ν_h	*% rev.*	ν_h	*% rev.*
550	38	0.47	49	62	0.79	34	1.16	40
620	25	0.58	38	75	1.72	38	2.30	38
750	23	1.01	35	77	3.45	39	4.46	39
620 (f-SO_4)	21	0.96	67	79	3.57	79	4.53	77

tetrahedra. In practice, higher temperatures generally show a greater preference for exchanges between oxygens of different tetrahedra than do lower temperatures, but in all cases, such exchanges outnumber those between oxygens of the same tetrahedron by a margin of two or three to one. Fixing the SO_4 tetrahedra pushes that margin even further.

Unlike in the case of the chemical-bond dynamics, freezing the degrees of freedom of the SO_4 tetrahedra does not prevent reconfiguration of the hydrogen-bond network via bond breaking and forming. In fact, Table 5.3 reveals that inhibiting SO_4 rotation actually enhances the frequency of hydrogen-bond breaking and forming, particularly for bonds exchanged be-

tween oxygens of neighboring tetrahedra. However, some degree of rotation is required in order to explore a larger region of configuration space and prevent repeated visitation of identical configurations—a necessary stipulation for enabling long-range macroscopic proton transport in the material.

The point of separation of the hydrogen-bond autocorrelation curves for the fixed-SO_4 and fully mobile system, as seen in the inset of Figure 5-13, can be interpreted physically as a characteristic reversal time: if a newly formed hydrogen bond is to be accepted, enough SO_4 rotation must occur within the approximately 50 fs window to sufficiently alter and imbalance the energy landscape, thereby minimizing likelihood of back hopping. Accordingly, Table 5.3 shows that the observed fraction of hydrogen-bond network reorganization events that subsequently reverse themselves within this time period in the fixed-SO_4 simulation is more than double that of the fully mobile simulation at the same temperature (38% versus 77%).

A Fourier transform of the hydrogen-bond existence autocorrelation function $C_e(t)$ gives a good measure of the typical oscillation frequencies for the hydrogen-bond forming and breaking in the fixed-SO_4 simulation. Figure 5-14 compares this result to the vibrational density of states for the hydrogens in that simulation as well as in the fully mobile simulation. A comparison of Figures 5-14(b) and (c) allows us to distinguish the hydrogen vibrational modes that are not directly connected to hydrogen-bond breaking from those that are. Those not linked to changes in the hydrogen-bond network are represented by clusters of broader peaks around 15–20 THz, 30–40 THz, and 80–95 THz. Of these, the two lowest-frequency clusters most likely represent bending modes, whereas the highest-frequency cluster contains stretching modes. The primary peaks associated with bond breaking and forming are a low-frequency peak near 9 THz and a fundamental second peak at 28 THz, along with its accompanying overtone peaks at higher frequencies. Since these peaks are completely suppressed in the result for the fully mobile simulation shown in Figure 5-14(a), they represent the signature oscillations inhibited upon stabilization of new configurations by reorientations of the SO_4 tetrahedra. Notably, the half-period switching time represented by the low-frequency peak matches the characteristic reversal threshold obtained from Figure 5-13. The higher-frequency peak at 28 THz is also evident in that same figure, appearing as shallow oscillations at short timescales. The existence of pronounced overtones for the 28 THz peak in both the vibrational and bond-breaking frequency spectra suggests significant anharmonicity in the potential for the H$\cdots$O bond.

Since the primary effect of suppressing SO_4 rotation is to encourage reversal of hydrogen-bond network reorientation phenomena rather than to inhibit such reorientations altogether, SO_4 rotation alone cannot satisfactorily account for the full network dynamics. Rather, we observe that the dominant mechanism for hydrogen-bond network reorganization involves hydrogen-bond transitions that are best described as rapid, discrete angular jumps between two stable states rather than as a smooth evolution driven by SO_4 tetrahedral rotations, as has generally been proposed previously. These two states correspond to different orientations for which the $\angle$S–O–H angle for chemically bonded hydrogens is maintained near the tetrahedral

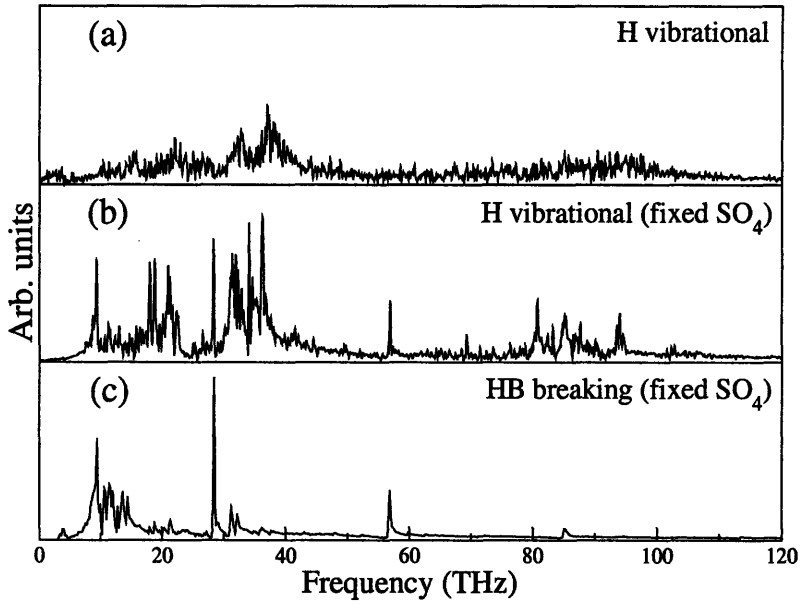

FIGURE 5-14: Vibrational density of states for the protons in (a) the fully mobile and (b) the fixed-SO_4 simulations, along with (c) the hydrogen-bond switching frequency spectrum for the fixed-SO_4 simulation. Data are from simulations at 620 K, and densities of states were obtained from a Fourier transform of the appropriate velocity autocorrelation function. The strong peaks at 9 THz and 28 THz visible in panels (b) and (c) can be associated with the breaking and forming of hydrogen bonds.

angle of 109.5°. This phenomenon is depicted schematically in Figure 5-8(c) and resembles the proposed diffusion mechanism in a recent simulation of liquid water [174].

Additional evidence for the angular hopping model appears in Figure 5-15, which outlines distributions for certain geometrically relevant angles in both the fully mobile and fixed-SO_4 simulations at 620 K. The ∠S–O–H angles for chemically bonded protons have a relatively small spread and are peaked around the described tetrahedral geometry. Angles greater than 145° are not represented, indicating that the protons lie primarily on the surface of a cone centered on the S–O bond and with a half-angle of 65–70°. Notably, the angular distribution does not change appreciably between the fully mobile and fixed-SO_4 simulations. Although hydrogen-bonded protons are generally less constrained, the ∠S–O$\cdots$H distributions for both simulations are still peaked near 110°. However, for the fixed-SO_4 simulation, a second peak appears in the angular distribution at around 140° as a byproduct of the hydrogen-bond hops. The separation of the two peaks for the fixed-SO_4 case in Figure 5-15(b) indicates that generally a net SO_4 tetrahedral reorientation of around 30°, involving either the hydrogen-bond donor or acceptor tetrahedron, accompanies the hop to alleviate the lattice strain it induces. This value for the SO_4 angular rotation agrees well with what has been proposed in the literature [155, 169, 175, 176], but our resolution is insufficient to pinpoint which of the particular competing models is most likely to be correct. Such reorientation is also responsible for alter-

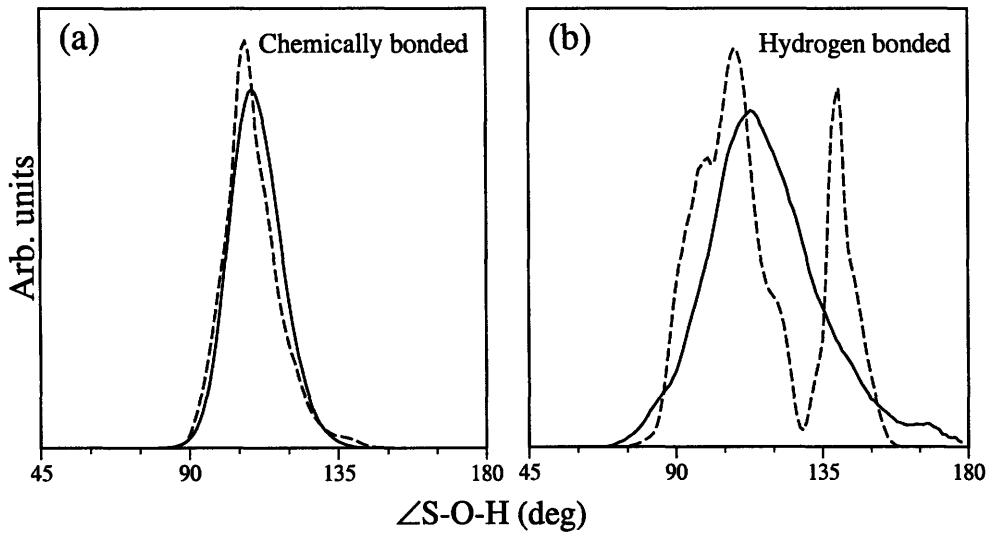

FIGURE 5-15: ∠ S–O–H angles for (a) chemically bonded and (b) hydrogen-bonded protons in fully mobile (solid) and fixed-SO_4 (dashed) simulations at 620 K. The ~30° separation between the two peaks of the ∠ S–O···H distribution for the fixed-SO_4 simulation indicates the angular strain that must be alleviated by the rotation of an SO_4 moiety.

ing the potential energy surface to minimize back hopping.

5.5 Dynamics of the sulfate tetrahedra

Since it has already been established that the 30° reorientation of the SO_4 tetrahedra must take place within a 50 fs window to maximize the potential for non-reversing transitions, we can obtain 10.5 rad/ps as a back-of-the-envelope estimate for the minimum SO_4 angular velocity required to prevent reversal following a hydrogen-bond switch. The SO_4 angular velocities follow a Boltzmann distribution and are plotted in Figure 5-16. The plot reveals that velocities of this magnitude, although somewhat rare, are indeed accessible, representing about 8–9% of the SO_4 tetrahedra in the 620 K simulation at any given time.

Figure 5-16(c) shows an isosurface of the angular velocity unit vectors $\hat{\omega}$ for the rotation of the SO_4 tetrahedra, averaged over all such groups in the 620 K simulation. Areas of high density therefore represent preferred axes of rotation, a clear structure for which is visible in the figure. These rotation axes do not align towards the chemically bonded hydrogen or its accompanying oxygen, as is evident from Figure 5-16(b). Instead, they orient along the edges of a cube rotated $\pi/4$ in the (001) crystal plane with respect to the conventional unit cell, thereby correlating with the centers of the nearest-neighbor tetrahedra. The SO_4 rotational orientations thus appear to be governed by the locations of nearby SO_4 tetrahedra rather than the location of the locally bonded hydrogen or the orientation of its corresponding chemical

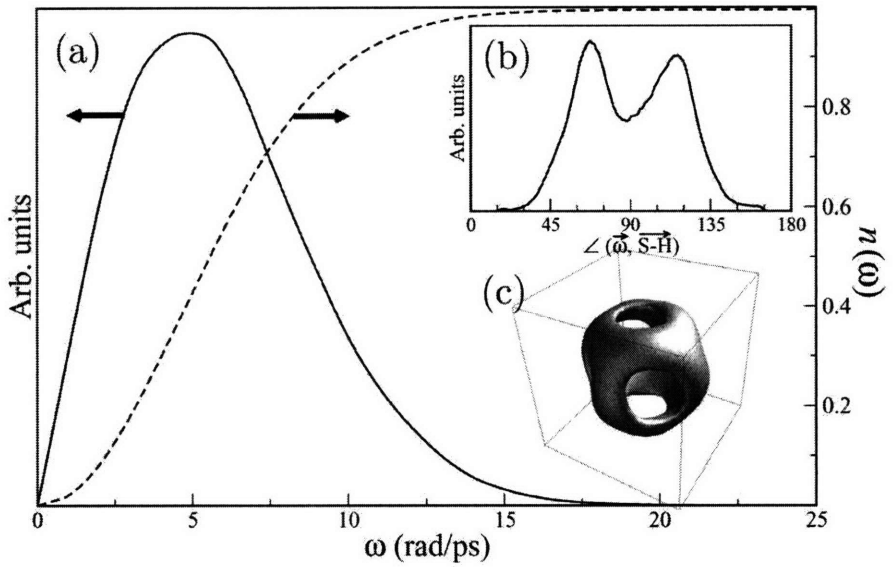

FIGURE 5-16: (a) Angular velocity profile for the SO_4 tetrahedra at 620 K (solid), along with the corresponding fraction of tetrahedra $n(\omega)$ with angular velocities $\leq \omega$ (dashed). Inset (b) shows the angular distribution of the sulfate tetrahedral axes of rotation $\hat{\omega}$ with respect to $\hat{\mathbf{r}}_{SH}$, and inset (c) shows the radial distribution of the $\hat{\omega}$ vectors in space with respect to the primary crystallographic axes.

bond. In other words, rotational axes align along $\hat{\mathbf{r}}_{SS}$ rather than $\hat{\mathbf{r}}_{SH}$ or $\hat{\mathbf{r}}_{SO}$.

Having established that SO_4 rotation is generally highly constrained and has a preferred directionality, we can obtain a quantitative measure of the degree of constraint by comparing the plateaued value of the oxygen mean-square displacement (not shown) to a free-rotation model involving random walk on the surface of a sphere. In doing so, we are assuming that a freely rotating sulfate group has a stationary sulfur center and that the S–O bond length R_{SO} is fixed and well defined. The mean-square distance between a point on the surface of a sphere of radius R_{SO} and any other point on that sphere is given by the simple expression $2R_{SO}^2$ [177, 178], or around 4.5 Å^2. Yet the converged value of the oxygen mean-square displacement that we observe is only 2.4–3.2 Å^2, depending on temperature.

In view of the fact that angular jumps alone, stabilized by small, rapid tetrahedral reorientation events of about 30°, account for much of the hydrogen bond network dynamics (see Section 5.4.2), it is desirable to analyze and requantify the relative contribution of larger-scale rotational motion. Figure 5-17, which shows the averaged distributions of angular distances traveled by SO_4 tetrahedra as a function of time, illustrates one effect of slower rotational dynamics. There is evidence of the appearance of a second peak in the distributions representing a new, stable equilibrium configuration at 75–80° rotation with respect to the original tetrahedral orientation. This peak begins to manifest in statistically measurable quantities only after 250 fs (see inset of figure), making the quickest of such reorientation events several times slower than the timescale of the fast 30° reorientation event described previously. We note that

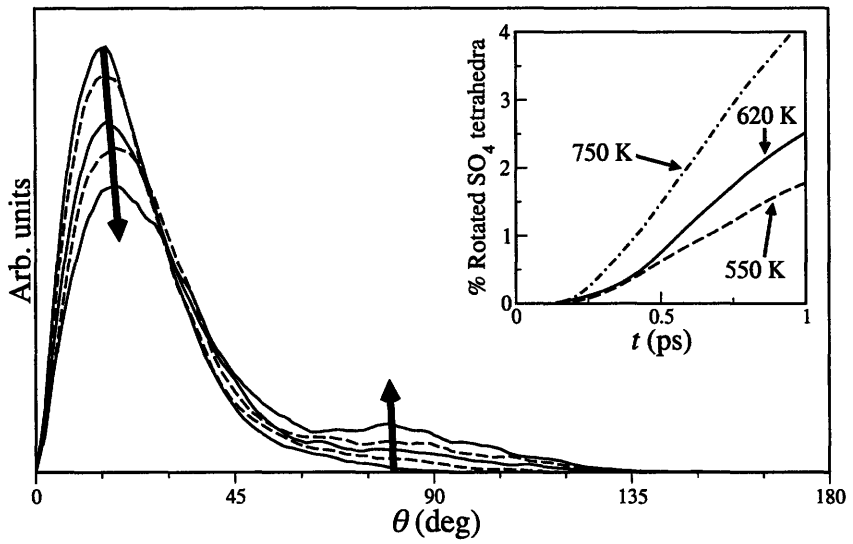

FIGURE 5-17: Distribution of angular distances traveled by sulfate tetrahedra as a function of time at 620 K. Successive curves represent values at 0.5, 1, 2, 3, and 5 ps. For longer times, the growth of a second peak around 70–80° can be seen, indicating the presence of a second stable configuration for the tetrahedron. The inset gives a measure of the fraction of tetrahedra with greater than 70° rotation from their initial positions as a function of time at 550 K, 620 K, and 750 K.

the faster dynamics with the smaller reorientation angle cannot be distinguished in Figure 5-17 since it is buried within the first peak, which primarily depicts the fast librational modes.

Additional confirmation of the existence of multiple distinct timescales for the tetrahedral orientation can be seen in Figure 5-18, which portrays the angular time autocorrelation of tetrahedral configurations. We calculate this quantity according to

$$C_\theta(t) = \frac{1}{N}\sum_{i=1}^{N}\langle \hat{\mathbf{r}}_{SO}(t)\cdot\hat{\mathbf{r}}_{SO}(0)\rangle, \tag{5.3}$$

where in this case, the summation index i runs over all of the S–O bonds in the system. In simple terms, Equation 5.3 produces a measure of the cosine of the average angular distance traveled by an S–O unit vector $\hat{\mathbf{r}}_{SO}$ as a function of time. The slower rotation events manifest themselves as a quasi-linear decay in the autocorrelation at longer times. At short times (<250 fs), the slope is appreciably steeper, indicating faster dynamics on average. Expectedly, the separation between these two regimes agrees with the timescale of the emergence of the slow rotation in Figure 5-17. In addition, a shoulder indicating the timescale of a rotation to a nearby local minimum is clearly distinguishable at around 50–60 fs, in agreement with our previous indicators of fast dynamics on that scale. This shoulder repeats itself as periodic oscillations and is also detectable as a peak in the Fourier transform (not shown) of the curve in Figure 5-18. The oscillations also span the intermediate region in which rotations of both short

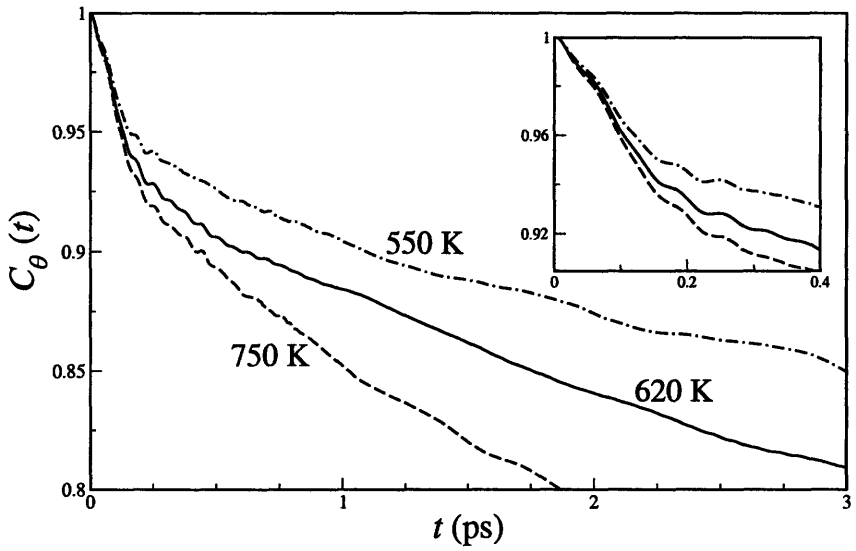

FIGURE 5-18: Autocorrelation function for angular distance traveled between SO_4 tetrahedral orientations separated by time t. The inset expands the region for small times. The small oscillations visible at short times correspond to fast reorientations of the tetrahedra.

and long timescales are manifest before they are lost in the slower dynamics at longer times. We further note that changes in temperature have no appreciable effect on the timescale of the fast rotation, as measured by the locations of the shoulders and oscillations in the figure. This is consistent with a picture in which the reorientation is connected to a hydrogen-bond hop and therefore has an almost negligible rotational barrier.

The anisotropy of the diffusion tensor for $CsHSO_4$ has been documented experimentally [179] and is a geometric consequence of the greater angular distance that must be traversed by a diffusing proton traveling across two sulfate layers along the [001] or [00$\bar{1}$] directions compared to a similar journey parallel to the (001) plane (117° versus 78°; see Figure 5-19). Our results confirm that locally, diffusion parallel to the (001) plane dominates: the directional mean-square displacement of the individual hydrogen atoms systematically rises 2.5 to 5 times faster along the [010] or [100] directions than along the [001] direction. As a crude approximation, this corresponds to a difference in the respective barrier heights of around 0.12 eV (it should be noted that the anisotropy that we observe is more pronounced than that which is seen experimentally; likely reasons for this will be discussed later). The disparity suggests a different dominant mechanism for diffusion along a ⟨001⟩ direction, in part because the angular distance is too great to be easily accommodated by the described hydrogen bond hopping mechanism, and in part because the corresponding angular velocities that would have to be reached by the sulfate tetrahedra to prevent backhopping in such a scheme are unreasonably high. Instead, we find that slower SO_4 rotation plays the dominant role in overcoming the larger barrier, in line with the more traditional model of proton transport in $CsHSO_4$ (depicted

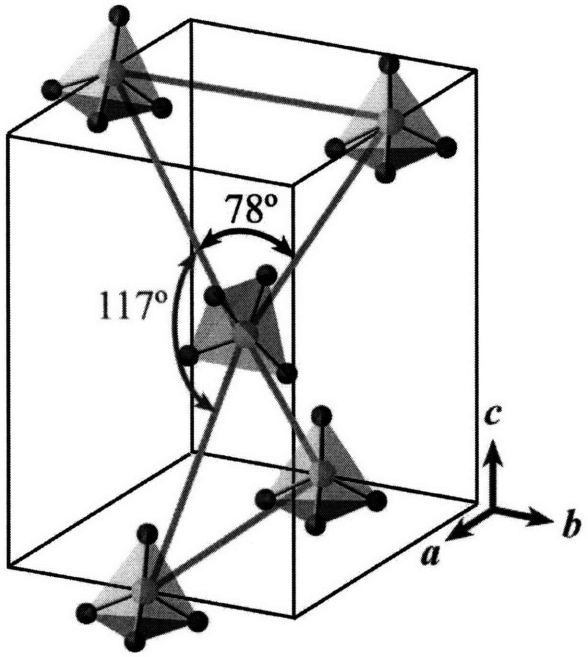

FIGURE 5-19: Illustration of the geometric anisotropy in the arrangement of SO_4 units in Phase-I $CsHSO_4$. A hydrogen-bond jump across two sulfate layers along the [001] direction must traverse an angle of 117°, whereas a hydrogen-bond jump parallel to the (001) plane needs only to traverse a 78° angle.

in Figure 5-8(b)). In this case, the dynamics are slow enough that the timescale of the large-scale rotation is no longer a hindrance. We further note that the approximately 40° difference in the angular distance that must be traveled in the [001] direction with respect to a similar journey in the (001) plane, combined with the aforementioned 30° SO_4 reorientation, satisfactorily accounts for the appearance of the second peak in Figure 5-17 to within a rough estimate. This suggests that for diffusion in the [001] direction, the slow rotation is probably followed by a rapid hydrogen-bond hop, although the former clearly determines the timescale.

5.6 Hydrogen-bond network topology

We have also analyzed the basic topology of the hydrogen-bond network. Table 5.4 shows the relative probabilities of various SO_4 bonding configurations at 550, 620, and 750 K, organized according to the number of hydrogen bonds donated (N_d) and accepted (N_a) by the SO_4 tetrahedron. In our definition, a donated bond is formed between a local chemically bonded hydrogen and one or more oxygens on a neighboring tetrahedron; an accepted bond is a hydrogen bond formed between one or more local oxygens and a hydrogen that is chemically bonded to a neighboring tetrahedron. Thus for an ideal one-dimensional network, one would expect all tetrahedra to have $N_d = N_a = 1$. In our simulations, we observe this type of or-

TABLE 5.4: Observed relative probabilities (%) of SO_4 bonding configurations, organized according to the number of hydrogen bonds accepted (rows) and the number donated (columns) by the SO_4 tetrahedron. Data are from simulations at 550/620/750 K.

% Prob.	$N_d = 0$	$N_d = 1$	$N_d = 2$	$N_d = 3$
$N_a = 0$	2 / 3 / 7	3 / 4 / 6	1 / 1 / 2	1 / 1 / 1
$N_a = 1$	18 / 22 / 26	61 / 53 / 41	11 / 15 / 14	1 / 1 / 1
$N_a = 2$	1 / 1 / 2	<1 / <1 / 1	0 / 0 / 0	0 / 0 / 0

TABLE 5.5: Average lifetimes (fs) of SO_4 bonding configurations, organized according to the number of hydrogen bonds accepted (rows) and the number donated (columns) by the SO_4 tetrahedron. Data are from simulations at 550/620/750 K.

Lifetime (fs)	$N_d = 0$	$N_d = 1$	$N_d = 2$	$N_d = 3$
$N_a = 0$	48 / 53 / 55	47 / 43 / 42	21 / 19 / 25	34 / 21 / 24
$N_a = 1$	176 / 159 / 117	238 / 169 / 105	128 / 119 / 75	81 / 92 / 54
$N_a = 2$	27 / 20 / 24	20 / 17 / 20	0 / 0 / 0	0 / 0 / 0

dinary link only 41–61% of the time, suggesting the actual network topology is much more complicated. Other highly probable configurations include one with $(N_a, N_d) = (1,0)$, which can be thought of as a terminator in the hydrogen bond network (18–26%); and one with $(N_a, N_d) = (1,2)$, which can be interpreted as a network branching point (8–14%). This latter topology, consisting of one tetrahedron hydrogen bonded to two others, is similar to the bifurcated hydrogen-bond complexes found in water [180]. According to Table 5.4, there is a great deal of variability in the number of hydrogen-bond donors N_d, but configurations with $N_a \neq 1$ are comparatively rare. The primary effect of increasing the temperature seems to be a decrease in the number of ordinary linear network links with $N_d = N_a = 1$ in favor of network terminators with $(N_a, N_d) = (1,0)$, resulting in a more nodal network. Some of the rare (but nonetheless statistically significant) configurations are signatures of Grotthuss-type jumps in progress: immediately following a standard chemical-bond jump from one SO_4 tetrahedron to another, nucleated at a link in an ordinary linear chain, the source tetrahedron registers a topological configuration of the form $(N_a, N_d) = (2,0)$, whereas the H_2SO_4 destination complex acquires a configuration of the form $(N_a, N_d) = (0,2)$.

Table 5.5 lists the average lifetimes of the local topologies listed in Table 5.4. Although these values are averages and do not account for the complete distribution of possible lifetimes as do the autocorrelation curves of Figure 5-20 (discussed later), they are nonetheless useful for purposes of qualitative comparison. Lifetimes are generally well correlated with relative frequencies, with hydrogen bonding to a single secondary tetrahedron ($N_a = 1$) acting as a stabilizing force. As the temperature increases, the lifetimes of configurations with $N_a \neq 1$ are affected very little, but we observe a sharp systematic decline in nearly all configurations with $N_a = 1$. Notably, this trend does not always follow that of the relative frequencies in Table 5.4. For example, at high temperatures, network terminators with $(N_a, N_d) = (1,0)$ exhibit

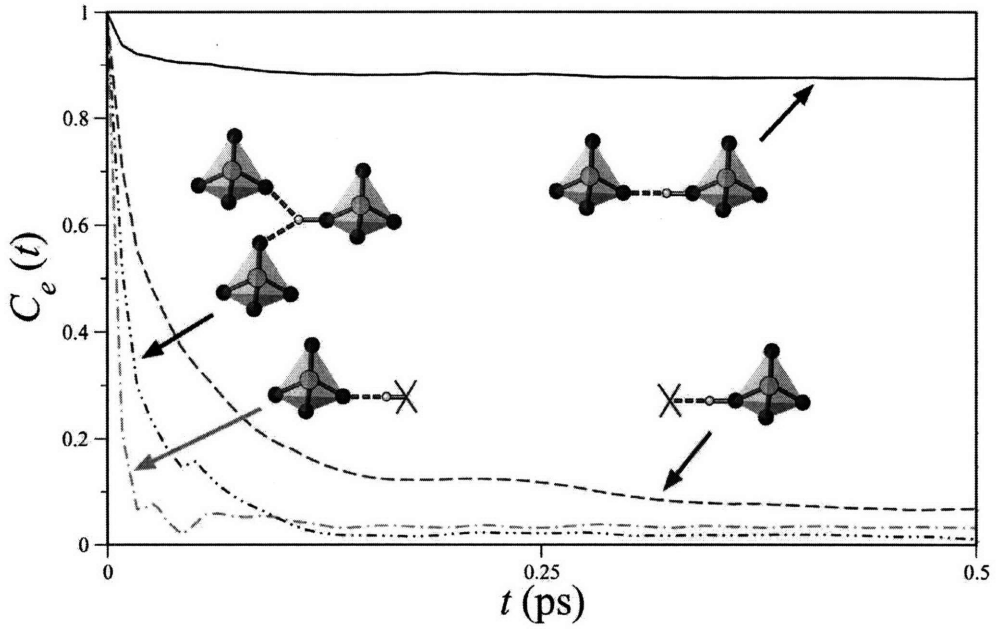

FIGURE 5-20: Existence autocorrelation functions for four of the most likely SO_4 tetrahedral bonding configurations at 620 K. In the schematic diagrams, a solid line represents a chemical bond, a dashed line represents a hydrogen bond, and an "X" indicates the absence of a bond.

a decrease in average lifetime but an increase in their overall commonality, suggesting a more nodal but also more dynamic network.

Tables 5.4 and 5.5 neglect hydrogen bonds to the same SO_4 tetrahedron as the host, in accordance with our original definition of the hydrogen bond. However, if we relax the hydrogen-bonding restriction requiring bonds to be between oxygens of different tetrahedra, we find that these "self-hydrogen bonded" defects, although short-lived, are nonetheless relatively common, representing about 3% of the total O$\cdots$H interactions at 620 K. Moreover, we find that hydrogens involved in chemical and hydrogen bonds to the same SO_4 tetrahedron do not permit simultaneous hydrogen bonding to oxygens of neighboring tetrahedra, meaning these complexes function as terminators for the hydrogen-bond network chains. Also, the velocity of the oxygens in self-hydrogen bonded SO_4 complexes is consistently about 10% higher on average than in ordinary complexes with $N_d = N_a = 1$. This suggests that underbonding lessens the degree of constraint and enhances oxygen mobility in such units, likely aiding further reorganization of the hydrogen-bond network.

In addition to examining the network topology in terms of connectivity between neighboring SO_4 tetrahedra, one can obtain a slightly different topological gauge by looking at the number of chemical and hydrogen bonds formed by a single proton. Figure 5-20 shows the existence autocorrelation curves for four of the most common topologically distinct bonding configurations for a proton. These curves give an idea of the characteristic decay times for each

configuration. The result for a standard bonding configuration, in which a proton forms one chemical and one hydrogen bond (black curve) is shown for timescale reference. We note that topologies with protons forming a single chemical bond but no hydrogen bond (red curve) are surprisingly stable, with a characteristic decay time that is relatively large on the timescale of both the hydrogen-bond hopping and its corresponding strain-relaxing SO_4 reorientation. Defects of this class are less constrained and more mobile than their ordinary counterparts, and as in the case of the self-hydrogen bonded complexes, the increased mobility facilitates network reorganization much more readily. Network-branching configurations with multiple hydrogen bonds (blue curve) play a more direct role in the reorganization of the hydrogen-bond network but have only intermediate stability. A common function of these complexes is as a transition state for stabilizing hydrogen-bond hopping, as discussed in Reference [167]. It should be noted that in addition to the bond topology shown schematically in the figure panel (in which hydrogen bonding is to multiple distinct tetrahedra), network-branching configurations can also involve multiple hydrogen bonds of a proton to different oxygens of a single destination tetrahedron (of the type suggested to exist in water by the authors of Reference [181]); the autocorrelation functions for these cases are essentially indistinguishable. Configurations with no chemical bond (green curve) are extremely short-lived.

Techniques involving the graph-theoretic adjacency matrix (see Appendix B) also offer a convenient way of characterizing the topology of the overall network and extracting configurations most likely to induce a diffusive event. In particular, we are able to further classify the network topology in terms of *rings*, meaning some part of the network ultimately connects back to itself in a closed loop; and *chains*, meaning the network either remains linear or branches, with the restriction that any two network vertices are connected by exactly one unique directed path (i.e., a graph-theoretic tree). Examples of these topologies are depicted schematically in Figure 5-21, and the specifics of our classification algorithm are detailed in Appendix B. It should be noted that such a dichotomy requires classification of every node as either a chain or a ring but does not allow any given node to be doubly counted as belonging to both categories. Table 5.6 lists the likelihood of finding a tetrahedron in various ring and chain topologies in an ordinary simulation timestep versus a timestep immediately preceding a chemical- or hydrogen-bond jump event.

For ordinary configurations not involving a jump event, the network favors rings over chains at 550 K, whereas the trend is reversed at 750 K. The intermediate temperature of 620 K is a topological transition zone and shows a marked increase in configurations simultaneously containing both rings and chains. There is also a notable decrease in the average length of a chain and a slight decrease in the average size of a ring at 620 K compared to the other temperatures. This is a further indication that the network is midway in a transition process from primarily rings to primarily chains, as a network configuration containing both would tend to inhibit the growth of either one at the expense of the other.

Our findings indicate that at all temperatures, the presence of topological chains has a dra-

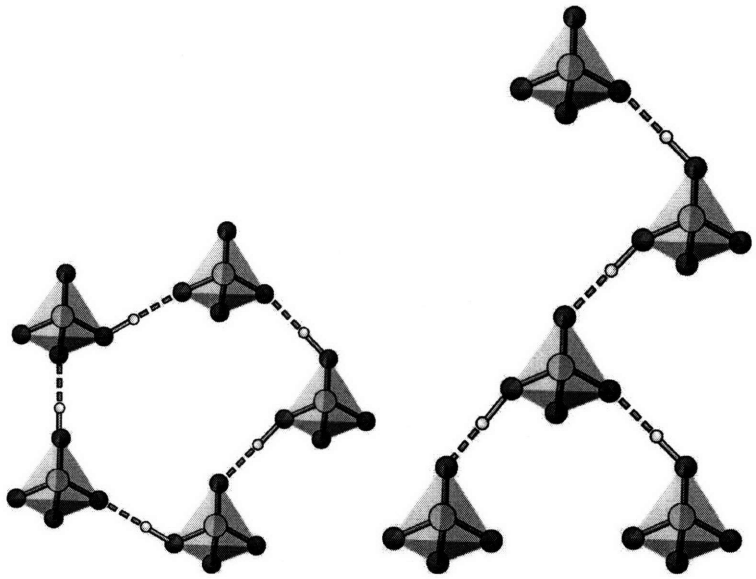

FIGURE 5-21: Schematic illustration of (a) ring and (b) chain hydrogen-bond network topologies in $CsHSO_4$ (see text for definition).

matic effect in enhancing the likelihood of occurrence of either sort of jump event. Conversely, the presence of rings strongly inhibits jumping. The trend is much more evident when one examines frames containing either rings or chains as the only topological species: in frames preceding a chemical-bond jump, we see a 23–24% increase in likelihood of the frame to contain exclusively chains and a corresponding 13–23% decrease in its likelihood to contain exclusively rings, as compared to a frame in an ordinary non-jumping configuration. This difference is especially pronounced at higher temperatures. Nonuniform configurations containing both rings and chains also show an overall decrease in jump likelihood. One likely reason for this is that chains are inherently less constrained chains, allowing for easier formation of intrinsic superprotonated H_2SO_4 complexes. The trends in the chain and ring data also evidence that from a purely topological perspective, a configuration favorable for a hydrogen-bond jump lies midway between an ordinary configuration and one favorable for a chemical-bond jump. We conclude that the network ring and chain topology is a good predictor of both hydrogen- and chemical-bond jump likelihood and is substantially more effective in that capacity than the measure of the oxygen-oxygen distance across the O–H$\cdots$O complex.

We wish to note that the influence of the long-range network structure on proton jump behavior points to the possible existence of larger structural defect complexes that contribute to topological chain formation while stabilizing and enhancing local proton diffusion. These may be thought of as analogous to the Eigen and Zundel hydrogen-bond complexes in liquid

TABLE 5.6: Observed relative probabilities (%) for various hydrogen-bond network topologies in an ordinary timestep, compared with similar quantities for timesteps immediately preceding a chemical- or hydrogen-bond jump event. Also listed are the relevant average ring and chain sizes for frames where those topologies exist. Ring sizes are calculated based on the number of tetrahedra involved in the ring, whereas chain sizes denote the maximum individual branch length within the graph-theoretic tree structure. Data are from simulations at 550/620/750 K.

Description	*No jump*	*Hydrogen-bond jump*	*Chemical-bond jump*
Rings	71 / 78 / 52	64 / 72 / 49	47 / 55 / 28
Chains	60 / 74 / 70	69 / 81 / 75	83 / 87 / 84
Rings only	40 / 26 / 30	31 / 19 / 25	17 / 13 / 16
Chains only	29 / 22 / 48	36 / 28 / 51	53 / 45 / 72
Rings + chains	31 / 52 / 22	34 / 52 / 24	29 / 42 / 12
Avg. ring size	5.6 / 4.5 / 4.7	5.3 / 4.5 / 4.6	4.9 / 4.5 / 4.5
Avg. chain size	6.9 / 5.4 / 6.2	6.9 / 5.4 / 6.0	6.8 / 5.6 / 6.0

water [171, 172, 182, 183]. The necessity of including the oxygen modes in a dynamical description of proton transfer, as well as the relative frequency and stability of the nonstandard bonding configurations discussed above, lends additional credence to such a hypothesis.

It is worthwhile mentioning that periodic boundary conditions and limited supercell sizes have two major topological consequences that must be considered in any analysis: first, they limit the maximum length of chains that can be formed; and second, they tend to artificially inflate the number of smaller rings, since creation of periodic images tends to wrap the network back onto itself prematurely. As such, the values in Table 5.6 should not be taken as absolutes, but qualitative comparisons are nonetheless useful and relevant.

5.7 Proton kinetics and the isotope effect

We can estimate the general three-dimensional proton self-diffusion coefficient D^* from the mean-square displacement of the individual hydrogen atoms using the Einstein relation, which we reproduce here:

$$D^* = \lim_{t\to\infty} \left\{ \frac{1}{6t} \frac{1}{N} \sum_{I=1}^{N} \left\langle |\mathbf{r}_i(t) - \mathbf{r}_i(0)|^2 \right\rangle \right\}. \tag{5.4}$$

From Equation 5.4, we estimate D^* in our simulations to be 1.8–3.5×10^{-6} cm^2/s over the 550–750 K temperature range, about an order of magnitude greater than extrapolations of experimental measurements [160] to the same range (1.9–3.4×10^{-7} cm^2/s). Although this represents a significant error in terms of the magnitude of the calculated diffusion coefficients, we nonetheless observe the proper scaling of D^* with temperature, indicating correct calculation of the effective energetic barriers for the collective diffusion process (around 0.11 eV, assuming a thermally activated barrier and a negligible temperature dependence for the exponential prefactor).

It should be noted that calculations of these coefficients are notoriously difficult to converge, particularly when diffusivities are small and statistics are limited. A simple indication that our limited statistics may be insufficient to obtain well-converged results for D^* can be found by comparing diffusion projected along the [001] and [010] directions, whose values differ by as much as 20% in our simulations despite being geometrically equivalent. An alternative is to use the Green-Kubo relation based on the velocity autocorrelation function to extract the diffusion coefficient, rather than the mean-square displacement; however, this method exhibits even poorer convergence in our simulations, likely due to a combination of the presence of weak long-time correlations and insufficient statistics. Instead, we estimate the accuracy of our diffusion coefficients using a discrete sampling technique in intervals of the 0.2 ps calculated correlation time (see Appendix C). This results in an error margin of ±15% for the calculation of D^*.

Equation 5.4 measures the average self-diffusion of *individual* protons rather than the collective long-range diffusion that is generally detected macroscopically (this point is discussed in detail in Appendix C). In this respect, such results are best compared with a tracer diffusion experiment. An alternative approach involves evaluating a collective diffusion coefficient D_J that describes the motion of the center of mass of the hydrogen atoms:

$$D_J = \lim_{t\to\infty} \left\{ \frac{1}{6t}\frac{1}{N} \left\langle \left| \sum_{I=1}^{N} \left[\mathbf{r}_i(t) - \mathbf{r}_i(0)\right] \right|^2 \right\rangle \right\}. \tag{5.5}$$

Using Equation 5.5 in place of Equation 5.4 systematically deflates our previous results by 35–40%. The discrepancy between the two methods indicates the presence of significant cross correlations between mean-square displacements of different individual particles at different times (see Appendix C), as should be expected for Grotthuss-type successive proton transfer. Given its inclusion of these correlations, the collective diffusion coefficient might seem a better measure of the actual hydrogen mobility; however, it also results in substantially elevated estimates of numerical uncertainty (as high as ±60%), as is evident in Figure 5-22.

Equations 5.4 and 5.5 may be inadequate for describing diffusion in a framework that can be connected to the macroscopic conductivity of the material, however. This becomes obvious upon noting that within the cooperative Grotthuss mechanism, a proton arriving at a tetrahedral SO_4 moiety to form an H_2SO_4 complex is not typically the first to subsequently depart that complex to propagate along the hydrogen-bond backbone. As a result, significant discrepancies are expected when relating our local short-range transport model to any macroscopic long-range measurement of ionic conductivity, analogous to the disparity between group and phase velocities in wave mechanics. One possible way of dealing with this would be to track the trajectories of quasiparticles representing local structural deviations from ideality, such as the superprotonated H_2SO_4 unit. Such an approach would be more in keeping with a model of structural diffusion. However, we have already shown that not every microscopic proton

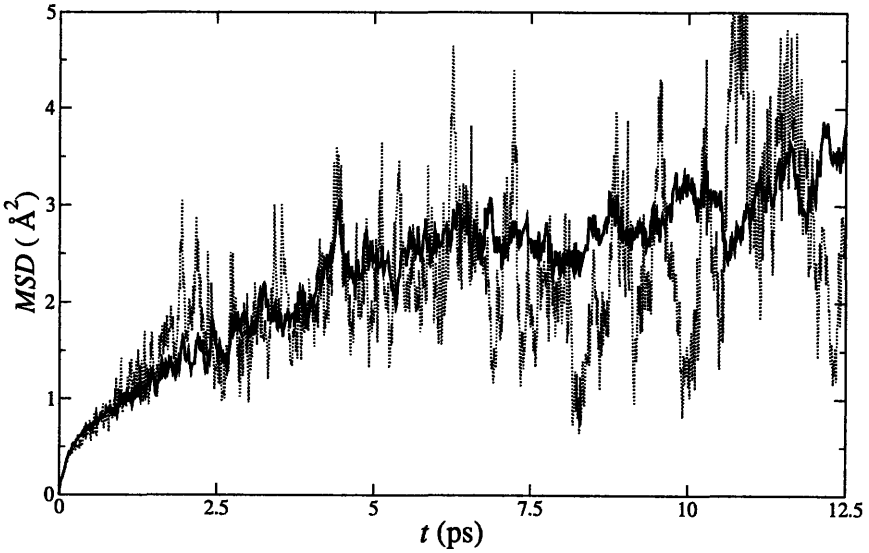

FIGURE 5-22: Mean-square displacement of the hydrogen atoms at 550 K. Results are shown for the self-diffusion model used in Equation 5.4 (solid line) and for the collective diffusion model used in Equation 5.5 (dotted line). The collective model results in slower diffusion, but the associated statistical error is significantly higher.

transfer process can be assumed to be a Grotthuss-type jump, meaning that one would have to carefully track the continual creation and annihilation of every possible type of quasiparticle—an imposing task given the varied and dynamic nature of the hydrogen-bond network topology. Moreover, the timescales accessible to our simulations are sufficiently short that statistical sampling errors from the quasiparticle method would likely be very high, as we would be averaging over relatively few such structures. As such, we present only the results based on the self-diffusion and collective diffusion methods but offer the above discussion as a reminder that one should remain somewhat wary of any direct comparison with experimental results.

We have also mentioned the difficulty in accounting for correlation and reversal of collective sequences of jump events. In the limit of the short length- and timescales accessible by first-principles methods, it is expected that any diffusive correlations that persist over large regions of either time or space would be lost, resulting in inflated diffusion statistics. Similarly, jump events that remain localized due to high incidences of back-hopping and correlation are counted as contributors to diffusion on the timescale accessible to our simulations, whereas these would not appear in a macroscopic measurement. Since it is reasonable in a network solid to expect correlations to persist over long distances and times, and since our simulations have a relatively short 25 ps production time, it is extremely likely that this factor represents the primary source of error in our calculated diffusion coefficients. Moreover, it makes sense that this long-range memory effect should manifest itself more strongly in the proposed mechanism for diffusion parallel to the (001) plane, given that the rate of reversal for the relevant jump events has already been shown to be extremely high. Similarly, cor-

relation should be expected to play less of a role in the SO_4 rotation that governs transport perpendicular to the (001) plane, since the timescales involved are long enough and the relevant barriers high enough that a significant rearrangement of the network topology can be expected between such events, thereby limiting the corresponding memory effect. This offers a likely explanation for our observed overpronouncement of the anisotropy in the diffusion characteristics. It also means our results for diffusion along the [001] principal direction are likely better converged than those along the [100] or [010] principal directions; indeed, these values are substantially closer to their experimental counterparts [160,179].

We have also mentioned the artificially high number of small rings due to periodic boundary conditions as a potential consequence of small supercell size. Table 5.6 suggests a possible correlation between smaller average ring size and a higher propensity to jump, particularly at the lower temperature, meaning our finite size effects could result in a measurable increase in jump statistics and diffusion coefficients. However, any such decrease in average ring size from the periodic boundary conditions is likely to be accompanied by an increase in the overall number of rings. Since we have established the overall propensity for ring existence to inhibit hydrogen- and chemical-bond dynamics, the competition between these two effects should attenuate any potential impact on the macroscopic properties.

Additional errors may be attributed to our choice of the PBE functional for calculating the exchange-correlation energy. The selection of PBE was motivated by its general success in describing hydrogen-bonded systems [184–186]. However, it has also been shown [187] to underestimate proton transfer barriers in several instances, which may help in offering an explanation for the enhanced self-diffusion that we observe.

It should be noted that we are neglecting any quantum behavior of the protons. However, an analysis of experiments on $CsDSO_4$ suggests the isotope effect is relatively small [179,188]. In addition, theoretical work [189] on the topologically similar material KDP concluded that the predominant effect of quantum delocalization of the protons was limited to structural considerations, in that it decreased the H$\cdots$O–H distance and consequently also the lattice parameter. The KDP analysis is also consistent with experimental comparisons of $CsDSO_4$ and $CsHSO_4$ [155,169].

A closer examination of the specific rate-limiting mechanisms covered in our analysis of proton diffusion in $CsHSO_4$ provides additional insight into the lack of any substantial isotope effect. Our findings indicate that the chemical-bond dynamics are much faster than previous analyses have suggested, of the same order as the hydrogen-bond dynamics. Rather, the primary limitation is manifest in the dynamics of the SO_4 tetrahedra, since these appear to govern the reversal rates of both chemical-bond jumping and hydrogen-bond hopping. Accounting for proton tunneling across the O–H$\cdots$O double-well potential would therefore have little effect on the overall jump statistics, since the mobility of the SO_4 groups is classically controlled. In addition, we have established the importance of the chain and ring topology of the hydrogen-bond network in promoting diffusive events. However, changes in the topology are

promoted by two factors—hydrogen-bond hopping and slow rotation of the SO_4 tetrahedra. Slow SO_4 rotation is clearly a classical phenomenon, and hydrogen-bond hopping is coupled to a 30° reorientation of the heavy SO_4 tetrahedron, meaning its dynamics are also ultimately classical.

5.8 Summary and conclusions

We have presented a detailed analysis of proton dynamics in superprotonic Phase-I $CsHSO_4$ based on first-principles molecular dynamics simulations. Our results confirm that the chemical-bond dynamics are dominated by local Grotthuss-style hops which propagate successively along the hydrogen-bond network backbone. Individually, these hops are comparatively frequent, pointing to a low diffusion barrier, but the net effective rate of the chemical-bond dynamics is limited by an anomalously high rate of jump reversal. We find that the propensity for such forward- and back-hopping along the O–H$\cdots$O complex is in turn heavily influenced by the dynamics of the SO_4 tetrahedra rather than by static local geometry alone.

We have also shown that the dynamics of the hydrogen-bond network are dominated by fast, discrete angular jumps between neighboring oxygens rather than by slow rotations of the SO_4 tetrahedra. Such jumps occur with greater frequency between oxygens belonging to different SO_4 tetrahedra than between oxygens of the same tetrahedron, by a factor of two or three. The hydrogen-bond jumps are accompanied by an approximately 30° reorientation of the participating SO_4 tetrahedra to alleviate the lattice strain induced by the hop, thereby minimizing the likelihood of jump reversal. We have isolated a window of 50 fs for successful completion of this "fast" reorientation event and showed that it exists independently of a second, slower reorientation mechanism, operating on a timescale at least five times greater than its counterpart. The slower mechanism amounts to ordinary SO_4 rotation on a longer timescale, and we propose this to be the dominant hydrogen-bond network reorientation mechanism for diffusion along the [001] direction, for which angular hops are significantly more difficult and less frequent, owing to the anisotropy of the $CsHSO_4$ lattice.

Our topological analysis of the hydrogen-bond network revealed a significant number of branching and network-terminating nodes, indicating a substantial deviation from linearity, particularly at higher temperatures. We postulate that the underbound network terminators play a role in network reconfiguration by aiding SO_4 rotational mobility. Graph-theoretic methodology offered a way to isolate chains and rings as dominant topological features in the network, and we discovered that the presence of chains and the absence of rings is a substantial predictor of likelihood for either a hydrogen- or chemical-bond jump event to occur. We propose that our topological analysis could be easily extended to similar well-defined, hydrogen-bonded network solids.

Finally, we apply our analysis to offer an explanation for the lack of a significant isotope

effect in the $CsHSO_4/CsDSO_4$ system. In particular, we tie both the chemical- and hydrogen-bond dynamics to the classical dynamics of the SO_4 tetrahedra and argue that the inclusion of proton quantum tunneling should play a relatively minor role in the rate-limiting steps of the diffusion mechanism.

An overview of this work can be found in Reference [190].

CHAPTER 6

$NaAlH_4$: Structural phase transitions and hydrogen transport

6.1 Background and motivation

COMPLEX LIGHT METAL HYDRIDES represent among the most promising current materials solutions to the hydrogen-storage problem [38–40]. Such materials have the potential for relatively high gravimetric storage capacities and can be engineered to possess kinetics favorable for hydrogen release at operating temperatures. Of the complex metal hydrides, sodium alanate ($NaAlH_4$) has attracted particular interest as a potential hydrogen storage material over the past decade. It allows for a high theoretical gravimetric hydrogen release of approximately 5.6 wt.% H, just short of the 6 wt.% H milestone target proposed by the U.S. Department of Energy for the year 2010 [36,37]. The absorption/desorption reaction for sodium alanate is a two-step process and proceeds as follows [191,192]:

$$NaAlH_4 \rightleftarrows \tfrac{1}{3}\,Na_3AlH_6 + \tfrac{2}{3}\,Al + H_2 \tag{6.1}$$

$$Na_3AlH_6 \rightleftarrows 3\,NaH + Al + \tfrac{3}{2}\,H_2 \tag{6.2}$$

Unfortunately, undoped sodium alanate exhibits irreversible hydrogen release and possesses unacceptably slow desorption kinetics. However, in 1997 Bogdanović and Schwickardi successfully demonstrated [191] that the kinetic barrier for absorption and desorption of hydrogen in $NaAlH_4$ could be substantially lowered and the reactions made reversible by the addition of small quantities of transition metal dopants, most notably titanium. Further kinetic enhancements involving new processing techniques and additional dopant species were subsequently demonstrated [193,194]. At ambient pressure and in the presence of $TiCl_3$ at low dopant concentrations ($\sim$ 2 mol%), the first reaction (Equation 6.1) proceeds forward above 306 K, releasing a theoretical 3.7 wt.% H in the process. The second reaction (Equation 6.2)

becomes favorable above 383 K and releases an additional theoretical 1.8 wt.% H.

Despite the aforementioned improvements, hydrogen desorption kinetics in $NaAlH_4$ are still too slow for adoption as a market-ready solution to the hydrogen storage problem. The system is also short of the long-term targets for gravimetric hydrogen capacity and volumetric density. Nevertheless, it is generally agreed [36, 195] that $NaAlH_4$ possesses tremendous potential as a template for developing new complex metal hydrides that are structurally and chemically similar to their parent but are not subject to the same shortcomings. Modeling and simulation represent excellent tools for probing new materials; however, systematic improvements rely on a fundamental understanding of the precise mechanism of dehydrogenation in existing complex metal hydrides such as $NaAlH_4$, and of the role of the catalytic dopants in enhancing the reaction chemistry. To this end, there have been several recent density-functional energetics studies addressing the structure and thermodynamics of the sodium alanate system, both in its pure form and in the presence of various dopants or defects [196–205]. However, in the absence of an accurate dynamical picture, it is difficult to isolate predominant reaction pathways. Moreover, an understanding of the desorption kinetics is vital to evaluating the viability of any hydrogen storage material, yet the complexity of the configurational phase space in complex metal hydrides generally renders static energetic calculations insufficient in this regard. To our knowledge, no dynamics simulations (either classical or first-principles) have been performed on this system, revealing a clear avenue for making a meaningful contribution to the scientific canon. The present work uses first-principles molecular dynamics simulations to study the sodium alanate system, focusing on understanding hydrogen mobility and the overall dehydrogenation process in the forward reaction of the first of the two steps, as given in Equation 6.1.

In a broad sense, the study of a hydrogen storage material may seem an unlikely inclusion alongside the other materials discussed in this thesis. However, to facilitate the dehydrogenation process, sodium alanate requires high mobility of hydrogen and in this sense is not dissimilar to the fast-ion conductors discussed in Chapters 4 and 5. Indeed, it will be demonstrated that studying $NaAlH_4$ provides an interesting and appropriate complement to our investigation of superionic α-AgI and $CsHSO_4$-I. For AgI we showed that inhibiting the structural phase transformation at the fast-ion conducting phase boundary did not suppress the independent phase transition of the silver ions, prompting us to suggest that the mobility of the silver lattice likely drives the rearrangement of the base anionic structure. In contrast, in studying $CsHSO_4$ we encountered a situation in which proton transfer depends on a structural transition involving the activation of SO_4 rotational modes. For $NaAlH_4$, we will demonstrate a mechanism distinct from either of the two previous cases, in which hydrogen mobility can be studied independently from the underlying structural transition of the host lattice. This phenomenological symmetry makes our investigation into the mobility, kinetics, and transition pathways of sodium alanate a fitting conclusion for this thesis work.

6.2 Computational parameters

Ultrasoft pseudopotentials for Al ($3s^2 3p^2$ valence configuration) and H were taken from the Quantum-ESPRESSO website [124]. A suitable norm-conserving pseudopotential for Na was generated with a $3s^{0.5} 3p^{0.05}$ valence configuration using the Atom code of Paolo Giannozzi [168]. As with the other pseudopotentials generated for this work, the Troullier-Martins recipe was used. Since sodium is an alkali metal, nonlinear core correction (Section 2.4) was also implemented to account for the overlap between the core and valence electrons. Detailed reports on transferability tests for our newly generated Na pseudopotential are given in Appendix A. All pseudopotentials used the Perdew-Burke-Ernzerhof exchange-correlation functional. Energy cutoffs of 25 and 200 Ry for the wavefunctions and charge density respectively were obtained by verifying the convergence of interatomic forces in perturbed test structures to within a ~ 0.05 eV/Å threshold.

Except where indicated, Car-Parrinello molecular dynamics simulations were performed on 2×2×1 supercells of $NaAlH_4$ (96 atoms for the perfect crystal) at a variety of temperatures ranging from 100 K to 650 K. Simulations were performed in both the *NVT* and *NPT* ensembles, with temperatures maintained using Nosé-Hoover chains. For the simulations on the defect-free crystal, the fictitious electronic mass was chosen to be $\mu = 500$ au with $\Delta t = 6$ au, which allowed the system to remain well behaved throughout the duration of the runs (Figures 6-1 and 6-2). For simulations in the presence of surfaces or point defects, these values were adjusted as necessary such that fluctuations in the Car-Parrinello constant of motion were held to within 3% of the magnitude of the fluctuations in the total energy (Figures 6-3 and 6-4). Bulk simulations were run for 25 ps and surface simulations for 15 ps, each following 5 ps of equilibration time. Simulations of hydrogen mobility in the presence of defects were run for 25–30 ps, also following 5 ps of equilibration.

The lattice parameters for the fixed-volume simulations of the tetrahydride were chosen based upon the zero-temperature relaxed values introduced in the next section. For the simulations discussed in Section 6.4.3, the choice of the lattice parameter was motivated by examining the average geometry in a variable-cell simulation at 300 K.

6.3 Structure

The body-centered tetragonal unit cell of the α phase of the tetrahydride $NaAlH_4$ is shown in Figure 6-5. This structure transforms into the hexahydride Na_3AlH_6, which possesses the monoclinic structure depicted in Figure 6-6.

The system geometry of the tetrahydride $NaAlH_4$ was determined by fitting the results of self-consistent zero-temperature energetic calculations for a given c/a ratio to a Murnaghan equation of state. For each volume, the local minimum-energy ionic configuration was obtained using a BFGS minimization scheme. Calculations were performed on the 12-atom

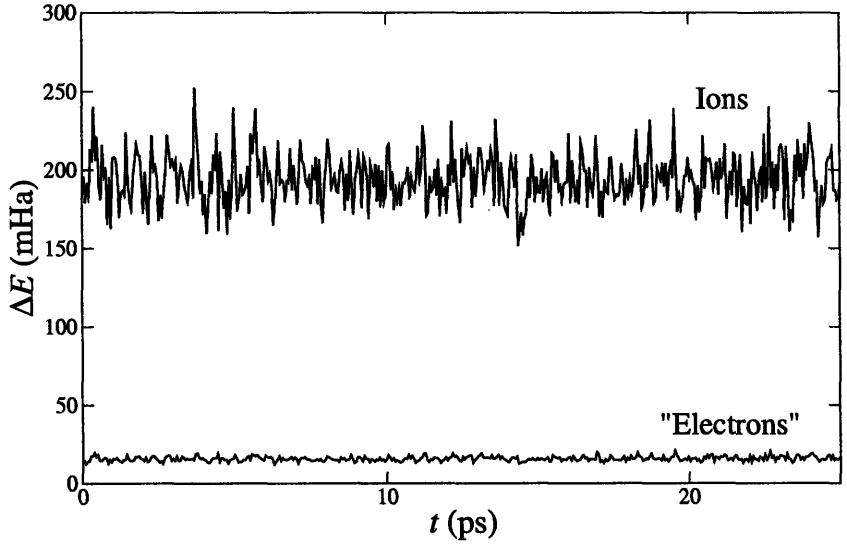

FIGURE 6-1: Evolution of the kinetic energies of the ionic and fictitious electronic systems in a constant-pressure simulation of bulk $NaAlH_4$ at 425 K.

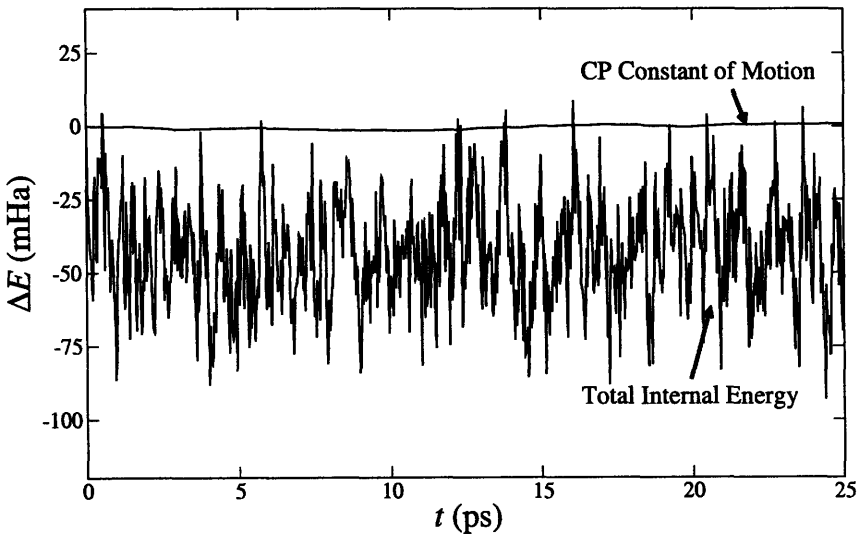

FIGURE 6-2: Evolution of the total internal energy and the Car-Parrinello constant of motion in a constant-pressure simulation of bulk $NaAlH_4$ at 425 K.

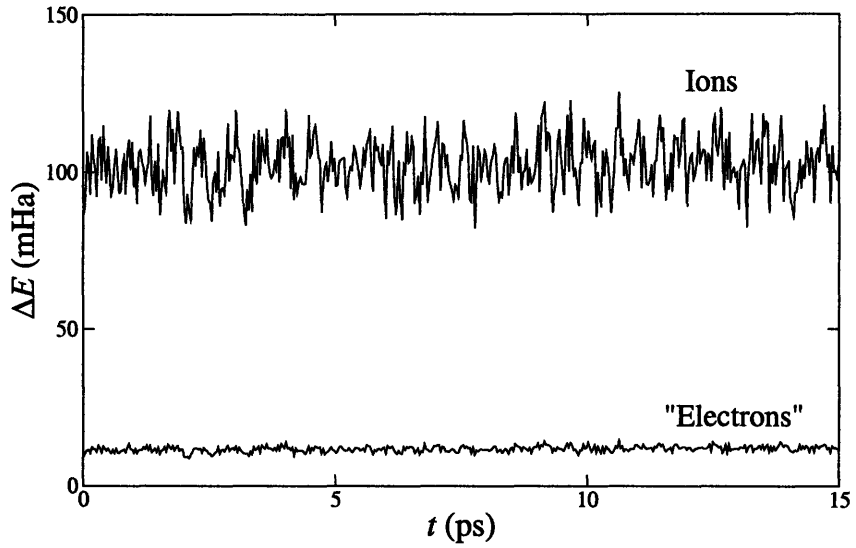

FIGURE 6-3: Evolution of the kinetic energies of the ionic and fictitious electronic systems in a simulation of a (001) surface slab of $NaAlH_4$ at 225 K.

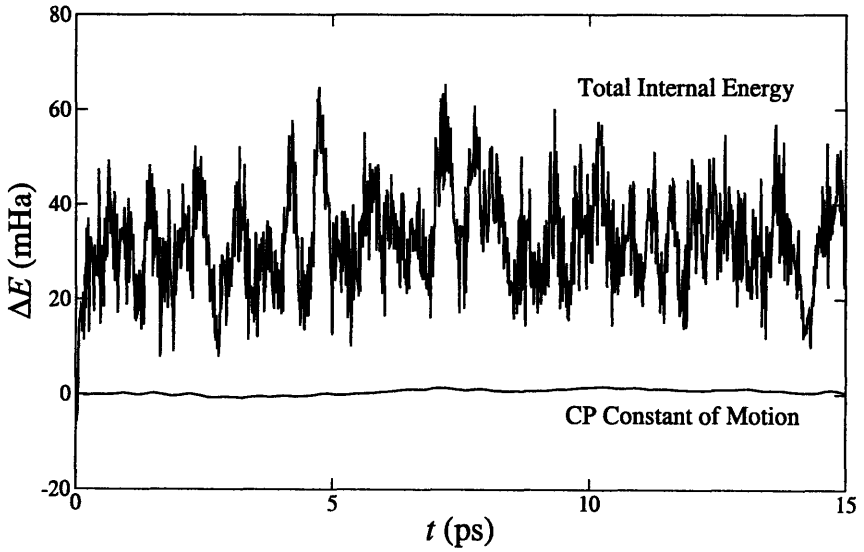

FIGURE 6-4: Evolution of the total internal energy and the Car-Parrinello constant of motion in a simulation of a (001) surface slab of $NaAlH_4$ at 225 K.

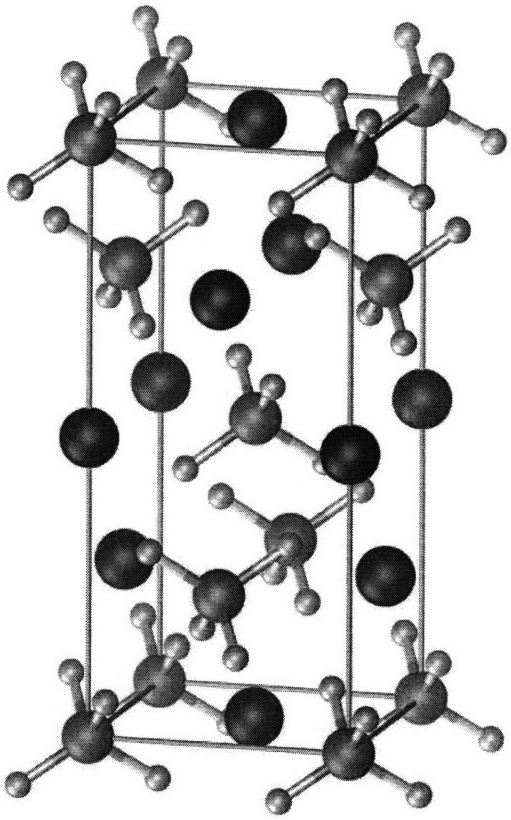

FIGURE 6-5: Structure of the conventional unit cell of α-$NaAlH_4$ (space group $I4_1/a$). Hydrogen atoms are shown in white, aluminum in green, and sodium in blue.

TABLE 6.1: Calculated lattice parameters a and c, as well as various interatomic distances, for the tetrahydride α-$NaAlH_4$. Calculations were performed on the 12-atom primitive cell using a 2×2×1 grid of k-points and an electronic wavefunction cutoff energy of 25 Ry. Experimental values are from References [206,207].

Description	*This work*	*Experiment*	*% Deviation*
a (Å)	5.148	5.02	+2.5
c (Å)	11.202	11.33	-1.1
d(Al–H)	1.629	1.627	+0.1

body-centered tetragonal primitive cell using a 2×2×1 **k**-point mesh. The results of the lattice parameter calculation are summarized in Figure 6-7 and Table 6.1 and show good agreement with experimental values. As we saw with $CsHSO_4$, $NaAlH_4$ demonstrates only minor energy changes with respect to perturbations in the lattice parameter c.

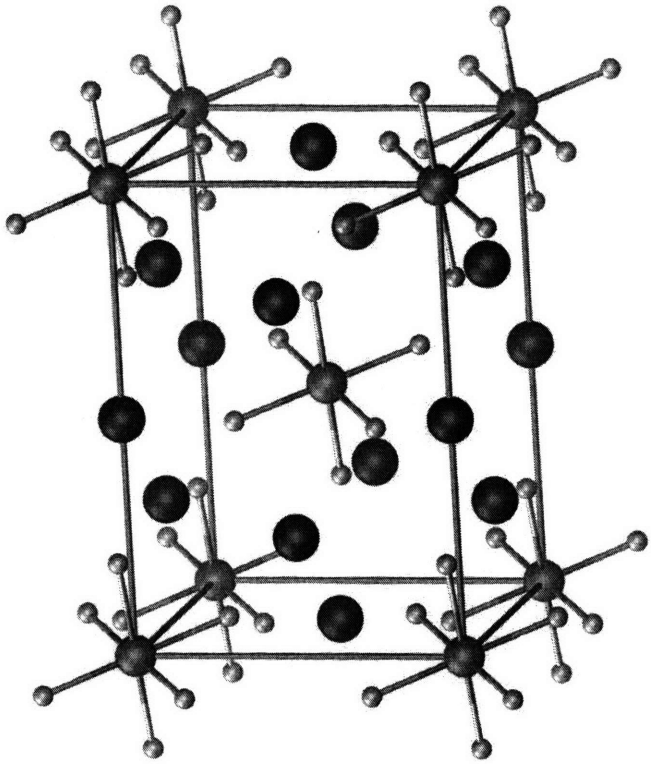

FIGURE 6-6: Structure of the conventional unit cell of α-Na_3AlH_6 (space group $P2_1/c'$). The color scheme follows that of Figure 6-5.

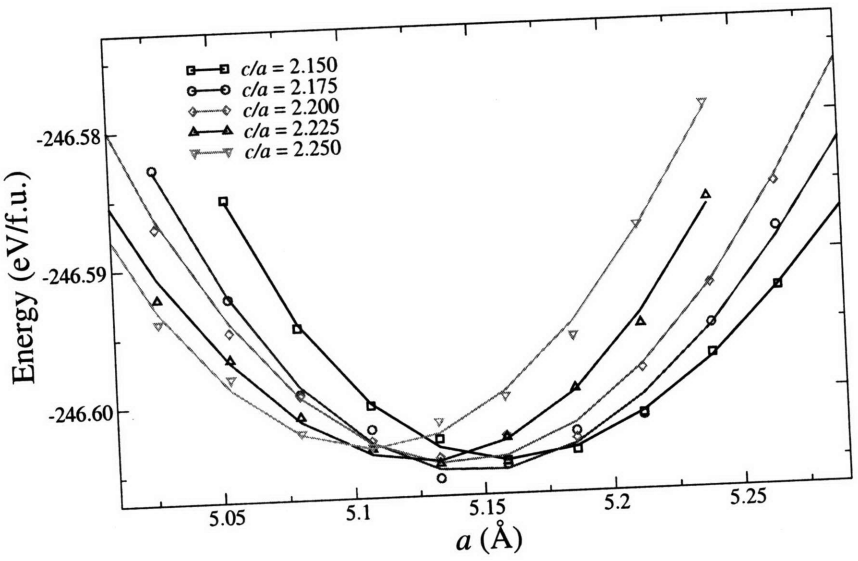

FIGURE 6-7: Equation-of-state calculations for various values of the c/a ratio in the tetrahydride α-$NaAlH_4$. Calculations were performed on the 12-atom primitive cell using a 2×2×1 grid of k-points and an electronic wavefunction cutoff energy of 25 Ry.

6.4 The structural transition

Intuitively, two possible scenarios for dehydrogenation emerge as most likely: first, that hydrogen becomes mobile and is released as a direct byproduct of the structural phase transformation of the complete lattice; and second, that hydrogen becomes mobile above the $NaAlH_4$--to-Na_3AlH_6 transition temperature and immediately begins to escape the bulk, forming the hexahydride only as part of the subsequent lattice reorganization process. In other words, we can ask whether the hydrogen mobility drives the phase transformation (as was the case for the α-AgI) or the reverse is true. The following sections explore both possibilities in depth, ultimately concluding that neither is correct, and that the structural transition can be considered independently from the hydrogen mobility. Instead, we will argue that hydrogen mobility results from the formation of point defects in the lattice.

6.4.1 Simulating bulk $NaAlH_4$

We performed an initial Car-Parrinello molecular dynamics simulation on bulk $NaAlH_4$ in the canonical *NVT* ensemble at 400 K. This temperature was well within the stable range for driving the dehydrogenation reaction of Equation 6.1. The lattice parameters were fixed based upon the values listed in Table 6.1. In 25 ps of equilibrated production time, the bulk $NaAlH_4$ demonstrated no transport of hydrogen. Moreover, we detected no visible sign of a nucleation site for the phase transition to the hexahydride form, such as a local lattice distortion, a disordering of the AlH_4- or Na substructures, or reorientation of AlH_4^- tetrahedra. This was confirmed in a series of zero-pressure Parrinello-Rahman simulations (Section 3.4) at 350, 400, 425, 500, 550, and 650 K. Temperatures at or below 500 K likewise demonstrated no nucleation of the phase transition or indication of hydrogen mobility, in spite of the fact that this method explicitly considers the cell vectors as additional degrees of freedom in the simulation. The first evidence of any sort of lattice distortion in the constant-pressure simulations occurred only upon melting at $T \geq 550$ K. This can be seen in the Al–Al and Na–Na pair correlation functions, which are plotted in Figure 6-8. Interestingly, even at these elevated temperatures, no Al–H bonds were broken in the course of the simulations. Instead, the AlH_4^- tetrahedra always remained structurally intact as they rotated and migrated away from their original lattice positions. This important point will be discussed further in Section 6.5. We also note that the observed melting point is somewhat higher than the experimental value of 455 K at ambient pressure, as is typical in small-scale simulations.

Assuming density-functional theory is sufficiently capable of properly characterizing the free energy surface, two possible explanations emerge for the lack of an observed $NaAlH_4$--to-Na_3AlH_6 transition in our simulations. First, the constraints of our small system size and short simulation time may preclude long-range or kinetically limited disordering vital to phase transformation nucleation. If this is true, it is unlikely that any of our first-principles simu-

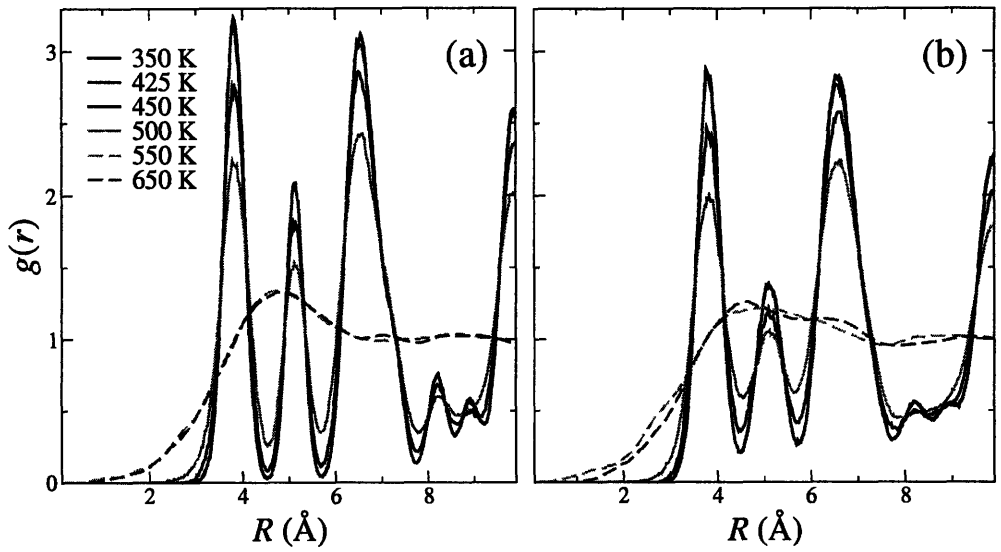

FIGURE 6-8: Pair correlation functions for (a) Al-Al and (b) Na-Na atom pairs in bulk *NPT* simulations of $NaAlH_4$ at 350, 400, 425, 500, 550, and 650 K. The breakdown of the structure at the two higher temperatures indicates melting.

lations will be able to adequately describe the transition. However, the fact that the AlH_4^- moieties remain intact in the melt and migrate freely and independently through the cell suggests that the interionic interactions between Na^+ ions and AlH_4^- tetrahedra is predominantly ionic. This in turn implies that interactions should be limited to short-range effects. A second possible explanation owes to the fact that these simulations neglect the presence of defects which may play a necessary role in mediating transport. These include surface effects and point defects, the potential role of which has also been discussed at length in the literature [201,204,208,209]. The remainder of this section will explore surface effects, whereas the role of point defects forms the focus of Section 6.5.

6.4.2 Simulating the (001) surface slab

We have also run simulations to study the (001) surface, which has previously been calculated to be the most stable among the high-symmetry crystalline surfaces [210]. Canonical *NVT* simulations of $NaAlH_4$ were run at 150, 175, 225, 275, 300, 400, and 475 K in a 96-atom (four atomic layers thickness) supercell slab surrounded by vacuum. In order to ensure sufficient vacuum separation between successive images in the $\hat{c}$ direction, we performed a force-convergence with a threshold of ~ 0.05 eV/Å. As a safety precaution, the vacuum interlayer was then expanded by an additional 50%, resulting in a 14 Å separation distance. In each case, surface configurations were first optimized using damped molecular dynamics before the initial equilibration period.

Significant differences were discovered between the behavior of the bulk and the surface

slab. In addition to the low-temperature α phase and the high-temperature liquid phase, a third stable phase was seen to emerge for intermediate temperatures. Figure 6-9 compares the final, equilibrated configurations of the 96-atom surface slab at each of the simulated temperatures. For $T \leq 225$ K (Figure 6-9(a) through (c)), the surface slab remains coherent and is structurally identical to the bulk α phase (although minor initial disordering of one of the outermost surface layers is visible at 225 K). For $T \geq 400$ K (Figure 6-9(g) and (h)), we observe a melting of the entire slab following an initial expansion of the slab along $\hat{c}$ and the activation of the AlH_4^- rotational degrees of freedom. However, for temperatures in the range ($225 < T < 400$ K; Figure 6-9(d) through (f)), we observe an unexpected spontaneous reordering of the $NaAlH_4$ slab into a hitherto unknown phase with a different symmetry and an expanded lattice parameter c. We will denote this new phase as γ throughout the remainder of this text.[†]

In order to confirm that the expression of the γ phase in the surface slab is not merely an unintended consequence of finite-size effects in our small simulation cell, we ran three additional simulations at 300 K. In the first of these, we increased our simulation supercell in the ab plane and added one additional layer, giving a total of 270 atoms (3×3×1.25). For the second simulation, we increased the thickness of our slab by a factor of two but left the parameters in the $\hat{a}$ and $\hat{b}$ directions unchanged, for a total of 192 atoms (2×2×2). The third simulation was run in the *NPT* ensemble, so we also allowed the cell parameters to adjust themselves. Notably, all three simulations evidenced the same transition to the γ phase, although the overall process occurred slower in the larger simulations. The variable-cell simulation demonstrated an additional $\sim 10\%$ decrease in the cell lattice parameter a (a point to which we will return when we analyze the precise structure of the γ phase in Section 6.4.3), but the qualitative behavior matched that of the fixed-volume simulations at the same temperature.

Figure 6-10 offers a schematic illustration of the basic structural differences between α-$NaAlH_4$ and γ-$NaAlH_4$ when viewed along the $\hat{a}$ or $\hat{c}$ crystallographic axes, based on the locations of the aluminum atoms before and after the transition. Certain qualitative features of the transformation are immediately detectable: first, the shear of the ab crystal planes to generate the new lattice symmetry of the γ phase; second, the expansion of the lattice parameter c upon entering the γ phase; and third, the rotational disordering of the AlH_4^- tetrahedra that marks the departure from the alpha phase.

In characterizing the $\alpha \rightarrow \gamma$ transition, it is useful to quantify the three features discussed above. In order to measure the transformation of the lattice symmetry in the ab plane due to shearing of the ab crystal planes, it is useful to introduce an order parameter λ that can act as a reaction coordinate to mark the progress of the transition from the α phase to the γ phase. To do so, we exploit the fact that when either the Al or Na atomic species is projected into the ab plane, the α and γ phases feature a different occupancy of crystallographic lattice sites,

[†]The $NaAlH_4$ system also possesses a high-pressure monoclinic β phase [211].

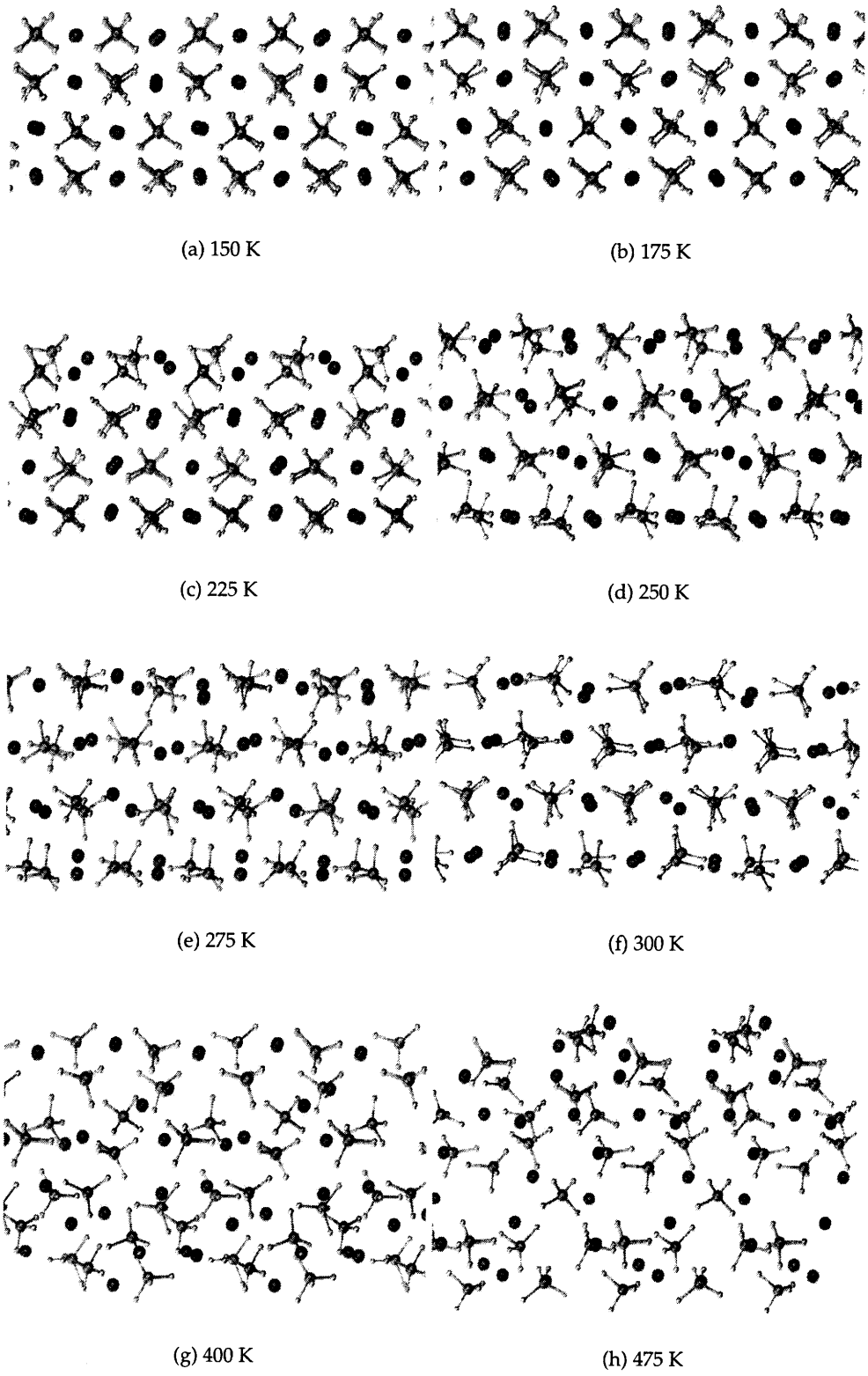

FIGURE 6-9: Equilibrated structure of a four-layer (001) surface slab of $NaAlH_4$ at various simulation temperatures. The new γ phase is evident in the equilibrated structures at 250, 275, and 300 K (d–f).

as described in Figure 6-10. In particular, we begin by defining two sublattices s_1 and s_2 in terms of relative fractional crystallographic coordinates as $s_1 = \left\{ (\ell, m), (\ell + \frac{1}{2}, m + \frac{1}{2}) \right\}$ and $s_2 = \left\{ (\ell + \frac{1}{2}, m), (\ell, m + \frac{1}{2}) \right\}$, where m and ℓ are integers. Using this notation, it is clear that in the α phase, both s_1 and s_2 are occupied in equal proportion, whereas in the γ phase, only s_1 is occupied. The reaction coordinate λ can therefore be calculated by examining the ratio f_2/f_1 between the respective occupancies of sublattices s_2 and s_1. It is worth emphasizing that no assumptions are made as to the specific values of the lattice constants for the α and γ phases, since the elements in the two sublattices are given in relative crystallographic coordinates rather than in any absolute reference frame. Our specific algorithm for calculating λ at each dynamics timestep proceeds as follows:

1. Project all atomic coordinates $\vec{\mathbf{R}}$ along $\hat{c}$ into the ab plane and transform to fractional crystallographic coordinates $\vec{\mathbf{R}}'$ in the primitive unit cell.

2. For each atom pair (I,$J \neq I$):

   (a) Transform atom J to coordinates relative to atom I by evaluating $\mathbf{R}'_{IJ} \equiv \mathbf{R}'_J - \mathbf{R}'_I$.

   (b) Find the nearest crystallographic lattice point $\tilde{\mathbf{R}} = (\tilde{X}, \tilde{Y}) = (\ell/2, m/2)$ to $\mathbf{R}'_{IJ}$, where ℓ and m are integers.

   (c) Evaluate the weighting factor $w = \exp\left\{ -|\mathbf{R}'_{IJ} - \tilde{\mathbf{R}}|^2 / 2\sigma^2 \right\}$ for the site occupancy, where the width of the Gaussian σ is chosen to be $1/4$.

   (d) Increment the appropriate sublattice occupancy (f_1 or f_2) according to the rule that $f_1 = f_1 + w$ if $\tilde{X} + \tilde{Y} = n$, or else $f_2 = f_2 + w$ if $\tilde{X} + \tilde{Y} = n + 1/2$, where n is an integer.

3. Evaluate the order parameter according to $O = 1 - (2/N) \times f_2/f_1$, where N represents the total number of atom pairs (I,$J \neq I$).

The weighting factor of Step 2c is included to penalize atoms for deviation from ideal crystallographic sites. When applied to a single ion species, this algorithm results in $\lambda = 0$ for the pure α phase and $\lambda = 1$ for the pure γ phase. Figure 6-11 demonstrates the effectiveness of λ as an order parameter. The occupancies of s_1 and s_2 are plotted across the phase transition and demonstrate the desired behavior of $\{f_1, f_2\} \rightarrow \{\frac{1}{2}, \frac{1}{2}\}$ for the α phase and $\{f_1, f_2\} \rightarrow \{\frac{1}{2}, 0\}$ for the γ phase. The figure also evidences the general agreement of the method whether applied to the Al substructure or the Na substructure.

Choosing to focus on the ordering of the Al atoms, we plot the complete evolution of λ in the (001) surface slab at various temperatures in Figure 6-12. At 225 K, for which no transition is observed (see Figure 6-9), λ remains near zero throughout the simulation, whereas higher temperatures demonstrate the expected behavior of $\lambda \rightarrow 1$. At 275 K, the transformation initializes early but then partially reverses itself before proceeding to completion. Figure

6-12 also includes the results for one of the larger slabs (270 atoms) at 300 K, in which two intermediate metastable states are evident as plateaus in the order parameter. By examining the simulation snapshots, we were able to identify these states as successive shearing of *ab* planes, beginning with the outermost surface layer and proceeding inwards. We note that at temperatures exhibiting the $\alpha \rightarrow \gamma$ transition, nucleation generally begins earlier at higher temperatures, although the process takes longer to complete for the larger cell (300 K), as has been mentioned. Finally, in the melted slab (400 K), there is no discernible trend in λ, since lattice sites no longer carry any meaning in a liquid.

The definition of the order parameter λ as a reaction coordinate allows us to isolate an estimate for the energetic barrier associated with the $\alpha \rightarrow \gamma$ transformation by averaging the internal energies of all configurations corresponding to a given value of λ. Figure 6-13 illustrates the result of this process for the 270-atom simulation at 300 K. The metastable states from Figure 6-12 are distinctly visible along the reaction pathway. The figure also indicates a low energy barrier for transition ($\sim$ 8 meV/atom), as well as a relatively small energetic difference between initial and final configurations, which will be quantified more accurately in Section 6.4.3 using static total-energy techniques.

The rotational mobility of the AlH_4^- tetrahedral moieties in the gamma phase with respect to the alpha phase can be quantified by defining an angular mean-square displacement as follows:

$$\langle \mathrm{MSD}_\theta(t) \rangle = \frac{1}{N} \sum_{i=1}^{N} \left\langle \left| \cos^{-1} \left\{ \hat{\mathbf{r}}_{\mathrm{AlH}}(t) \cdot \hat{\mathbf{r}}_{\mathrm{AlH}}(0) \right\} \right|^2 \right\rangle. \tag{6.3}$$

Here the index i is assumed to run over the N Al–H bonds in the system, and $\hat{\mathbf{r}}_{\mathrm{AlH}}$ represents the directional unit vector from an aluminum to one of its bonded hydrogens. The quantity obtained using Equation 6.3 should demonstrate a linear increase with time (up to a limiting value of π^2) only if the rotational modes of the AlH_4^- tetrahedra are activated. The angular mean-square displacement is plotted in Figure 6-14 for the (001) surface slab at 225, 250, and 300 K. For 225 K, MSD_θ plateaus after an initial ballistic regime to a value related to the magnitude of the librational motion of the AlH_4^- groups. For the two higher temperatures, however, the onset of AlH_4^- rotation is marked by a sudden increase in the quantity MSD_θ that continues as the simulation progresses. For the larger slab (270 atoms; 300 K), the increase begins sooner but takes longer to equilibrate than for the smaller slab at 250 K, in keeping with the results of Figure 6-12.

The inset of Figure 6-14 further separates the angular mean-square displacement at 300 K into averages over the various layers of the slab. Although there is little difference between the onset times of AlH_4^- rotation for the two innermost layers, the outermost layer clearly demonstrates rotation much sooner than its inner counterparts. This suggests that the rotational disordering begins at the surface before percolating into the slab.

We can examine the effect of the phase transition on the lattice parameter c by tracking the

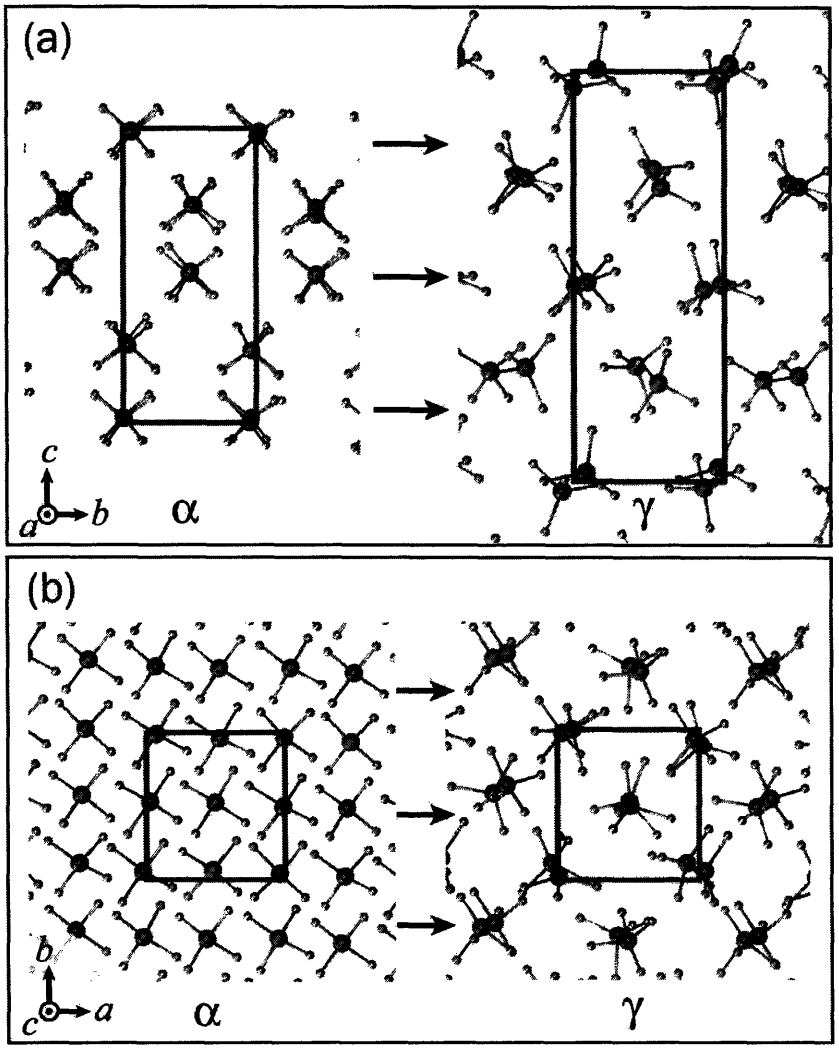

FIGURE 6-10: Schematic illustration of the fundamental geometric differences between the α (left panel) and γ (right panel) phases of $NaAlH_4$, viewed along the (a) $\hat{a}$ and (b) $\hat{c}$ crystallographic axes. One α unit cell becomes two γ cells stacked along the $\hat{c}$ direction, and the three central aluminum planes perpendicular to that direction shear to generate the new symmetry. The γ phase also features no occupancy of the sites represented by the centers of the edges of the square in (b), whereas the α phase does. Configurations are taken from a simulation of a 250 K surface slab before and after the $\alpha \rightarrow \gamma$ phase transition.

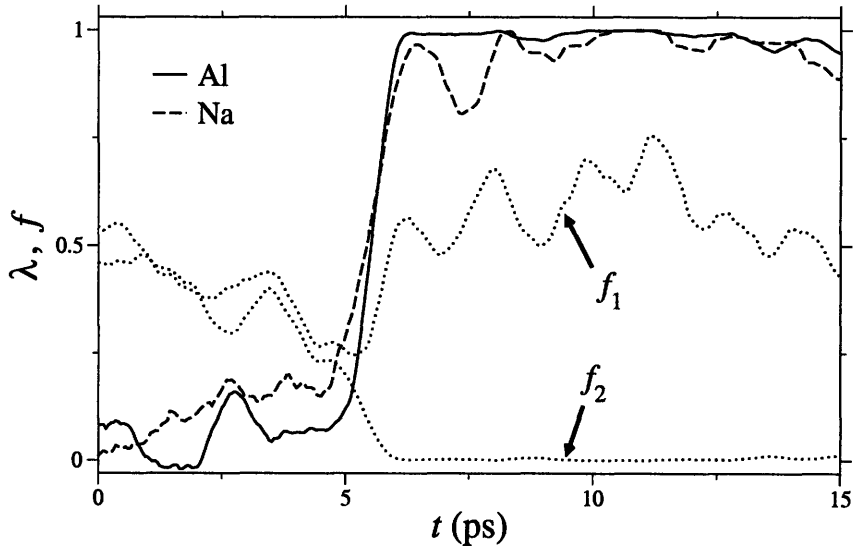

FIGURE 6-11: Comparison of the evolution of the order parameter λ for the aluminum (solid curve) and sodium (dashed curve) ionic substructures. A value of $\lambda = 0$ indicates the pure α phase, whereas $\lambda = 1$ means the pure γ phase is present. The $\alpha \rightarrow \gamma$ transition begins at $t = 5$ ps. Also shown are the average occupancies f_1 and f_2 of Al lattice site subgroups s_1 and s_2 (see text), normalized against the total number of available sites in each subgroup. Data is from a (001) surface slab simulation at 250 K.

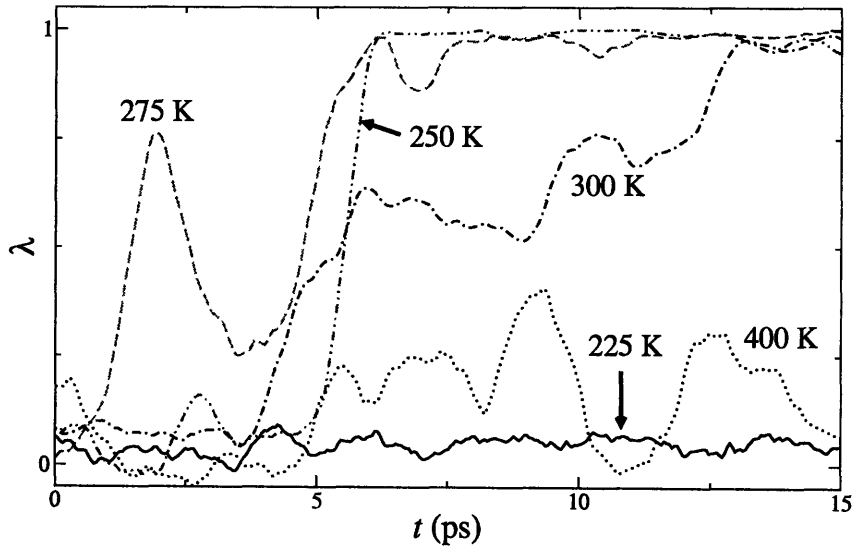

FIGURE 6-12: Evolution of the order parameter λ for a (001) surface slab of $NaAlH_4$ beginning from the α phase. A value of $\lambda = 0$ indicates the pure α phase, whereas $\lambda = 1$ means the pure γ phase is present. Data is from a series of 96-atom simulations at 225 K, 250 K, 275 K, and 400 K, as well as a 270-atom simulation at 300 K.

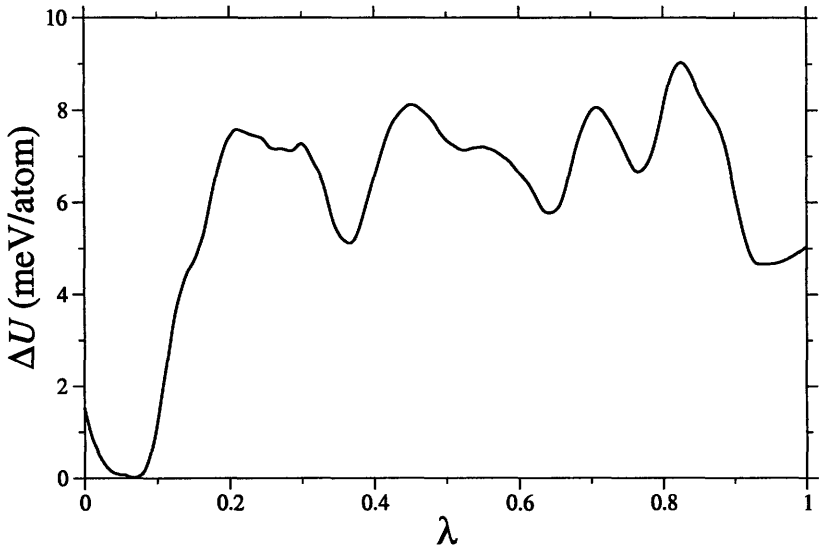

FIGURE 6-13: Change in the average internal energy $U(\lambda)$ of a (001) surface slab of $NaAlH_4$ as a function of the reaction coordinate λ during the $\alpha \rightarrow \gamma$ transition at 300 K (270 atoms). The initial α phase is represented by the local potential minimum near $\lambda = 0$, whereas the final γ phase is represented by the local minimum near $\lambda = 1$. Metastable intermediate states at $\lambda = 0.35$, 0.65, and 0.75 indicate shearing of successive slab layers.

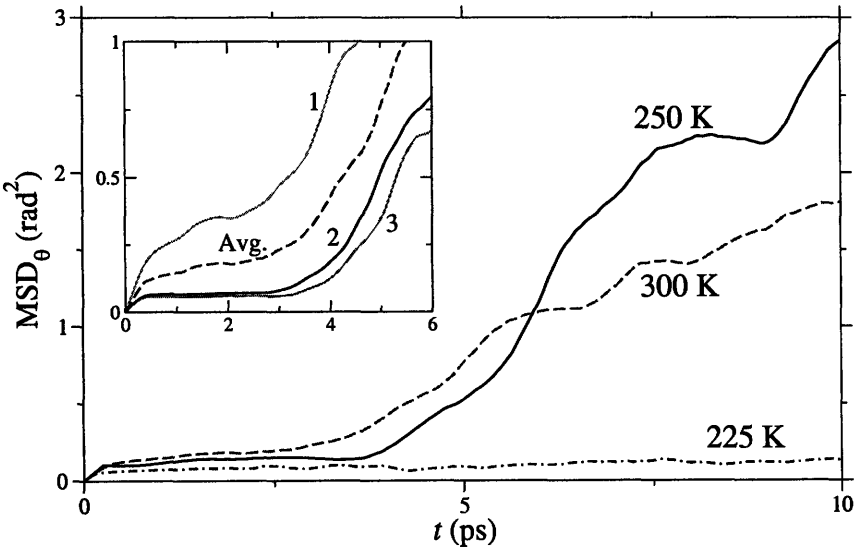

FIGURE 6-14: The angular mean-square displacement (Equation 6.3) of the AlH_4^- tetrahedral moieties in a (001) surface slab of $NaAlH_4$ beginning from the α phase. Data is from simulations at 225 K (96 atoms, blue curve), 250 K (96 atoms, black curve), and 300 K (270 atoms, red curve). The inset shows the angular mean-square displacement at 300 K averaged over the successive atomic layers perpendicular to the slab. Here "1" designates the average angular mean-square displacement for an outermost [surface] layer, whereas "2" represents a subsurface layer and "3" the innermost layer. According to the inset, the onset of rotation occurs most rapidly in the surface layer and begins to spread to the subsurface about 3 ps into the simulation.

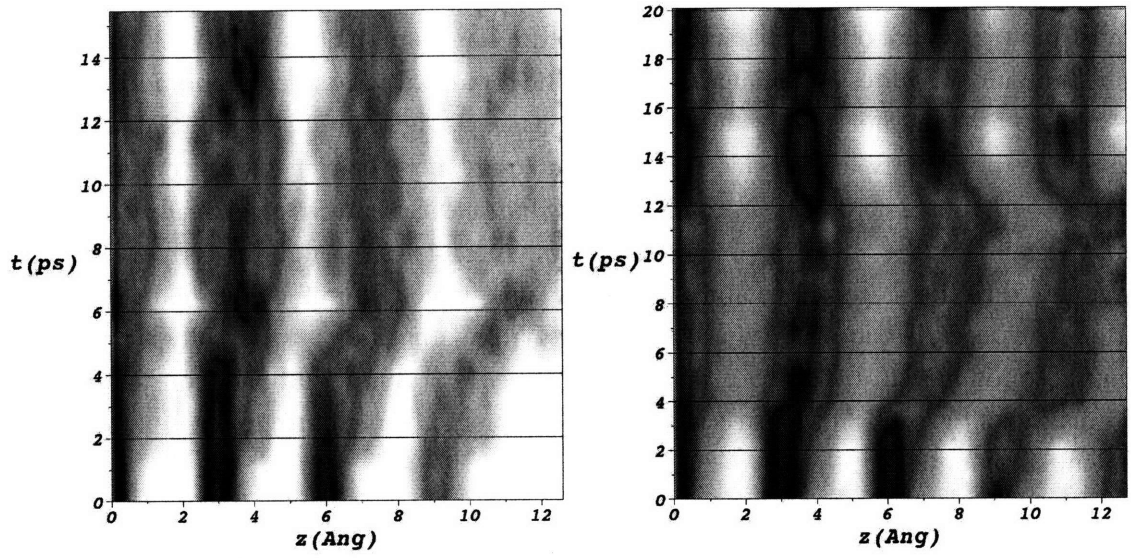

(a) 250 K (b) 300 K

FIGURE 6-15: Time evolution of the Al–Al linear pair correlation function $g_{\mathrm{Al\,Al}}(z)$ describing the relative probability of finding two Al atoms in *ab* planes separated by a distance z. The increase in the perpendicular spacing of the lattice planes can be seen in the shift of the $g_{\mathrm{Al\,Al}}(z)$ peak locations at about 4 ps into the simulation. Data is taken from simulations at (a) 250 K, 96 atoms; and (b) 300 K, 270 atoms.

interlayer distance perpendicular to the slab. Accordingly, Figure 6-15 shows the time evolution of the *linear pair correlation function* $g_{\mathrm{Al\,Al}}(z)$, which describes the relative probability of finding two Al atoms in planes separated by a given distance z along the [001] lattice direction. For both simulations (250 K and 300 K), there is a clear time marker at which the increase in c begins. Moreover, as we saw with the onset of AlH_4^- rotation, the event begins at the surface before percolating through the slab.

A comparison of Figures 6-12, 6-14, and 6-15 also yields valuable information on the relative timescales of the onset of the three described processes; namely, shear of the *ab* lattice planes, activation of the AlH_4^- rotational modes, and expansion of the lattice parameter c. For both of the intermediate-temperature simulations (250 K and 300 K), activation of the AlH_4^- rotational modes is the first of the processes to manifest itself, followed soon after (within half of a picosecond) by the beginning of a lattice expansion along the $\hat{c}$ direction and finally (after another picosecond or so) by the *ab* planar shear. Coupled with the information from the inset of Figure 6-14, a complete picture of the motivations for the various stages of the transformation can be generated. We conclude that the transition to the γ phase begins by first activating the rotational modes of the outermost surface AlH_4^- groups. As the rotational disorder permeates the slab structure, the slab thickness increases to compensate. This in turn lowers the activation barrier for the shear of *ab* planes to generate the new lattice symmetry.

Our analysis also provides some insight towards understanding why the $\alpha \rightarrow \gamma$ phase transformation is not observable in the constant-pressure simulations of bulk α-$NaAlH_4$. The transformation requires an initial activation of the rotational degrees of freedom for the AlH_4^- tetrahedra as a first nucleation step, yet the α phase has rigid tetrahedral units that evidence no rotational mobility in the bulk, suggesting a large kinetic barrier. On the other hand, the barrier to rotational mobility for an AlH_4^- unit at the surface is much lower, readily facilitating the nucleation of the γ phase, which subsequently percolates through the crystal. Moreover, once the transition is complete, the γ phase remains stable within the intermediate temperature range described above, further confirming that the transition is kinetically limited rather than thermodynamically limited. This fact was verified in an additional constant-pressure simulation of the bulk γ phase at 300 K, which demonstrated no return to the α phase in 15 ps of simulation time.

6.4.3 Characterizing the γ phase

Structure and energetics

In order to pinpoint the structure of γ-$NaAlH_4$, we ran a series of energetic calculations of the structure for different values of the lattice parameters a, b, and c, as well as of the cell angles α and β. For each geometry, a 2×2×1 k-point mesh was used, and a complete BFGS ionic relaxation was performed starting from the average equilibrium positions of the ions in our slab simulations. Energy surface contours for different values of c/a are plotted in Figure 6-16. The final lattice geometry that we obtain indicates a tetragonal unit cell with $a = 4.851$ Å and $c = 7.253$ Å, representing a 15% volumetric increase over our relaxation calculation for the α phase.[‡] The minimum-energy structure that we obtain is depicted in Figure 6-17. Notably, the zero-temperature γ structure has decreased lattice parameters with respect to those seen in our variable-cell dynamics simulations of the (001) surface slab. It also features an ordered array of hydrogens, with the central ab plane shifted slightly with respect to its neighbors. However, at the temperatures for which the γ phase is manifest ($T \geq 250$ K), the hydrogen substructure does not order, and the shifting of the central plane is manifest only weakly (see Figure 6-10). These features are subdued upon activation of the AlH_4^- rotational dynamics, which breaks the symmetry of the structure. It is also likely that the disorder induced by this rotation is the primary agent responsible for the increase in the finite-temperature lattice parameter a, since the structure must expand to accommodate free rotation of the tetrahedra.

It is useful to obtain a more precise measure of the energetic difference between the zero-temperature ground-state α structure and the local-minimum γ structure. To do so, we calculated the energy of the two relaxed structures at their theoretical lattice geometries and As it

[‡]An additional variable-cell relaxation was run in which the BFGS algorithm was used to minimize the energy with respect to the lattice vectors in addition to the ionic positions; the results of this calculation were consistent with those of the equation-of-state calculation.

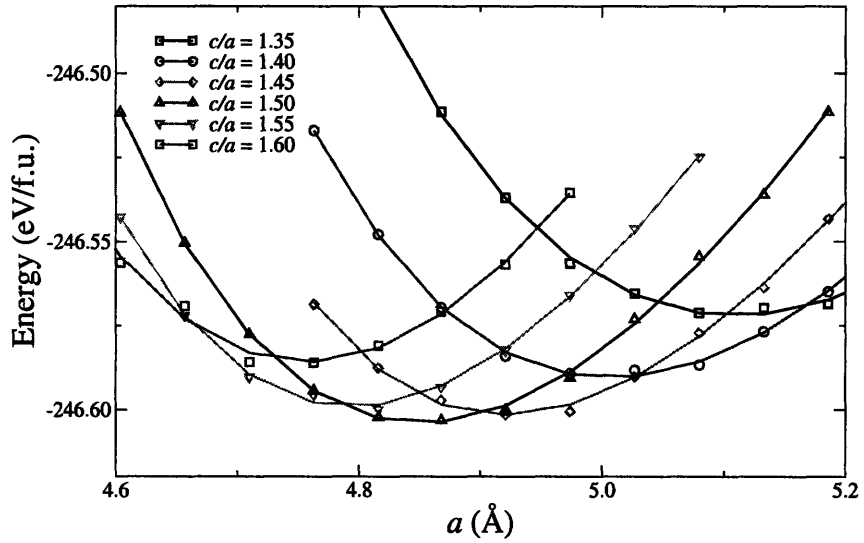

FIGURE 6-16: Equation-of-state calculations for various values of the c/a ratio in the γ phase of $NaAlH_4$. Calculations were performed on a 12-atom unit cell using an evenly spaced 2×2×1 grid of k-points and an electronic wavefunction cutoff energy of 25 Ry.

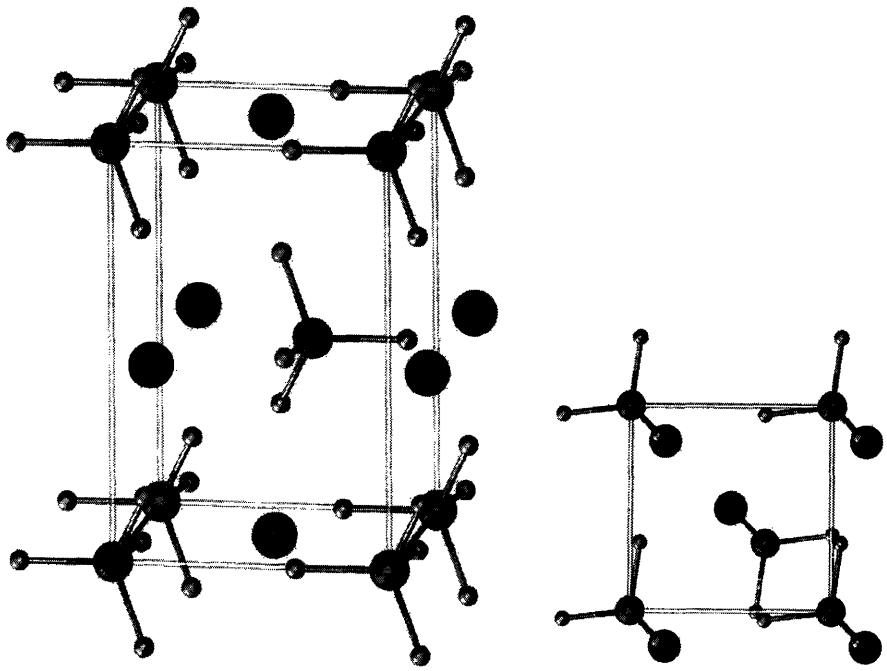

FIGURE 6-17: Structure of the unit cell of γ-$NaAlH_4$, shown in (a) the standard view and (b) a top view (along the $\hat{c}$ axis). The color scheme follows that of Figure 6-5.

turns out, the gamma phase is extremely stable with respect to the reference α phase, with a calculated energy difference of only ~ 1.3 meV per formula unit. The lattice expansion caused by the AlH_4^- rotation likely increases the energy of the γ phase at elevated temperatures; nevertheless, the associated entropic gain appears to compensate readily. This minor energy difference between the two phases further evidences that thermodynamics are not the limiting factor in inhibiting the $\alpha \rightarrow \gamma$ phase transition in the bulk.

A possible connection to Na_3AlH_6

An examination of Figures6-6 and 6-17 suggests certain geometric similarities in the aluminum substructures in γ-$NaAlH_4$ and Na_3AlH_6 that offer a possible phenomenological connection of the observed $\alpha \rightarrow \gamma$ phase transformation to the $NaAlH_4 \rightarrow Na_3AlH_6$ transition in the real material. Indeed, it turns out that lattice parameters a and b of α-$NaAlH_4$ ($a = 5.02$ Å; Reference [206]) and α-Na_3AlH_6 ($a = 5.410$ Å, $b = 5.539$ Å; Reference [212]) are compatible to within about 10%, and the monoclinic angle β between the $\hat{a}$ and $\hat{c}$ axes in Na_3AlH_6 is very close to 90° (90.18°). The most significant geometric component of the transformation (aside from the altered symmetry group) is the change in the lattice parameter c, which is compatible with what we observed in the $\alpha \rightarrow \gamma$ transition. Moreover, the 40% increase in the lattice parameter c that we observe in the slab thickness upon entering into the γ phase agrees well with the experimental 30% decrease upon transitioning to Na_3AlH_6 if one considers that one complete unit cell of α-$NaAlH_4$ bifurcates into two unit cells of γ-$NaAlH_4$.

One aspect of the structural similarity between γ-$NaAlH_4$ and Na_3AlH_6 is quantified in Figure 6-18, which compares the Al-Al pair correlation function $g_{Al\,Al}$ in a (001) surface slab both before and after the $\alpha \rightarrow \gamma$ phase transition with a similar quantity for an ideal crystal of Na_3AlH_6 that is lattice matched to our cell. More precisely, the Na_3AlH_6 value was obtained by first mapping the monoclinic unit cell to a tetragonal cell while maintaining fixed values for the fractional crystallographic coordinates of the atoms and then isotropically changing the resulting cell volume to match the lattice parameters of our cell in the ab plane. The agreement between the locations of the cell peaks for the modified Na_3AlH_6 and for γ-$NaAlH_4$ offers a further indication of a possible connection between the two phases.

6.5 Mobility of atomic species

As was the case for the variable-cell simulations of bulk α-$NaAlH_4$, not a single Al–H bond was broken throughout the course of any of the (001) surface decomposition simulations. Notably, this was the case even at temperatures in excess of the melting point of the slab. (This finding also agrees with the combined experimental and theoretical results of Reference [213]). However, breaking and forming of Al–H bonds represent a necessary component in dehydrogenation, since AlH_6^{3-} octahedra and metallic aluminum are both produced as known byprod-

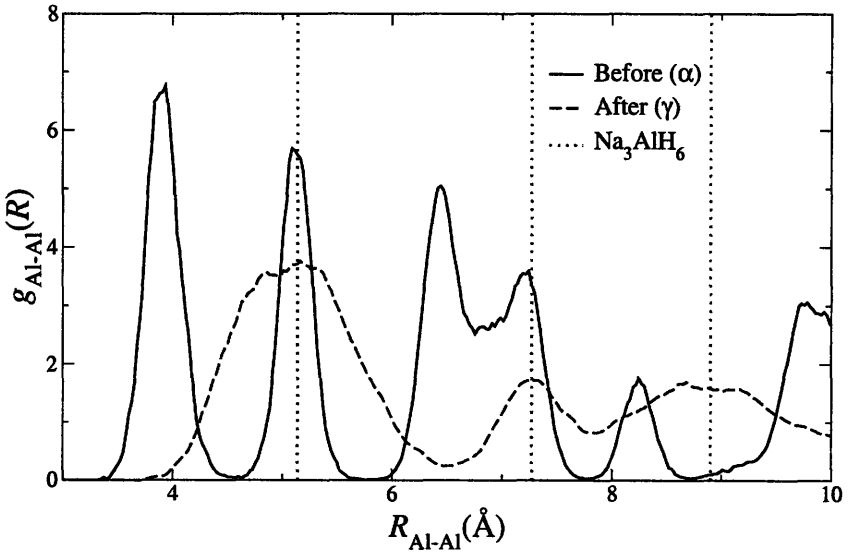

FIGURE 6-18: Comparison of the Al–Al pair correlation function $g_{\mathrm{Al\,Al}}$ for the (001) surface slab at 250 K before the $\alpha \rightarrow \gamma$ transition (black solid line) with that after the transition (blue dashed line). The red dotted lines are the corresponding values for the lattice-matched ideal crystal of Na_3AlH_6 (see text for definition). The general agreement of the peak locations for γ-$NaAlH_4$ and Na_3AlH_6 indicates a possible connection between the corresponding aluminum substructures.

ucts. Assuming the dynamics of bond breaking are not beyond the timescale of the simulation (a reasonable assumption, given the rapidity of the phase transition and the absence of Al–H bond breaking even at elevated temperatures), we conclude that the $\alpha \rightarrow \gamma$ structural transition must necessarily be accompanied by a secondary phenomenon to induce hydrogen mobility.

We have already discussed the similarities between the aluminum substructures in γ-$NaAlH_4$ and Na_3AlH_6. However, in order to properly isolate the missing potential pathway between the intermediate γ phase and the end product Na_3AlH_6, it is necessary to examine the key structural differences between the two. In addition to the obvious difference in the hydrogen coordination of the aluminum atoms, a comparison of Figures 6-6 and 6-17 reveals that the γ phase of $NaAlH_4$ features missing planes of sodium atoms that lie midway between the aluminum planes perpendicular to [001]. Completion of the $NaAlH_4 \rightarrow Na_3AlH_6$ transition therefore requires additional absorption of both hydrogen and sodium (in equal molar proportions) into the gamma phase. This sort of argument may seem counterintuitive to the reader, since we are in fact examining the *dehydrogenation* reaction. However, it must be remembered that absorption in one region implies depletion in another. Accordingly, our proposed scheme has the metallic aluminum and molecular hydrogen of Equation 6.1 left behind following a partial mass hydrogen exodus from a local depletion region to a local hydrogen-rich region to form the AlH_6^{3-} hexahydride complexes.

Two possibilities emerge as the most likely explanations for our inability to observe nucle-

ation of the hexahydride. First, low concentrations of point defects may facilitate hydrogen mobility, thereby driving formation of the hexahydride. Second, it is conceivable that on the short lengthscales accessible to our simulations, nucleation can occur only given the precise proper stoichiometry. Under ordinary circumstances, our tetrahydride simulations do not provide this. The following sections examine each of these possibilities in depth.

6.5.1 Hydrogen transport in the presence of point defects

A possible notion of how hydrogen transport might work in $NaAlH_4$ can be derived from the structural resemblance of α-$NaAlH_4$ to Phase-I $CsHSO_4$ (compare Figures 6-5 and 5-3). We remind the reader that we identified and discussed a causal link between structure and mobility for $CsHSO_4$ in Chapter 5. By extension, the similarity of the structures means it is not implausible that an analogous transport mechanism may be responsible for hydrogen mobility in the sodium alanate system. Extending the simple analogy to $CsHSO_4$ would suggest that once the network of AlH_4^- tetrahedral moieties becomes disordered, then hydrogen may be passed between neighboring such complexes until it escapes at the surface.

In simulating hydrogen self-diffusion in $CsHSO_4$, we were able to observe common spontaneous formation of over- and underprotonated structural defects, such as H_2SO_4 or isolated SO_4. These resulted from a sufficiently weak barrier to hydrogen mobility in terms of chemical-bond jumping (see Section 5.4.1). However, the Al–H bond in $NaAlH_4$ is much stabler than the O–H bond in $CsHSO_4$. Accordingly, thermal energy alone is insufficient to allow for the intrinsic formation of under- and overcoordinated AlH_x complexes that can be detected on the timescales of the bulk simulations we performed. Nevertheless, it is worthwhile investigating the effect of explicit inclusion of point defects with relatively low formation energies, since these defects might be expected to occur naturally in the real material. Moreover, since it is known that the inclusion of titanium substantially improves the dehydrogenation reaction kinetics even at very low concentrations (< 2 mol% [191]), it is not unreasonable to assume that point defects could have a nonnegligible impact on hydrogen mobility (the role of Ti will be discussed in more detail in Section 6.6).

In an attempt to assess the potential role of point defects in enhancing hydrogen mobility or nucleating a phase transformation, we began by running a series of simulations in a $2\times2\times1$ supercell of bulk $NaAlH_4$ in the presence of various point defects at 400 K. Motivated by formation energy calculations performed previously by M.Y. Chou (Table 6.2, Reference [214]), we selected three of the most stable vacancies for simulation: H, AlH_3, and NaH.* For the case of the hydrogen vacancy, we simulated the system twice, once in the presence of a neutral H_v^0 vacancy and once in the presence of a charged H_v^- vacancy. For the charged simulation, a dif-

*Calculation of accurate formation energies depends upon a proper selection of reference states; this issue has led to discrepancy in reported values in the literature [215–217]. Nonetheless, the motivation for this study being an understanding of the kinetics and heuristics of hydrogen transport, we are primarily concerned with qualitative trends in formation energies and therefore accept the values in Table 6.2 as sufficiently accurate for our purposes.

TABLE 6.2: Calculated DFT formation energies ΔE_f for various vacancies in 2×2×1 bulk α-$NaAlH_4$. The reference state for each calculation is taken to be standard bulk state of the constituents at 350 K. From Reference [214].

Description	ΔE_f (eV)
H_v^0	1.69
$(AlH_3)_v^0$	1.63
$(NaH)_v^0$	1.38

fuse jellium of opposite charge and equal magnitude was implicitly added to maintain charge neutrality across the simulation cell, and a spin-polarized calculation was used. In all cases, the ionic positions were initially relaxed locally using a damped-dynamics run prior to the equilibration period. Also, in order to maintain proper adherence to the Born-Oppenheimer adiabatic surface, simulations were performed using a Car-Parrinello fictitious electronic mass of $\mu = 350$ au, with the timestep adjusted to $\Delta t = 5$ au.

Since the initial positioning of the defects may affect simulation results, attempts were made to place them in their "logical" sites. For the NaH vacancy, this simply implied removal of a nearest-neighbor sodium-hydrogen pair from the bulk. For the AlH_3 vacancy, an entire AlH_4^- tetrahedral complex was removed and replaced with a lone hydrogen atom in the position formerly occupied by the aluminum. For the H vacancy, the sites are functionally equivalent, so an arbitrary atom was chosen for removal.

Through 15 ps of equilibrated simulation time, none of our vacancy calculations demonstrated mass transport of sodium or aluminum through the lattice. However, certain of the point defects did have a substantial impact in enhancing hydrogen mobility. This is evident upon examination of the ensemble-averaged mean-square displacement of the hydrogen atoms in the presence of each of the vacancies, which quantity is plotted for bulk α-$NaAlH_4$ in Figure 6-19(a). We note a slow, linear increase in the MSD indicating diffusive behavior of the hydrogens in the presence of an AlH_3 vacancy as well as in the presence of a charged H vacancy (curiously, no hydrogen diffusive behavior is noted for the neutral H vacancy; we will return to this point later).

A closer examination of these two cases reveals a diffusion mechanism that bears a great resemblance to the dominant transport process in $CsHSO_4$, in accordance with our original hypothesis. Turning first to the case of the AlH_3 vacancy, mobility results following an initial capture of the lone hydrogen by a neighboring AlH_4^- to form an AlH_5^{2-} complex, which then shares its additional hydrogen with one of its aluminum nearest neighbors to form an $Al_2H_9^{3-}$ defect. When the shared Al–H–Al bond is broken, the hydrogen can find itself bonded to the neighboring Al, resulting in net propagation of the AlH_5^{2-} complex. This new complex is then free to share one of its additional hydrogens and form a new $Al_2H_9^{3-}$ defect structure. As was the case for $CsHSO_4$, successive hydrogen transfers need not involve the original lone hydrogen. However, despite evidence of hydrogen mobility in the presence of the AlH_3 vacancy, we

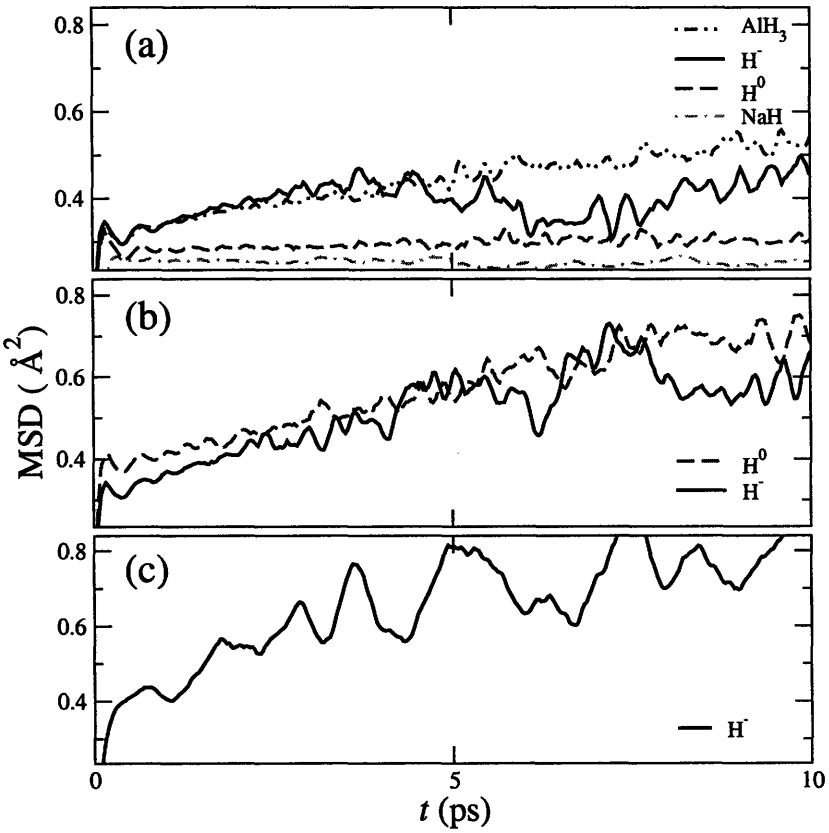

FIGURE 6-19: Mean-square displacement of the hydrogen atoms (calculated according to Equation 3.26) in the presence of (a) NaH, AlH_3, H^0, and H^- vacancies in bulk α-$NaAlH_4$ at 400 K; (b) H^0 and H^- interstitials in bulk α-$NaAlH_4$ at 400 K; and (c) an H^- vacancy in a (001) surface slab of α-$NaAlH_4$ at 225 K. A linear increase is observed in all instances except the NaH and H^0 vacancy simulations in the bulk, indicating net diffusion of hydrogen. The scales in the three panels are identical.

also find that the mobile hydrogen stays loosely bound to the original immobile Al vacancy site, always remaining within one nearest-neighbor aluminum complex. As a result, any hydrogen transport we observe in this scenario is highly localized and is therefore unlikely to play a significant role in macroscopic mass transport.

The fact that the mobile hydrogen remains localized in the presence of an AlH_3 vacancy in bulk α-$NaAlH_4$ does not negate the potential role of overcoordinated aluminum complexes in mass transport of hydrogen, however. Additional confirmation of the role of these structural defects can be seen in another pair of simulations that we ran involving a single AlH_5^{2-} defect in the presence of otherwise pure $NaAlH_4^-$. As was the case with the hydrogen vacancy, the resulting simulations of the hydrogen interstitial were run in both the charged (H_i^-) and uncharged (H_i^0) states. This scenario was selected because there should be no preferred site for the extra hydrogen. Indeed, the results for both the charged and uncharged configurations show substantially enhanced hydrogen mobility without any apparent localization of the de-

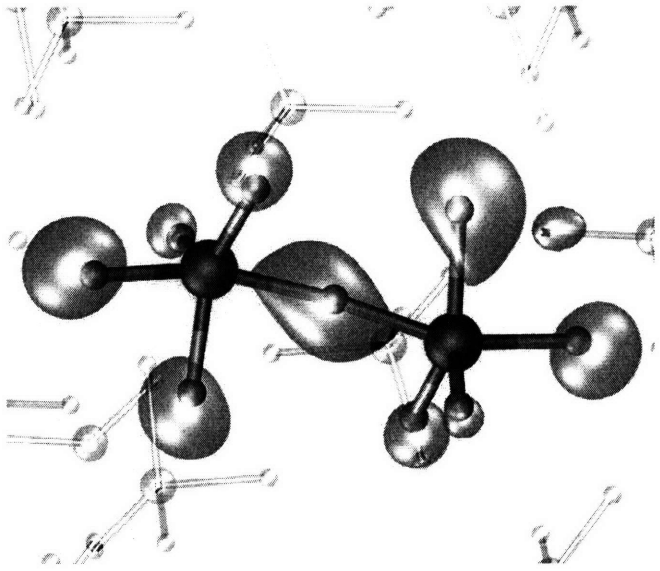

FIGURE 6-20: Isosurface (95%) of the charge density difference $|\rho^{-}(\mathbf{r}) - \rho^{0}(\mathbf{r})|$ between a singly charged hydrogen interstitial in bulk α-$NaAlH_4$ and a neutral hydrogen interstitial in the identical position. Formation of an $Al_2H_9^{3-}$ defect is observed, and the isosurface indicates that most of the additional electronic density in the presence of the charged interstitial is spread across the defect.

fect. In fact, the results of the MSD calculation for the case of the hydrogen interstitial, given in Figure 6-19(b), demonstrate faster hydrogen transport than is observed for any of the studied vacancies in the bulk. This is true for both the charged and uncharged defect states.

The basic underlying mechanism of hydrogen transport in the presence of an extra H mirrors that described for the AlH_3 vacancy and involves simple Grotthuss-style passing of one of the hydrogens in the AlH_5^{2-} defect to a neighboring AlH_4^{-} when the complexes rotate to a configuration energetically favorable for transfer. One such event is depicted in Figure 6-21. However, a subtle difference is detectable between the neutral interstitial and charged interstitial cases. For the neutral case, we do not generally observe formation of the $Al_2H_9^{3-}$ complex; rather, the hydrogen remains associated with a single aluminum. On the other hand, for the charged defect, the additional hydrogen prefers to be shared across an $Al_2H_9^{3-}$ complex. Figure 6-20 examines the difference between the charged and uncharged states in terms of the electronic density. It is evident that the additional charge introduced in the case of the former is shared across the entire $Al_2H_9^{3-}$ complex, thereby stabilizing it electronically. This offers a further indication that for the charged defect, the hydrogen in the Al–H–Al bond is best viewed as belonging to the entire $Al_2H_9^{3-}$ unit rather than to one individual aluminum.

According to Figure 6-19(a), hydrogen diffusion in the presence of a charged hydrogen vacancy is significantly slower than for either an AlH_3 vacancy or an H interstitial in the bulk solid. However, having already established the critical role of the (001) surface in promoting the transition to the hexahydride, we ran an additional simulation of a charged H_v^{-} vacancy in the outermost layer of a 2×2×1 (001) surface slab of α-$NaAlH_4$ to see if its impact on hydrogen

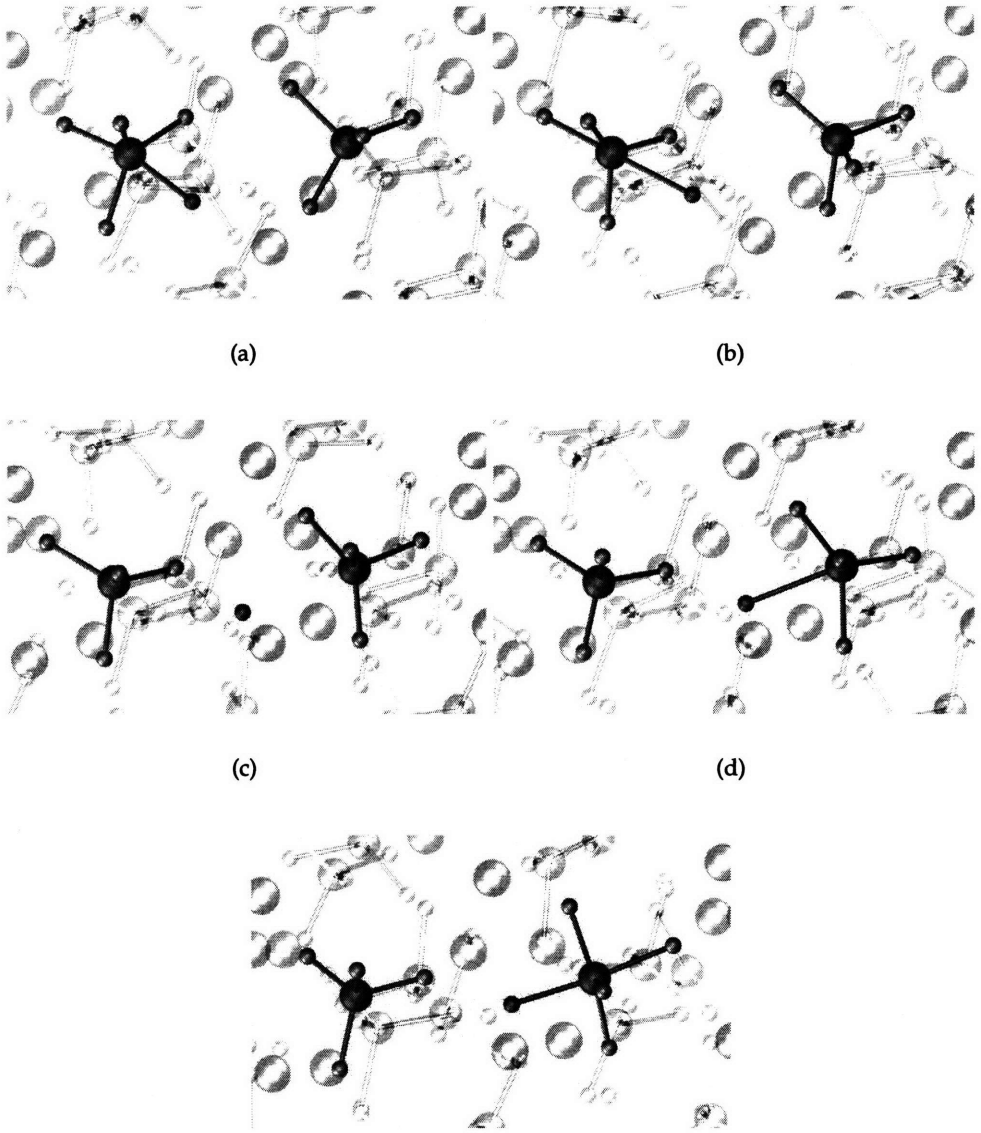

FIGURE 6-21: Progression of a Grotthuss-type hydrogen transfer event in the presence of an AlH_5^{2-} defect in bulk $NaAlH_4$. Once the AlH_x complexes have rotated to a configuration favorable for transfer, the Al–H bond associated with the traveling hydrogen (a) elongates and then (b) breaks. The hydrogen then (c) passes through a saddle point before it (d) nears the neighboring Al and (e) is captured into a new bond, resulting in net transport of the AlH_5^{2-} defect.

mobility was enhanced with respect to the same vacancy in the bulk. The results, which are plotted in panel (c) of Figure 6-19, indeed evidence a hydrogen mobility that is not only higher than what we observe in the bulk simulation in the presence of a hydrogen vacancy but is actually the highest mobility we recorded in any of our simulations. This is particularly significant given that the temperature of the slab was set to only 225 K (the highest temperature for which the α phase is preferred), whereas the bulk calculations were performed at 400 K.

The diffusion mechanism in the presence of a charged hydrogen vacancy in a (001) surface slab of $NaAlH_4$ is illustrated in Figure 6-22. The mechanism resembles the interstitial hydrogen case in that it involves the formation of aluminum defect complexes. Similar to the case for the additional charged hydrogen and the for the AlH_3 vacancy, these defect complexes generally involve two AlH_x neighbors bound together, in this case into an $Al_2H_7^-$ intermediate complex rather than a single, unbound AlH_3 defect. This $Al_2H_7^-$ structure, which shares a single hydrogen equally between two adjacent aluminum atoms, can propagate in a two-step process analogous to that already discussed for $Al_2H_9^{3-}$. First, one of the bonds in the shared Al–H–Al complex is broken, releasing one AlH_4^- and one AlH_3 unit. Second, the aluminum in the AlH_3 unit forms a bond with a hydrogen from a different AlH_4^- neighbor, resulting in the formation of a new $Al_2H_7^-$ complex with a new shared hydrogen.

We have already noted that no hydrogen transport is observed in the presence of the neutral H vacancy. This can be explained in terms of the aluminum defect complexes: much like for the additional neutral hydrogen, there appears to be no tendency for the formation of $Al_2H_7^-$ complexes. However, diffusion in the case of the charged vacancy relies on the propagation of this structure; we do not generally observe the simple "hopping" of a hydrogen away from one AlH_4^- unit to an AlH_3 unit. The high apparent cost of such an event precludes its occurrence in our simulations, yet the lower barrier to propagation of the entire $Al_2H_7^-$ unit via the described mechanism makes it readily accessible in those simulations for which $Al_2H_7^-$ formation is possible.

The mechanisms depicted in Figures 6-21 and 6-22 are both examples of *structural diffusion*. In this model, individual mobile hydrogens cannot be distinguished, and the diffusion can instead be considered by tracking large defect complexes (in this case, $Al_2H_7^-$ and $Al_2H_9^{3-}$) that propagate through the system as a result of bond breaking and forming. In fact, the role of the aluminum defect complexes in mediating hydrogen transport bears a clear resemblance to the role of the $H_5O_2^+$ Zundel complex as one of the structural diffusion elements responsible for proton transport in liquid water [171, 172, 182, 183]. The delicate issue of how diffusion should be quantified in such materials was introduced in Chapter 5 and applies again here. One possibility is to examine the mean-square displacement of the center of mass of the defect complex (see also Appendix C). This solution was dismissed for $CsHSO_4$ for logistical reasons, but it can be applied straightforwardly to $NaAlH_4$ since the defects are easily tracked. Figure 6-23 explores this idea by comparing the standard mean-square displacement of the hydrogen atoms to the mean-square displacement of the $Al_2H_7^-$ complex in the (001) surface slab

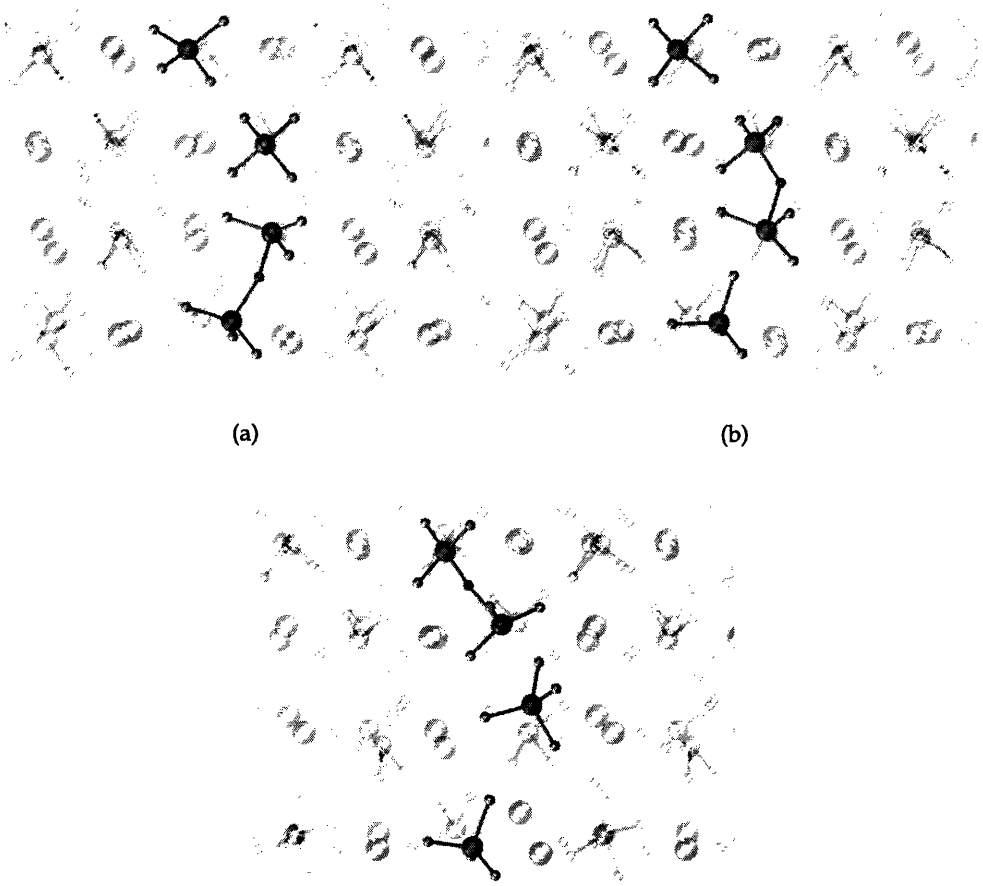

FIGURE 6-22: Propagation of an $Al_2H_7^-$ structural defect complex in a simulation of a (001) α-$NaAlH_4$ surface slab in the presence of a hydrogen vacancy at 225 K. The defect, initially placed in the outermost surface layer, moves through the slab via a phenomenon known as structural diffusion, in which one of the shared Al–H–Al bonds is broken and a new one forms with a different neighboring aluminum.

simulation in the presence of a charged hydrogen vacancy. It is immediately evident that the structural diffusion is about 40 times faster than the ordinary hydrogen diffusion, suggesting extremely rapid *apparent* mobility of the aluminum defect complex. Note that this is despite the fact that no actual net motion of the aluminum atoms is registered and the contribution of the diffusive hydrogen atoms is comparatively minor. The structural diffusion model is particularly compelling because it provides a viable explanation for experimental evidence [208,209] for the existence of highly mobile hydrogen-containing defect complexes.

All of the defect simulations that feature net transport of hydrogen (H_v^-, $(AlH_3)_v$, H_i^-, H_i^0) share a common thread in that they require rotational mobility of the AlH_x complexes. This can be seen in Figure 6-24, which displays the angular mean-square displacement (Equa-

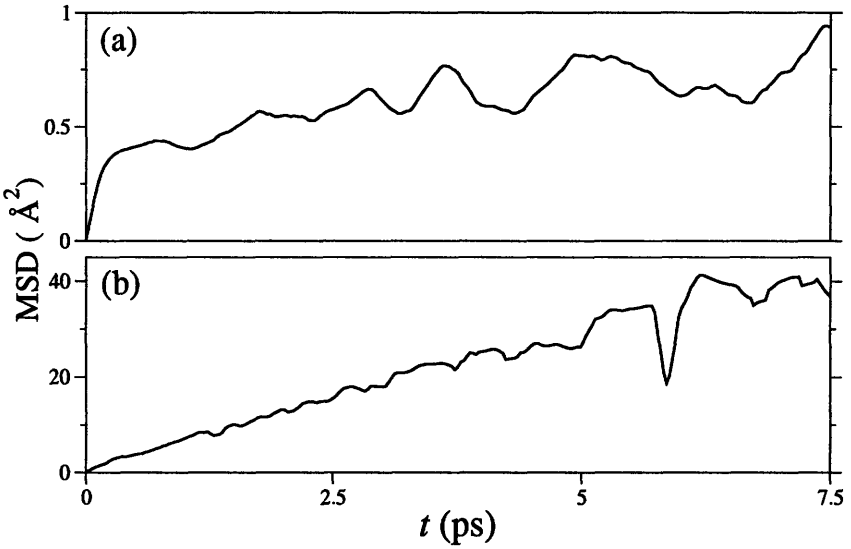

FIGURE 6-23: Comparison of the mean-square displacements of the (a) hydrogen atoms and (b) the center of mass of the $Al_2H_7^-$ defect complex in a simulation of a (001) surface slab of α-$NaAlH_4$ at 225 K with a singly-charged hydride vacancy. The different slopes of the two curves indicate that the apparent diffusion of the defect complex is about 40 times as fast as that of the individual hydrogen atoms.

tion 6.3) for the defect simulations in Figure 6-19. Conversely, the simulations that do not exhibit AlH_x rotation (H_v^0, $(NaH)_v$) also do not exhibit any hydrogen transport, suggesting that such rotational mobility is in fact a necessary precursor for hydrogen diffusion. Whether or not the AlH_x rotational modes are activated upon inclusion of point defects therefore appears to be an excellent predictor of whether or not hydrogen diffusion will be induced in the material.

6.5.2 Accounting for stoichiometry

Although our defect simulations are successful in providing a compelling picture of the relevant mechanisms involved in hydrogen transport, such an analysis cannot account for the mass transport of sodium that is necessary to complete the $NaAlH_4 \rightarrow Na_3AlH_6$ transition. As a reminder, the γ phase of $NaAlH_4$ differs from Na_3AlH_6 in that it lacks the intermediate planes of sodium atoms between the aluminum planes perpendicular to the $\hat{c}$ axis. Therefore, in order to finalize a clear connection between γ-$NaAlH_4$ and Na_3AlH_6, the mechanism of sodium transport also needs to be investigated.

Given the relatively small system sizes that are accessible to our simulations, it is easy to imagine that nucleation of the hexahydride (and more particularly, absorption of the sodium atoms into the lattice and migration to their respective lattice destinations) might necessitate exact stoichiometry for the complete supercell. However, testing this hypothesis requires that we develop a way of introducing additional sodium atoms that is unbiased towards any par-

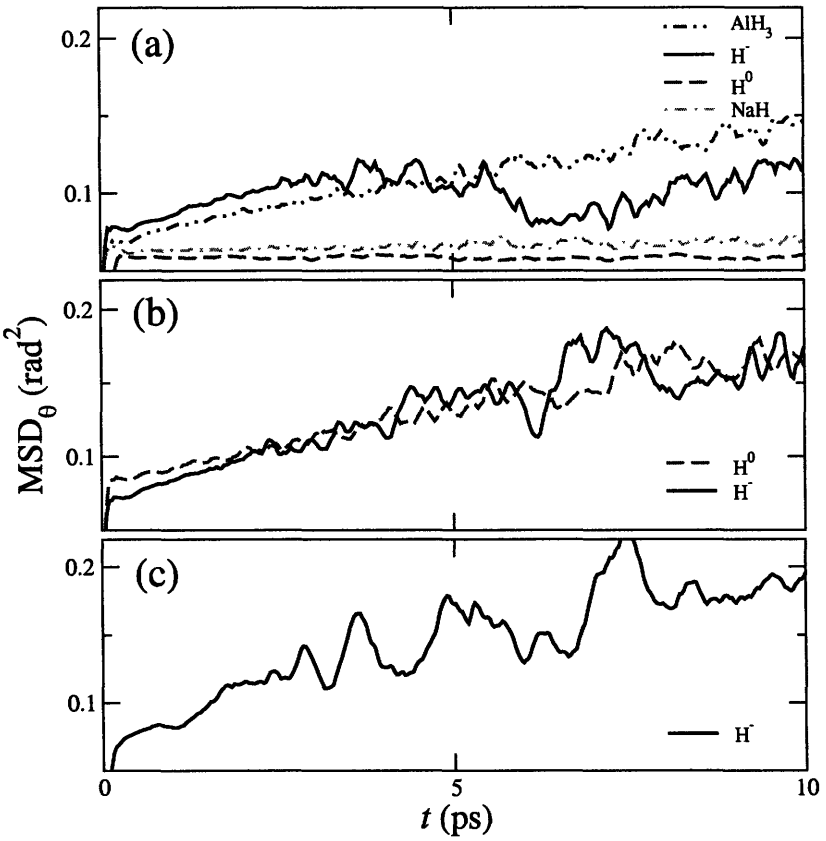

FIGURE 6-24: Angular mean-square displacement of the hydrogen atoms (calculated according to Equation 6.3) in the presence of (a) NaH, AlH_3, H^0, and H^- vacancies in bulk α-$NaAlH_4$ at 400 K; (b) H^0 and H^- interstitials in bulk α-$NaAlH_4$ at 400 K; and (c) an H^- vacancy in a (001) surface slab of α-$NaAlH_4$ at 225 K. Linear increases are observable in each of the simulations featuring mobile hydrogen atoms (i.e., all except the NaH and H^0 vacancy simulations in the bulk), indicating the presence of AlH_4 rotation. The scales in the three panels are identical.

ticular lattice site preference. To do so, we ran a series of simulations in which sodium and hydrogen were added in equal ratios to as to generate the proper Na_3AlH_6 stoichiometry for the overall supercell, with the positions for the additional atoms generated randomly to minimize bias. To account for the extremely high interatomic forces that may be generated in random positioning, in each case we first ran a damped dynamics simulation before equilibrating the system.

First, our simulations evidence that spontaneous absorption of Na or H into the $NaAlH_4$ lattice from a diffuse NaH mixture may be difficult in the absence of an external agent. We observed no appreciable absorption of either Na or H when the two were added to the vacuum interlayer between (001) surface slabs of γ-$NaAlH_4$; the outermost surface layer disordered, but there was no further absorption of Na or H into the lattice. Fixing the aluminum locations eliminated the surface disordering but did not enhance absorption. Similar behavior was de-

tected in a simulation involving an isolated 96-atom supercell of γ-$NaAlH_4$ with Na and H added randomly throughout the vacuum border region, meaning permeation is equally unlikely across the (001) plane. We also simulated a liquid layer of NaH sandwiched between slabs of bulk γ-$NaAlH_4$ uniaxially compressed along either the $\hat{c}$ or $\hat{a}$ lattice directions. The motivation for these simulations was to introduce an external pressure to force the Na and H into the lattice. However, in these instances, the compressed $NaAlH_4$ instead reformed into an amorphous high-pressure configuration that prevented any additional absorption of Na or H. Moreover, in each of these simulations, formation of a liquid layer of NaH was preferred over lattice absorption.

However, the γ-$NaAlH_4 + 2\,Na + 2\,H \rightarrow Na_3AlH_6$ transition was at last observed when we fixed the aluminum lattice in the bulk γ configuration and inserted the Na and H atoms into random positions without any change in the corresponding lattice parameters. This suggests that once additional Na and H are properly introduced into the γ lattice of $NaAlH_4$, the transition to the hexahydride will indeed be favored. Figure 6-25 offers a quantitative measure of the timescale of the migration of the additional sodium atoms and hydrogen atoms to their new hexahydride sites by plotting the "reverse" mean-square displacement (Equation 3.25) of the sodium atoms over the entire 50 ps simulation time. Here the reference configuration is the final simulation timestep, which has the proper geometry of the hexahydride. The first stages of the relocation takes place within only a few picoseconds, with the diffusion of the sodium ions initially even faster than the hydrogens. The system then occupies a sequence of metastable states until the final configuration is achieved almost 40 ps into the simulation.

It is interesting to examine the diffusion mechanisms for the hydrogen and sodium atoms as they seek their final lattice configurations. The hydrogen is observed to diffuse via a mechanism similar to that seen in the H_i^- defect simulation, with formation of both $Al_2H_9^{3-}$ and $Al_2H_{11}^{5-}$ defect complexes as metastable intermediaries as the hydrogens travel between Al hosts via alternative Al–H bond breaking and forming (see Section 6.5.1 for details). Diffusion of sodium ions, on the other hand, follows a simple vacancy hopping mechanism. To analyze the diffusion pathways for the Na atoms, we have run four additional simulations of fixed-Al γ-$NaAlH_4$ with Na and H inserted in different initial random configurations. The occupation density method (Equation 3.17 was then used to track the Na trajectories in each simulation, and the results were averaged over all five simulations. The resulting isosurface of preferred Na diffusion pathways is graphed in Figure 6-26. According to the figure, migration of Na ions into the previously unoccupied interlayer positions is most likely to occur via the octahedral interstitial sites at the centers of the (001) planes.

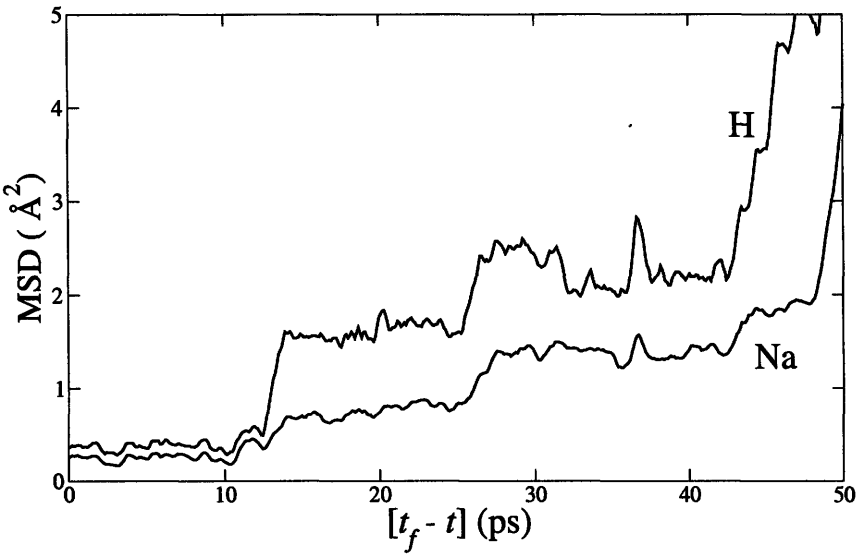

FIGURE 6-25: Mean-square displacement of the hydrogen and sodium atoms, calculated using Equation 3.25 by comparing the configuration at time t to that at the final timestep t_f. Data is from a simulation of bulk 96-atom γ-$NaAlH_4$ with 32 additional Na atoms and 32 additional H atoms placed randomly throughout the supercell. The total simulation covers 50 ps, with the initial nonequilibrated configuration represented by the $t = 50$ ps data point. The final Na_3AlH_6 configuration is reached 12 ps before the end of the simulation, or 38 ps from the starting frame.

6.6 Speculating on the tetrahydride-to-hexahydride transition

In light of the above discussions, it now becomes possible to construct a speculative framework for describing the complete process of dehydrogenation in sodium alanate. Our proposed mechanism proceeds as follows: the first step for inducing both hydrogen mobility and the necessary structural transformation involves activation of the AlH_x rotational modes, which is inhibited in the perfect bulk crystal but can take place either in the presence of certain point defects to facilitate hydrogen migration or else at exposed surfaces or grain boundaries to prompt transformation to the γ structure. As surface rotation enables the structural transformation, the lattice exhibits local expansion along the $\hat{c}$ lattice direction, finally resulting in a shear of successive *ab* planes to form the required symmetry of the final phase, beginning at the surface and percolating through the bulk. Meanwhile, induced migration of hydrogens from another region of the system overcoordinated AlH_x complexes in the destination region (which will become the hexahydride) and undercoordinated AlH_x complexes in the depleted region, inducing further hydrogen diffusion in both regions via a structural diffusion mechanism. Sodium atoms are also injected into the nucleated hexahydride from the depleted region as the transformation occurs, possibly as a result of disordering at the boundary interface between grains. As local growth of the Na_3AlH_6 phase progresses, the reaction proceeds forward by entirely depleting the source of sodium and much of the hydrogen. Alane (AlH_3)

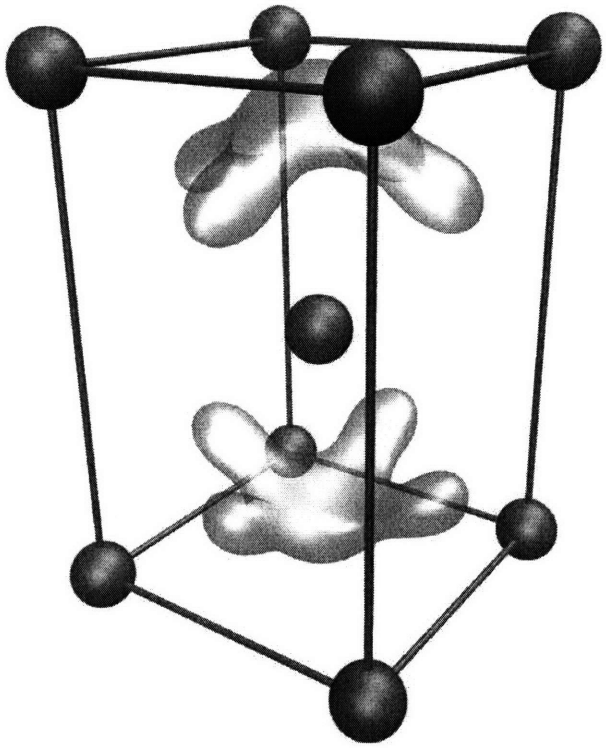

FIGURE 6-26: Occupation density isosurface representing the most commonly traveled pathways for the additional sodium ions during the conversion of a unit cell of γ-$NaAlH_4$ into Na_3AlH_6. The points of the two cross-like isosurfaces represent the eight final lattice sites. Migration to these sites is via the octahedral sites at the centers of the (001) planes, which correspond to the centers of the two isosurface crosses. The positions of the aluminum atoms are shown for reference.

is left behind as a byproduct in the depleted region but is thermodynamically unstable at the temperatures in question [39,218] and therefore further decomposes into aluminum metal and molecular hydrogen. The H_2 is subsequently released, most likely at the interface between the hexahydride and the depleted region.

As a final note, the proposed framework also allows one to further speculate as to the specific role of the titanium dopant in catalyzing the dehydrogenation reaction. There exists significant disagreement as to the preferred location of the Ti in the host lattice; most studies suggest it lies near the surface and is substituted either for a sodium atom [204, 219] or an aluminum atom [203,220,221], whereas others conclude that it resides in an interstitial site or penetrates into the bulk [199,222,223]. To aid in our discussion, we relaxed the structures of Na-substituted and Al-substituted Ti on the (001) surface of $NaAlH_4$ using damped molecular dynamics in a 96-atom slab. Table 6.3 lists the enthalpies of substitution for these two cases, as

TABLE 6.3: Calculated DFT enthalpies of substitution ΔH_s for a Ti dopant atom in a 2×2×1 (001) surface slab of α-$NaAlH_4$.

Description	ΔH_s (eV/atom)[a]	ΔH_s (eV/atom)[b]
Ti → Al	0.016	-0.007
Ti → Na	0.031	-0.022

(a) Reference [203], using pure $NaAlH_4$ and bulk metal as reference state
(b) Reference [204], using pure $NaAlH_4$ and isolated atoms as reference state

calculated by the authors of References [203] and [204]. Using David Vanderbilt's uspp package [224], we generated an ultrasoft Ti pseudopotential in a $3s^2 3p^6 4s^2 3d^2$ valence configuration (details of the pseudopotential are documented in Appendix A). The final configurations of the Al-substituted and Na-substituted simulations following the damped dynamics are graphed in Figure 6-27. Titanium substituted in the aluminum site prefers higher hydrogen coordination than the replaced aluminum and takes those hydrogen atoms from neighboring AlH_4^- complexes, creating undercoordinated AlH_3 complexes that could become mobile via the process described in Section 6.5.1. Conceivably, titanium in the aluminum site could also act as a hydrogen donor for creating nearby overcoordinated AlH_x complexes, which have also already been shown to induce hydrogen mobility. Titanium in the sodium site has a similar effect, in that it interacts with hydrogens bonded to neighboring AlH_4^- units to create larger defect complexes, thereby weakening nearby Al–H bonds. This potential kinetic effect of Ti in enhancing the breakup of Al–H bonds via formation of new cluster geometries is also discussed in Reference [213]. Significantly, in both site substitutions, the relaxation results in a reorientation and distortion of the tetrahedral geometry of neighboring AlH_4^- groups to maximize local Ti–H interaction (this finding is in agreement with the results of Reference [225]). Since activation of the AlH_x rotational modes has already been established as a key ingredient in the tetrahydride-to-hexahydride transition, this represents another likely benefit of Ti doping. Finally, in addition to the potential reasons already mentioned, it could be that the primary contribution of titanium to the dehydrogenation process is the creation and promotion of stable alloys with aluminum or sodium, as has been proposed by the authors of References [204] and [226]. If this were the case, these alloys could facilitate mass transport of the metallic elements and free bound hydrogens in the process.

6.7 Summary and conclusions

In this chapter, an in-depth analysis of the dehydrogenation reaction in the sodium alanate system based on a variety of first-principles molecular dynamics simulations has been presented. We find that the formation of the Na_3AlH_6 product is a result of a cooperative interplay between a structural transition that nucleates at an exposed surface or grain boundary, and the defect-driven migration of hydrogen through the lattice structure. We show that these two

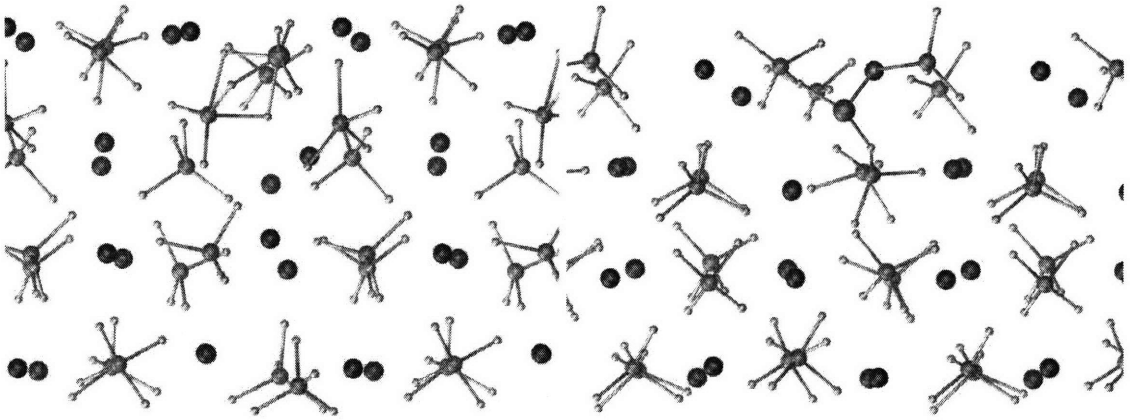

(a) (b)

FIGURE 6-27: Configuration of atoms in a $2 \times 2 \times 1$ (001) surface slab of α-$NaAlH_4$ with a surface Ti dopant atom (orange) substituted in (a) the Al site and (b) the Na site. Geometries were extracted following a full system relaxation using damped molecular dynamics. Views are along the $\hat{b}$ axis, with the $\hat{c}$ axis pointing upwards.

phenomena can be treated independently of one another and offer a detailed examination of each in turn.

We have also discovered and characterized a new phase of $NaAlH_4$ that we label γ. It is shown that the transition to the γ phase is kinetically inhibited in the bulk but occurs readily in a (001) surface slab at simulation temperatures above 225 K and below 400 K. This transition takes place by first activating the rotational modes of the AlH_4^- tetrahedra at the surface. This disordering percolates into the bulk, following which the lattice expands along the $\hat{c}$ direction, and then the ab planes shear to generate a new symmetry. A possible structural link between the γ phase and the known Na_3AlH_6 dehydrogenation product is also discussed.

Next, it is demonstrated that hydrogen mobility is enabled and enhanced by the presence of an H^- vacancy or the addition of an extra hydrogen or hydride. For the charged defects, structural diffusion of shared-hydrogen Al_2H_x complexes represents the dominant process in transporting hydrogen between aluminum hosts. We also find that the mobility of hydride vacancies is higher at the (001) surface than it is in the bulk. In each case, hydrogen mobility is signaled by the onset of rotational dynamics of the AlH_x units. We also discuss a possible connection of the vacancy-hopping mechanism for sodium migration to the conversion of γ-$NaAlH_4$ into Na_3AlH_6. Finally, we speculate on the possible role of the Ti dopant in enhancing the dehydrogenation reaction kinetics.

CHAPTER 7

Concluding remarks

"It is unworthy of excellent men to lose hours like slaves in the labor of calculation which could be relegated to anyone else if machines were used."

— Gottfried Wilhelm von Leibnitz

IN SUMMARY, extensive first-principles molecular dynamics results have been presented on three technologically relevant highly diffusive materials: AgI, $CsHSO_4$, and $NaAlH_4$. This chapter begins by reviewing the key findings of those simulation results. The broader vision of this work is then re-examined through an exploration of the phenomenological similarities and differences among the three studied materials. Finally, we discuss the impact of our results in terms of understanding the relationship between ionic diffusion and phase transitions in these and similar materials.

In Chapter 4, we characterized the transition to the fast-ion conducting phase, as well as the lattice and electronic structures of the archetypal Type-I fast-ion conductor α-AgI. Significantly, we found that fast-ion conduction in the material is signaled by a phase transition of the silver ions alone. It was also discovered that in the fast-conducting phase, the first silver shell surrounding an iodine displays a distinct dynamical structure that would escape a time-averaged characterization; we captured this structure in a set of ordering rules that govern the instantaneous distribution of silvers surrounding an iodine. The electronic structure was also shown to demonstrate a unique chemical signature of the weakest-bound silver in the first shell, which we in turn identified as the most likely to diffuse. The paradoxical nature of the fast-ion conducting phase as an exotic order-disorder transition, an independent phase transition of the silvers, and an unusual entropically stabilized phase was also discussed.

In Chapter 5, we presented a detailed study of proton dynamics in the hydrogen-bonded proton conductor $CsHSO_4$, isolating the subtle interplay between the dynamics of the O–H chemical bonds, the O$\cdots$H hydrogen bonds, and the SO_4 tetrahedra in promoting proton diffusion. We found that the Grotthuss mechanism of proton transport is primarily responsible

for the dynamics of the chemical bonds, whereas the reorganization of the hydrogen-bond network is dominated by rapid angular hops in concert with small reorientations of the SO_4 tetrahedra. A detailed statistical analysis revealed that frequent proton jumping across the O–H$\cdots$O complex is countered by a high rate of jump reversal. We showed that reversal rate is connected to the dynamics of the SO_4 tetrahedra, resulting in a diminished $CsHSO_4/CsDSO_4$ isotope effect. We also presented evidence of multiple timescales for SO_4 reorientation events, leading to distinct diffusion mechanisms along the different crystal lattice directions. Finally, we employed a variety of graph-theoretic techniques to characterize the topology of the hydrogen-bond network and demonstrated a clear relationship between the likelihood for diffusive jump events and the presence of connectivity configurations favoring linear network chains over closed network rings.

Chapter 6 focused on simulations of the dehydrogenation reaction in the sodium alanate system, a complex light metal hydride with tremendous promise as a hydrogen storage material. At least two processes were found to be necessary components in driving the phase transition: first, the structural reorganization of the lattice, and second, the defect-driven transport of hydrogen. We further showed that these can be treated independently. We reported the discovery of a new phase (γ) of the tetrahydride $NaAlH_4$, and the transition to this new phase was recorded in simulations of a (001) surface slab of $NaAlH_4$. The geometric connection of the γ phase to the Na_3AlH_6 structure was then demonstrated, and a timescale analysis was used to isolate the progression of the three dominant processes driving the transition. Next, we discussed how hydrogen mobility is induced in the presence of additional hydrogens, hydrides, or hydride vacancies and described the underlying transport mechanism in each of these cases. We also isolated the pathways for sodium relocation in the lattice, and these results were combined with our results on hydrogen diffusion and lattice structural reorganization to provide a complete picture of the $NaAlH_4 \rightarrow Na_3AlH_6$ transition.

As a final note, we wish to emphasize that fast ionic diffusion can be an elaborate phenomenon that manifests itself uniquely in very different classes of materials. As such, developing a universally applicable framework for understanding its various complexities remains a difficult task. Nonetheless, we have demonstrated that novel insights into certain diffusive materials can in fact be gained from atomistic simulations. In fact, many of these conclusions retain relevance across wide ranges of known ionic conductors, owing to the emergence of patterns in the coupling between ionic and electronic configurations in the studied materials. For instance, each features mobile ions that can transition rapidly between two distinct electronic or chemical configurations. For AgI, this change was identified as a transition to a state containing covalent character. In $CsHSO_4$, on the other hand, we found that it arises in the back-and-forth hopping of protons across the hydrogen-bond complex. And in $NaAlH_4$, it was detected in the effect that inclusion of hydrogen-related defects had on the aluminum-hydrogen binding energy. Moreover, in all cases, such events drive local ion migration, but they are also phonon-coupled to classical disordering phenomena that exhibit behavior on

longer time- and length scales. In AgI, it is the silver lattice ordering and the subsequent reorganization of the iodine lattice; in $CsHSO_4$, it is the topological behavior of the hydrogen-bond network structure and the coupling to the rotational dynamics of the SO_4 units. Finally, in $NaAlH_4$, it can be seen in the connection between hydrogen mobility and the structural phase transition of the host lattice.

The phenomenological differences between the three materials are equally significant, however, in that they demonstrate the variability that exists in the interplay of atomistic process in different types of conductors. Notably, although all three exhibit structural phase transitions that are linked to microscopic diffusive phenomena, the relationship between these two differs substantially from one to the next. In particular, for AgI we found that it is the mobility of the silver lattice that likely drives the rearrangement of the base anionic structure. In contrast, $CsHSO_4$ represents an instance in which enabling proton transfer depends upon a structural transition to a phase with rotational freedom for the SO_4 units. For $NaAlH_4$, we saw that defect-driven hydrogen mobility can be treated entirely independently from the transition to the γ phase but that both are necessary ingredients in the transformation to Na_3AlH_6.

To conclude, we reiterate that for each of three systems that were studied in this thesis, it is impossible to attribute ionic diffusion to any one factor. Instead, an attempt has been made to explore a wide variety of possible motivations, showcasing the power of first-principles methodology in illuminating multiple facets of what can prove a very intricate phenomenon. The resulting picture is a tapestry of kinetic, thermodynamic, geometric, and electronic effects whose significance may seem marginal when considered individually, but when woven together emerge as a richly complex diffusion mechanism.

Funding for this thesis work was provided by the U.S. Department of Energy Computational Science Graduate Fellowship, with additional support from MURI Grant DAAD 19-03-1-0169 and the U.S. Department of Energy Hydrogen Program Contract DE-FG02-05ER46253. Computational facilities were provided under National Science Foundation Grant DMR-0414849. All calculations have been performed using the Quantum-ESPRESSO software package [124], distributed under the GNU Public License. Most figures were generated using the Grace [227] and VMD [228] packages.

APPENDIX A

Pseudopotential parameters

THIS APPENDIX details the input parameters and test results for the I, Cs, Na, and Ti pseudopotentials generated for this thesis work. Table A.1 summarizes the relevant input parameters for each of the generated pseudopotentials. Tables A.2, A.3, and A.4 compare the results of select lattice parameter and bulk modulus calculations for I, Cs, and Na, respectively. In each case, results are given for the pseudoatom in the bulk and in at least one common binary compound. Verification of the suitability of the Ti pseudopotential can be found in Reference [229], from which the input parameters were taken. It should be noted that Tables A.2, A.3, and A.4 do not include the results of the lattice parameter calculations for the materials studied directly in this work; these can be found in the text of Chapters 4–6.

TABLE A.1: Input parameters for generating the I, Cs, Na, and Ti pseudopotentials used in this work. Parameters for the Ti pseudopotential are taken from Reference [229]. For the pseudopotential type, 'TM' denotes the norm-conserving Troullier-Martins formalism [126] and 'US' denotes the Vanderbilt ultrasoft formalism [74]. 'NLCC' indicates use of the nonlinear core correction method of Reference [73]. In each case, the reference energy is taken to be the eigenenergy of the highest occupied orbital.

Input parameter	*I*	*Na*	*Cs*	*Ti*
Valence configuration	$5s^2 5p^5$	$6s^{0.5} 5d^{0.05} 6p^{0.05}$	$3s^{0.5} 3p^{0.05}$	$3s^2 3p^6 3d^2 4s^2$
Pseudopotential type	TM	TM	TM	US
Software used	Ref. [125]	Ref. [168]	Ref. [168]	Ref. [224]
NLCC	N	Y	Y	N
Radial cutoffs (au)	$5s = 2.15$	$6s = 4.19$	$3s = 2.64$	*all* = 1.80
	$5p = 2.24$	$6p = 6.01$	$3p = 3.90$	
		$5d = 3.01$		

TABLE A.2: Calculated NaI lattice parameter and I_2 bond length using the generated pseudopotential for iodine. Experimental values are from Reference [230].

Description	*This work*	*Experiment*	*% Deviation*
NaI lattice parameter (Å)	6.605	6.470	+2.1
I_2 bond length (Å)	2.699	2.660	+1.5

TABLE A.3: Calculated lattice parameters and bulk moduli for bulk Cs and CsCl using the generated pseudopotential for cesium. Experimental values are from Reference [230].

Description	*This work*	*Experiment*	*% Deviation*
Cs lattice parameter (Å)	6.134	6.046	+1.5
Cs bulk modulus (kbar)	19.2	21.5	-10.7
CsCl lattice parameter (Å)	4.197	4.123	+1.8
CsCl bulk modulus (kbar)	163.8	169.6	-3.4

TABLE A.4: Calculated lattice parameters and bulk moduli for bulk Na, NaCl, and NaI using the generated pseudopotential for sodium. Experimental values are from Reference [230].

Description	*This work*	*Experiment*	*% Deviation*
Na lattice parameter (Å)	4.191	4.291	-2.3
Na bulk modulus (kbar)	75	63	+19.0
NaI lattice parameter (Å)	6.605	6.470	+2.1
NaCl lattice parameter (Å)	5.850	5.640	+3.7

APPENDIX B

Graph-theoretic methodology

IN THIS APPENDIX, we offer a detailed account of the graph-theoretic methods used to calculate the hydrogen-bond network topology of $CsHSO_4$ in Chapter 5. We begin by representing the network as a directed graph with the edge vector pointing along the O–H$\cdots$O bond direction; that is, from the sulfate tetrahedron acting as the hydrogen-bond donor in the complex to the sulfate tetrahedron acting as the hydrogen-bond acceptor. The adjacency matrix A_{ij} can then be constructed as an $N \times N$ matrix, where N is the number of tetrahedra in the unit cell and the indices i and j run over the donor and acceptor sulfate groups, respectively:

$$A_{ij} = \begin{cases} 1 & \text{if there exists a direct link } i \rightarrow j \\ 0 & \text{otherwise} \end{cases} \tag{B.1}$$

The diagonal elements A_{ii} are set to zero. Topological characterization of a single node is then a straightforward process of performing a row sum to get the number of nodes to which it donates (N_d) and a column sum to get the number of nodes donating to it (N_a). It is also easy to categorize jump events by analyzing the difference of the adjacency matrices of successive timesteps.

To determine ring connectivity and size, we exploit the property of adjacency matrices [231] that element (i, j) of A^n gives the number of unique directed pathways from i to j of length n. We take the size of the ring containing the i^{th} node to be the lowest value of n in the interval [2, (N–1)] for which the diagonal element $A^n_{ii} \neq 0$. If $A^n_{ii} = 0$ for all n in the interval, the node is not considered part of a ring.

Deriving chain sizes is more complex, since we must account for multiple branching topologies and for topological mixtures of rings and chains. We first decompose the network into clusters of unconnected subgraphs. This is done using the connectivity matrix C_{ij}, which has the property that $C_{ij} = 1$ if there is a path *of any length* connecting nodes i and j. We form the symmetric C_{ij} from A_{ij} using Warshall's algorithm [232].

We proceed to construct a matrix S_{ij} that contains the shortest path between each pair of nodes (i, j), $i \neq j$, by taking the lowest value of n in the interval [2, $(N-1)$] for which $A^n_{ij} \neq 0$. We can then take the maximum value of S_{ij} across the columns to get a row array of maximum path lengths for chains originating at the i^{th} node. The chain size is then determined by finding the maximum value of the resultant array over the nodes contained in each connected cluster, which can be easily determined by parsing C_{ij}. Finally, we add the restriction that none of the links in the chain can themselves be members of rings. This prevents counting of chains that are fictitiously long due to intermediate or terminating rings and ensures a clear separation between ring and chain topologies. The resulting chain size is then calculated as the maximum span of the graph-theoretic tree.

Very large networks may necessitate more efficient algorithms due to the expense of calculating $A^{(N-1)}$. However, the system sizes in our study are sufficiently small to readily allow calculations using the described method.

APPENDIX C

On the calculation of diffusion coefficients from molecular dynamics

IN CHAPTERS 4 AND 5, we provided estimates of diffusion coefficients in fast-ion conductors calculated using molecular dynamics data. This Appendix briefly evaluates the various methods that can be used to calculate the diffusion coefficient and discusses the relationship of these methods to experimental measures. Finally, methods for estimating the error associated with the calculation of transport coefficients are mentioned, including the specific techniques used in this thesis.

We begin by reviewing the methods discussed in Chapter 3. The first approach uses the Green-Kubo relation to evaluate the self-diffusion coefficient D^* by integrating the velocity autocorrelation function (Equation 3.28) [85]:

$$D^* = \frac{1}{3} \lim_{t \to \infty} \int_0^t \langle \mathrm{VAF}(t') \rangle \, \mathrm{d}t'. \tag{C.1}$$

An alternative choice is to use the Einstein relation and the slope of the mean-square displacement (Equation 3.26) [85]:

$$D^* = \lim_{t \to \infty} \frac{1}{6t} \langle \mathrm{MSD}(t) \rangle. \tag{C.2}$$

Despite their mathematical equivalence, Equations C.1 and C.2 are not numerically identical in finite simulations. In practice, it may be preferable to use one method or the other. The VAF method converges more rapidly to an approximate value for D, since the MSD method requires significant sampling beyond the initial ballistic regime. As such, Equation C.1 may be preferable for short simulations, especially of systems with short correlation times between "independent" frames. However, the evolution of the ionic positions is significantly smoother than the evolution of the ionic velocities. This means that extremely fine VAF sampling is re-

quired to capture the full phenomenology in the Green-Kubo integration. The MSD, on the other hand, can be sampled at relatively coarse intervals without loss of pertinent data. The smoothness issue also means that the errors accrued for long-time values of the MSD—for which there are few intervals over which to average—are generally much less than those for long-time values of the VAF. This results in more robust convergence of the calculated diffusion coefficient for long times. The MSD method is further beneficial in that one does not have to account for the numerical integration error that is accrued in the VAF method. Therefore, Equation C.2 is often preferable for sufficiently long simulations or simulations of systems with long correlation times, and is the method that is generally used throughout this work.

Chitra and Yashonath [233] examined the dependence of the calculated diffusion coefficient on the simulation time using both the Einstein and Green-Kubo methods. They discovered that although both methods converge readily to an approximate value, convergence to a final, stable value can be extremely slow. They also determined that diffusion coefficients calculated from short molecular dynamics simulations tend to be overstimated with respect to longer simulations, even in systems with low correlation in the motion of the diffusive species. This was found to be particularly true for the MSD method, owing to the deceptively long tail of the ballistic regime. One would expect this effect to be amplified in materials with complex, correlated diffusion pathways (such as $CsHSO_4$), since visitation of all possible configurations could not be guaranteed within the relatively short simulation time.

It should be noted that Equations C.1 and C.2 give expressions for the self-diffusion coefficient, which are best compared to the results of diffusion experiments using radioactive isotopes or NMR tracing. However, for fast-ion conductors, well-resolved data can be difficult to obtain using these methods, given the high operating temperatures and fast diffusion kinetics, as well as a potential lack of availability of proper isotopes. Instead, diffusion coefficents may be obtained directly from conductivity measurements or by using a polarizing field and assuming a formal charge for the diffusive ionic species. On the atomistic scale, such measurements are more appropriately compared to the *chemical diffusion coefficient*, which describes diffusion in a chemical potential gradient and is the quantity which generally enters into Fick's Law [234].

The chemical diffusion coefficient D_C can be written as [235,236]:

$$D_C = \left(\frac{\langle (\delta N)^2 \rangle}{\langle N \rangle} \right)^{-1} D_J, \tag{C.3}$$

where D_J is the "collective diffusion coefficient" or "jump diffusion coefficient", defined as:

$$D_J = \lim_{t \to \infty} \left\{ \frac{1}{6t} \frac{1}{N} \left\langle \left| \sum_{I=1}^{N} \left[\mathbf{R}_I(t) - \mathbf{R}_I(0) \right] \right|^2 \right\rangle \right\}. \tag{C.4}$$

The leading term on the right-hand side of Equation C.3 refers to the fluctuations $\langle (\delta N)^2 \rangle$ in

the particle number N of the diffusing species. In principle, this quantity should be calculated from a grand-canonical simulation. However, it may be well approximated by instead considering number fluctuations in a subregion of fixed volume [235].

For our *ab-initio* simulations, the fluctuations in the particle number are seen to depend strongly on the size of the subregion partitions, indicating our simulation supercell is too small to obtain a reliably converged measure. As such, we do not attempt to calculate the chemical diffusion coefficients D_C in this work. On the other hand, the collective diffusion coefficient D_J is readily calculable. This quantity measures the center-of-mass motion of the entire diffusive substructure rather than the average motion of the individual diffusive atoms. The primary result is that the collective diffusion coefficient properly accounts for the possibility of cross correlations between particle dynamics [237] (in the absence of cross correlations, Equations C.2 and C.4 should be expected to give identical results). Since the fast-ion conductors we study demonstrate highly correlated motion of the diffusive species, the collective diffusion coefficient is likely to be a more appropriate measure of the actual self diffusion. However, tracking only the center of mass results in a substantial reduction in usable statistics. This is verified in Chapter 5, in which we ultimately conclude that calculation of D_J for the hydrogen atoms in $CsHSO_4$ has an unacceptably high statistical error for practical use given our simulation timescales.

In cases where structural diffusion represents the predominant transport mechanism (such as for the defect complexes of Chapter 6), choosing a proper microscopic formulation of the diffusion coefficient becomes still more difficult. This is due to the fact that small actual motion of diffusive atoms can result in large apparent motion of structural defect complexes. One possibility is to adopt a quasiparticle approach, in which the diffusion coefficient is calculated by tracing the apparent mean-square displacement of the center of mass of the defect structure rather than the individual motion of atoms:

$$D_Q = \lim_{t\to\infty} \left\{ \frac{1}{6t} \frac{1}{N} \left\langle \mathbf{R}_Q(t) - \mathbf{R}_Q(0) \right\rangle^2 \right\}. \tag{C.5}$$

Here $\mathbf{R}_Q(t)$ represents the time-dependent center of mass of the quasiparticle defect.

In principle, Equation C.5 could yield results that point to near-infinite diffusion. In practice, D_Q will be determined by the lifetime of the metastable defect intermediary (for the $Al_2H_7^-$ defect in Chapter 6, it led to a 40-fold increase with respect to the traditional method). It should be noted that this method destroys the smoothness of the trajectories, which could lead to slow convergence and an increase of numerical error for a finite simulation.

Accurate estimation of error in the calculation of the diffusion coefficient is not a straightforward process. In principle, one must track the error both in the calculation of the VAF or MSD and in the use of the appropriate quantity to extract the diffusion coefficient. The error in the calculation of the VAF or MSD results from replacing the true equilibrium ensemble average by a time average over a finite simulation length. In general, this error should be pro-

portional to the square root of number of independent data points available in the simulation, i.e., to the simulation duration [238]. However, when using the averaging methods of Equations 3.26 and 3.28, data points at short times are inherently more precise than those at long times. This is due to the fact that at short times, there exist more intervals over which to average. This in turn means that there is no absolute measure of error in the calculation of the MSD or VAF. It also means that when the diffusion coefficient is calculated, using the long-time data will introduce more error. On the other hand, both the Green-Kubo and Einstein approaches rely on long-time limits, making it unclear which is the optimal data range to be used in the calculation of D.

For the results presented in this thesis, we used only the first half of our MSD or VAF results in calculating the diffusion coefficient, as described in Chapter 3. This ensured that data points with high errors were not included in the calculation. The choice was then made to ignore any error differences across the remaining data points in the MSD or VAF, since the error in the calculation of the diffusion coefficient should dominate the end result.

Probably the most common method for estimating the error in the final calculation of D is that discussed by Wood in Reference [239]. In this scheme, the total run is subdivided into smaller runs. The diffusion coefficients from each smaller run are then compared to get a final measure of the error. In principle, this method is robust, although the choice of the number of subdivisions is somewhat arbitrary and may affect results. However, in this method, two fundamental assumptions are made that may not be appropriate to the systems studied here. First, it is assumed that each smaller run has enough data to reliably approximate the behavior of the system at long times. Since we have already established that the diffusion coefficient can be slow to converge, this assumption can be dangerous for the short simulation times accessible to our methodology. Second, it is assumed that the system reaches equilibrium rapidly, such that each smaller simulation demonstrates equivalent diffusive behavior. However, for systems with a long equilibration time or highly correlated particle motion, this is unlikely to be true. It is also problematic for systems near a phase transition, since these can exhibit extreme fluctuations in dynamical quantities that are averaged out only over very long intervals.

For this work, we have instead developed an error estimation procedure that uses discrete sampling based on correlation times. In this sense, it draws on ideas similar to those used in the method of Smith and Wells [240]. An estimate for the correlation time τ—the time between "independent" dynamics timesteps—is first obtained by examining the short-time behavior of the velocity autocorrelation function.[†] The method then proceeds as follows:

1. Discretize a grid representing half of the total simulation time into intervals of the corre-

[†]A naïve approach at this point would be to simply sample the MSD data discretely in fixed intervals of τ. However, in doing so, we would be willingly ceding relevant statistical information and might also be giving undue preference to individual abberant data points. Averaging results for D based on discrete sampling in intervals of τ but using different starting configurations does little to improve the situation, since different data sets would still be cross correlated.

lation time τ.

2. For each grid point t' larger than a predefined cutoff:
   (a) Choose a starting timestep at random from the first half of the simulation data.
   (b) Calculate the mean-square displacement at time t' by comparing the randomly selected starting timestep with a frame at a time t' later.
3. Extract a diffusion coefficient based on the data obtained in Step 2 by performing a linear regression and using Equation C.2. Keep track of the standard error (i.e., 95% confidence interval) in the calculation of the slope.
4. Repeat Steps 2 and 3 to obtain a handful of diffusion coefficients (say, 5–10).
5. Extract the standard error (i.e., 95% confidence interval) from the set of individually obtained diffusion coefficients, assuming a normal distribution.
6. Compound the error from Step 5 with the average of the errors obtained in Step 3 to obtain the final estimate.

The cutoff in Step 2 is introduced to eliminate the ballistic regime in the MSD calculation.

Figure C-1 demonstrates the suitability of our method by comparing the diffusion coefficient calculated using the Green-Kubo approach (Equation C.1) to the calculated error bounds in the result using the Einstein relation (Equation C.2). This method was also used to calculate the error bounds in the diffusion coefficients in Figure 4-13. Note that the approach outlined here should not be applied to discretely sample the VAF and extract the Green-Kubo coefficients. This is because the VAF is not a robust quantity with respect to coarse sampling as is the MSD.

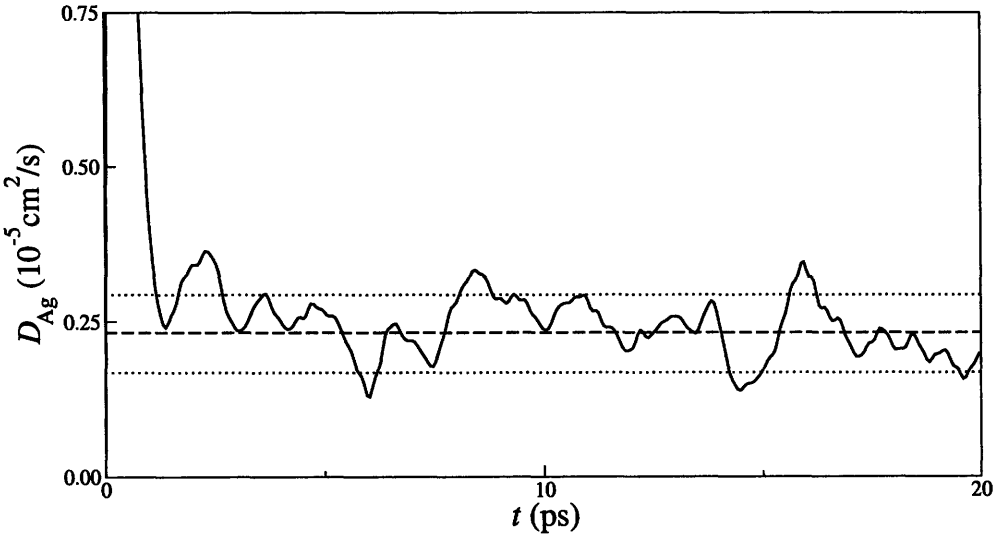

FIGURE C-1: Comparison of the Green-Kubo integral of the velocity autocorrelation function (solid line) with the self-diffusion coefficient obtained from the Einstein relation (dashed line). Error bounds for the Einstein-relation method, calculated using the method described in this Appendix, are shown as dotted lines to illustrate the general agreement between the two methods. Data is from a 200 K simulation of α-AgI.

Bibliography

[1] S. EMMOTT & S. RISON (Editors). *Towards 2020 Science*. Microsoft Research, Cambridge, UK (2006).

[2] S. MUGGLETON, V. VINGE, A. SZALAY, J. GRAY, R. BRENT, J. BRUCK, & I. FOSTER. 2020 vision: How computers will change the face of science. *Nature (Special Edition)* **440** (2006).

[3] B. J. ALDER & T. E. WAINWRIGHT. Phase transition for a hard-sphere system. *Journal of Chemical Physics* **27**, 1208–1209 (1957).

[4] B. J. ALDER & T. E. WAINWRIGHT. Studies in Molecular Dynamics. I. General Method. *Journal of Chemical Physics* **31**, 459–466 (1959).

[5] A. RAHMAN. Correlations in the Motion of Atoms in Liquid Argon. *Physical Review* **136**, A405–A411 (1964).

[6] F. H. STILLINGER & A. RAHMAN. Improved simulation of liquid water by molecular dynamics. *Journal of Chemical Physics* **60**, 1545–1557 (1974).

[7] R. CAR & M. PARRINELLO. Unified Approach for Molecular Dynamics and Density-Functional Theory. *Physical Review Letters* **55**, 2471–2474 (1985).

[8] D. A. KEEN. Disordering phenomena in superionic conductors. *Journal of Physics: Condensed Matter* **14**, R819–R857 (2002).

[9] S. HULL. Superionics: crystal structures and conduction processes. *Reports on Progress in Physics* **67**, 1233–1314 (2004).

[10] M. FARADAY. On conducting power generally. In *Experimental Researches in Electricity, Series IV*, 119–126. Royal Institution, London (1833).

[11] M. FARADAY. Effect of heat on conduction. In *Experimental Researches in Electricity, Series XII*, 436–450. Royal Institution, London (1839).

[12] W. HITTORF. Über das elektrische Leitungsvermögen des Schwefelsilbers und Halbschwefelkupfers. *Annalen der Physik und Chemie* **84**, 1–28 (1851).

[13] W. NERNST. Über die elektrolytische Leitung fester Körper bei sehr hohen Temperaturen. *Zeitschrift für Elektrochemie* **6**, 41–43 (1900).

[14] F. HABER & A. MOSER. Das Generatorgas- und das Kohlenelement. *Zeitschrift für Elektrochemie* **11**, 593–609 (1905).

[15] M. KATAYAMA. Über Amalgamkonzentrationsketten, chemische Ketten, und Daniellketten mit festen Electrolyten. *Zeitschrift für Physikalische Chemie* **61**, 566–587 (1908).

[16] W. SCHOTTKY. Zur Stromlieferung geeignetes galvanisches Element bzw, Elementkette. German Patent No. 650224 (1937).

[17] P. KNAUTH & H. L. TULLER. Solid-state ionics: Roots, status, and future prospects. *Journal of the American Chemical Society* **85**, 1654–1680 (2002).

[18] C. CAVAZZONI, G. L. CHIAROTTI, S. SCANDOLO, E. TOSATTI, M. BERNASCONI, & M. PARRINELLO. Superionic and Metallic States of Water and Ammonia at Giant Planet Conditions. *Science* **283**, 44–46 (1999).

[19] E. MARRIS. Giant planets may host superionic water. *Nature News* (March 2005).

[20] N. GOLDMAN & L. E. FRIED. First principles simulation of a superionic phase of hydrogen fluoride (HF) at high pressures and temperatures. *Journal of Chemical Physics* **125**, 044501 (2006).

[21] C. MILLER. An overview of the potassium channel family. *Genome Biology* **1**, R0004.1–R0004.5 (2000).

[22] J. H. MORAIS-CABRAL, Y. ZHOU, & R. MACKINNON. Energetic optimization of ion conduction rate by the K+ selectivity filter. *Nature* **414**, 37–42 (2001).

[23] S. BERNÈCHE & B. ROUX. A microscopic view of ion conduction through the K+ channel. *Proceedings of the National Academy of Sciences* **100**, 8644–8648 (2003).

[24] T. ALLEN, O. S. ANDERSEN, & B. ROUX. Energetics of ion conduction through the gramicidin channel. *Proceedings of the National Academy of Sciences* **101**, 117–122 (2003).

[25] K. TERABE, T. HASEGAWA, T. NAKAYAMA, & M. AONO. Quantized conductance atomic switch. *Nature* **433**, 47–50 (2005).

[26] N. MIURA, S. YAO, Y. SHIMIZU, & N. YAMAZOE. Carbon dioxide sensor using sodium ion conductor and binary carbonate auxiliary electrode. *Journal of the Electrochemical Society* **139**, 1384–1388 (1992).

[27] G. LU, N. MIURA, & N. YAMAZOE. Mixed potential hydrogen sensor combining oxide ion conductor with oxide electrode. *Journal of the Electrochemical Society* **143**, L154–L155 (1999).

[28] K. H. HSU, P. L. SCHULTZ, P. M. FERREIRA, & N. X. FANG. Electrochemical nanoimprinting with solid-State superionic stamps. *Nano Letters* **7**, 446–451 (2007).

[29] M. LEE, R. O'HAYRE, F. B. PRINZ, & T. M. GUR. Electrochemical nanopatterning of Ag on solid-state ionic conductor $RbAg_4I_5$ using atomic force microscopy. *Applied Physics Letters* **85**, 3552–3554 (2004).

[30] J. OHI. Hydrogen energy cycle: An overview. *Journal of Materials Research* **20**, 3180–3187 (2005).

[31] B. C. HACKER & J. M. GRIMWOOD. *On the shoulders of Titans: A history of Project Gemini.* NASA, Washington, D.C. (1977).

[32] K. V. KORDESCH. 25 Years of fuel cell development (1951–1976). *Journal of the Electrochemical Society* **125**, 77C–88C (1978).

[33] M. L. PERRY & T. F. FULLER. A historical perspective on fuel cell technology in the 20th century. *Journal of the Electrochemical Society* **149**, S59–S67 (2002).

[34] A. ZUTTEL. Materials for hydrogen storage. *Materials Today* **6**, 24–33 (2003).

[35] U.S. DEPARTMENT OF ENERGY. Hydrogen Storage "Think Tank" Report (2003). Available at http://www1.eere.energy.gov/hydrogenandfuelcells/pdfs/h2_storage_think_tank.pdf.

[36] U.S. DEPARTMENT OF ENERGY. Hydrogen Program: 2006 Annual Progress Report. Available at http://www.hydrogen.energy.gov/annual_progress06.html.

[37] U.S. DEPARTMENT OF ENERGY. A Multiyear Plan for the Hydrogen R & D Program: Rationale, Structure, and Technology Road Maps (1999). Available at http://www.eere.energy.gov/hydrogenandfuelcells/pdfs/bk28424.pdf.

[38] W. GROCHALA & P. P. EDWARDS. Thermal decomposition of the non-interstitial hydrides for the storage and production of hydrogen. *Chemical Reviews* **104**, 1283–1316 (2004).

[39] F. SCHÜTH, B. BOGDANOVIĆ, & M. FELDERHOFF. Light metal hydrides and complex hydrides for hydrogen storage. *Chemical Communications* **2004**, 2249–2258 (2004).

[40] D. CHANDRA, J. REILLY, & R. CHELLAPPA. Metal hydrides for vehicular applications: The state of the art. *JOM: Journal of the Minerals, Metals, & Materials Society* 26–32 (February 2006).

[41] L. SCHLAPBACH & A. ZÜTTEL. Hydrogen-storage materials for mobile applications. *Nature* **414**, 353–358 (2001).

[42] M. BORN & J. R. OPPENHEIMER. Zur Quantentheorie der Molekeln. *Annalen der Physik* **84**, 457–484 (1927).

[43] C. ECKART. The Kinetic Energy of Polyatomic Molecules. *Physical Review* **46**, 383–387 (1934).

[44] G. CHESTER. The theory of the interaction of electrons with lattice vibrations in metals. *Advances in Physics* **10**, 357–400 (1961).

[45] W. KOHN. Electronic Structure of Matter-Wave Functions and Density Functionals. *Nobel Lecture* (1998). Available at http://www.nobel.se/chemistry/laureates/1998/kohn-lecture.html.

[46] P. HOHENBERG & W. KOHN. Inhomogeneous Electron Gas. *Physical Review* **136**, B864–B871 (1964).

[47] M. LEVY. Universal Variational Functionals of Electron Densities, First-Order Density Matrices, and Natural Spin-Orbitals and Solution of the v-Representability Problem. *Proceedings of the National Academy of Sciences* **76**, 6062–6065 (1979).

[48] M. LEVY. Electron densities in search of Hamiltonians. *Physical Review A* **26**, 1200–1208 (1982).

[49] E. H. LIEB. Density functionals for Coulomb systems. *International Journal of Quantum Chemistry* **24**, 243–277 (1983).

[50] W. KOHN & L. J. SHAM. Self-Consistent Equations Including Exchange and Correlation Effects. *Physical Review* **140**, A1133–A1138 (1965).

[51] H. W. PRESS, P. B. FLANNERY, S. A. TEUKOLSKY, & W. T. VETTERLING. *Numerical Recipes*. Cambridge University Press (1986).

[52] I. STICH, R. CAR, M. PARRINELLO, & S. BARONI. Conjugate gradient minimization of the energy functional: A new method for electronic structure calculation. *Physical Review B* **39**, 4997–5004 (1989).

[53] M. C. PAYNE, M. P. TETER, D. C. ALLAN, T. A. ARIAS, & J. D. JOANNOPOULOS. Iterative minimization techniques for ab initio total-energy calculations: molecular dynamics and conjugate gradients. *Reviews of Modern Physics* **64**, 1045–1097 (1992).

[54] O. GUNNARSSON & B. I. LUNDQUIST. Exchange and correlation in atoms, molecules, and solids by the spin-density-functional formalism. *Physical Review B* **13**, 4274–4298 (1976).

[55] O. GUNNARSSON & B. I. LUNDQUIST. Exchange and correlation in inhomogeneous electron systems. *Solid State Communications* **24**, 765–768 (1977).

[56] J. P. PERDEW & Y. WANG. Accurate and simple analytic representation of the electron-gas correlation energy. *Physical Review B* **45**, 13244–13249 (1992).

[57] J. P. PERDEW, K. BURKE, & M. ERNZERHOF. Generalized Gradient Approximation Made Simple. *Physical Review Letters* **77**, 3865–3868 (1996).

[58] R. MARTIN. *Electronic Structure: Basic Theory and Practical Methods*. Cambridge University Press (2004).

[59] W. KOCH & M. C. HOLTHAUSEN. *A Chemist's Guide to Density Functional Theory*. Wiley-VCH (2001).

[60] N. ASHCROFT & N. MERMIN. *Solid State Physics*. Thompson Learning (1976).

[61] F. BLOCH. Über die Quantenmechanik der Elektronen in Kristallgittern. *Zeitschrift für Physik* **52**, 555–600 (1928).

[62] A. BALDERESCHI. Mean-Value Point in the Brillouin Zone. *Physical Review B* **7**, 5212–5215 (1973).

[63] K. J. CHADI & M. L. COHEN. Special Points in the Brillouin Zone. *Physical Review B* **8**, 5747–5753 (1973).

[64] H. J. MONKHORST & J. D. PACK. Special points for Brillouin-zone integrations. *Physical Review B* **13**, 5188–5192 (1976).

[65] D. R. HAMANN, M. SCHLÜTER, & C. CHIANG. Norm-Conserving Pseudopotentials. *Physical Review Letters* **43**, 1494–1497 (1979).

[66] R. W. SHAW & W. A. HARRISON. Reformulation of the Screened Heine-Abarenkov Model Potential. *Physical Review* **163**, 604–611 (1967).

[67] M. L. COHEN & V. HEINE. *Solid State Physics*, volume 24. Academic Press (1970).

[68] L. KLEINMAN & D. M. BYLANDER. Efficacious Form for Model Pseudopotentials. *Physical Review Letters* **48**, 1425–1428 (1982).

[69] X. GONZE, P. KÄCKELL, & M. SCHEFFLER. Ghost states for separable, norm-conserving, Iab initioP pseudopotentials. *Physical Review B* **41**, 12264–12267 (1990).

[70] X. GONZE, R. STUMPF, & M. SCHEFFLER. Analysis of separable potentials. *Physical Review B* **44**, 8503–8513 (1991).

[71] M. S. HYBERTSEN & S. G. LOUIE. Electron correlation in semiconductors and insulators: Band gaps and quasiparticle energies. *Physical Review B* **34**, 5390–5413 (1986).

[72] G. THEURICH & N. A. HILL. Self-consistent treatment of spin-orbit coupling in solids using relativistic fully separable ab initio pseudopotentials. *Physical Review B* **64**, 073106 (2001).

[73] S. G. LOUIE, S. FROYEN, & M. L. COHEN. Nonlinear ionic pseudopotentials in spin-density-functional calculations. *Physical Review B* **26**, 1738–1742 (1982).

[74] D. VANDERBILT. Soft self-consistent pseudopotentials in a generalized eigenvalue formalism. *Physical Review B* **41**, 7892–7895 (1990).

[75] K. LAASONEN, A. PASQUARELLO, R. CAR, C. LEE, & D. VANDERBILT. Car-Parrinello molecular dynamics with Vanderbilt ultrasoft pseudopotentials. *Physical Review B* **47**, 10142–10153 (1993).

[76] P. E. BLÖCHL. Generalized separable potentials for electronic-structure calculations. *Physical Review B* **41**, 5414–5416 (1990).

[77] G. H. WANNIER. The structure of electronic excitation levels in insulating crystals. *Physical Review* **52**, 191–197 (1937).

[78] N. MARZARI & D. VANDERBILT. Maximally localized generalized Wannier functions for composite energy bands. *Physical Review B* **56**, 12847–12865 (1997).

[79] P. L. SILVESTRELLI, N. MARZARI, D. VANDERBILT, & M. PARRINELLO. Maximally-localized Wannier functions for disordered systems: Application to amorphous silicon. *Solid State Communications* **107**, 7–11 (1998).

[80] S. BARONI, S. DE GIRONCOLI, & A. D. CORSO. Phonons and related crystal properties from density-functional perturbation theory. *Reviews of Modern Physics* **73**, 515–561 (2001).

[81] S. BARONI, P. GIANNOZZI, & A. TESTA. Elastic Constants of Crystals from Linear-Response Theory. *Physical Review Letters* **59**, 2662–2665 (1987).

[82] M. BORN & K. HUANG. *Dynamical Theory of Crystal Lattices*. Oxford University Press (1954).

[83] L. VERLET. Computer 'experiments' classical fluids. I. Thermodynamical properties of Lennard-Jones molecules. *Physical Review* **159**, 98–103 (1967).

[84] S. AUERBACH & A. FRIEDMAN. Long-time behavior of numerically computed orbits: Small and intermediate timestep analysis of one-dimensional systems. *Journal of Computational Physics* **93**, 189–223 (1991).

[85] M. P. ALLEN & D. J. TILDESLEY. *Computer Simulation of Liquids*. Oxford University Press (1987).

[86] W. C. SWOPE, H. C. ANDERSEN, P. H. BERENS, & K. R. WILSON. A computer simulation method for the calculation of equilibrium constants for the formation of physical clusters of molecules: Application to small water clusters. *Journal of Chemical Physics* **76**, 637–649 (1982).

[87] D. FRENKEL & B. SMIT. *Understanding Molecular Simulation: From Algorithms to Applications*. Academic Press (1996).

[88] H. C. ANDERSEN. Molecular dynamics simulations at constant pressure and/or temperature. *Journal of Chemical Physics* **72**, 2384–2393 (1980).

[89] G. GALLI & A. PASQUARELLO. First-principles molecular dynamics. In *Computer Simulation in Chemical Physics*, volume 73, 261–313. Kluwer Academic Publishers (1993).

[90] M. E. TUCKERMAN & M. PARRINELLO. Integrating the Car-Parrinello equations. I. Basic integration techniques. *Journal of Chemical Physics* **101**, 1302–1315 (1994).

[91] P. H. HÜNENBERGER. Thermostat algorithms for molecular dynamics simulations. *Advances in Polymer Science* **173**, 105–149 (2005).

[92] P. UMARI & A. PASQUARELLO. Ab initio Molecular Dynamics in a Finite Homogeneous Electric Field. *Physical Review Letters* **89**, 157602 (2002).

[93] I. SOUZA, J. I. NIGUEZ, & D. VANDERBILT. First-Principles Approach to Insulators in Finite Electric Fields. *Physical Review Letters* **89**, 117602 (2002).

[94] S. NOSÉ. A unified formulation of the constant temperature molecular dynamics methods. *Journal of Chemical Physics* **81**, 511–519 (1984).

[95] S. NOSÉ. A molecular dynamics method for simulations in the canonical ensemble 1. *Molecular Physics* **52**, 255–268 (1984).

[96] S. NOSÉ. An extension of the canonical ensemble molecular dynamics method. *Molecular Physics* **57**, 187–191 (1986).

[97] W. G. HOOVER. Canonical dynamics: Equilibrium phase-space distributions. *Physical Review A* **31**, 1695–697 (1985).

[98] W. G. HOOVER. Constant-pressure equations of motion. *Physical Review A* **34**, 2499–2500 (1986).

[99] P. E. BLÖCHL & M. PARRINELLO. Adiabaticity in first-principles molecular dynamics. *Physical Review B* **45**, 9413–9416 (1992).

[100] G. J. MARTYNA, M. L. KLEIN, & M. E. TUCKERMAN. Nose-Hoover chains: The canonical ensemble via continuous dynamics. *Journal of Chemical Physics* **97**, 2635–2643 (1992).

[101] M. PARRINELLO & A. RAHMAN. Crystal Structure and Pair Potentials: A Molecular-Dynamics Study. *Physical Review Letters* **45**, 1196–1199 (1980).

[102] M. PARRINELLO & A. RAHMAN. Polymorphic transitions in single crystals: A new molecular dynamics method. *Journal of Applied Physics* **52**, 7182–7190 (1981).

[103] D. C. RAPAPORT. *The Art of Molecular Dynamics Simulation*. Cambridge University Press (1995).

[104] D. A. MCQUARRIE. *Statistical Mechanics*. Harper and Row (1976).

[105] C. TUBANDT & E. LORENZ. Molekularzustand und elektrisches Leitvermögen kristallisierter Salze. *Zeitschrift für Physikalische Chemie (Leipzig)* **87**, 513–542 (1914).

[106] T. MINAMI, T. SAITO, & M. TATSUMISAGO. Preparation and characterization of α-AgI frozen superionic glasses. *Solid State Ionics* **86-8**, 415–420 (1996).

[107] P. BOOLCHAND & W. J. BRESSER. Mobile silver ions and glass formation in solid electrolytes. *Nature* **410**, 1070–1073 (2001).

[108] L. W. STROCK. Kristallstruktur des Hochtemperatur-Jodsilbers α-AgJ. *Zeitschrift für Physikalische Chemie (Leipzig)* **B25**, 441–459 (1934).

[109] L. W. STROCK. Ergänzung und Berichtigung zu: "Kristallstruktur des Hochtemperatur-Jodsilbers α-AgJ". *Zeitschrift für Physikalische Chemie (Leipzig)* **B31**, 132–136 (1936).

[110] R. J. CAVA, F. REIDINGER, & B. J. WUENSCH. Single Crystal Neutron-Diffraction Study of AgI Between 23 and 300 °C. *Solid State Communications* **24**, 411–416 (1977).

[111] A. KVIST & A. M. JOSEFSON. The electrical conductivity of solid and molten silver iodide. *Zeitschrift für Naturforschung A* **23**, 625 (1968).

[112] A. KVIST & R. TÄRNEBERG. Self-diffusion of silver ions in the cubic high temperature modification of silver iodide. *Zeitschrift für Naturforschung A* **25**, 257–259 (1970).

[113] B.-E. MELLANDER. Electrical conductivity and activation volume of the solid electrolyte phase α-AgI and the high-pressure phase fcc AgI. *Physical Review B* **26**, 5886–5896 (1982).

[114] J. AKELLA, S. N. VAIDYA, & G. KENNEDY. Melting of Silver Halides at High Pressure. *Journal of Applied Physics* **40**, 2800–2805 (1969).

[115] V. M. NIELD, D. KEEN, W. HAYES, & R. L. MCGREEVY. Structure and fast-ion conduction in α-AgI. *Solid State Ionics* **66**, 247–258 (1993).

[116] P. VASHISHTA & A. RAHMAN. Ionic Motion in α-AgI. *Physical Review Letters* **40**, 1337–1340 (1978).

[117] M. PARRINELLO, A. RAHMAN, & P. VASHISHTA. Structural Transitions in Superionic Conductors. *Physical Review Letters* **50**, 1073–1076 (1983).

[118] J. L. TALLON. Constant-stress molecular dynamics: The phase diagram of silver iodide. *Physical Review B* **38**, 9069–9079 (1988).

[119] F. SHIMOJO & M. KOBAYASHI. Molecular Dynamics Studies of Molten AgI. I. Structure and Dynamical Properties. *Journal of the Physical Society of Japan* **60**, 3725–3735 (1991).

[120] K. O'SULLIVAN, G. CHIAROTTI, & P. A. MADDEN. Silver-ion disorder in α-AgI: A computer simulation study. *Physical Review B* **43**, 13536–13548 (1991).

[121] F. ZIMMER, P. BALLONE, J. MAIER, & M. PARRINELLO. Charge carrier interactions in ionic conductors: A classical molecular-dynamics and Monte Carlo study on AgI. *Journal of Chemical Physics* **112**, 6416–6423 (2000).

[122] Y. YOKOYAMA & M. KOBAYASHI. Nano-scaled dynamics of iodine-tetrahedron in α-AgI. *Solid State Ionics* **159**, 79–87 (2003).

[123] C. R. I. CHISHOLM, Y. H. JANG, S. M. HAILE, & W. A. GODDARD III. Superprotonic phase transition of $CsHSO_4$: A molecular dynamics simulation study. *Physical Review B* **72**, 134103 (2005).

[124] S. BARONI, A. D. CORSO, S. DE GIRONCOLI, P. GIANNOZZI, C. CAVAZZONI, G. BALLABIO, S. SCANDOLO, G. CHIAROTTI, P. FOCHER, A. PASQUARELLO, K. LAASONEN, A. TRAVE, R. CAR, N. MARZARI, & A. KOKALJ. Quantum-ESPRESSO software package. Available for download at http://www.quantum-espresso.org/.

[125] M. FUCHS & M. SCHEFFLER. Ab initio pseudopotentials for electronic structure calculations of poly-atomic systems using density-functional theory. *Computer Physics Communications* **119**, 67–98 (1999). fhi98pp software package available for download at http://www.rz-berlin.mpg.de/th/fhi98md/.

[126] N. TROULLIER & J. L. MARTINS. Efficient pseudopotentials for plane-wave calculations. *Physical Review B* **43**, 1993–2006 (1991).

[127] F. BIRCH. Finite strain isotherm and velocities for single-crystal and polycrystalline NaCl at high pressures and 300 degrees K. *Journal of Geophysical Research* **83**, 1257–1268 (1978).

[128] G. H. SHAW. Elastic behavior near phase transitions with negative dP/dT. *Journal of Geophysical Research B* **83**, 3519–3524 (1978).

[129] J. L. TALLON & R. G. BUCKLEY. Fast-ion transition in FCC silver iodide. *Solid State Communications* **47**, 563–566 (1983).

[130] L. J. SHAM & W. KOHN. One-Particle Properties of an Inhomogeneous Interacting Electron Gas. *Physical Review* **145**, 561–567 (1966).

[131] P. VOGL. Dynamical effective charges in semiconductors: A pseudopotential approach. *Journal of Physics C: Solid State Physics.* **11**, 251–262 (1978).

[132] P. BRÜESCH, W. BÜHRER, & H. J. M. SMEETS. Far-infrared, microwave, and inelastic neutron scattering experiments of the superionic conductor α-AgI. *Physical Review B* **22**, 970–981 (1980).

[133] D. DE FONTAINE. Mechanical instabilities in the BCC lattice and the beta to omega phase transformation. *Acta Metallurgica* **18**, 275–279 (1970).

[134] C. STASSIS, J. ZARETSKY, & N. WAKABAYASHI. Lattice dynamics of bcc zirconium. *Physical Review Letters* **41**, 1726–1729 (1978).

[135] K. WAKAMURA. Correlation among the transition and melting temperatures and dielectric parameters in some fast ionic conductors. *Solid State Communications* **82**, 705–710 (1992).

[136] M. ANIYA & K. WAKAMURA. Phonons and the mechanism of ion transport in some superionic conductors. *Physica B* **219&220**, 463–465 (1996).

[137] B. J. WUENSCH. Cation distributions, bonding and transport behavior in silver and copper fast-ion conductors with simple anion packings. *Materials Science and Engineering* **B18**, 186–200 (1993).

[138] H. ARAKI, T. KOISHI, & S. TAMAKI. Transport Properties in Molten Silver Iodide. *Journal of the Physical Society of Japan* **68**, 134–139 (1999).

[139] P. A. MADDEN, K. F. O'SULLIVAN, & G. CHIAROTTI. Ordering of the silver ions in α-AgI: A mechanism for the $\alpha \rightarrow \beta$ phase transition. *Physical Review B* **45**, 10206–10212 (1992).

[140] C. SEOK & D. W. OXTOBY. Phase transitions in AgI. *Physical Review B* **56**, 11485–11492 (1997).

[141] C. SEOK & D. W. OXTOBY. Mechanism of Ag^+ ordering in AgI. *Physical Review B* **58**, 5146–5148 (1998).

[142] G. SZABÓ. Lattice gas model on tetrahedral sites of a BCC lattice. *Journal of Physics C: Solid State Physics* **19**, 3775–3787 (1986).

[143] W. BIERMANN & W. JOST. Elektrische Leitfahigkeit fester Elektrolyte mit strukturellen Fehlordnung. *Zeitschrift für Physikalische Chemie (Frankfurt am Main)* **17**, 139–141 (1960).

[144] B. C. WOOD & N. MARZARI. Dynamical structure, bonding, and thermodynamics of the superionic sublattice in α-AgI. *Physical Review Letters* **97**, 166401 (2006).

[145] S. DUNN. Hydrogen futures: toward a sustainable energy system. *International Journal of Hydrogen Energy* **27**, 235–264 (2002).

[146] K. D. KREUER. On solids with liquidlike properties and the challenge to develop new proton-conducting separator materials for intermediate-temperature fuel cells. *ChemPhysChem* **3**, 771–775 (2002).

[147] S. HAILE. Fuel cell materials and components. *Acta Materialia* **51**, 5981–6000 (2003).

[148] A. I. BARANOV, L. A. SHUVALOV, & N. M. SHCHAGINA. Superion conductivity and phase transitions in $CsHSO_4$ and CsHSeO4 crystals. *JETP Letters* **36**, 459–462 (1982).

[149] S. M. HAILE, D. A. BOYSEN, C. R. I. CHISHOLM, & R. B. MERLE. Solid acids as fuel cell electrolytes. *Nature* **410**, 910–913 (2001).

[150] D. A. BOYSEN, T. UDA, C. R. I. CHISHOLM, & S. M. HAILE. High-performance solid acid fuel cells through humidity stabilization. *Science* **303**, 68–70 (2004).

[151] S. M. HAILE, C. R. I. CHISHOLM, K. SASAKI, D. A. BOYSEN, & T. UDA. Solid acid proton conductors: from laboratory curiosities to fuel cell electrolytes. *Faraday Discussions* **134**, 17–39 (2007).

[152] A. V. BELUSHKIN, M. A. ADAMS, S. HULL, A. I. KOLESNIKOV, & L. A. SHUVALOV. Structure and dynamics of different phases of the superprotonic conductor $CsHSO_4$. *Physica B* **213-214**, 1034–1036 (1995).

[153] E. G. PONYATOVSKII, V. I. RASHCHUPKIN, V. V. SINITSYN, A. I. BARANOV, L. A. SCHUVALOV, & N. M. SHCHAGINA. P-T phase diagram of a proton superionic conductor $CsHSO_4$. *JETP Letters* **41**, 139–141 (1985).

[154] M. PHAM-THI, P. COLOMBAN, A. NOVAK, & R. BLINC. Phase transitions in superionic protonic conductors $CsHSO_4$ and $CsHSeO_4$. *Solid State Communications* **55**, 265–270 (1985).

[155] B. V. MERINOV, A. I. BARANOV, L. A. SHUVALOV, & B. A. MAKSIMOV. Crystal structure of superionic phase $CsDSO_4$. *Kristallografiya* **32**, 86–92 (1987).

[156] K. D. KREUER. Fast proton conductivity: A phenomenon between the solid and the liquid state? *Solid State Ionics* **94**, 55–62 (1997).

[157] A. V. BELUSHKIN, R. L. MCGREEVY, P. ZETTERSTROM, & L. A. SHUVALOV. Mechanism of superprotonic conductivity in $CsHSO_4$. *Physica B* **241-243**, 323–325 (1998).

[158] P. ZETTERSTRÖM, A. V. BELUSHKIN, R. L. MCGREEVY, & L. A. SHUVALOV. Structure and proton conduction in $CsDSO_4$. *Solid State Ionics* **116**, 321–329 (1999).

[159] J. C. BADOT & P. COLOMBAN. RF-microwave dielectric relaxations and phase transitions in superionic protonic acid sulphates (selenates). *Solid State Ionics* **35**, 143–149 (1989).

[160] A. V. BELUSHKIN, C. J. CARLILE, & L. A. SHUVALOV. The diffusion of protons in the superionic conductor $CsHSO_4$ by quasielastic neutron scattering. *Journal of Physics: Condensed Matter* **4**, 389–398 (1992).

[161] C. J. T. VON GROTTHUSS. Sur la décomposition de l'eau et des corps qu'elle tient en dissolution à l'aide de l'électricité galvanique. *Annales de Chimie* **58**, 54–73 (1806).

[162] S. CUKIERMAN. Et tu Grotthuss! and other unfinished stories. *Biochimica et Biophysica Acta - Bioenergetics* **1757**, 876–885 (2006).

[163] N. AGMON. The Grotthuss mechanism. *Chemical Physics Letters* **244**, 456–462 (1995).

[164] W. MÜNCH, K. D. KREUER, U. TRAUB, & J. MAIER. A molecular dynamics study of the high proton conducting phase of $CsHSO_4$. *Solid State Ionics* **77**, 10–14 (1995).

[165] W. MÜNCH, K. D. KREUER, U. TRAUB, & J. MAIER. Proton transfer in the three-dimensional hydrogen bond network of the high temperature phase of $CsHSO_4$: a molecular dynamics study. *Journal of Molecular Structure* **281**, 1–8 (1996).

[166] X. KE & I. TANAKA. Proton transfer mechanism in solid $CsHSO_4$ by first-principles study. *Solid State Ionics* **172**, 145–148 (2004).

[167] X. KE & I. TANAKA. Atomistic mechanism of proton conduction in solid $CsHSO_4$ by a first-principles study. *Physical Review B* **69**, 165114 (2004).

[168] P. GIANNOZZI. Atom: A pseudopotential generation package. Available for download at http://www.nest.sns.it/~giannozz/.

[169] A. V. BELUSHKIN, W. I. F. DAVID, R. M. IBBERSON, & L. A. SHUVALOV. High-resolution neutron powder diffraction studies of the structure of $CsDSO_4$. *Acta Crystallographica Section B* **B47**, 161–166 (1991).

[170] K. ITOH, T. UKEDA, T. OZAKI, & E. NAKAMURA. Redetermination of the structure of caesium hydrogensulfate. *Acta Crystallographica Section C* **46**, 358–361 (1990).

[171] M. TUCKERMAN, K. LAASONEN, M. SPRIK, & M. PARRINELLO. Ab initio molecular dynamics simulation of the solvation and transport of hydronium and hydroxyl ions in water. *Journal of Chemical Physics* **103**, 150–161 (1995).

[172] D. MARX, M. E. TUCKERMAN, J. HUTTER, & M. PARRINELLO. The nature of the hydrated excess proton in water. *Nature* **397**, 601–604 (1999).

[173] S. HAYASHI & M. MIZUNO. Proton diffusion in the superprotonic phase of $CsHSO_4$ studied by 1H NMR relaxation. *Solid State Ionics* **171**, 289–293 (2004).

[174] D. LAAGE & J. HYNES. A molecular jump mechanism of water reorientation. *Science* **311**, 832–835 (2006).

[175] Z. JIRAK, M. DLOUHA, S. VRATISLAV, A. M. BALAGUROV, A. I. BESKROVNYI, V. I. GORDELII, I. D. DATT, & L. A. SHUVALOV. A neutron-diffraction study of the superionic phase in $CsHSO_4$. *Physica Status Solidi A* **100**, K117–K123 (1987).

[176] A. V. BELUSHKIN, C. J. CARLILE, W. I. F. DAVID, R. M. IBBERSON, L. A. SHUVALOV, & W. ZAJAC. Neutron scattering study of crystal structure and proton diffusion in protonic conductors with hydrogen bonds. *Physica B* **174**, 268–271 (1991).

[177] J. M. HAMMERSLEY. The distribution of distance in a hypersphere. *Annals of Mathematical Statistics* **21**, 447–452 (1950).

[178] R. D. LORD. The distribution of distance in a hypersphere. *Annals of Mathematical Statistics* **25**, 794–798 (1954).

[179] V. V. SINITSYN, E. G. PONYATOVSKII, A. I. BARANOV, A. V. TREGUBCHENKO, & L. SHUVALOV. Proton-conductivity anisotropy in $CsHSO_4$ and $CsDSO_4$ crystals and its response to hydrostatic pressure. *Soviet Physics JETP* **73**, 386–393 (1991).

[180] P. A. GIGUÈRE. Bifurcated hydrogen bonds in water. *Journal of Raman Spectroscopy* **15**, 354–359 (1984).

[181] M. BOERO, K. TERAKURA, T. IKESHOJI, C. C. LIEW, & M. PARRINELLO. Hydrogen bonding and dipole moment of water at supercritical conditions: a first-principles molecular dynamics study. *Physical Review Letters* **85**, 3245–3248 (2000).

[182] M. BOERO, T. IKESHOJI, & K. TERAKURA. Density and temperature dependence of proton diffusion in water: a first-principles molecular dynamics study. *ChemPhysChem* **6**, 1775–1779 (2005).

[183] S. IZVEKOV & G. A. VOTH. Multiscale coarse graining of liquid-state systems. *Journal of Chemical Physics* **123**, 044505 (2005).

[184] D. R. HAMANN. H_2O hydrogen bonding in density-functional theory. *Physical Review B* **55**, R10157–R10160 (1997).

[185] M. ERNZERHOF & G. E. SCUSERIA. Assessment of the PerdewBurkeErnzerhof exchange-correlation functional. *Journal of Chemical Physics* **110**, 5029–5036 (1999).

[186] J. IRETA, J. NEUGEBAUER, & M. SCHEFFLER. On the Accuracy of DFT for Describing Hydrogen Bonds: Dependence on the Bond Directionality. *Journal of Physical Chemistry A* **108**, 5692–5698 (2004).

[187] Y. KANAI, X. WANG, A. SELLONI, & R. CAR. Testing the TPSS meta-generalized-gradient-approximation exchange-correlation functional in calculations of transition states and reaction barriers. *Journal of Chemical Physics* **125**, 234104 (2006).

[188] K. D. KREUER. Proton conductivity: materials and applications. *Chemistry of Materials* **8**, 610–641 (1996).

[189] S. KOVAL, J. KOHANOFF, R. L. MIGONI, & E. TOSATTI. Ferroelectricity and isotope effects in hydrogen-bonded KDP crystals. *Physical Review Letters* **89**, 187602 (2002).

[190] B. C. WOOD & N. MARZARI. Proton dynamics in superionic $CsHSO_4$. *Physical Review B (accepted)* (2007).

[191] B. BOGDANOVIĆ & M. SCHWICKARDI. Ti-doped alkali metal aluminum hydrides as potential novel reversible hydrogen storage materials. *Journal of Alloys and Compounds* **253&254**, 1–9 (1997).

[192] B. BOGDANOVIĆ, R. A. BRAND, A. MARJANOVIC, M. SCHWICKARDI, & J. TOLLE. Metal-doped sodium aluminium hydrides as potential new hydrogen storage materials. *Journal of Alloys and Compounds* **302**, 36–58 (2000).

[193] R. A. ZIDAN, S. TAKARA, A. G. HEE, & C. M. JENSEN. Hydrogen cycling behavior of zirconium and titanium-zirconium-doped sodium aluminum hydride. *Journal of Alloys and Compounds* **285**, 119–122 (1999).

[194] C. M. JENSEN, R. ZIDAN, N. MARIELS, A. HEE, & C. HAGEN. Advanced titanium doping of sodium aluminum hydride: Segue to a practical hydrogen storage material? *International Journal of Hydrogen Energy* **24**, 461–465 (1999).

[195] S. V. ALAPATI, J. K. JOHNSON, & D. S. SHOLL. Identification of destabilized metal hydrides for hydrogen storage using first principles calculations. *Journal of Physical Chemistry B* **110**, 8769–8776 (2006).

[196] M. E. ARROYO Y DE DOMPABLO & G. CEDER. First principles investigations of complex hydrides AMH_4 and A_3MH_6 (A=Li,Na,K, M=B,Al,Ga) as hydrogen storage systems. *Journal of Alloys and Compounds* **364**, 6–12 (2004).

[197] A. PELES, J. A. ALFORD, Z. MA, L. YANF, & M. Y. CHOU. First-principles study of $NaAlH_4$ and Na_3AlH_6 complex hydrides. *Physical Review B* **70**, 165105 (2004).

[198] A. AGUAYO & D. J. SINGH. Electronic structure of the complex hydride $NaAlH_4$. *Physical Review B* **69**, 155103 (2004).

[199] J. ÍÑIGUEZ, T. YILDIRIM, T. J. UDOVIC, M. SULIC, & C. M. JENSEN. Structure and hydrogen dynamics of pure and Ti-doped sodium alanate. *Physical Review B* **70**, 060101 (2004).

[200] V. OZOLINS, E. H. MAJZOUB, & T. J. UDOVIC. Electronic structure and Rietveld refinement parameters of Ti-doped sodium alanates. *Journal of Alloys and Compounds* **375**, 1–10 (2004).

[201] C. M. ARAÙJO, S. LI, R. AHUJA, & P. JENA. Vacancy-mediated hydrogen desorption in $NaAlH_4$. *Physical Review B* **72**, 165101 (2005).

[202] O. M. LØVVIK, O. SWANG, & S. M. OPALKA. Modeling alkali alanates for hydrogen storage by density-functional band-structure calculations. *Journal of Materials Research* **20**, 3199–3213 (2005).

[203] O. M. LØVVIK & S. M. OPALKA. Density functional calculations of Ti-enhanced $NaAlH_4$. *Physical Review B* **71**, 054103 (2005).

[204] J. ÍÑIGUEZ & T. YILDIRIM. First-principles study of Ti-doped sodium alanate surfaces. *Applied Physics Letters* **86**, 103109 (2005).

[205] X. KE & I. TANAKA. Decomposition reactions for $NaAlH_4$, Na_3AlH_6, and NaH: First-principles study. *Physical Review B* **71**, 024117 (2005).

[206] J. W. LAUHER, D. DOUGHERTY, & P. J. HERLEY. Sodium tetrahydroaluminate. *Acta Crystallographica B* **35**, 1454–1456 (1979).

[207] B. C. HAUBACK, H. W. BRINKS, C. M. JENSEN, K. MURPHY, & A. J. MAELAND. Neutron diffraction structure determination of $NaAlD_4$. *Journal of Alloys and Compounds* **358**, 142–145 (2003).

[208] O. PALUMBO, R. CANTELLI, A. PAOLONE, C. M. JENSEN, & S. S. SRINIVASAN. Motion of point defects and monitoring of chemical reactions in sodium aluminium hydride. *Journal of Alloys and Compounds* **404-406**, 748–751 (2005).

[209] O. PALUMBO, R. CANTELLI, A. PAOLONE, C. M. JENSEN, & S. S. SRINIVASAN. Point defect dynamics and evolution of chemical reactions in alanates by anelastic spectroscopy. *Journal of Physical Chemistry B* **109**, 1168–1173 (2005).

[210] T. J. FRANKCOMBE & O. M. L. VVIK. The crystal structure and surface energy of $NaAlH_4$: A comparison of DFT methodologies. *Journal of Physical Chemistry B* **110**, 622–630 (2006).

[211] R. S. KUMAR, E. KIM, O. TSCHAUNER, & A. L. CORNELIUS. Pressure-induced structural phase transition in $NaAlH_4$. *Physical Review B* **75**, 174110 (2007).

[212] J. P. BASTIDE, B. BONNETOT, J. M. LETOFFE, & P. CLAUDY. Polymorphic transition of the trisodium hexahydroaluminate Na_3AlH_6. *Materials Research Bulletin* **16**, 91–96 (1981).

[213] E. H. MAJZOUB & K. F. MCCARTY. Lattice dynamics of $NaAlH_4$ from high-temperature single-crystal Raman scattering and ab initio calculations: Evidence of highly stable AlH_4^- anions. *Physical Review B* **71**, 024118 (2005).

[214] M.-Y. CHOU. Private communication (2006).

[215] T. VEGGE. Equilibrium structure and Ti-catalyzed H_2 desorption in $NaAlH_4$ nanoparticles from density functional theory. *Physical Chemistry Chemical Physics* **14**, 4853–4861 (2006).

[216] S. LI, P. JENA, & R. AHUJA. Effect of Ti and metal vacancies on the electronic structure, stability, and dehydrogenation of Na_3AlH_6: Supercell band-structure formalism and gradient-corrected density-functional theory. *Physical Review B* **73**, 214107 (2006).

[217] C. WOLVERTON, V. OZOLINS, & M. ASTA. Hydrogen in aluminum: First-principles calculations of structure and thermodynamics. *Physical Review B* **69**, 144109 (2004).

[218] A. ZALUSKA & L. ZALUSKI. Structure, catalysis and atomic reactions on the nano-scale: a systematic approach to metal hydrides for hydrogen storage. *Applied Physics A* **72**, 157–165 (2001).

[219] A. MARASHDEH, R. A. OLSEN, O. M. L. VVIK, & G.-J. KROES. A density functional theory study of Ti-doped $NaAlH_4$ clusters. *Chemical Physics Letters* **426**, 180–186 (2006).

[220] C. M. ARAUJO, R. AHUJA, & J. M. O. GUILLEN. Role of titanium in hydrogen desorption in crystalline sodium alanate. *Applied Physics Letters* **86**, 251913 (2005).

[221] J. M. BELLOSTA VON COLBE, B. BOGDANOVIĆ, M. FELDERHOFF, A. POMMERIN, & F. SCHÜTH. Recording of hydrogen evolution - A way for controlling the doping process of sodium alanate by ball milling. *Journal of Alloys and Compounds* **370**, 104–109 (2004).

[222] D. SUN, T. KIYOBAYASHI, H. T. TAKESHITA, N. KURIYAMA, & C. M. JENSEN. X-ray diffraction studies of titanium and zirconium doped $NaAlH_4$: elucidation of doping induced structural changes and their relationship to enhanced hydrogen storage properties. *Journal of Alloys and Compounds* **337**, L8–L11 (2002).

[223] K. J. GROSS, E. H. MAJZOUB, & S. W. SPANGLER. The effects of titanium precursors on hydriding properties of alanates. *Journal of Alloys and Compounds* **356**, 423–428 (2003).

[224] D. VANDERBILT. USPP: Ultrasoft Pseudopotential Generation Package. Available for download at http://www.physics.rutgers.edu/~dhv/uspp/.

[225] A. J. DU, S. C. SMITH, & G. LU. Role of charge in destabilizing AlH_4 and BH_4 complex anions for hydrogen storage applications: Ab initio density functional calculations. *Physical Review B* **74**, 193405 (2006).

[226] R. T. WALTERS & J. H. SCOGIN. A reversible hydrogen storage mechanism for sodium alanate: the role of alanes and the catalytic effect of the dopant. *Journal of Alloys and Compounds* **379**, 135–142 (2004).

[227] P. J. TURNER. Grace: A WYSIWYG 2D Plotting Tool. Available for download at http://plasma-gate.weizmann.ac.il/Grace/.

[228] W. HUMPHREY, A. DALKE, & K. SCHULTEN. VMD – Visual Molecular Dynamics. *Journal of Molecular Graphics* **14**, 33 (1996). Available for download at http://www.ks.uiuc.edu/Research/vmd/.

[229] J. YATES. *First principles calculation of NMR parameters*. Ph.D. thesis, Cambridge University, UK (2002).

[230] A. EARNSHAW & N. GREENWOOD. *Chemistry of the Elements (2nd Ed.)*. Pergamon Press Ltd. (1997).

[231] C. D. GODSIL & G. F. ROYLE. *Algebraic Graph Theory*. Graduate Texts in Mathematics. Springer-Verlag (2001).

[232] S. WARSHALL. A theorem on Boolean matrices. *Journal of the Association of Computing Machinery* **9**, 11–12 (1962).

[233] R. CHITRA & S. YASHONATH. Estimation of error in the diffusion coefficient from molecular dynamics simulations. *Journal of Physical Chemistry B* **101**, 5437–5445 (1997).

[234] A. VAN DER VEN, G. CEDER, M. ASTA, & P. D. TEPESCH. First-principles theory of ionic diffusion with nondilute carriers. *Physical Review B* **64**, 184307 (2001).

[235] C. UEBING & R. GOMER. Determination of surface diffusion coefficients by Monte Carlo methods: Comparison of fluctuation and KuboGreen methods. *Journal of Chemical Physics* **100**, 7759–7766 (1994).

[236] Y. ZHOU & G. H. MILLER. Green-Kubo formulas for mutual diffusion coefficients in multicomponent systems. *Journal of Physical Chemistry* **100**, 5516–5524 (1996).

[237] R. GOMER. Diffusion of adsorbates on metal surfaces. *Reports on Progress in Physics* **53**, 9170–1002 (1990).

[238] R. ZWANZIG & N. K. AILAWADI. Statistical Error Due to Finite Time Averaging in Computer Experiments. *Physical Review* **182**, 280–283 (1969).

[239] W. W. WOOD. In *Physics of Simple Liquids*. North-Holland, Amsterdam (1968).

[240] E. B. SMITH & B. H. WELLS. Estimating errors in molecular simulation calculations. *Molecular Physics* **52**, 701–704 (1984).